JYU DISSERTATIONS 844

Ilia Sokolovskii

Multiscale Molecular Dynamics Simulations of Enhanced Excitation Energy Transport in Organic Microcavities

UNIVERSITY OF JYVÄSKYLÄ
FACULTY OF MATHEMATICS
AND SCIENCE

JYU DISSERTATIONS 844

Ilia Sokolovskii

Multiscale Molecular Dynamics Simulations of Enhanced Excitation Energy Transport in Organic Microcavities

Esitetään Jyväskylän yliopiston matemaattis-luonnontieteellisen tiedekunnan suostumuksella
julkisesti tarkastettavaksi Ylistönrinteen auditoriossa Kem4
marraskuun 11. päivänä 2024 kello 12.

Academic dissertation to be publicly discussed, by permission of
the Faculty of Mathematics and Science of the University of Jyväskylä,
in Ylistönrinne, auditorium Kem4, on November 11, 2024, at 12 o'clock.

JYVÄSKYLÄN YLIOPISTO
UNIVERSITY OF JYVÄSKYLÄ

JYVÄSKYLÄ 2024

Editors
Gerrit Groenhof
Department of Chemistry, University of Jyväskylä
Päivi Vuorio
Open Science Centre, University of Jyväskylä

ISBN 978-952-86-0379-5
ISSN 2489-9003

Permanent link to this publication: http://urn.fi/URN:ISBN:978-952-86-0379-5

ABSTRACT

Sokolovskii, Ilia
Multiscale Molecular Dynamics Simulations of Enhanced Excitation Energy Transport in Organic Microcavities

Organic photovoltaics provide an alternative to conventional silicon-based solar cells, which currently dominate the global photovoltaics market. Despite several critical advantages of organic solar cells over their inorganic counterparts, the energy transport in organic materials is severely impeded by the structural disorder, which makes the excitation carriers move by means of incoherent hops between neighbouring molecular sites. This process is inefficient in comparison with the motion of electrons and holes in inorganic materials, resulting in significantly lower efficiencies of the organic solar cells. To address this challenge, mixing molecular excitations with confined light modes of optical cavities has been proposed. In the limit of strong interaction, these two constituents hybridize into quasiparticles called polaritons, which inherit properties of both molecular excitons and cavity light modes. Owing to the group velocity of polaritons, their propagation should be ballistic and long-range. However, according to experiments, the transport of polaritons is more intricate and can be either ballistic or diffusive depending on the parameters of the light-matter system. To bring atomistic insights into this phenomenon, we utilise a multiscale molecular dynamics model based on a hybrid Quantum Mechanics/Molecular Mechanics description of the molecules and their chemical environment. In this dissertation, we focus on a systematic investigation of the excitation energy transport in organic microcavities. The results of the performed simulations allow us to propose a general mechanism of such a cavity-enhanced transport. Furthermore, we investigate how the transport is modified along the polariton dispersion and with a change in the cavity quality factor. We also suggest and test a practical means of efficient excitation energy transport by a photochemical reaction. We believe that the insights provided in the dissertation, pave the way towards rational design of molecule-cavity systems for coherent exciton transport.

Keywords: strong light-matter coupling, polaritons, excitation transport, molecular dynamics

TIIVISTELMÄ (ABSTRACT IN FINNISH)

Sokolovskii, Ilia
Viritysenergian tehostuneen kuljetuksen tutkiminen orgaanisissa mikrokaviteeteissa monitasoisilla molekyylidynamiikkasimulaatioilla

Orgaaniset aurinkosähköratkaisut tarjoavat vaihtoehdon tavanomaisille piipohjaisille aurinkokennoille, jotka tällä hetkellä hallitsevat globaaleja aurinkosähkömarkkinoita. Huolimatta useista keskeisistä orgaanisten aurinkokennojen hyödyistä verrattuna epäorgaanisiin aurinkokennoihin, energian kuljetus orgaanisissa materiaaleissa on selvästi hitaampaa johtuen niiden rakenteellisesta epäjärjestyksestä. Tästä epäjärjestyksestä aiheutuen viritysten kantajat liikkuvat vierekkäisten molekyylipaikkojen välillä epäkoherenttien siirtymien avulla, mikä on tehotonta verrattuna elektronien ja aukkojen liikkeeseen epäorgaanisissa materiaaleissa, tehden orgaanisista aurinkokennoista huomattavasti epäorgaanisia tehottomampia. Ratkaisuna tähän on esitetty molekulaaristen viritysten sekoittamista optisten kaviteettien rajoitettujen valomoodien kanssa. Vahvan vuorovaikutuksen vallitessa nämä kaksi osatekijää hybridisoituvat polaritoneiksi kutsutuiksi kvasihiukkasiksi, joilla on sekä molekyyliviritysten että kaviteetin valomoodien ominaisuudet. Polaritonien ryhmänopeuden vuoksi niiden etenemisen pitäisi olla ballistista ja pitkän kantaman etenemistä. Kokeellisten tulosten mukaan polaritonien eteneminen on kuitenkin monimutkaisempaa, ja se voi olla joko ballistista tai diffuusiota riippuen valo-ainesysteemin parametreista. Saadaksemme atomitason tietoa tästä ilmiöstä hyödynnämme monitasoista molekyylidynamiikkamallia, jossa molekyylejä ja niiden kemiallista ympäristöä mallinnetaan käyttäen kvantti- ja molekyylimekaniikan yhdistelmää. Tässä väitöskirjassa keskitymme systemaattisesti tutkimaan viritysenergian kuljettamista orgaanisissa mikrokaviteeteissa. Simulaatioiden tulosten perusteella esitämme yleisen mekanismin kaviteetin tehostamalle kuljetukselle. Lisäksi tutkimme kuinka kuljetus muuttuu riippuen polaritonien dispersiosta ja kaviteetin laatukertoimesta. Esitämme ja testaamme myös käytännöllistä keinoa tehokkaaseen viritysenergian kuljetukseen fotokemiallisen reaktion avulla. Uskomme, että tässä väitöskirjassa esitetyt näkemykset tasoittavat tietä kohti molekyyli-kaviteettisysteemien rationaalista suunnittelua koherenttia eksitonikuljetusta varten.

Avainsanat: vahva valo-aine vuorovaikutus, polaritonit, eksitonikuljetus, molekyylidynamiikka

Author

Ilia Sokolovskii
Nanoscience Center and Department of Chemistry
University of Jyväskylä
Jyväskylä, Finland

Supervisor

Professor Gerrit Groenhof
Nanoscience Center and Department of Chemistry
University of Jyväskylä
Jyväskylä, Finland

Reviewers

Professor Karl Börjesson
Department of Chemistry and Molecular Biology
University of Gothenburg
Gothenburg, Sweden

Doctor Johannes Schachenmayer
Centre Européen de Sciences Quantiques
University of Strasbourg
Strasbourg, France

Opponent

Assistant professor Milan E. Delor
Department of Chemistry
Columbia University
New York, USA

ACKNOWLEDGEMENTS

The research presented in this dissertation has been performed at the Nanoscience Center, Department of Chemistry at the University of Jyväskylä during the years 2020–2024, thanks to financial support of the Academy of Finland (projects 323996 and 332743) and generous computational resources provided by the CSC Finnish IT Center for Science.

This work would not have been possible without the support and aid of many people. First and foremost, I am grateful to my supervisor Professor Gerrit Groenhof for the opportunity to work in a very motivating and at the same time cheerful environment, constant support and the chance to immerse myself into a fascinating realm of molecular polaritonics.

I am also grateful to the past and present members of our research group, namely Dr. Pavel Buslaev, Dr. Ruth Tichauer, Dr. Noora Aho, Dr. Dmitry Morozov, Dr. Arun Kanakati, Dr. Emmi Pohjolainen, Yunyi Luo, Santiago Gomez, for the precious time spent together at work and outside of it, which helped me remain full of optimism throughout my four years in the research group, even during the hard times of the pandemic.

I would like to express my gratitude to our collaborators Prof. Jussi Toppari from the Nanoscience Center at the University of Jyväskylä, Prof. Johannes Feist from the University of Madrid, as well as Prof. Jaime Gómez Rivas and Dr. Anton Matthijs Berghuis from the Eindhoven University of Technology.

I would like to thank the pre-examinators of this dissertation, Prof. Karl Börjesson from the University of Gothenburg and Dr. Johannes Schachenmayer from the University of Strasbourg, for the time spent to read and evaluate my work.

I have been happy to be working at the Nanoscience Center thanks to its great environment and a lot of people who I had the chance to discuss science and many other interesting topics. In particular, I am grateful to "Helsinki Complainers" and people from the table tennis gang, who became my good friends. Also, I am thankful to all my friends at the university and other places for a wonderful time shared together, and to Soho football team.

Finally, I am very grateful to my parents Vadim and Victoria, my grandmother Larisa and my brother Evgeny for their invaluable support during this journey.

ABBREVIATIONS

BODIPY	boron-dipyrromethen
BSW	Bloch surface wave
CIS	single excitation configuration interaction
DBR	distributed Bragg reflector
DFT	density functional theory
DOF	degrees of freedom
DS	dark states
ESC	electronic strong coupling
ESIPT	excited-state intramolecular proton transfer
FP	Fabry-Pérot (microcavity)
HBQ	10-hydroxybenzo[h]quinoline (molecule)
HOMO	highest occupied molecular orbital
LP	lower polariton
LUMO	lowest unoccupied molecular orbital
MD	molecular dynamics
MeB	Methylene Blue
MSD	mean squared displacement
MP	middle polariton
PV	photovoltaics
QM/MM	quantum mechanics/molecular mechanics
RMSD	root mean squared displacement
RWA	rotating-wave approximation
SLR	surface lattice resonance
TDDFT	time-dependent density functional theory
UP	upper polariton
VSC	vibrational strong coupling

LIST OF INCLUDED ARTICLES

PI	I. Sokolovskii, R.H. Tichauer, D. Morozov, J. Feist, G. Groenhof. Multi-scale molecular dynamics simulations of enhanced energy transfer in organic molecules under strong coupling. *Nature Communications,* 14, 6613, **2023**.
PII	R.H. Tichauer, I. Sokolovskii, G. Groenhof. Tuning the Coherent Propagation of Organic Exciton-Polaritons through the Cavity Q-factor. *Advanced Science,* 10, 2302650, **2023**.
PIII	A.M. Berghuis, R.H. Tichauer, L.M.A. de Jong, I. Sokolovskii, P. Bai, M. Ramezani, S. Murai, G. Groenhof, J. Gómez Rivas. Controlling Exciton Propagation in Organic Crystals through Strong Coupling to Plasmonic Nanoparticle Arrays. *ACS Photonics,* 9, 2263–2272, **2022**.
PIV	I. Sokolovskii, Y. Luo, G. Groenhof. Disentangling Enhanced Diffusion and Ballistic Motion of Excitons Coupled to Bloch Surface Waves with Molecular Dynamics Simulations. Submitted to *ACS Photonics*, **2024**.
PV	I. Sokolovskii, G. Groenhof. Photochemical initiation of polariton-mediated exciton propagation. *Nanophotonics,* 13, 2687–2694, **2024**.

For Publications I and II, the author of this dissertation developed an analytical model of exciton-polariton transport, as well as took part in performing and analysing the results of molecular dynamics simulations and writing the paper's manuscript. For Publication III, he was involved in performing molecular dynamics simulations and interpreting their results. For Publications IV and V, he performed simulations and was actively involved in writing the text of the corresponding manuscripts.

OTHER PUBLICATIONS TO WHICH THE AUTHOR HAS CONTRIBUTED

API	R.H. Tichauer, D. Morozov, I. Sokolovskii, J.J. Toppari, G. Groenhof. Identifying Vibrations that Control Non-adiabatic Relaxation of Polaritons in Strongly Coupled Molecule–Cavity Systems. *The Journal of Physical Chemistry Letters*, 13, 6259–6267, **2022**.
APII	I. Sokolovskii, G. Groenhof. Non-Hermitian Molecular Dynamics Simulations of Exciton-Polaritons in Lossy Cavities. *The Journal of Chemical Physics*, 160, 092501, **2024**.
APIII	A. Dutta, V. Tiainen, I. Sokolovskii, L. Duarte, N. Markešević, D. Morozov, H.A. Qureshi, S. Pikker, G. Groenhof, J. Toppari. Thermal Disorder Prevents the Suppression of Ultra-Fast Photochemistry in the Strong Light-Matter Coupling Regime. *Nature Communications*, 15, 6600, **2024**.
APIV	I. Sokolovskii, D. Morozov, G. Groenhof. One Molecule to Couple Them All: Towards Realistic Numbers of Molecules in Multiscale Molecular Dynamics Simulations of Exciton-Polaritons . *The Journal of Chemical Physics*, 161, 134106, **2024**.

CONTENTS

1 INTRODUCTION

On the way towards a sustainable future, gradual abandonment of non-renewable fossil fuels such as coal, petroleum and natural gas, in favor of alternative energy sources is required. The latter include renewable sources like sun, wind, water etc., as well as non-renewable fossil fuels with a low carbon footprint as, for instance, nuclear fuel [1]. Individually, none of the alternative energy sources can replace traditional fossil fuels, that is why it is important to systematically develop technologies for using each of these sources for their integrated use in the future.

One of the important technologies for the green transition is the solar energy technology. Despite the fact that this technology nowadays occupies less than 10% of the global energy market [2], a growing role of photovoltaics in energy production has been predicted [3, 4]. However, in order to live up to even the most humble of these predictions, solar energy technology needs to make a step forward in terms of efficiency while simultaneously ensuring low cost and small carbon footprint. In this regard, photovoltaics (PV) based on organic materials seem promising owing to a low production cost, abundance of organic materials, and their non-toxicity. However, the widespread dissemination of organic PV technology in the global solar cells market is impeded by the low efficiency of the solar cells due to a poor transfer of the excitation energy in organic materials.

Different methods have been proposed to tackle this challenge. One of the most promising methods relies on permanent delocalisation of the excitation over a large amount of molecules due to the strong interaction of the molecular excitations with confined light modes of optical resonators, or cavities [5–7]. Under this so-called *strong light-matter coupling* condition, the molecular excitations and the cavity light modes hybridise into new states, called *polaritons*, which acquire properties of both participants of the interaction. This hybrid light-matter nature of polaritons makes them promising for different kinds of applications, including enhancement of the excitation energy transport. Indeed, an improved energy transport beyond the diffusion length in bare molecules has been successfully demonstrated in a variety of cavities [8–22]. However, a detailed understanding of the mechanism of the cavity-enhanced excitation energy transport has remained missing.

The aim of this dissertation is to thoroughly investigate the excitation energy transport in organic microcavities by means of multiscale quantum-classical molecular dynamics simulations of various molecules and cavity structures. By simulating large molecular ensembles with more than a thousand molecules involved in strong coupling with realistic cavities, we first study a general mechanism of polariton transport on the atomistic level (Publication I). Then, we explore how the transport is influenced by the cavity quality, *i.e.* by how long the electromagnetic field remains in the cavity before it leaks out of it (Publication II). Likewise, we investigate how the transport properties change with the energy of polaritonic states and explore the role of molecular vibrations in such an energy-dependency (Publications III and IV). Finally, we propose and test an idea of launching excitation energy transport by a photochemical reaction as an alternative to a laser excitation normally employed in experiments on strong light-matter coupling (Publication V). These studies allow us to expand our knowledge of the excitation energy transport in organic microcavities, which is not only of fundamental interest but also paves the way for designing optoelectronic devices based on coherent exciton transport.

The dissertation is organised in the following way. In Chapter 2, we discuss the current state of the global PV market as well as the role of organic solar cells in it. Then, we describe the strong light-matter phenomenon and its main features. We close the chapter with a discussion of how excitation energy transport can be improved in the cavity and give a brief literature review of the topic. In Chapter 3, we give an overview of our multi-scale molecular dynamics (MD) method and the theory behind it. In Chapter 4, we share the main results of the dissertation. In the end, we complete the dissertation with a brief summary and outlook in Chapter 5.

2 ENERGY TRANSPORT IN ORGANIC MATERIALS

> Wikipedia is the best thing ever. Anyone in the world can write anything they want about any subject. So you know you are getting the best possible information.
>
> *Michael Scott, The Office*

2.1 Current Status of the Global Photovoltaics Market and the Place of Organic Materials in It

Currently, the global photovoltaics market is dominated by silicon technology [23] due to several advantages: *i)* along with oxygen, silicon is the most abundant element in the earth's crust, which makes it inexpensive; *ii)* the technology for producing silicon solar cells is well studied and developed; *iii)* the band gap of silicon (1.12 eV at room temperature) is optimal for absorbing solar radiation.

However, the technology approaches its ceiling and there is little room for further improvement. For example, efficiency of the best laboratory silicon solar cell has reached 26.1% [24], which is very close to the theoretical limit of 29.4% for a single-junction silicon solar cell [25]. Further increase in efficiency is complicated by the impossibility of obtaining perfectly pure silicon samples, as well as avoiding losses associated with absorption in the accompanying layers.

In this regard, one searches for ways to go beyond this Shockley–Queisser limit for silicon. One of the possible solutions is multi-junction solar cells, which combine materials with absorption at different wavelengths for a more efficient use of solar irradiation. While the efficiency of the best laboratory-produced multi-junction solar cell achieved a record value of 39.5% [26], industrial scaling of the technology is difficult due to the complexity of manufacturing, the scarcity of the materials used, and the low throughput stemming from a slow material growth rate [27].

Purely technical solutions such as utilisation of concentrators for more efficient absorption of sunlight and of anti-reflective coating for reduced reflection, are also proposed. Whereas such solutions do lead to better efficiency, the gain is very limited since the problem of fundamental losses remains unsolved.

In addition to silicon solar cells, various PV technologies based on alternatives to silicon have found their niche. For example, solar cells based on III-V semiconductors such as gallium arsenide, which have a better efficiency with respect to silicon photovoltaic cells but a much higher price, are actively used in space technologies. A small but non-zero part of the PV market is also occupied by thin-film technologies based on cadmium telluride and copper indium gallium selenide multicomponent semiconductors.

Special attention has been recently paid to perovskite solar cells. Owing to the ease of deposition and the possibility of tuning the bandgap in a wide range, perovskites are now considered one of the most promising alternatives to silicon. Remarkably, perovskite solar cells have already approached silicon solar cells in terms of efficiency in laboratory conditions [28]. Unfortunately, perovskites suffer from poor chemical stability under normal conditions and lose their transport properties over time, which delays the commercialization of perovskite solar panels. This challenge has yet to be solved [29].

In this dissertation, we focus on organic optoelectronic materials. Such materials are advantageous due to low production cost, small weight, high flexibility, and simple disposability. However, because excitation energy carriers in organic materials travel via incoherent hops between neighbouring molecules, their transport is diffusive and inefficient to compete with ultra-fast deactivation processes such as radiative and non-radiative decay. Taking into account also that diffusion is hindered by thermal disorder, the diffusion length, which is a measure of the propagation distance of the excitation carriers, typically remains below 10 nm in organic materials [30]. This poses a limitation on the width of the active layer and hence on the amount of solar irradiation that can be absorbed.

Several solutions to this challenge have been proposed, which include increasing the lifetime of excitations via triplet formation [31, 32], using bulk heterojunctions [33], or growing organic crystals to suppress structural disorder. In the latter case, unlike inorganic semiconductor crystals in which electrons and holes can freely propagate in the conductive and valence bands, electrons and holes in organic crystals form so-called Frenkel excitons, which are strongly bound to distinct molecules and hence propagate by incoherent hops as in molecular films. Nevertheless, ordering molecules in crystals allows to reduce structural disorder, leading to enhanced mobility. However, the effect is limited, and the diffusion length of excitons in organic crystals remains below 100 nm [30].

A new avenue for optimizing excitation energy transfer in organic materials is transient delocalisation [34]. This phenomenon is realised when molecules are closely packed and ordered so that the wave functions of excitons can overlap [35], at least temporarily. This allows for the excitons to hop over larger distances than usual, which results in an enhanced propagation length. While the first experimental observation of the phenomenon looks promising [36], it might be difficult to find materials satisfying the criteria for efficient transient delocalisation, although some predictions have been made [37].

There is another direction that utilises a conceptually different approach, namely strongly coupling the excitons to the confined electromagnetic field of an optical cavity. Because such a solution does not require chemical modifications of the molecules, which may influence other properties, placing molecules in the cavity could lead to improving the performance of organic optoelectronic devices, and a few attempts have already been made [38–40]. The main goal of this thesis is to investigate the mechanism of the in-plane excitation energy transport under strong light-matter coupling in a cavity. In the next sections, we give a brief overview of the strong coupling phenomenon and discuss how it can be used to enhance excitation transport.

2.2 Strong Light-Matter Coupling

In a free space, the interaction of an electromagnetic wave with a material results in multiple effects such as reflection, scattering, refraction etc. Let us consider interaction with a molecule, for simplicity represented as a two-level system (Figure 1**a**). If the energy of the electromagnetic wave matches the gap between the energy levels of the molecule, the wave and the molecule are said to be resonant. In such an event, the wave can be absorbed by the molecule with a concomitant creation of a bound electron-hole pair, or exciton. Such a state is not stable and decays after some time with an emission of a photon. The illustrated interaction is sometimes called weak coupling.

It turns out that the interaction can be drastically modified when placing a molecule in an optical cavity made, for example, of two parallel metallic mirrors (Figure 1**b**). The cavity acts as a resonator that supports only those electromagnetic waves whose half-wavelength fits between the mirrors an integer number of times. Such waves exist in the form of standing waves and are "trapped" in the cavity for a certain amount of time dictated by the cavity losses. Therefore, a photon emitted by a molecule in the cavity has a good chance of being re-absorbed by the molecule, resulting in a constant energy exchange between the cavity and the molecule. If the frequency of such an exchange is greater than the rates associated with cavity losses and molecular deactivation, the system is said to be in the *strong light-matter coupling* regime, and the energy of light is somewhat smeared out between the two subsystems.

Strong coupling is a resonant effect. Similar to the resonant interaction between two coupled pendulums, which results in either in-phase or out-of-phase coordinated oscillation of the pendulums with a frequency different from their natural frequencies [41], or to the formation of bonding and antibonding orbitals of a hydrogen molecule, the resonant interaction between the electromagnetic

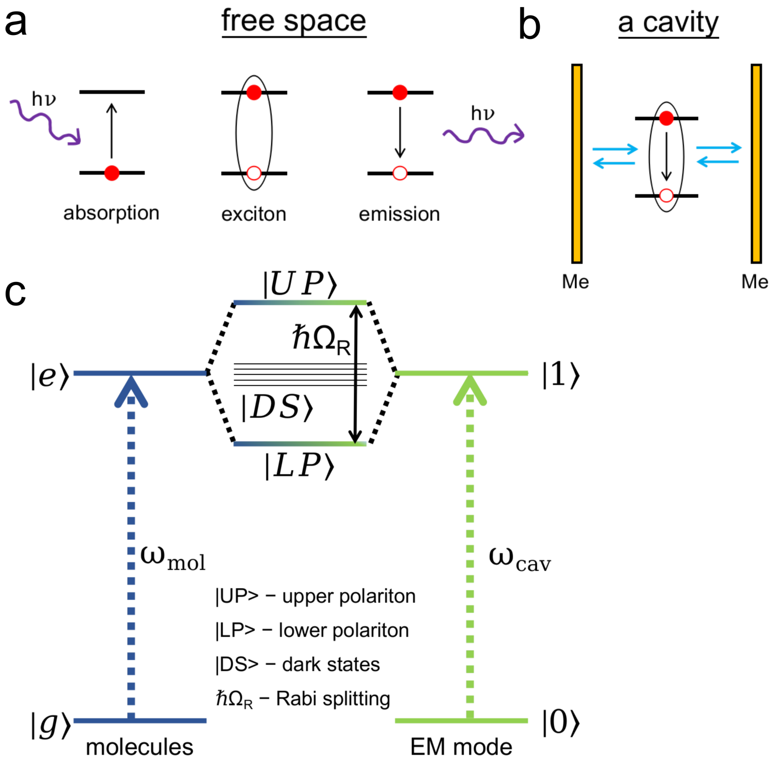

FIGURE 1 Panels **a** and **b**: Simplified representation of the interaction between a molecule and an electromagnetic wave in free space (**a**) and in a cavity made of two metallic (Me) mirrors (**b**). Panel **c**: Schematic illustration of the formation of upper (UP) and lower (LP) polaritons, as well as of dark states (DS) at a resonant interaction between an energy excitation of molecules and an electromagnetic mode (EM mode) in the cavity. The energy splitting between UP and LP is the Rabi splitting, $\hbar\Omega_R$.

field and a molecular excitation results in the formation of two hybrid states that inherit properties of both components. Such states are conventionally called upper and lower polaritonic states and are separated by the so-called Rabi splitting, $\hbar\Omega_R$ (Figure 1**c**). The Rabi splitting defines the frequency of energy exchange in the light-matter system. Therefore, the strong coupling condition can be written via the Rabi splitting as

$$\Omega_R > \gamma_{cav} + \kappa, \tag{1}$$

where γ_{cav} is the cavity decay rate and κ is the rate of molecular deactivation (radiative plus non-radiative). We note, that this condition is rather arbitrary, and its several different versions can be found in literature [41]. The value of the Rabi splitting is proportional to the strength of the electric field, which is, as we discuss in Section 3.1, inversely proportional to the volume of the electromagnetic mode sustained by the cavity. This explains the need to use a cavity because it allows to confine light into a small volume and hence achieve a large Rabi splitting to fulfill the strong coupling condition.

In practice, strong coupling of the cavity field can be achieved with energy transitions between electronic levels of molecules or with molecular vibrations. In the former case, the strong coupling is electronic, or ESC, and in the latter case, the strong coupling is vibrational, or VSC. While vibrational strong coupling has gained great interest due to a potential to modify chemical reactivity [42], in the current dissertation we are interested in the ESC only.

When multiple molecules are placed inside a cavity, they collectively interact with the cavity electromagnetic field. This leads to an enhanced light-matter interaction strength and hence an enhanced Rabi splitting,

$$\hbar\Omega_{\mathrm{R}}^{N} = \hbar\Omega_{\mathrm{R}}^{1}\sqrt{N}, \tag{2}$$

where $\hbar\Omega_{\mathrm{R}}^{N}$ is the collective Rabi splitting of N identical molecules and $\hbar\Omega_{\mathrm{R}}^{1}$ is the single-molecule Rabi splitting. Furthermore, in addition to the upper and lower polaritonic states, $N-1$ dark states are formed (Figure 1**c**). The name of the dark states refers to the fact that they lack contribution from the electromagnetic field and therefore cannot be excited with light. Whereas dark states have the same energy as bare molecular excitations, there is an important difference, since the dark states are collective excitations delocalised over the whole ensemble of molecules participating in strong coupling.

Practically, strong coupling is realised in planar resonators such as Fabry-Pérot (FP) and distributed Bragg reflector (DBR) microcavities, as well as in plasmonic structures [43, 44], on the surface of photonic crystals [45], and on the boundary between two dielectrics [16, 46]. In addition, polaritons can naturally appear due to self-hybridization in multiple structures such as slabs, nanorods, and even water droplets [47, 48], pointing out the ubiquity of polaritons in natural systems.

Being hybrid light-matter states, polaritons combine such properties of both their "parents" as the existence of the effective mass and coherent interaction (matter properties), as well as a large propagation velocity and delocalisation (light properties). This opens up plenty of potential applications of polaritons, in particular for the enhancement of the excitation energy transport. This can be achieved owing to two different properties of polaritons, namely their delocalised character and a large group velocity. In the next section, we discuss both these cavity-enhanced transport mechanisms.

2.3 Excitation Energy Transport in Optical Microcavities

One can distinguish two kinds of polariton-assisted transport depending on which property of polaritons is responsible for the enhanced transport. In the first type, one makes use of the delocalised nature of exciton-polaritons. The idea of such an energy transfer is schematically depicted in Figure 2**a**. Two molecular species, which play the role of a donor (D) and acceptor (A) are coupled to the same cavity mode (red sinusoidal line). Because the excitation energies of the donor and acceptor are generally different, the interaction with the cavity mode leads to the formation of three polariton states, namely lower polariton (LP), middle polariton (MP), and upper polariton (UP) states. As polariton states are formed due to the strong coupling of all donor and all acceptor molecules, these states are delocalised over the whole molecular ensemble, which opens up a possibility to transfer the excitation between the two molecular species (yellow arrows) through the polariton states. As shown at the bottom of Figure 2**a**, excitation of the UP state, primarily associated with the donor molecules, can lead to an efficient population transfer to the LP state, chiefly contributed by the acceptor molecules, or to the reservoir of dark states associated with the acceptor molecules, via MP states. This population transfer is similar to Kasha's rule in photochemistry, with the decay of higher energy states dominated at room temperature by the non-radiative channel towards low-energy states [49]. Because the polariton states are delocalised between all molecules, energy transfer between the donor and the acceptor may proceed more efficiently than out of the cavity.

This type of polariton-mediated energy transfer has been demonstrated in a series of experiments [50–56]. Remarkably, the effect occurs even when the donor and acceptor are spatially separated by a spacer layer [50, 52, 54], as long as the strong coupling condition is maintained, which implies a possibility to transfer the excitation much beyond the Förster limit.

Experimentally, energy transfer due to delocalisation usually occurs in the out-of-plane direction, although this is not a requirement as both the donor and acceptor molecules can be blended together, for example, in a polymer matrix.

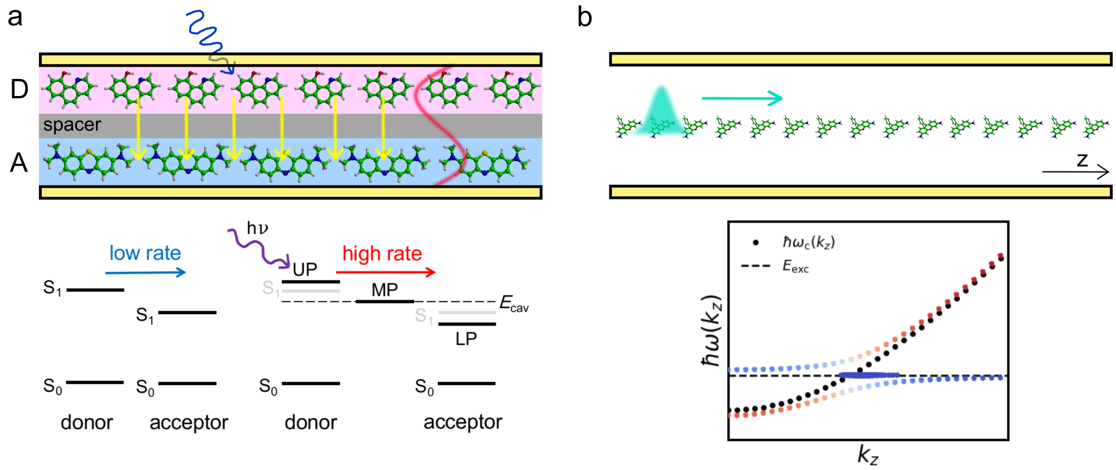

FIGURE 2 Panel **a**: Schematic illustration of excitation transfer due to delocalisation of polariton states. Placing donor (D) and acceptor (A) molecules in a cavity permits them to strongly interact with the same cavity light mode (red line), resulting in the formation of lower (LP), middle (MP), and upper (UP) polariton states. Excitation of the UP state in such a system might lead to an efficient polariton-mediated energy transfer between the donor and acceptor molecules with a higher rate than between the same molecules out of the cavity, even if the molecules are spatially separated by a spacer. Panel **b**: Schematic illustration of excitation transfer due to the group velocity of polaritons. An external pumping (cyan) creates a superposition of polaritonic states that can propagate in the in-plane, z, direction with the group velocity according to the polariton dispersion (bottom panel).

The second mechanism of the polariton-enhanced energy transfer takes advantage of the fact that polariton states possess dispersion in certain directions. To describe this effect, let us consider as an example a two-dimensional Fabry-Pérot cavity, as shown in Figure 2**b**. Up until now, we have considered the interaction of molecules with a single cavity mode only. In reality, the cavity supports an infinite number of modes. In the direction perpendicular to the cavity mirrors, the modes can be classically described as standing waves with discrete wavelengths. In the in-plane, z, direction, the modes are propagating waves with a continuous energy spectrum with frequencies dependent on the wave vector, which is defined via the wavelength as $|\mathbf{k}| = 2\pi/\lambda$ and is collinear with the propagation direction of an electromagnetic wave. This dependence of energy on the wave vector is called *dispersion* and is linear in a vacuum, *i.e.* $\omega = |\mathbf{k}|c$, where c is the speed of light. In the cavity, the boundary conditions result in a modified dispersion. Because polariton states are hybrid states of both molecular and cavity modes excitations, polaritons inherit dispersion from the cavity, as schematically shown at the bottom of Figure 2**b**.

Because no radiation source can emit at a single wavelength, which is precluded by the uncertainty principle, an external excitation of polaritons leads to the excitation of multiple states. The phases and amplitudes of these states interfere constructively only over a small region of space forming a wave packet, which is then able to propagate with a group velocity determined by the dispersion, $v_{\text{gr}} = \frac{\partial \omega(k)}{\partial k}$ (Figure 2**b**). It turns out that the group velocity of polaritons can approach the speed of light, which makes them promising for very fast transfer of excitation energy.

Enhanced in-plane polariton transport due to dispersion has been experimentally demonstrated with inorganic [8, 11–13, 15], organic [9, 10, 14, 16–18, 20], as well as mixed organic-inorganic [19, 21, 22] materials in a variety of microcavity structures.

In the dissertation, we focus on the second type of polariton-enhanced excitation transport, *i.e.* the transport due to group velocity, and aim to investigate the general mechanism of such a transport.

3 MOLECULAR DYNAMICS IN THE COLLECTIVE STRONG COUPLING REGIME

Over the past two decades, organic polaritonics have gained a growing attention thanks to its potential *i)* to increase the efficiency of optoelectronic devices such as solar cells and light-emitting diodes [53, 57, 58], *ii)* to achieve low-threshold lasing with organic molecules [59], *iii)* to develop logical elements for classical and quantum computing [60], and even *iv)* to control photochemistry [61]. The effect of strong light-matter coupling has been extensively studied from both experimental [62] and theoretical [63] sides. However, because the majority of experiments have been conducted in multimode optical cavities containing macroscopic numbers of molecules ($\sim 10^5$-10^8) [64–67], while most of theoretical works have been focused on a highly accurate description of the coupling between single molecules and single photon modes [68–71], a gap between these two approaches has remained.

To bridge this gap and model the strong coupling between *multiple* molecules and *many* cavity light modes, we propose an alternative methodology, which is based on semi-classical MD simulation with a multiscale quantum mechanics/molecular mechanics (QM/MM) Hamiltonian [72, 73]. This approach, on the one hand, provides a reasonable description of the electronic structure of the molecules participating in strong coupling, and, on the other hand, allows for simulation of more than a thousand strongly coupled molecules including their molecular environment. Although this is still smaller than the number of molecules in real cavities, our method allows us to approach experimentally relevant parameters such as, for example, an average velocity of polariton propagation [74] or the strength of non-adiabatic coupling [75], which single molecule/single cavity mode methods are unable to do. Additionally, since molecules are allowed to move during MD simulations, the method accounts for important effects as dynamical excitation energy disorder and vibronic coupling, which facilitates a better description and hence understanding of the dynamics of molecular systems in the regime of strong light-matter coupling.

In this chapter, we give an overview of our multiscale MD approach. We start from a general description of a charged particle in a radiation field and develop it to the renowned Tavis-Cummings model for simple few-level atoms or molecules interacting with a single electromagnetic mode [76]. Then, we extend the Tavis-Cummings model for the case of realistic molecules with their environment and a discrete spectrum of the cavity light modes. We also discuss the QM/MM approach for treating molecules at *ab initio* level of quantum chemistry and how the semi-classical dynamics simulations of molecules are performed in our model.

3.1 Derivation of the Light-Matter Hamiltonian

We start from the *minimal coupling* prescription for an electron in a radiation field [77]:

$$\hat{H} = \frac{1}{2m}\left(\mathbf{p} - e\mathbf{A}\right)^2 - e\phi + \hat{H}_{\text{field}} \tag{3}$$

with m, e and $\mathbf{p}$ the mass, charge and momentum of the electron, $\mathbf{A}$ and ϕ the vector and scalar potentials of the electromagnetic field, and $\hat{H}_{\text{field}}$ the free radiation field, which will be discussed later when quantising the photonic degrees of freedom (DOF). Generally, in the minimal coupling prescription, particles are assumed to have only a monopole charge and no higher-order electric moments, and the corresponding Hamiltonian is justified since it correctly reproduces the Lorentz equations of motion of the particles in the electromagnetic field [77].

The motion of the electron can be quantised by applying the first quantization principle, *i.e.* $\mathbf{p} \to -i\hbar\nabla$, $\mathbf{r} \to \mathbf{r}$. This leads to the following Hamiltonian:

$$\begin{aligned} \hat{H} &= \tfrac{1}{2m}\left[-i\hbar\nabla - e\mathbf{A}(\mathbf{r},t)\right]^2 - e\phi + \hat{H}_{\text{field}} = \\ &\quad -\tfrac{\hbar^2}{2m}\nabla^2 + \tfrac{ie\hbar}{2m}\left[\mathbf{A}(\mathbf{r},t)\cdot\nabla + \nabla\cdot\mathbf{A}(\mathbf{r},t)\right] + \tfrac{e^2}{2m}\mathbf{A}^2(\mathbf{r},t) - e\phi + \hat{H}_{\text{field}}. \end{aligned} \tag{4}$$

It can be shown that the radiation field is independent of the variation of the vector and scalar potentials by, respectively, the gradient and derivative of an arbitrary scalar function χ. This independence of the field affords one a certain freedom in transforming the potentials according to $\mathbf{A} \to \mathbf{A} - \nabla\chi$ and $\phi \to \phi + \partial\chi/\partial t$ for a more convenient or thoughtful solution of a particular problem. For instance, in the widely used *Coulomb gauge*, the divergence of the vector potential is chosen to be zero, *i.e.* $\nabla \cdot \mathbf{A} = 0$, which modifies the Hamiltonian in equation 4 in the following way:

$$\hat{H} = -\frac{\hbar^2}{2m}\nabla^2 + \frac{ie\hbar}{2m}\mathbf{A}(\mathbf{r},t)\cdot\nabla + \frac{e^2}{2m}\mathbf{A}^2(\mathbf{r},t) - e\phi + \hat{H}_{\text{field}}. \tag{5}$$

Let us consider the Maxwell's equation of the vector potential in free space:

$$\left(\nabla^2 - \frac{1}{c^2}\frac{\partial^2}{\partial t^2}\right)\mathbf{A}(\mathbf{r},t) = 0 \tag{6}$$

The vector potential satisfying this equation can be represented as a superposition of plane waves:

$$\mathbf{A}(\mathbf{r},t) = \sum_k c_k(t)\exp\{\pm i\mathbf{k}\cdot\mathbf{r}\}, \tag{7}$$

where $c_k(t)$ are time-dependent expansion coefficients.

In problems related to the electronic and vibrational strong coupling, the wavelength of the corresponding visible and infrared waves is much larger compared to the typical size of an atom, *i.e.* $|\mathbf{k}\cdot\mathbf{r}| \ll 1$. Therefore, $\exp\{\pm i\mathbf{k}\cdot\mathbf{r}\} \approx 1$ in Equation 7 and the vector potential can be considered as a function of time only: $\mathbf{A}(\mathbf{r},t) \to \mathbf{A}(t)$. In this so-called *long-wavelength* (or *dipole*) approximation, the Hamiltonian becomes

$$\hat{H} = -\frac{\hbar^2}{2m}\nabla^2 + \frac{ie\hbar}{2m}\mathbf{A}(t)\cdot\nabla + \frac{e^2}{2m}\mathbf{A}^2(t) - e\phi + \hat{H}_{\text{field}}. \tag{8}$$

The second term in Equation 8 describes the light-matter interaction, and the third term is often referred to as the diamagnetic term, since it leads to the appearance of diamagnetism [78].

As was pointed out above, the last term in Equation 8 describes the energy of the free radiation field. According to classical electrodynamics, this term can be expressed through the electric and magnetic fields:

$$\hat{H}_{\text{field}} = \frac{\epsilon_0}{2}\int\left[\mathbf{E}^2(\mathbf{r},t) + c^2\mathbf{B}^2(\mathbf{r},t)\right]d^3\mathbf{r}, \tag{9}$$

where ϵ_0 is the vacuum permittivity.

The electric and magnetic fields can be written in the quantised form [77, 79]:

$$\mathbf{E}(\mathbf{r}) = i\sum_{\mathbf{k},\lambda}\sqrt{\frac{\hbar\omega_k}{2\epsilon_0 V}}\mathbf{u}_{\mathbf{k},\lambda}\left[\hat{a}_{\mathbf{k},\lambda}e^{i\mathbf{kr}} + h.c.\right], \tag{10}$$

$$\mathbf{B}(\mathbf{r}) = i\sum_{\mathbf{k},\lambda}\sqrt{\frac{\hbar}{2\omega_k\epsilon_0 V}}\left(\mathbf{u}_{\mathbf{k},\lambda}\times\mathbf{k}\right)\left[\hat{a}_{\mathbf{k},\lambda}e^{i\mathbf{kr}} + h.c.\right], \tag{11}$$

where V is the radiation modes' volume, $\hat{a}_{\mathbf{k},\lambda}$ is the creation operator of a photon with wave-vector $\mathbf{k}$ and polarization λ, and $\mathbf{u}_{\mathbf{k},\lambda}$ is the unit polarization vector of light mode $\{\mathbf{k},\lambda\}$. The abbreviation *h.c.* denotes hermitian conjugation of the first term in the square brackets.

After substitution of Expressions 10 and 11 in Equation 9 and performing some algebra, we can write down the quantised Hamiltonain of the free radiation field:

$$\hat{H}_{\text{field}} = \sum_{\mathbf{k},\lambda}\hbar\omega_k\left(\hat{a}^{+}_{\mathbf{k},\lambda}\hat{a}_{\mathbf{k},\lambda} + \frac{1}{2}\right), \tag{12}$$

where the second term stands for the zero-point energy. Because this term is a constant and only shifts the total energy, we can safely omit it in further derivations.

Equation 8 now looks like

$$\hat{H} = -\frac{\hbar^2}{2m}\nabla^2 + \frac{ie\hbar}{2m}\mathbf{A}(t)\cdot\nabla + \frac{e^2}{2m}\mathbf{A}^2(t) - e\phi + \sum_{\mathbf{k},\lambda}\hbar\omega_k\hat{a}^{+}_{\mathbf{k},\lambda}\hat{a}_{\mathbf{k},\lambda}. \tag{13}$$

At this point, it is convenient to make another gauge transformation, in which $\chi = e\mathbf{r}\cdot\mathbf{A}(t) = \hat{\mathbf{d}}\cdot\mathbf{A}(t)$ and $\hat{\mathbf{d}}$ is the electric dipole moment of the electron. Applying a unitary transformation $\hat{T} = \exp\{i\frac{e}{\hbar c}\chi\}$ to the Hamiltonian in Equation 13, i.e. $\hat{H} \to \hat{T}\hat{H}\hat{T}^{\dagger}$, we obtain an altered Hamiltonian [80, 81]

$$\hat{H} = -\frac{\hbar^2}{2m}\nabla^2 - \hat{\mathbf{d}}\cdot\mathbf{E}(t) + \sum_{\mathbf{k},\lambda}\frac{1}{2\epsilon_0 V}\left(\mathbf{u}_{\mathbf{k},\lambda}\cdot\hat{\mathbf{d}}\right)^2 - e\phi + \sum_{\mathbf{k},\lambda}\hbar\omega_k\hat{a}^{+}_{\mathbf{k},\lambda}\hat{a}_{\mathbf{k},\lambda}, \tag{14}$$

where we used the relation $\mathbf{E}(t) = -\frac{\partial\mathbf{A}(t)}{\partial t}$ between the electric field and vector potential in free space. As we can see, this so-called *Power-Zienau-Woolley*, or *length-gauge transformation* [77, 82, 83] eliminates the explicit form of the vector potential and describes the light-matter interaction as a dot product of the electric dipole moment and the electric field strength. Because it is easier to calculate dipole moments than the vector potential, we prefer to work with this Hamiltonian (Equation 14).

Whereas the diamagnetic term is now gone, another quadratic term, which is often referred to as the *polarisation*, or *self-energy* term, is present in Equation 14. Both the diamagnetic and self-energy terms are small compared to the interaction terms and therefore are usually ignored in the case of the strong coupling regime. However, when a system enters ultrastong coupling, these terms can become significant, and disregarding them might lead to different kinds of undesirable consequences such as breaking gauge invariance, the appearance of unphysical states, or the lack of the ground state [81, 84]. Nevertheless, because in this dissertation we consider only strong coupling and do not touch upon ultrastrong coupling, ignoring the quadratic term in Equation 14 is a reasonable approximation.

Extending the system of interest from a single electron to an atom or a molecule in the radiation field, we can re-write Equation 14 as

$$\hat{H} = -\sum_j\frac{\hbar^2}{2m_j}\nabla_j^2 - \hat{\mathbf{d}}\cdot\mathbf{E}(t) + V_{\text{int}} + \sum_{\mathbf{k},\lambda}\hbar\omega_k\hat{a}^{+}_{\mathbf{k},\lambda}\hat{a}_{\mathbf{k},\lambda}, \tag{15}$$

where m_j is the mass of particle j in the molecule, $\hat{\mathbf{d}}$ is now the electric dipole moment of the molecule, V_{int} is the interparticle Coulomb potential, and we neglected the spin-orbit coupling.

The solution of the Schrödinger equation for a molecule gives a discrete spectrum of energy levels. When the molecule is coupled to an electromagnetic wave with frequency ω_{f} (nearly) in resonance with electronic excitation energy ω_{eg} between the ground state $|g\rangle$ and an excited state $|e\rangle$ of this molecule, as relevant for strong coupling, the amplitude of light-driven oscillations is much larger than in the out-of-resonance situation. Therefore, only the states $|g\rangle$ and $|e\rangle$ are actively involved in the dynamics of the light-matter system, and the molecule can be approximated as a simple two-level system [85]. More generally, when electromagnetic field can be coupled to different molecular energy transitions, the molecule can be approximated as a muiltilevel system. Applying this quantised description to the matter part of the Hamiltonian 15, we obtain

$$\hat{H} = \sum_m \hbar\omega_m^{\text{eg}} \hat{\sigma}_m^+ \hat{\sigma}_m^- - \sum_m \hat{\mathbf{D}}_m \cdot \mathbf{E}(t) + \sum_{\mathbf{k},\lambda} \hbar\omega_k \hat{a}_{\mathbf{k},\lambda}^+ \hat{a}_{\mathbf{k},\lambda}, \tag{16}$$

where $\hbar\omega_m^{\text{eg}}$ is the excitation energy to the m^{th} excited state of the molecule, $\hat{\sigma}_m^+ = |m\rangle\langle g|$ and $\hat{\sigma}_m^- = |g\rangle\langle m|$ are the molecular excitation and de-excitation operators and hence $\hat{\sigma}_m^+\hat{\sigma}_m^- = |m\rangle\langle g|g\rangle\langle m| = |m\rangle\langle m|$. We also introduce operator $\hat{\mathbf{D}}_m$ to describe the molecular dipole moment and count for convenience the molecular energy ω_m^{eg} from the ground state.

Finally, we re-write the interaction term $\hat{H}_{\text{int}} = -\sum_m \hat{\mathbf{D}}_m \cdot \mathbf{E}$ in a quantised form as

$$\hat{H}_{\text{int}} = -\sum_m \sum_{\mathbf{k},\lambda} \sqrt{\frac{\hbar\omega_{\text{k}}}{2\epsilon_0 V}} \hat{\mathbf{D}}_m \cdot \left[\mathbf{f}_{\mathbf{k},\lambda}(\mathbf{r}) \hat{a}_{\mathbf{k},\lambda} + \mathbf{f}^*_{\mathbf{k},\lambda}(\mathbf{r}) \hat{a}^+_{\mathbf{k},\lambda} \right], \tag{17}$$

where the electric field strength (Equation 10) is put down in a generalised form, in which the plane wave is replaced by an arbitrary mode function $\mathbf{f}_{\mathbf{k},\lambda}(\mathbf{r})$, to account for the fact that the pattern of electromagnetic waves in a cavity may differ from that in free space.

It is convenient to move from a dipole moment in Equation 17 to a transition dipole moment $\hat{\boldsymbol{\mu}}_m = \langle m|\hat{\mathbf{D}}_m|g\rangle$ by multiplying the former by the identity operator $I = |m\rangle\langle m| + |g\rangle\langle g|$ from both sides:

$$\begin{aligned} \hat{\mathbf{D}}_m &= I\hat{\mathbf{D}}_m I = (|m\rangle\langle m| + |g\rangle\langle g|)\, \hat{\mathbf{D}}_m\, (|m\rangle\langle m| + |g\rangle\langle g|) \\ &= |m\rangle\langle m|\hat{\mathbf{D}}_m|m\rangle\langle m| + |m\rangle\langle m|\hat{\mathbf{D}}_m|g\rangle\langle g| + |g\rangle\langle g|\hat{\mathbf{D}}_m|m\rangle\langle m| + |g\rangle\langle g|\hat{\mathbf{D}}_m|g\rangle\langle g| \\ &= \hat{\boldsymbol{\mu}}|m\rangle\langle g| + \hat{\boldsymbol{\mu}}|g\rangle\langle m| = \hat{\boldsymbol{\mu}}\,(\hat{\sigma}_m^+ + \hat{\sigma}_m^-), \end{aligned} \tag{18}$$

where the first and the last terms in the second line turn to zero due to the odd parity of the dipole moment and hence the odd parity of the functions in the corresponding integrals. Additionally, we assumed that the dipole moment is real.

Having quantised both the matter and light components of the light-matter Hamiltonian, we obtain the following expression:

$$\begin{aligned} \hat{H} &= \textstyle\sum_m \hbar\omega_m^{\text{eg}} \hat{\sigma}_m^+ \hat{\sigma}_m^- + \hbar\omega_{\text{f}} \hat{a}^\dagger \hat{a} \\ &\quad - \textstyle\sum_m \sqrt{\frac{\hbar\omega_{\text{f}}}{2\epsilon_0 V}} \hat{\boldsymbol{\mu}}_m \cdot [\hat{\sigma}_m^+ + \hat{\sigma}_m^-]\, [\mathbf{f}(\mathbf{r})\hat{a} + \mathbf{f}^*(\mathbf{r})\hat{a}^+], \end{aligned} \tag{19}$$

where the number of light modes (Equation 17) was reduced to one. In the case of a two-level molecule, Expression 19 turns to the famous *quantum Rabi Hamiltonian*.

The interaction component of Equation 19 includes four terms. The $\hat{\sigma}_m^+ \hat{a}$ and $\hat{\sigma}_m^- \hat{a}^+$ terms involve either simultaneous molecular excitation and removal of a photon or simultaneous molecular de-excitation and creation of a photon. The $\hat{\sigma}_m^+ \hat{a}^+$ and $\hat{\sigma}_m^- \hat{a}$ terms, in turn, simultaneously create or destroy both a molecular excitation and a light mode and, strickly speaking, do not preserve the total energy of the system. Upon transformation of the Hamiltonian into the interaction picture, these last two terms, $\hat{\sigma}_m^+ \hat{a}^+ e^{i(\omega_m^{\mathrm{eg}}+\omega_{\mathrm{f}})t}$ and $\hat{\sigma}_m^- \hat{a} e^{-i(\omega_m^{\mathrm{eg}}+\omega_{\mathrm{f}})t}$, rapidly oscillate around zero and can be neglected as long as $\omega_m^{\mathrm{eg}} \approx \omega_{\mathrm{f}}$ and the system is below the ultrastong coupling limit (*i.e.*, when $\boldsymbol{\mu} \cdot \mathbf{E} < 0.1\ \hbar\omega_m^{\mathrm{eg}}$), because then these *counter-rotating* terms are much smaller than the *co-rotating* terms, $\hat{\sigma}_m^+ \hat{a} e^{-i(\omega_m^{\mathrm{eg}}-\omega_{\mathrm{f}})t}$ and $\hat{\sigma}_m^- \hat{a} e^{i(\omega_m^{\mathrm{eg}}-\omega_{\mathrm{f}})t}$. Within this so-called *rotating-wave approximation* (RWA), the Hamiltonian in Equation 19 turns into the *Jaynes-Cummings model* of quantum optics [86] extended to the case of multiple excited states:

$$\begin{aligned} \hat{H} &= \textstyle\sum_m \hbar\omega_m^{\mathrm{eg}} \hat{\sigma}_m^+ \hat{\sigma}_m^- + \hbar\omega_{\mathrm{f}} \hat{a}^\dagger \hat{a} \\ &\quad -\sqrt{\tfrac{\hbar\omega_{\mathrm{f}}}{2\epsilon_0 V}} \textstyle\sum_m \hat{\boldsymbol{\mu}}_m \cdot \left[\mathbf{f}(\mathbf{r}) \hat{\sigma}_m^+ \hat{a} + \mathbf{f}^*(\mathbf{r}) \hat{\sigma}_m^- \hat{a}^\dagger\right]. \end{aligned} \tag{20}$$

The Hamiltonian in Equation 20 can be extended to an ensemble of N molecules interacting with the same electromagnetic mode, resulting in the *Tavis-Cummings* Hamiltonian [76] extended to multiple excited states:

$$\begin{aligned} \hat{H}^{\mathrm{TC}} &= \textstyle\sum_j^N \sum_m \hbar\omega_{j,m}^{\mathrm{eg}} \hat{\sigma}_{j,m}^+ \hat{\sigma}_{j,m}^- + \hbar\omega_{\mathrm{f}} \hat{a}^\dagger \hat{a} \\ &\quad -\sqrt{\tfrac{\hbar\omega_{\mathrm{f}}}{2\epsilon_0 V}} \textstyle\sum_j^N \sum_m \hat{\boldsymbol{\mu}}_j \cdot \left[\mathbf{f}(\mathbf{r}) \hat{\sigma}_{j,m}^+ \hat{a} + \mathbf{f}^*(\mathbf{r}) \hat{\sigma}_{j,m}^- \hat{a}^\dagger\right] + V_{\mathrm{intermol}}, \end{aligned} \tag{21}$$

in which the potential V_{intermol} describes the intermolecular interactions.

The Tavis-Cummings model provides a conceptual understanding of polariton formation, but does not take into account the molecular chemical structure nor does it consider the mode structure of the cavities, both of which are crucial to fully capture and predict how strong light-matter coupling influences the physico-chemical properties of materials. To overcome these limitations and simulate the dynamics of large molecular ensembles strongly coupled to many cavity light modes, we replace the two-level systems in the Tavis-Cummings model by molecules, and introduce multiple discrete modes to account for the cavity dispersion. The following sections are dedicated to describing our model in more details.

3.2 Born-Oppenheimer Approximation in the Electronic Strong Coupling Regime

To model *electronic* strong coupling, we start from the Born-Oppenheimer approximation, in which the nuclei are separated from the electrons *plus* confined light modes [87]. To describe the combined electronic-photonic DOF, we replace the traditional two-level systems in the Tavis-Cummings Hamiltonian (Equation 21) with the molecular adiabatic electronic states, parametrically dependent on the nuclear coordinates, and include multiple cavity light modes:

$$\begin{aligned}\hat{H}^{\mathrm{TC}} \;=\;& \sum_j^N \sum_m \hbar\omega_m^{\mathrm{eg}}(\mathbf{R}_j)\hat{\sigma}_{j,m}^{+}\hat{\sigma}_{j,m}^{-} + \sum_j^N V_{\mathrm{S}_0}(\mathbf{R}_j) + \sum_p^{n_{\mathrm{modes}}} \hbar\omega_{\mathrm{cav}}(\mathbf{k}_p)\hat{a}_p^{\dagger}\hat{a}_p \\ & - \sum_j^N \sum_m \sum_p^{n_{\mathrm{modes}}} \sqrt{\frac{\hbar\omega_{\mathrm{f}}(\mathbf{k}_p)}{2\epsilon_0 V}}\,\hat{\boldsymbol{\mu}}_m(\mathbf{R}_j)\cdot\left[\mathbf{f}_p(\mathbf{R}_c^j)\hat{\sigma}_{j,m}^{+}\hat{a}_p + \mathbf{f}_p^{*}(\mathbf{R}_c^j)\hat{\sigma}_{j,m}^{-}\hat{a}_p^{\dagger}\right].\end{aligned} \tag{22}$$

Here, $\hat{\sigma}_{j,m}^{+} = |\mathrm{S}_m^j\rangle\langle\mathrm{S}_0^j|$ is an operator that excites molecule j with nuclear coordinates $\mathbf{R}_j$ from the electronic ground state $|\mathrm{S}_0^j\rangle$ with energy $V_{\mathrm{S}_0}(\mathbf{R}_j)$ into m^{th} electronic excited state $|\mathrm{S}_m^j\rangle$ with energy $V_{\mathrm{S}_m}(\mathbf{R}_j)$. Accordingly, the excitation energy is defined as $\hbar\omega_m^{\mathrm{eg}}(\mathbf{R}_j) = V_{\mathrm{S}_m}(\mathbf{R}_j) - V_{\mathrm{S}_0}(\mathbf{R}_j)$. Likewise, $\hat{\sigma}_{j,m}^{-} = |\mathrm{S}_0^j\rangle\langle\mathrm{S}_m^j|$ de-excites molecule j from electronic excited state $|\mathrm{S}_m^j\rangle$ into the electronic ground state $|\mathrm{S}_0^j\rangle$. Operators $\hat{a}_p^{\dagger}$ and $\hat{a}_p$ create and annihilate a photon of energy $\hbar\omega_{\mathrm{cav}}(\mathbf{k}_p)$ in cavity mode p with in-plane momentum $\mathbf{k}_p$.

Within the long-wavelength approximation, the light-matter interaction is calculated as the inner product between the transition dipole moment, $\hat{\boldsymbol{\mu}}_m(\mathbf{R}_j)$, associated with an excitation of molecule j into the m^{th} excited electronic state on the one hand, and the vacuum field associated with an excitation of a cavity mode p and described by the mode function $\mathbf{f}_p(\mathbf{R}_c^j)$, with $\mathbf{R}_c^j$ the geometrical center of molecule j, on the other hand. The second term in Equation 22 is the total ground state energy of the combined molecule-cavity system, with no molecules excited and no photons in the cavity. Note, that in the Hamiltonian (Equation 22), we do not include *direct* Coulomb or excitonic interactions between molecules, *i.e.* the term V_{intermol} (Equation 21). Although adding such interactions is straightforward [88], we assume that the molecules are sufficiently diluted in the cavity medium so that these interactions can be neglected.

3.3 Quantum Mechanics/Molecular Mechanics approach

Computing electronic wave functions of molecules, including transition dipole moments ($\hat{\boldsymbol{\mu}}_m(\mathbf{R}_j)$) and potential energy surfaces ($V_{\mathrm{S}_m}(\mathbf{R}_j)$), is the domain of Quantum Chemistry and one of the first practical applications of Quantum Mechanics. Thanks to relentless developments in this field, Quantum Chemistry has become an important and predictive technique in chemistry, physics and material science [89]. However, despite tremendous advances in computer power, the materials that have been studied experimentally in the context of polaritonic chemistry are still too large to be described at any level of *ab initio* electronic structure theory or density functional theory [90].

To go beyond such size limitations, MM force fields have been introduced, in which the potential energy is approximated by analytical functions that correspond to intuitive chemical concepts, such as bonds, angles and torsions at short intermolecular distances, and pairwise Coulomb and Lennard-Jones potentials at larger distances [91]. Electrons are ignored at this level of theory, but their influence is expressed by the empirical parameters in these functions, which correspond to the ground state of a given molecular structure. Therefore, processes involving rearrangements of electrons, such as photo-excitation into an electronic excited state [92] or chemical reactions in which bonds are formed and broken [93] cannot be described with an MM force field.

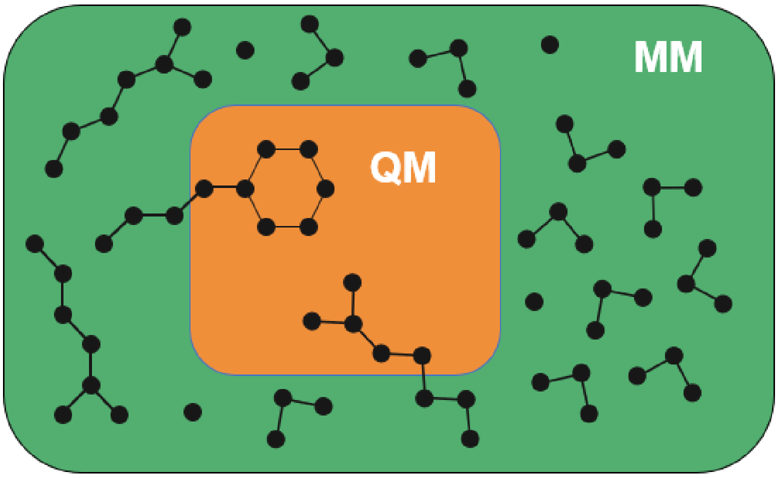

FIGURE 3 Schematic representation of the QM/MM concept [91, 94]. A small region (orange) important for a photochemical process, is treated at a reasonalbe level of QM theory. The rest of the system (green) is modeled at the MM level.

To overcome the system size limitations of a full Quantum Mechanical description on the one hand, and the lack of reactivity of a full Molecular Mechanics treatment on the other hand, it was proposed considering a small part of the system at the QM level of quantum chemistry, while applying the computationally cheaper force field (MM) for the remainder of the system. This multi-scale QM/MM strategy introduced almost five decades ago by Warshel and Levitt [95] and popularised by Karplus [96], is schematically depicted in Figure 3 [94]. The partitioning of a system into regions that are described at different levels of theory is justified by the local character of (photo)chemical processes in condensed phases, in particular photoexcitation of a molecule. Therefore, one can often distinguish between a "reaction center" with atoms directly participating in the process and a "spectator" region, in which the atoms are not directly involved, but provide an electrostatic or steric background.

The multi-scale QM/MM potential energy operator thus includes interactions between (*i*) atoms in the QM region, (*ii*) atoms in the MM region and (*iii*) QM and MM atoms. The interactions within the QM and MM regions are described at the QM and MM level, respectively. Modeling the interactions between the two subsystems is more challenging and can be done at various degrees of sophistication [91]. The most popular approaches are to either describe all interactions between the two subsystems at the force field level (mechanical embedding approach), or, alternatively, include all charged MM atoms into the electronic Hamiltonian as additional one-electron operators, and hence allow the MM environment to polarize the QM subsystem (electrostatic embedding approach). In our simulations, we routinely use both embedding schemes, depending on the characteristics of the system we want to investigate.

3.4 Multi-Scale Tavis-Cummings Hamiltonian

Within the Born-Oppenheimer approximation the nuclear DOF evolve on adiabatic potential energy surfaces that are the parametric nuclear-position-dependent eigenstates of the Tavis-Cummings Hamiltonian in Equation 22. To obtain these eigenstates, we introduce a basis, in which each state is a tensor product between the molecular electronic states $|S_m^j\rangle$, computed at the QM/MM level described above, and the Fock states $|n_p\rangle$ of the cavity modes:

$$\begin{aligned} |\phi_{\{j,m\},\{p,n\}}\rangle &= \Pi_{\{j,m\}}\Pi_{\{p,n\}}\hat{\sigma}^{+}_{j,m}(\hat{a}^{\dagger}_{p})^{n}|\mathrm{S}_0^1\mathrm{S}_0^2..\mathrm{S}_0^{N-1}\mathrm{S}_0^N\rangle \otimes |00..0\rangle \\ &= \Pi_{\{j,m\}}\Pi_{\{p,n\}}\hat{\sigma}^{+}_{j,m}(\hat{a}^{\dagger}_{p})^{n}|\Pi_i^N \mathrm{S}_0^i\rangle \otimes |\Pi_p^{n_{\mathrm{modes}}} 0_p\rangle \qquad (23) \\ &= \Pi_{\{j,m\}}\Pi_{\{p,n\}}\hat{\sigma}^{+}_{j,m}(\hat{a}^{\dagger}_{p})^{n}|\phi_0\rangle, \end{aligned}$$

where state $|\phi_0\rangle$ is the ground state of the molecule-cavity system with all molecules de-excited and no photons in the cavity:

$$|\phi_0\rangle = |\mathrm{S}_0^1\mathrm{S}_0^2..\mathrm{S}_0^{N-1}\mathrm{S}_0^N\rangle \otimes |00..0\rangle = |\Pi_i^N \mathrm{S}_0^i\rangle \otimes |\Pi_p^{n_{\mathrm{modes}}} 0_p\rangle. \tag{24}$$

The basis states in Equation 23 represent one, two, three, four, ..., N excitations among the N molecules, with the constraint that each molecule, j, can at most have a single excitation into one of its multiple excited electronic states, $|\mathrm{S}_m^j\rangle$. In contrast, because the cavity modes are bosonic, there is no restriction on the number of excitations, n_p, these modes can have. Therefore, the number of basis states in principle is infinite.

Because molecules only have a limited number of accessible (bound) electronic states, the total number of basis states required to find the adiabatic eigenstates of the Hamiltonian (Equation 22) is finite in practice, but still computationally intractable for all but the smallest systems. Therefore, we restrict molecular excitations to the first excited state, *i.e.* $m = 1$. In addition, under the weak driving conditions, usually employed in experiments on organic cavities, the Hamiltonian can furthermore be restricted to the single-excitation subspace. Thus, we only consider (*i*) basis states in which either one of the molecules is in the first electronic excited state (*i.e.*, $|\mathrm{S}_1^j\rangle$), while all other molecules are in their ground states (*i.e.*, $|\mathrm{S}_0^{i\neq j}\rangle$) and none of the cavity modes is excited:

$$|\phi_{j\leq N}\rangle = \hat{\sigma}_j^+|\phi_0\rangle \tag{25}$$

and (*ii*) basis states in which all molecules are de-excited, while one of the cavity modes is excited:

$$|\phi_{j>N}\rangle = \hat{a}_{j-N}^\dagger|\phi_0\rangle \tag{26}$$

Thus, under the RWA and within the single-excitation subspace, the multi-scale Tavis-Cummings Hamiltonian (Equation 22) rearranges into:

$$\begin{aligned}\hat{H}^{\mathrm{TC}} &= \textstyle\sum_j^N \hbar\omega^{\mathrm{eg}}(\mathbf{R}_j)\hat{\sigma}_j^+\hat{\sigma}_j^- + \sum_j^N V_{\mathrm{S}_0}(\mathbf{R}_j) + \sum_p^{n_{\mathrm{modes}}} \hbar\omega_{\mathrm{cav}}(\mathbf{k}_p)\hat{a}_p^\dagger\hat{a}_p \\ &\quad - \textstyle\sum_j^N \sum_p^{n_{\mathrm{modes}}} \sqrt{\frac{\hbar\omega_{\mathrm{f}}(\mathbf{k}_p)}{2\epsilon_0 V}}\hat{\boldsymbol{\mu}}(\mathbf{R}_j)\cdot\left[\mathbf{f}_p(\mathbf{R}_c^j)\hat{\sigma}_j^+\hat{a}_p + \mathbf{f}_p^*(\mathbf{R}_c^j)\hat{\sigma}_j^-\hat{a}_p^\dagger\right].\end{aligned} \tag{27}$$

3.5 Multimode Optical Cavities

For a proper description of strong coupling between molecular excitations and the confined modes of an optical microcavity, not only is it important to consider the dynamics of many realistic molecules, but it is also critical to reflect on multiple cavity light modes [73, 97–100]. In particular, going beyond a single mode description is necessary for the simulation of the *in-plane* polariton transport, as the cavity dispersion gives rise to the emergence of the group velocity of light and, consequently, of polaritons [5, 101, 102].

Due to the boundary conditions that the cavity geometry imposes on electromagnetic fields, the dispersion of the cavity differs from that in free space, *i.e.* $\omega = |\mathbf{k}|c$. As an example, Figure 4 schematically depicts a typical dispersion of light as well as of the corresponding polaritons for the three cavity structures considered in this work, namely the Fabry-Pérot, or FP, microcavity, structures supporting surface lattice resonances, or SLRs, and structures supporting Bloch surface waves, or BSWs. As a result of different dispersions, the distribution of the polariton group velocity along the wave vector is not the same in these structures. This implies that for a correct estimation of the propagation velocity of polaritons in a particular cavity structure, we should include the dispersion of that very structure in the photonic part of the Tavis-Cummings Hamiltonian, that is in the third term of Equation 27. In Chapter 4, we discuss in detail the three microcavity types considered in this dissertation, in particular their mode structure and dispersion.

To alleviate the computational cost of simulations without loss of generality, we reduce the dimension of the light-matter system to a one-dimensional chain of molecules in a one-dimensional cavity, as illustrated in Figure 5 using the example of a Fabry-Pérot microcavity. There, the light is confined in the x direction between two reflecting mirrors in a form of a standing wave and can propagate in the z direction as a plane wave. The molecules are positioned along the z direction in the anti-node of the first-order out-of-plane cavity mode to facilitate a

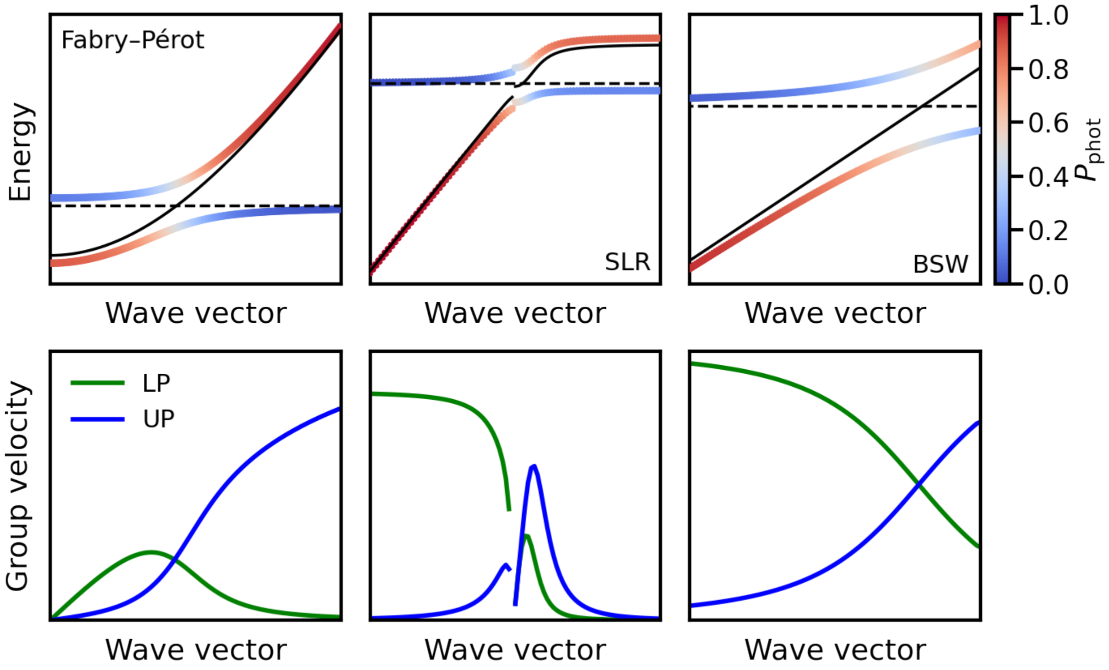

FIGURE 4 Typical dispersions of light and of the corresponding polaritons (upper panels) with their group velocities (lower panels) in the three cavity structures considered in this work: the Fabry-Pérot microcavity (left panels), structures supporting surface lattice resonances (SLR, middle panels), and structures supporting Bloch surface waves (BSW, right panels). In the upper panels, the black solid and dashed lines depict the dispersion of an empty cavity and of a bare molecular excitation, respectively, and the colors denote the contribution of the cavity light modes, P_{phot}, to a particular polaritonic state. Note that we do not show the numerical values because they are arbitrary and serve only to demonstrate the difference in the behaviour of the group velocity in different cavity structures.

stronger coupling. The corresponding polaritons are dispersive along the z direction, which makes it possible for energy to transfer over the molecular chain.

In principle, the number of light modes supported by a cavity is infinite (which is, however, smaller than the infinite number of modes in free space that results in such a peculiar phenomenon as the appearance of the attractive Casimir force between closely spaced conductive plates [103]). Nevertheless, only those modes which are not far away from resonance with a molecular excitation, are relevant for strong coupling. In our model, we follow Michetti and La Rocca [104] and apply periodic boundary conditions in the in-plane, z, direction, *i.e.*, $\mathbf{E}(z) = \mathbf{E}(z + L_z)$, with L_z the length of the cavity, which quantifies the wave vector $\mathbf{k}_z$ to discrete values, $k_{z,p} = 2\pi p / L_z$ with $p \in \mathbb{Z}$. Considering only the fundamental mode in the out-of-plane, x, direction, *i.e.* $k_x = \pi / L_x$ with L_x the width of the cavity, and employing a suitable cut-off for the dispersion in z direction [102], the number of modes n_{modes} is finite and the Hamiltonian in Equation 27 becomes an

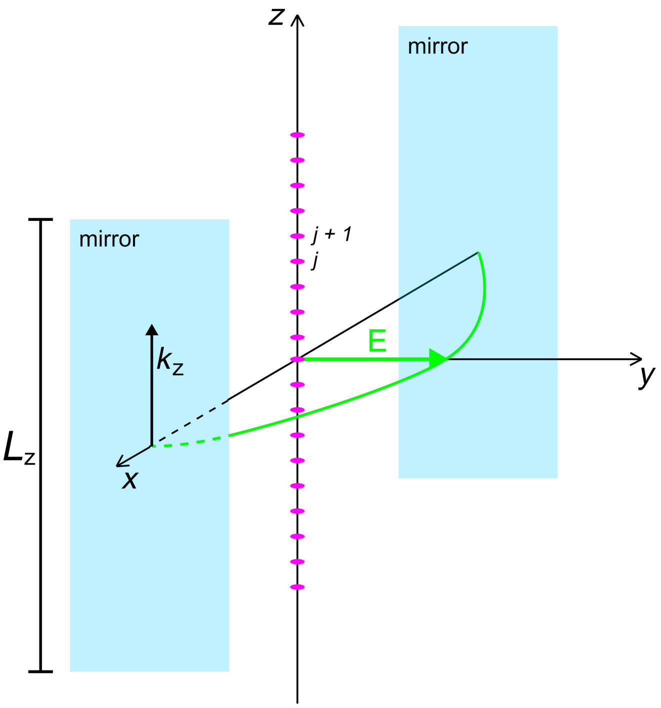

FIGURE 5 Schematic illustration of a one-dimensional Fabry-Pérot cavity. The light modes are confined in the x direction between the mirrors located at $-\frac{1}{2}x$ and $\frac{1}{2}x$, and can freely propagate along the z direction with in-plane momentum k_z and energy $\hbar\omega_{\text{cav}}(k_z)$. The vacuum electric field vector (green) is directed along the y-axis, and its maximum amplitude is reached at $x = 0$ where the N molecules (pink ellipses) are positioned at equal distances z_j along the z-axis.

$(N + n_{\text{modes}})$ by $(N + n_{\text{modes}})$ matrix containing four blocks [73]:

$$\mathbf{H}^{\text{TC}} = \begin{pmatrix} \mathbf{H}^{\text{mol}} & \mathbf{H}^{\text{int}} \\ \mathbf{H}^{\text{int}\dagger} & \mathbf{H}^{\text{cav}} \end{pmatrix}. \tag{28}$$

The upper left block, $\mathbf{H}^{\text{mol}}$, is an $N \times N$ matrix containing the one-photon molecular excitations. Since direct intermolecular excitations are neglected in our model, this block is diagonal, with elements labeled by the molecule indices j:

$$H^{\text{mol}}_{j,j} = \langle\phi_0|\hat{\sigma}_j \hat{H}^{\text{TC}} \hat{\sigma}_j^+|\phi_0\rangle, \tag{29}$$

for $1 \leq j \leq N$. Thus, each matrix element of $\mathbf{H}^{\text{mol}}$ represents the potential energy $V_{\text{S}_1}(\mathbf{R}_j)$ of molecule j in the electronic excited state $|\text{S}_1(\mathbf{R}_j)\rangle$ while all other molecules, $i \neq j$, are in the electronic ground state $|\text{S}_0(\mathbf{R}_i)\rangle$:

$$H^{\text{mol}}_{j,j} = V_{\text{S}_1}(\mathbf{R}_j) + \sum_{i \neq j}^{N} V_{\text{S}_0}(\mathbf{R}_i). \tag{30}$$

The potential energy surfaces of the molecules in the ground, $V_{\text{S}_0}(\mathbf{R})$, and excited states, $V_{\text{S}_1}(\mathbf{R})$, are computed at a suitable level of QM/MM theory (Section 3.3).

The lower right block, $\mathbf{H}^{\text{cav}}$, is an $n_{\text{modes}} \times n_{\text{modes}}$ diagonal matrix containing the one-photon excitations of the cavity modes:

$$H^{\text{cav}}_{p,p} = \langle \phi_0 | \hat{a}_p \hat{H}^{\text{TC}} \hat{a}^{\dagger}_p | \phi_0 \rangle, \tag{31}$$

for $1 \leq p \leq n_{\text{modes}}$, while all molecules are in the ground state $|\text{S}_0(\mathbf{R}_i)\rangle$. Here, $\hat{a}^{\dagger}_p$ excites cavity mode p with wave-vector $k_{z,p}$. Therefore, each matrix element of $\mathbf{H}^{\text{cav}}$ is the sum of the cavity energy at $k_{z,p}$ and the ground state energies of each molecule:

$$H^{\text{cav}}_{p,p} = \hbar\omega_{\text{cav}}(k_{z,p}) + \sum_j^N V_{\text{S}_0}(\mathbf{R}_j), \tag{32}$$

where $\omega_{\text{cav}}(k_{z,p})$ is the cavity dispersion (solid black lines in Figure 4).

The two $N \times n_{\text{modes}}$ off-diagonal blocks, $\mathbf{H}^{\text{int}}$ and $\mathbf{H}^{\text{int}\dagger}$, represent the light-matter interactions between the electronic excitations of molecules and the cavity modes within the dipole approximation:

$$\begin{aligned} H^{\text{int}}_{j,p} &= -\hat{\boldsymbol{\mu}}(\mathbf{R}_j) \cdot \mathbf{u}_{\text{y}} \sqrt{\frac{\hbar\omega_{\text{cav}}(k_{z,p})}{2\epsilon_0 V}} \langle \phi_0 | \hat{\sigma}_j \hat{\sigma}^{+}_j \hat{a}_p \mathbf{f}_p(z_j) \hat{a}^{\dagger}_p | \phi_0 \rangle \\ &= -\hat{\boldsymbol{\mu}}(\mathbf{R}_j) \cdot \mathbf{u}_{\text{y}} \sqrt{\frac{\hbar\omega_{\text{cav}}(k_{z,p})}{2\epsilon_0 V}} \mathbf{f}_p(z_j) \end{aligned} \tag{33}$$

for $1 \leq j \leq N$ and $1 \leq p \leq n_{\text{modes}}$. Here, z_j is the projection of center of the molecule on the z-axis of the cavity, and the index y of the polarization unit vector $\mathbf{u}_y$ implies that the light is polarised in the y direction (Figure 5). The form function $\mathbf{f}_p(z_j)$ is determined by the specific cavity type and will be discussed separately for each cavity structure considered in the dissertation.

Because the computation of the electronic energies, $V_{\text{S}_0}(\mathbf{R}_j)$ and $V_{\text{S}_1}(\mathbf{R}_j)$, and transition dipole moments, $\boldsymbol{\mu}(\mathbf{R}_j)$, can be performed in parallel, cavities with thousands of molecules can be efficiently modeled on high-performance computing resources [72], which allows to simulate polaritons in more realistic conditions than in the case of single-molecule models.

3.6 Semiclassical Molecular Dynamics

Diagonalizing the matrix representation of the multi-scale Tavis-Cummings Hamiltonian (Equation 27) in the basis of the single-excitation product states (Equation 28) yields the $N + n_{\text{modes}}$ hybrid light-matter *adiabatic* eigenstates $|\psi^m\rangle$:

$$|\psi^m\rangle = \left(\sum_j^N \beta^m_j \hat{\sigma}^{+}_j + \sum_p^{n_{\text{modes}}} \alpha^m_p \hat{a}^{\dagger}_p \right) |\phi_0\rangle \tag{34}$$

with eigenenergies E_m. The β^m_j and α^m_p expansion coefficients reflect the contribution of the molecular excitations, $|\text{S}_1(\mathbf{R}_j)\rangle$, and the cavity light modes, $|1_p\rangle$, to polariton $|\psi^m\rangle$. Due to their parametric dependence on the nuclear DOF, these eigenenergies form adiabatic potential energy surfaces $E_m(\mathbf{R})$, with $\mathbf{R}$ the $3 \times N_{\text{mol}} \times N_{\text{atoms}}$ coordinates of all atoms in the system.

Because for all but the smallest systems [105–110] a direct application of the time-dependent Schrödinger equation for the propagation of the combined photonic-electronic-nuclear DOF is computationally intractable, we model the nuclear degrees of freedom *classically* by means of MD instead [111]. Within this approximation, the classical trajectories are evolved by numerically integrating Newton's equations of motion under the influence of the forces due to the quantum DOF, for which the wave function, $|\Psi(t)\rangle$, is propagated along the trajectory.

Since the eigenstates, $|\psi^m\rangle$, of the Hermitian QM/MM Tavis-Cummings Hamiltonian (Equation 34) form a complete set, we expand the wave function in the basis of these states:

$$|\Psi(t)\rangle = \sum_m c_m(t)|\psi^m\rangle. \tag{35}$$

The equations of motion for the time-dependent expansion coefficients, $c_m(t)$, are obtained by substituting the wave function into the time-dependent Schrödinger equation:

$$\begin{aligned} \tfrac{\partial c_m(t)}{\partial t} &= -\tfrac{i}{\hbar}E_m(\mathbf{R})c_m(t) - \textstyle\sum_n \sum_j c_j(t)\langle\psi^m|\boldsymbol{\nabla}_n\psi^j\rangle \cdot \dot{\mathbf{r}}_n \\ &= -\tfrac{i}{\hbar}E_m(\mathbf{R})c_m(t) - \textstyle\sum_j c_j(t)\mathbf{d}_{mj} \cdot \dot{\mathbf{R}} \end{aligned} \tag{36}$$

with $\dot{\mathbf{r}}_n$ the velocity vector of nucleus n, and $\langle\psi^m|\boldsymbol{\nabla}_n\psi^j\rangle$ the non-adiabatic coupling vector between states m and j for a displacement of that nucleus. Likewise, $\dot{\mathbf{R}}$ and $\mathbf{d}_{mj}$ are the $3 \times N_{\text{mol}} \times N_{\text{atoms}}$ dimensional velocity and non-adiabatic coupling vectors of all atoms in the system.

The non-adiabatic coupling vector can also be expressed via the gradient of the Hamiltonian as

$$\mathbf{d}_{mj} = \sum_n \langle\psi^m|\boldsymbol{\nabla}_n\psi^j\rangle = \sum_n \frac{\langle\psi^m|\boldsymbol{\nabla}_n\hat{H}^{\text{TC}}|\psi^j\rangle}{E_j - E_n}. \tag{37}$$

Importantly, the non-adiabatic coupling vector is inversely proportional to the energy gap between states $|\psi^j\rangle$ and $|\psi^n\rangle$, which has an important role in the population relaxation between polaritonic states [75].

The non-adiabatic coupling vectors, $\mathbf{d}_{mj}$, account for the fact that adiabatic states can be changed along the nuclear trajectory. Thus, in the semi-classical MD simulations nuclear motions can induce population transfer between adiabatic states [111]. While the time-propagation of the quantum mechanical DOF is relatively straightforward, it remains ambiguous how to couple that evolution to the classical trajectories, despite decades of intensive research [112]. In our simulations, we rely on two approaches: mean-field, or Ehrenfest, MD and surface hopping.

Before describing these two approaches, we quickly mention that equivalent time-propagation of the coupled photonic-electronic DOF can also be achieved in the *diabatic* basis of product states between purely molecular and purely photonic (Fock) excitations (Equations 25 and 26). This equivalence is justified by the fact that the eigenstates $|\psi^m\rangle$ of the Hermitian Tavis-Cummings Hamiltonian (Equation 34) form a complete basis set, and therefore expanding the wave function in the adiabatic and diabatic bases is identical:

$$|\Psi(t)\rangle = \sum_m c_m(t)|\psi^m\rangle = \sum_j d_j(t)|\phi_j\rangle, \tag{38}$$

where expansion coefficients d_j reflect the contribution of molecular excitations ($j \leq N$, Equation 25) and cavity light modes ($j > N$, Equation 26) to the wave function $|\Psi(t)\rangle$.

Recently, we have extended our multiscale MD approach to perform simulations also in the diabatic basis. However, because the two representations are equivalent, in the next two sections we will focus on the Ehrenfest and surface hopping models in the adiabatic basis only, and for the details of simulations in the diabatic basis, we refer an interested reader to our recent publication [113].

3.7 Ehrenfest molecular dynamics

To demonstrate the idea of Ehrenfest approach, let us introduce a simple ansatz, in which the total nuclear-electonic-photonic wave function, $|\Phi(\mathbf{R}, \mathbf{r}, t)\rangle$, is represented as a product of the electronic-photonic wave function, $|\Psi(\mathbf{R}, \mathbf{r}, t)\rangle$ (Equation 35), and the nuclear wave function, $|\chi(\mathbf{R}, t)\rangle$:

$$|\Phi(\mathbf{R}, \mathbf{r}, t)\rangle = |\Psi(\mathbf{R}, \mathbf{r}, t)\rangle|\chi(\mathbf{R}, t)\rangle \exp\left[\frac{i}{\hbar}\int^t E^{\mathrm{TC}}(t')dt'\right], \tag{39}$$

where the total wave function depends explicitly on coordinates of both nuclei $\mathbf{R}$ and electrons $\mathbf{r}$, while the electronic-photonic wave function depends on the nuclear coordinates only parametrically. In Equation 39, the phase factor $\exp\left[\frac{i}{\hbar}\int^t E^{\mathrm{TC}}(t')dt'\right]$ with $E^{\mathrm{TC}} = i\hbar\langle\Psi|\frac{\partial\Psi}{\partial t}\rangle$, was introduced to simplify further derivations [114].

Inserting Equation 39 into the time-dependent Schrödinger equation and multiplying by $\langle\Psi(\mathbf{R}, \mathbf{r}, t)|$, we obtain an equation for the time-evolution of the nuclear wave function:

$$i\hbar\frac{\partial|\chi\rangle}{\partial t} = \langle\Psi|\hat{H}|\Psi\rangle|\chi\rangle = \hat{T}_N|\chi\rangle + \langle\Psi|\hat{H}^{\mathrm{TC}}|\Psi\rangle|\chi\rangle, \tag{40}$$

where $\hat{H} = \hat{T}_N + \hat{H}^{\mathrm{TC}}$ and $\hat{T}_N = -\sum_a \frac{\hbar^2}{2M_a}\nabla_a^2$ the kinetic energy of all nuclei in each atom a in the system.

The nuclear wave function can be expressed through the so-called Hamilton's principle function $S(\mathbf{R}, t)$ [115]:

$$|\chi(\mathbf{R}, t)\rangle = \exp\left[\frac{i}{\hbar}S(\mathbf{R}, t)\right]. \tag{41}$$

With this ansatz, Equation 40 is modified in the following way:

$$\frac{\partial S(\mathbf{R},t)}{\partial t}+\sum_a \frac{1}{2M_a}\left(\nabla_a S(\mathbf{R},t)\right)^2+\langle\Psi|\hat{H}^{\mathrm{TC}}|\Psi\rangle=i\hbar\sum_a\frac{1}{2M_a}\nabla_a^2 S(\mathbf{R},t). \quad (42)$$

Expression 42 has a form of the quantum Hamilton-Jacobi equation, in which the right-hand side can be regarded as a quantum correction. Therefore, assuming $\hbar \to 0$, we move to the classical Hamilton-Jacobi equation [116]:

$$\frac{\partial S(\mathbf{R},t)}{\partial t}+\sum_a \frac{1}{2M_a}\left(\nabla_a S(\mathbf{R},t)\right)^2+\langle\Psi|\hat{H}^{\mathrm{TC}}|\Psi\rangle=0, \quad (43)$$

in which $-\partial S(\mathbf{R},t)/\partial t = E(t)$ is the total energy of the system and $\mathbf{P}_a(\mathbf{R},t) = \nabla_a S(\mathbf{R},t)$ is the classical momentum of atom a. Thus, we can re-write Equation 43 as

$$E(t)=\sum_a\frac{\mathbf{P}_a^2(\mathbf{R},t)}{2M_a}+\langle\Psi|\hat{H}^{\mathrm{TC}}|\Psi\rangle. \quad (44)$$

The total energy of the system should be conserved. Therefore,

$$\frac{E(t)}{dt}=\sum_a\left[\frac{d\mathbf{P}_a(\mathbf{R},t)}{dt}+\langle\Psi|\nabla_a\hat{H}^{\mathrm{TC}}|\Psi\rangle\right]\boldsymbol{v}_a=0, \quad (45)$$

where in the second term, we used the chain rule, *i.e.* $\frac{d}{dt}=\sum_a\frac{d}{d\mathbf{r}_a}\frac{d\mathbf{r}_a}{dt}=\sum_a\nabla_a\times\boldsymbol{v}_a$ with $\boldsymbol{v}_a$ the velocity of atom a, and the expression $i\hbar\langle\Psi|\frac{\partial\Psi}{\partial t}\rangle = H^{\mathrm{TC}}|\Psi\rangle$ to show that $\langle\frac{d\Psi}{dt}|\hat{H}^{\mathrm{TC}}|\Psi\rangle = -\langle\Psi|\hat{H}^{\mathrm{TC}}|\frac{d\Psi}{dt}\rangle$.

The expression in the brackets of Equation 45 should be equal to zero, which gives us the Newton's equation of motion:

$$\mathbf{F}_a=\frac{d\mathbf{P}_a(\mathbf{R},t)}{dt}=-\langle\Psi|\nabla_a\hat{H}^{\mathrm{TC}}|\Psi\rangle, \quad (46)$$

and the *Hellmann–Feynman theorem* [117]. In Equation 46, $\mathbf{F}_a$ is the force acting on atom a.

Therefore, in Ehrenfest MD the nuclear trajectory evolves on the expectation value of the potential energy surface with respect to the total electronic-photonic wave function (Equation 35):

$$E^{\mathrm{mf}}(\mathbf{R})=\langle\Psi|\hat{H}^{\mathrm{TC}}|\Psi\rangle=\sum_j\sum_m c_j^* c_m\langle\psi^j|\hat{H}^{\mathrm{TC}}|\psi^m\rangle. \quad (47)$$

To propagate the nuclear trajectory, the matrix representation of the QM/MM Tavis-Cummings Hamiltonian (Equation 28) is diagonalized at every time step of the simulation, using the basis functions $|\phi_j\rangle$ (Equations 25 and 26), obtained from QM/MM calculations of the electronic states of the molecules [111]. Then, the derivatives of the mean-field potential energy surface (Equation 47) are computed from the molecular S_0 and S_1 gradients in combination with the expansion coefficients, $c_m(t)$, and used to integrate the positions of the classical nuclei over a discrete time interval, Δt [118], using the Hellmann–Feynman theorem:

$$\mathbf{F}_a=-\langle\Psi|\nabla_a\hat{H}^{\mathrm{TC}}|\Psi\rangle=-\sum_j\sum_m c_j^* c_m\langle\psi^j|\nabla_a\hat{H}^{\mathrm{TC}}|\psi^m\rangle. \quad (48)$$

In parallel, the wavefunction is propagated according to Equation 36 using the unitary propagation scheme proposed by Grannuci and co-workers [119].

One disadvantage of the Ehrenfest MD in general is that the trajectory, being evolved on an average potential of *all* adiabatic states $|\psi^m\rangle$, cannot decohere, *i.e.* to start behaving as a statistical ensemble of electronic states rather than a coherent superposition of them [116]. Nevertheless, in the case when there are many states close in energy [114], Ehrenfest dynamics performs well, hence it should be ideally suited for simulating polaritonic systems composed of very many collectively coupled molecules, in which the light-matter eigenstates form a dense manifold of nearly parallel potential energy surfaces [117], as, for instance, is shown in Figure 6.

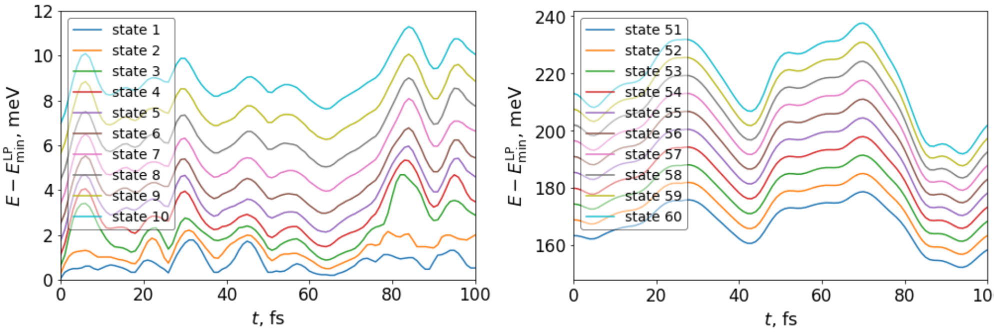

FIGURE 6 Time-evolution of the adiabatic polaritonic energies in a system of $N = 256$ Rhodamine molecules and $n_{\text{modes}} = 160$ cavity light modes at strong coupling characterised by a Rabi splitting of 325 meV. Because the energies remain parallel to each other during the dynamics, the mean-field potential is expected to have a similar trend, which justifies the usage of Ehrenfest MD approach.

3.8 Surface Hopping

An alternative method was suggested by Tully, in which a distinction is made between the *total* wave function, $|\Psi(t)\rangle$ (Equation 35), and an *auxiliary* adiabatic wave function, $|\psi^m\rangle$ (Equation 34) [120]. As in Ehrenfest MD, the total wave function determines all the system's observables, including the populations of the adiabatic (in our case, polaritonic) states, and is propagated along with the classical trajectory. The auxiliary adiabatic wave function, in turn, defines the potential energy surface on which the classical DOF evolve and is not explicitly propagated in time, but can stochastically change (hop) to other states.

To provide the correct quantum statistical distribution of states in an ensemble of surface hopping trajectories, the switching probabilities between different adiabatic states must represent the populations of these states in the total wave function. Based on Equation 36, the rate at which the populations change, is

$$\frac{\partial}{\partial t}|c_m|^2 = c_m \frac{\partial c_m^*}{\partial t} + c_m^* \frac{\partial c_m}{\partial t} = -\sum_j 2\Re[c_j^* c_m \mathbf{d}_{mj} \cdot \dot{\mathbf{R}}] = -\sum_j b_{mj}. \tag{49}$$

Tully argued that the number of hopping events should be minimised [120]. This is achieved in N^{traj} simulations if for a small time interval δt, $N^{\text{traj}} b_{mj} \delta t$ hops from $|\psi^j\rangle$ to $|\psi^m\rangle$ take place, and none from $|\psi^m\rangle$ to $|\psi^j\rangle$. Because in the beginning, $N^{\text{traj}}|c_j|^2$ of the trajectories are in state $|\psi^j\rangle$, the switching probability to state $|\psi^m\rangle$ is defined as

$$p_{j\to m} = \frac{N^{\text{traj}} b_{mj} \delta t}{N^{\text{traj}} |c_j|^2} = \frac{b_{mj}\delta t}{|c_j|^2}, \tag{50}$$

and the switching probability in the opposite direction should be zero. Thus, the probability to switch from $|\psi^j\rangle$ to $|\psi^m\rangle$ is computed as

$$p_{j\to m} = \max\left[0, \frac{b_{mj}\Delta t}{|c_j|^2}\right], \tag{51}$$

where Δt is the integration time step in the MD simulation. To decide if a hop between states $|\psi^j\rangle$ and $|\psi^m\rangle$ occurs, a random number ζ is taken from a uniform distribution between 0 and 1. Then, the hop is considered allowed if $\sum_{q\neq j}^{m} p_{j\to q} < \zeta < \sum_{q\neq j}^{m+1} p_{j\to q}$. After the hop, the evolution of the classical trajectory continues on the adiabatic potential energy surface, $E_m(\mathbf{R})$, of state $|\psi^m\rangle$. Because the hopping probabilities are based on the rates at which populations change, surface hops only occur when the trajectory reaches regions, in which the non-adiabatic coupling vectors $\mathbf{d}_{jm}$ (Equation 37) are not negligible. Otherwise, the vectors are close to zero and the adiabatic state populations do not change.

After a switch between two adiabatic states with different energies is made, the velocities of the nuclei are adjusted to conserve the total energy. Because such switching can only be induced by the nuclei if their velocity vectors overlap with the non-adiabatic coupling vectors ($\dot{\mathbf{R}} \cdot \mathbf{d}_{mj}$), the velocity adjustment is made parallel to the coupling vectors [121]. This can be thought of as applying a force to the nuclei in the direction of the non-adiabatic coupling vector, with the work done by the force being used to facilitate a switch between states [122–124].

While this so-called fewest switches surface hopping algorithm [120] found success in modeling non-adiabatic dynamics of systems with several excited states [112], a large number of simulations may be required to attain convergence in modeling systems with hundreds to thousands of near-degenerate states, as in the case of molecule-cavity systems in the strong coupling regime. Furthermore, because hops are stochastic, the trajectories are not deterministic, which not only contradicts the principles of classical dynamics but can also lead to inconsistencies between the potential energy surface on which the trajectory is evolved and the total polaritonic wave function, $|\Psi(t)\rangle$ (Equation 35). While for bare molecules such inconsistencies can be overcome with decoherence corrections [125–127], these corrections are *ad hoc* and lack a physical basis. Therefore, it is not *a priori* clear how to apply such corrections to polaritonic systems. Nevertheless, for simulations with fewer molecules, in particular when these molecules can undergo photo-chemical reactions, surface hopping remains the semi-classical method of choice [128–130].

3.9 Cavity decay

Because no realistic cavity is a closed system, the excitation is able to irrevocably leak into the environment through, for example, imperfect mirrors or ultrafast plasmon dephasing. The decay into the environment can be incorporated into the *density matrix formalism* of quantum mechanics. In this formalism, the Markovian dynamics of an *open quantum system* can be described by the Lindblad master equation [131]:

$$\frac{d\hat\rho}{dt} = -i\left[\hat H, \hat\rho\right] + \sum_j \frac{1}{2}\Gamma_j\left(2\hat L_j\hat\rho\hat L_j^\dagger - \hat L_j^\dagger\hat L_j\hat\rho - \hat\rho\hat L_j^\dagger\hat L_j\right), \tag{52}$$

where $\hat H$ is the Hamiltonian of the system of interest, $\hat L_j^+$ and $\hat L_j$ are the jump operators describing pumping and dissipation into the environment with index j labeling the possible quantum jumps, and Γ_j is the dissipation rates. The last two terms in the parenthesis of Equation 52 describe the relaxation into environment, while the first term accounts for the possibility of the excitation to appear in a new state after the decay. We assume that this "refilling" term is slow compared to the direct decay into the environment and take it out of consideration:

$$\frac{d\hat\rho}{dt} = -i\left[\hat H, \hat\rho\right] - \sum_j \frac{1}{2}\Gamma_j\left(\hat L_j^\dagger\hat L_j\hat\rho + \hat\rho\hat L_j^\dagger\hat L_j\right). \tag{53}$$

Without dissipation, Equation 53 reduces to the *von Neumann equation* for the evolution of the density operator [131].

Assuming $\hat H = \hat H^{\text{TC}}$, $\hat L_j^\dagger = \hat a_j^\dagger$ and $\Gamma_j = \gamma_j$ the cavity decay rate, Equation 53 is equivalent to the time-dependent Schrödinger equation for the *non-Hermitian* Tavis-Cummings Hamiltonian:

$$\begin{aligned}
\hat H^{\text{TC}}_{\text{non-Herm}} \quad = \quad & \textstyle\sum_j^N \hbar\omega^{\text{eg}}(\mathbf{R}_j)\hat\sigma_j^+\hat\sigma_j^- + \sum_j^N V_{\text{S}_0}(\mathbf{R}_j) \\
& + \textstyle\sum_p^{n_{\text{modes}}} \hbar\left[\omega_{\text{cav}}(\mathbf{k}_p) - \frac{i}{2}\gamma_p\right]\hat a_p^\dagger\hat a_p \\
& - \textstyle\sum_j^N\sum_p^{n_{\text{modes}}} \sqrt{\frac{\hbar\omega_{\text{cav}}(k_{z,p})}{2\epsilon_0 V}}\boldsymbol{\mu}(\mathbf{R}_j)\cdot\left[\mathbf{f}_p(\mathbf{R}_c^j)\hat\sigma_j^+\hat a_p + \mathbf{f}_p^*(\mathbf{R}_c^j)\hat\sigma_j^-\hat a_p^\dagger\right],
\end{aligned} \tag{54}$$

where the term proportional to γ_p relates to the radiative decay of cavity mode p.

Because the Hamiltonian in Equation 54 is non-Hermitian, its eigenvalues are complex and the eigenvectors are not orthogonal. Different methods have

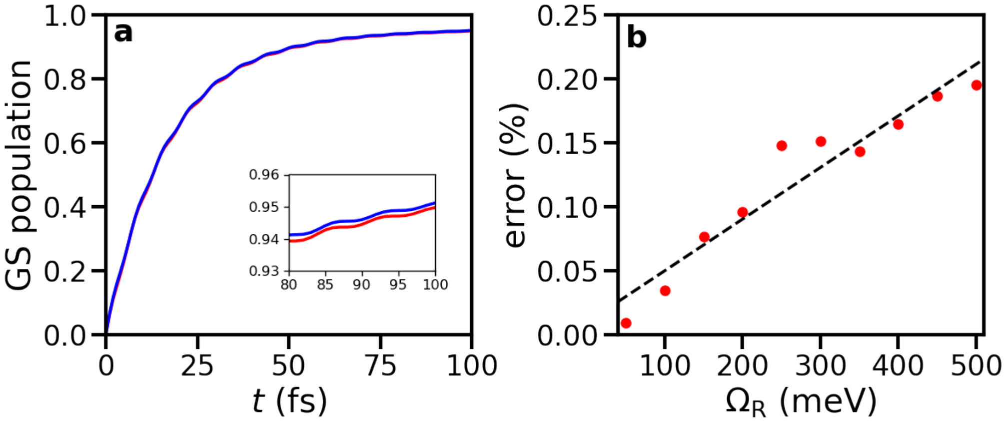

FIGURE 7 Panel **a**: Ground state (GS) population in a system of 1024 two-level excitons ($\hbar\omega^{\text{eg}} = 4.18$ eV) strongly coupled to 160 lossy ($\gamma = 66.7\ \text{ps}^{-1}$) cavity modes of a Fabry-Pérot cavity after excitation of a single cavity mode. The Rabi splitting was 300 meV. Panel **b**: Relative error between GS populations after 100 fs of simulations with the cavity losses inserted explicitly in the Hamiltonian (blue line in panel **a**) and added as a first-order decay rate (red line in panel **a**), plotted as a function of the Rabi splitting. The black dashed line displays a linear fit to the calculated values.

been proposed to run dynamics of systems described by such non-Hermitian Hamiltonians. Here, we adapt a method proposed by Granucci *et al.* [119], in which the wave function, $\Psi(t)$, is propagated under the influence of the non-Hermitian Hamiltonian $\hat{H}^{\text{TC}}_{\text{non-Herm}}$ with the expansion coefficients evolving in a similar way as in Equation 36, while the nuclear DOF are propagated on real adiabatic potential energy surfaces associated with the Hermitian Tavis-Cummings Hamiltonian (Equation 27). The details of the method and its implementation can be found in our recent publication [113].

Alternatively, cavity losses can be introduced as an *ad hoc* first-order decay of population from adiabatic states, $|\psi^m\rangle$, with a rate that is proportional to the total contribution of the cavity mode excitations to that state (*i.e.*, $\Gamma_m = \sum_p^{n_{\text{modes}}} \gamma_p |\alpha_p^m|^2$) [72]. Due to this decay, the norm of the wave function $\sum_m |c_m(t)|^2$ (Equation 35) is not conserved, but decreases to reflect the radiative losses:

$$\sum_m |c_m(t)|^2 = \sum_m |c_m(0)|^2 \exp\left[-\sum_p^{n_{\text{modes}}} \gamma_p |\alpha_p^m|^2 t\right]. \tag{55}$$

Although the two cavity decay implementations are not equivalent, they yield quantitatively very similar ground state populations, as exemplified in Figure 7. For this reason, in our simulations, we routinely utilise both schemes.

We note that, although possible, we do not consider molecular radiative decay in our simulation. This is a reasonable approximation, given that for most molecules fluorescence occurs on a nanosecond timescale which is a few orders of magnitude larger than both typical cavity decay rates and the simulation timescales.

4 RESULTS

In this chapter, results of multi-scale MD simulations of excitation energy transport in organic molecules strongly coupled to confined cavity light modes are presented. First, a general transport mechanism, suggested by the simulations, is discussed in Section 4.1. Then, the effect of the cavity decay rate on the lifetime and propagation distance of polaritons is examined in Section 4.2. Additionally, in Section 4.3, simulations of molecules in two particular cavity types, namely nanoparticle arrays supporting SLRs and structures supporting BSWs, are performed, and the dependence of the transport mechanism and the propagation distance on the photonic content of polaritonic states is studied. Finally, as a possible means of an efficient practical initiation of exciton propagation, a photochemical reaction is suggested and discussed in Section 4.4. Together, these results contribute to a comprehensive understanding of the mechanism of the in-plane excitation energy transport under strong light-matter coupling in optical microcavities.

4.1 General Mechanism of the Excitation Energy Transport in Organic Microcavities (Publication I)

In this section, we share the results of publication I, which is considered the core publication of the thesis. The main goal of this study was to propose a general mechanism for excitation energy transport in optical microcavities that would explain recent experimental observations [10]. The project was inspired by an early work of Agranovich and Gartstein on exciton-polariton transport in semiconductor planar microcavities [5]. Although this work made valuable predictions regarding the nature of exciton-polariton transport, such as the occurrence of ballistic propagation of ideal polariton wave packets and localisation of disordered polariton wave packets due to elastic scattering by "off-resonant" electronic transitions [101], the model introduced in the article lacked atomistic details of molecules nor did it account for thermal motions. In particular, it was not clear what would be the role of molecular vibrations on the transport and localisation of exciton-polaritons. Therefore, to make the model more realistic and allow for inclusion of such important effects as dynamical excitation energy disorder, interaction with molecular environment, as well as vibronic coupling, we extended this model to the multiscale QM/MM model as was described in Chapter 3.

In this work, we considered a chain of Rhodamine molecules (inset in Figure 8) in a one-dimensional Fabry-Pérot microcavity (Figure 5). While the choice of molecular species influences such characteristics as the strength of excitation energy disorder and of non-adiabatic coupling, it should not affect the general mechanism of exciton-polariton transport, which only relies on the hybrid light-matter nature of polaritons. Nevertheless, to check this, we have also performed simulations with two other molecules, namely Methylene Blue and Tetracene. Because the results of simulations with the three molecular species are, indeed, consistent, we only present the results of the transport simulation in a chain of Rhodamine molecules in the following.

Additionally, the choice of cavity type may quantitatively affect the propagation speed of exciton-polaritons through dispersion, but, again, the qualitative predictions are expected to be the same.

The dispersion of a Fabry-Pérot cavity is given by the following relation:

$$\hbar\omega_{\text{cav}}(\mathbf{k}) = \frac{\hbar c|\mathbf{k}|}{n_{\text{r}}} = \frac{\hbar c}{n_{\text{r}}}\sqrt{k_x^2 + k_y^2 + k_z^2}, \tag{56}$$

where n_{r} is the refractive index of the medium inside the cavity. For the cavity structure displayed in Figure 5, light forms a standing wave in the x direction, and hence k_x is discrete, *i.e.* $k_{x,q} = q\frac{\pi}{L_x}$ with $q \in \mathbb{Z}$ [132], while in the y and z directions, the light propagates freely as a plane wave so that k_y and k_z are continuous and $\mathbf{f}(k_x) = e^{ik_x x}$ and $\mathbf{f}(k_y) = e^{ik_y y}$. At $k_z \to 0$ and fixed k_x and k_y, the dispersion is parabolic, $\omega(k_z) = w_0 + \alpha k_z^2$ with $\alpha = \frac{c}{n_{\text{r}}k_x}$, and at large k_z the dispersion asymptotically approaches the dispersion of light, that is $\omega(k_z) = \frac{ck_z}{n_{\text{r}}}$. Because we are interested in a one-dimensional propagation of the excitation along the molecular chain in the z direction, we disregard the k_y component of the wave vector in Equation 56. Also, we limit the number of modes in the x direction to a single mode with $q = 1$, which is the fundamental mode. Lastly, we introduce periodic boundary conditions in the z directions, which makes the k_z component of the wave vector discrete, *i.e.* $k_{z,p} = p\frac{2\pi}{L_z}$ with $p = 1, ..., n_{\text{modes}}$ [104], and limit the number of cavity modes by $n_{\text{modes}} = 160$. With the cavity length of $L_z = 50$ μm and width of $L_x = 163$ nm, the dispersion spans the energy range from 3.81 eV to 5.48 eV (dashed-dotted line in Figure 8) and becomes resonant with the absorption maximum of Rhodamine at 4.18 eV at CIS/3-21G levels of quantum chemistry (dashed line in Figure 8) at $k_z^{\text{res}} = 8.7$ μm^{-1}. As a result of strong interaction between excitons in Rhodamine molecules and the cavity light modes, the dispersive UP and LP branches, separated by the Rabi splitting of $\sim$325 meV, are formed (blue and cyan lines in Figure 8). We note that because the cavity modes volume and hence the electric field strength is a parameter in our model, we can easily adjust the Rabi splitting by choosing a suitable electric field strength. Here, the Rabi splitting of $\sim$325 meV was achieved with $|\mathbf{E}| = 0.26\ \mathrm{MVcm}^{-1}$.

We note that because we consider excitation transport in only one direction, we cannot properly account for the elastic scattering of polaritons, since in a one-dimensional cavity, due to the conservation law, such scattering is possible only with a change in the sign of the wave vector, *i.e.* $|\mathbf{k}| \rightarrow -|\mathbf{k}|$, which is unlikely. Although considering a two-dimensional cavity would allow a better description of elastic scattering, this would require modeling a large number of molecules, which is currently not feasible with our available computational resources.

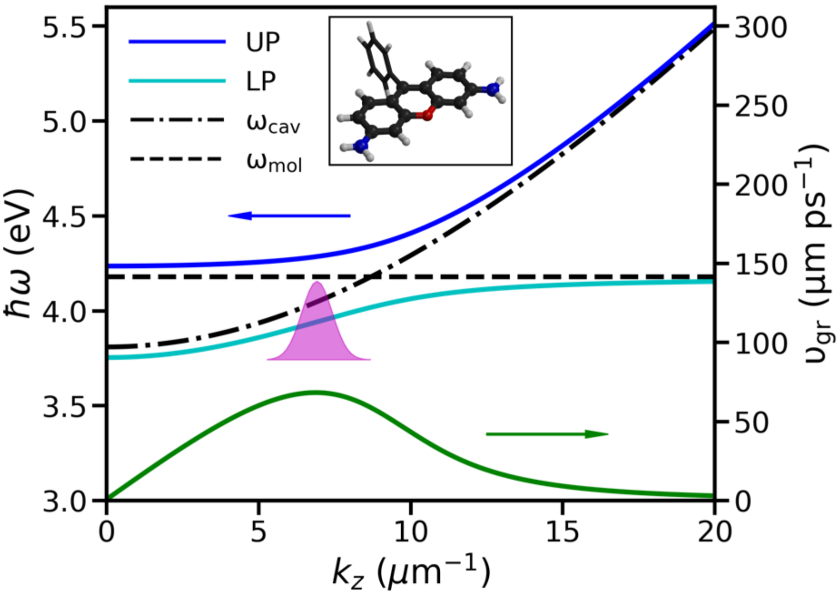

FIGURE 8 Polariton dispersion in a system of Rhodamine molecules in a Fabry-Pérot microcavity. The bare cavity, ω_{cav}, and molecular, ω_{mol}, dispersions are shown as the dashed-dotted and dashed black lines. The corresponding dispersons of the upper (UP) and lower polariton (LP) branches are depicted in blue and cyan. With the cavity electric field strength $|\mathbf{E}| = 0.26\ \mathrm{MVcm}^{-1}$, the Rabi splitting between the LP and UP is $\sim$ 325 meV. The green line shows the group velocity, v_{gr}, of the LP branch, and the magenta bell sketches the position of the initial Gaussian wave packet of lower polaritons in the reciprocal space. In the inset, the structure of Rhodamine molecule is shown. The QM part, consisted of three in-plane rings, is described at the HF/3-21G and CIS/3-21G levels of theory in the electronic ground (S_0) and excited (S_1) states, respectively. The MM part, consisted of the out-of-plane ring atoms of Rhodamine, as well as the water molecules (not shown), are modelled with the Amber03 force field.

Experimentally, exciton-polariton transport can be initiated either directly by resonantly pumping polaritonic states, or indirectly by pumping higher-energy excited states of molecules. Below, we consider both excitation schemes separately.

4.1.1 Resonant excitation

In practice, resonant excitation of polaritons is achieved by adjusting the energy of a laser to the energy of polaritons. The spatial profile of a laser beam is well approximated by the Gaussian distribution, as is the profile in the reciprocal space. Therefore, in our simulations we realise resonant excitation by creating a Gaussian wave packet of polaritons [5]:

$$c_m(0) = \left(\frac{\zeta}{2\pi^3}\right)^{\frac{1}{4}} \exp[-\zeta(k_z^m - k_c)^2] \tag{57}$$

with $c_m(0)$ expansion coefficients of the total wave function (Equation 35) at the beginning of the simulations, $\sqrt{\zeta} = 10^{-6}$ m characteristic width of the wave packet, k_z^m the expectation value of the in-plane momentum of polariton $|\psi_m\rangle$ (i.e., $\langle k_z^m \rangle = \sum_p^{n_{\text{modes}}} |\alpha_p^m|^2 k_{z,p} / \sum_p^{n_{\text{modes}}} |\alpha_p^m|^2$), and k_c position of the wave packet's centre. As shown in Figure 8, the wave packet consists of the polaritonic states in the LP branch and is centred at the wave vector $k_c = 6.9\ \mu\text{m}^{-1}$, corresponding to the maximal group velocity, $v_{\text{gr}}^{\text{max}} = 68\ \mu\text{mps}^{-1}$.

Figure 9**a** shows the time-propagation of such a polaritonic wave packet in a system containing 1024 molecules in a lossless cavity ($\gamma_{\text{cav}} = 0\ \text{ps}^{-1}$). Initially, the wave packet propagates ballistically with an average speed corresponding to the centre of the wave packet, *i.e.* $v_{\text{gr}}^{\text{max}}$ (dashed line in Figure 9**a**). This ballistic motion is manifested by a linear increase of the expectation value of the position of the wave packet, $\langle z \rangle$ (Figure 9**c**), and a quadratic increase of the mean squared displacement (MSD, purple line in Figure 9**d**) during about 100 fs of simulation. Thereafter, the wave packet slows down, as clearly seen in the plot of $\langle z \rangle$, and the MSD becomes linear (cyan line in Figure 9**d**), which suggests a transition from ballistic to diffusive transport.

While the front of the wave packet moves at the maximal speed, the whole packet broadens and sharp features, visible as vertical lines in the time-space map of the probability amplitude of the wave function, $|\Psi|^2$ (Figure 9**a**), appear. These peaks also emerge when the simulation is repeated with frozen nuclear DOF and different excitation energies of molecules. Therefore, the appearance of the peaks is related to the excitation energy disorder, which causes localisation of polaritons on particular molecules, as was previously suggested by Agranovich and Gartstein based on the analysis of two-level systems with static energy disorder [5].

The transition between ballistic and diffusive transport regimes occurs when the contribution of molecular excitons to the total wave packet exceeds the contribution of the cavity light modes, as shown in Figure 9**b**. As there are no losses in the system, the decrease in the photonic contribution is due to population transfer from initially excited LP states to the entropically favourable reservoir of dark states [133]. Because the dark states lack group velocity and direct intermolecular couplings are not included in our model, these states are stationary and hence cannot contribute to the diffusive propagation of the polariton wave packet, and the bright states must still be involved. Thus, our simulations suggest that while, initially, population is transferred from the propagating bright states into the sta-

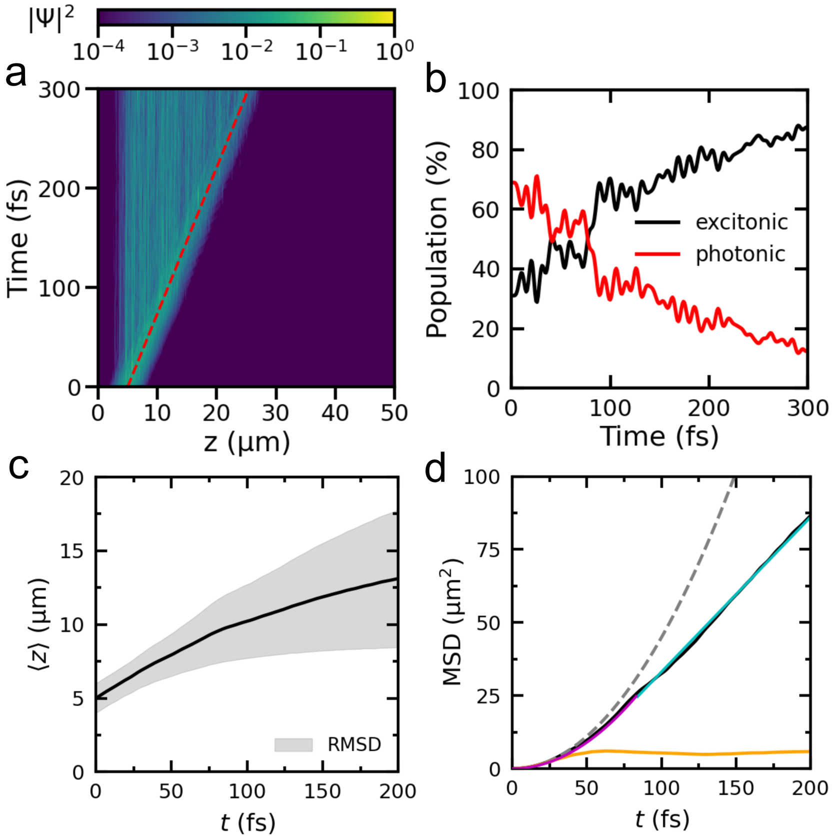

FIGURE 9 Panel **a**: Probability density, $|\Psi|^2$, of the polariton wave function (Equation 35) as a function of distance and time after *resonant* excitation in a system of 1024 Rhodamine molecules strongly coupled to a multimode cavity. The red dashed line corresponds to the maximum group velocity of the LP branch. Panel **b**: Contribution of molecular excitons (black) and cavity light modes (red) to $|\Psi|^2$ as a function of time. Panel **c**: Expectation value, $\langle z \rangle$ (black line), and root mean squared displacement (RMSD, grey area) of the position of the polariton wave function. Panel **d**: MSD of the polariton wave function at $T = 300$ K (solid black line) and $T = 0$ K (dashed grey line) in a lossless cavity, as well as at $T = 300$ K in a lossy cavity ($\gamma_{\text{cav}} = 66.7\ \text{ps}^{-1}$, solid orange line). The magenta and cyan lines are quadratic and linear fits to the MSD in a lossless cavity at $T = 300$ K.

tionary dark states [75], this process is reversible, so that the bright LP states get "fed" by the dark states thus forming propagating wave packets within the full range of LP group velocities. This continuous process of creation and destruction of wave packets eventually results in a diffusive-like transport of polaritons, which is manifested as a linear MSD of the probability amplitude.

Because the non-adiabatic coupling vector, responsible for population transfer, is inversely proportional to the energy gap between states (Equation 37), the turnover from ballistic to diffusive transport depends on the overlap between the molecular absorption spectrum and polaritonic states, and can hence be controlled by tuning the excitation energy and wave vector along a polariton branch.

We note that when the nuclear DOF are frozen, a polariton wave packet displays a linear uniform motion, typical of ballistic transport, and the corresponding MSD remains quadratic (dashed line in Figure 9**d**), even in the event of a moderate disorder. In contrast, when the disorder strength is well beyond that of Rhodamine, the wave packet becomes localised and no coherent polariton transport occurs [5]. This demonstrates the importance of treating molecules as dynamic entities, since only then can a transition from ballistic to diffusive transport be observed.

So far, we have discussed transport in a perfect cavity without losses. The inclusion of cavity decay brings an additional relaxation channel, which depletes the population from bright polaritonic states and competes with the transfer into the dark states. This leads to a faster turnover to the diffusive transport and an overall smaller MSD (orange line in figure 9**d** for simulation with $\gamma_{\text{cav}} = 66.7\ \text{ps}^{-1}$). Because cavity losses restrict the lifetime of bright LP states, the maximal distance a wave packet can reach is limited by two factors: (i) a shortening of the ballistic phase, and (ii) a reduction of the diffusion coefficient in the second phase (the orange line in figure 9**d** looks flat compared to the purple line). This implies that the propagation speed is significantly lower than in the perfect cavity. In Section 4.3 we address this connection between the cavity lifetime and the propagation speed and distance in detail.

Experimentally, polariton transport at resonant excitation was first demonstrated in an inorganic structure. In the experiment of Freixanet *et al.*, fully ballistic propagation of polaritons was observed for a strongly coupled quantum dot at cryogenic temperatures [8]. In our simulations, such a purely ballistic transport can be achieved with frozen molecules (dashed line in Figure 9**d**). Recently, a room-temperature polariton motion in strongly coupled organic molecules was also studied, and the ballistic transport followed by diffusion was observed [16]. Our simulations agree with these transient absorption measurements and suggest that the observed transition between the propagation regimes can be attributed to reversible population transfers between propagating bright states and stationary dark states.

4.1.2 Off-resonant excitation

Besides resonant excitation, transport of polaritons can be initiated indirectly, when a higher-energy electronic state of the molecules is pumped [9, 10, 14, 20]. According to Kasha's rule, after such excitation, a molecule quickly relaxes to the first excited state, S_1. If this molecule is a part of a strongly coupled ensemble of molecules, the population can be transferred to bright states, causing exciton-polariton transport.

To model off-resonant excitation, we start simulations in the S_1 state of a single molecule, j, placed at $z_j = 5\ \mu\text{m}$. In the diabatic basis, this is achieved by setting the expansion coefficient corresponding to this molecule to one, *i.e.* $d_j(0) = 1$, while all the other coefficients are zero, $d_{i \neq j}(0) = 0$ (Equation 38). In the adiabatic basis, in turn, excitation of a molecule is not an eigenstate of the Hamiltonian and hence should be represented as a linear combination of the polaritonic states (Equation 34):

$$|\Psi(0)\rangle^{(\text{loc. on } j)} = \sum_{m}^{N+n_{\text{modes}}} c_m(0)|\psi^m\rangle = \sum_{m}^{N+n_{\text{modes}}} U^{\dagger}_{mj}|\psi^m\rangle = \sum_{m}^{N+n_{\text{modes}}} \beta^m_j|\psi^m\rangle \quad (58)$$

with $U^{\dagger}_{mj}$ the elements of the unitary matrix $\mathbf{U}$ that diagonalises $\hat{H}^{\text{TC}}$. Because we intend to localise excitation on molecule j, these matrix element are nothing more than the expansion coefficients, β^m_j, associated with this molecule (Equation 34).

Figure 10**a** shows the propagation of the probability density of the wave function, $|\Psi|^2$, after such an off-resonant excitation in an imperfect cavity with decay rate $\gamma_{\text{cav}} = 66.7\ \text{ps}^{-1}$. Although only a single molecule is excited in the beginning of the simulation, the population rapidly spreads to other molecules. Because the initial state is a superposition of both stationary dark states and bright states moving with different group velocities, the wave packet displays a complex behaviour, in which the front initially moves with the maximum group velocity of the LP branch (dashed line in Figure 10**a**), while the average propagation speed is much slower (Figure 10**c**).

Unlike resonant excitation, at which the initial excitation is composed of bright polaritonic states moving ballistically, the mixed character of the initial state at off-resonant excitation results in the absence of a ballistic phase, and the wave packet travels in a diffusive manner from the very beginning of the simulation (cyan line in figure 10**d**). During this phase, the motion of bright polaritonic states is continuously interrupted and then restarted with different group velocities, as was also observed in the diffusive phase at the resonant excitation (Section 4.1.1).

Along with the population exchange between bright and dark states, manifested in Figure 10**b** as oscillations in the excitonic and photonic contribution to the polaritonic wave function, cavity decay leads to a monotonous build-up of the total ground state population (blue line in Figure 10**b**). This depletion of the bright states restricts the distance covered by the wave packet. Nevertheless, this distance is still about micrometer scales, which is extraordinary for excitons in organic materials. A rough estimation of the diffusion coefficient from the linear fit of the MSD in Figure 10**d**, *i.e.* $\text{MSD}(t) = 2Dt$, gives the value of D around 8.8 $\mu\text{m}^2\text{ps}^{-1}$, which exceeds the typical diffusion coefficients of excitons in organic semiconductors by a few orders of magnitude [30].

Dark states, having a minor contribution from the cavity light modes, decay at a much slower timescale compared to bright states, whose lifetime is primarily determined by the cavity lifetime [62, 134]. Therefore, in addition to slowing down the wave packet by "trapping" the population through non-adiabatic transfers, dark states provide bright states with protection from cavity losses. Indeed, the polariton wave packet survives for much longer (at least 300 fs; blue line in Figure 10**b**) than expected from the bare cavity decay rate (dashed grey line in Figure 10**b**). Considering that the rate of population transfer into the DS reservoir is proportional to the molecular density of states, this protection effect may explain the detection of polariton signatures on a picosecond timescale in realistic cavities with billions of molecules [10, 61].

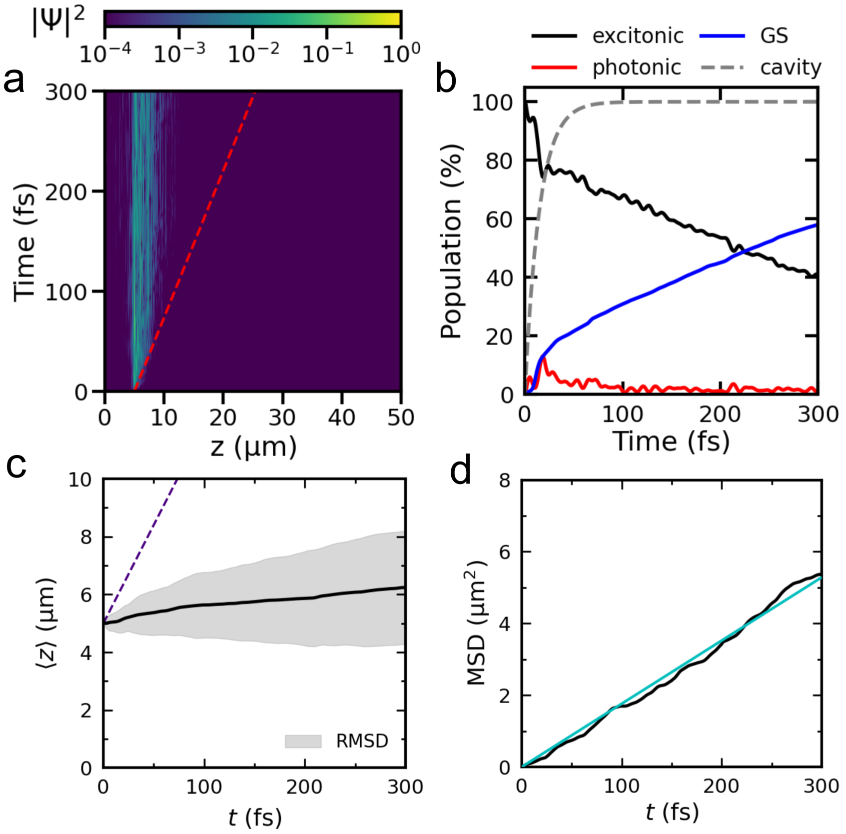

FIGURE 10 Panel **a**: Probability density, $|\Psi|^2$, of the polariton wave function (Equation 35) as a function of distance and time after *off-resonant* excitation in a system of 1024 Rhodamine molecules strongly coupled to a multimode lossy cavity ($\gamma_{\text{cav}} = 66.7\ \text{ps}^{-1}$). The red dashed line corresponds to the maximum group velocity of the LP branch. Panel **b**: Contribution of molecular excitons (black) and cavity light modes (red) to $|\Psi|^2$, as well as the population of the total ground state (GS) in MD simulations (blue) and as expected from the cavity decay rate (*i.e.* $1 - \exp(-\gamma_{\text{cav}} t)$, dashed grey line), as a function of time. Panel **c**: Expectation value, $\langle z \rangle$ (black line), and RMSD (grey area) of the position of the polariton wave function. As a reference, the dashed line shows the distance corresponding to the maximum group velocity of the LP, *i.e.* $v_{\text{gr}}^{\text{max}} t$. Panel **d**: MSD of the polariton wave function at $T = 300$ K. The cyan line is a linear fit to the MSD.

It is important to note that in addition to non-adiabatic transfers from dark states resulting in the formation of propagating wave packets, polariton spreading at off-resonant excitation is also caused by Rabi oscillations, in particular at the start of simulations. Additional simulations with frozen nuclear DOF, when only the second mechanism is operational, showed a reduced wave packet's propagation, with the excitation remaining more localized on the molecule that was initially excited, compared with simulations at room temperature, which underlines the importance of molecular motions on the transport of polaritons.

In one of the first experimental observations of organic exciton-polariton transport, the polariton emission pattern after off-resonant excitation was found to remind a diffusion process with a propagation speed a few orders of magnitude smaller than the group velocity from the polariton dispersion [10]. The results of our simulations qualitatively agree with these observations and suggest that reversible population transfers between dark states with no group velocity and propagating bright states make polariton transport appear diffusive.

4.1.3 Summary

We summarise the main conclusions of Publication I suggested by the performed MD simulations:

- Strong coupling of organic molecules with the confined light modes of an optical microcavity leads to a micrometer-range in-plane excitation energy transfer, which is a few orders of magnitude beyond the typical diffusion lengths of bare excitons in organic molecules [30];
- Upon resonant excitation of polaritonic states, the excitation initially ballistically propagates as a wave packet with the group velocity according to the polariton dispersion;
- After a short ballistic phase, the propagation becomes diffusive at longer times due to reversible population exchange between propagating bright states and non-propagating dark states;
- For off-resonant excitation, transport is diffusive from the very beginning;
- Dark states extend the lifetime of the molecule-cavity system [117], resulting in polariton propagation observed on timescales far beyond the cavity lifetime [10].

4.2 Effect of the Cavity Lifetime on Polariton Transport (Publication II)

In the previous section, we have discussed that the leakage of excitation through the cavity mirrors leads to depletion of bright polaritonic states. Because the cavity decay rate is typically much faster than the rate of both fluorescence and radiationless decay in organic molecules, the lifetime of organic polaritons is determined by the lifetime of the cavity modes [62, 134]. For that reason, one can anticipate a connection between the cavity lifetime and the survival time of polaritons and hence of the propagation distance.

Recently, such a connection was scrutinised experimentally by Pandya *et al.* [17]. In a series of DBR microcavities with similar dispersions but different quality factors, or Q-factors, related to the cavity lifetime, $\tau_{\text{cav}} = \gamma_{\text{cav}}^{-1}$, as $Q = \omega_{\text{cav}}\tau_{\text{cav}}$, propagation of a polariton wave packet in a cavity with boron-dipyrromethen-R (BODIPY-R) dyes was imaged by femtosecond transient absorption microscopy. After initial broadband excitation of polaritonic states (Figure 11**a**), a ballistic spreading of a polaritonic wave packet followed by shrinking, was observed (Figure 11**e**). Moreover, the effect was most pronounced in the cavity with a larger Q-factor, which manifested itself in an increased propagation distance in the ballistic phase, as well as a longer duration of this phase (black line in Figure 11**e**).

To bring theoretical insights into these experimental observations, we have carried out simulations of excitation energy transport in a Fabry-Pérot microcavity filled with 512 Rhodamine molecules. With the dispersion of the cavity and hence of polaritons, the same as in Section 4.1 (Figure 11**b**), the only control parameter was the cavity lifetime, of which three values were selected: $\tau_{\text{cav}} = 15,\ 30$, and 60 fs. To correspond to experimental conditions, a broadband excitation of upper polaritons, centred at $\hbar\omega = 4.41$ eV and covering the whole UP branch, was used (pink rectangle in Figure 11**b**).

In the simulation, the choice of Rhodamine instead of BODIPY-R, which was used in the experiment, was made because BODIPY-R (and other derivatives of the BODIPY family of molecules) is a rather complex molecule to simulate its excited state properties [135]. Therefore, to simulate multiple molecules in a cavity on a sub-picosecond timescale, we chose Rhodamine to work with. As we made sure in the simulation of three different molecular species in Section 4.1, the mechanism of polariton transport remains the same regardless of the choice of the molecule in simulations, which further justifies the choice of Rhodamine.

Figure 11**c** displays the spatio-temporal propagation of the probability density of the polariton wave function in the best-quality cavity, *i.e.* with lifetime $\tau_{\text{cav}} = 60$ fs. The initially localised wave packet rapidly spreads on a micrometer scale and then splits into two components. The first component propagates faster than the maximal group velocity of the LP branch (magenta line in Figure 11**c**) with its front moving with the maximal group velocity of the UP branch (yellow line in Figure 11**c**). Therefore, we attribute this fast propagation to upper polaritonic states with a high group velocity. Because such states are energetically separated from the manifold of dark states (cyan line in Figure 11**b**), and the rate of population transfer between polaritonic states is inversely proportional to the energy gap between the states (Equation 37), the main relaxation channel for the highest-speed upper polaritons is radiative decay to the ground state. As a result, the fast-moving component of the wave function vanishes at around 200 fs after the excitation.

Because the lifetime of polaritonic states is determined by the cavity lifetime, the moment when the faster component of the wave packet disappears should also depend on the cavity lifetime. In the experiment, this dependence was captured by measuring the position-dependent transient transmission of the cavity, $\Delta T(z,t)/T_0$, where $\Delta T = T^* - T_0$ with T_0 and T^* the transmission spectra before pumping, *i.e.* associated with the ground state, and at time t after pumping [49]. For a direct comparison with the experiment, we have developed an

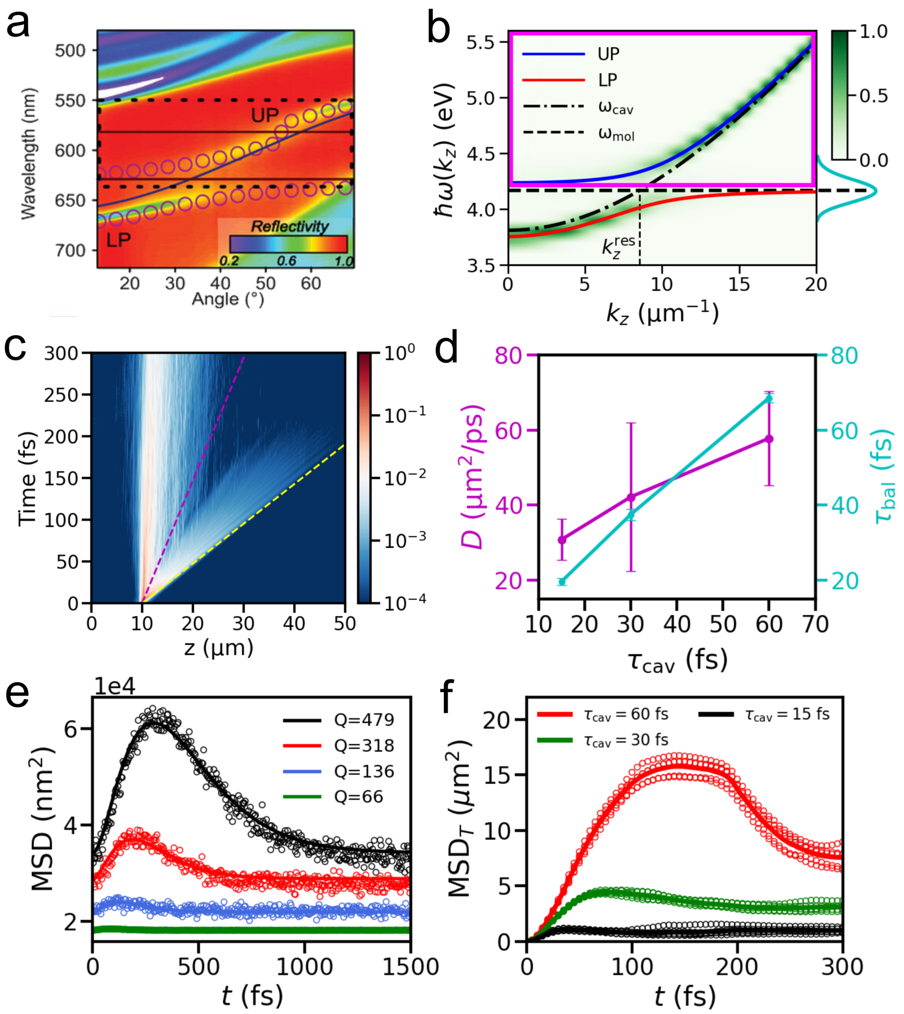

FIGURE 11 Panel **a**: Angle-resolved reflectivity of a microcavity used in study [17]. The circles indicate the LP and UP branches, and the dashed rectangle marks the range of wavelengths covered by the pump pulse used in transient absorption measurements. Panel **b**: Normalised angle-resolved absorption spectrum of the cavity, used in MD simulations. The blue and red solid lines indicate the UP and LP branches, and the dashed and dashed-dotted lines indicate the excitation energy of Rhodamine and the cavity dispersion, respectively. The pink rectangle marks the range of initially excited UP states, and the cyan line sketches the absorption spectrum of Rhodamine. Panel **c**: Probability density, $|\Psi|^2$, of the polariton wave function as a function of distance and time in the cavity with the lifetime of 60 fs. The magenta and yellow lines correspond to the maximal group velocity of the LP (68 μm ps^{-1}) and UP (212 μm ps^{-1}), respectively. Panel **d**: Duration of the ballistic phase (cyan) and diffusion coefficient in the diffusive phase (magenta) as a function of the cavity lifetime. Panel **e**: MSD$_T$ obtained in experiment [17] with cavities having different quality factors. Panel **f**: MSD$_T$ obtained in MD simulations with different cavity lifetimes. Panels **a** and **e** are reproduced with permission from Pandya *et al.*, Adv. Sci. **9**, 2105569 (2022). Copyright 2022 John Wiley & Sons, Inc.

expression for the MSD of this position-dependent transient transmission:

$$\mathrm{MSD}_T = \sum_i^N (z_i - z_0)^2 \frac{\Delta T(z,t)}{T_0} = \sum_i^N (z_i - z_0)^2 \left[\exp\left(\varepsilon_\mathrm{a} d |\Psi(z_i,t)|^2\right) - 1\right], \quad (59)$$

where z_0 is the expectation value of the position of the wave packet at the start of a simulation and the sum goes over the positions z_i of all 512 molecules. As we show in the Supporting Information of Publication II, the absorption coefficient ε_a and the distance d over which the light passes through the material inside the cavity, which is Rhodamine in our case, do not influence the shape of the MSD and hence can be chosen freely.

The time-dependence of the MSD_T in the three cavities with a different lifetime is shown in Figure 11**f**. In all cases, the initial growth of the MSD_T is quadratic, implying a ballistic propagation. To estimate the duration of this ballistic phase, an equation proposed in the experimental study [17], was used to fit the MSD_T from $t = 0$ to $t = t_{MSD_T^\mathrm{max}}$ when the MSD_T reaches its maximum:

$$\mathrm{MSD}_T(t) = v_\mathrm{bal}^2 t^2 \exp\left(-t/\tau_\mathrm{bal}\right) \quad (60)$$

with v_bal and τ_bal the propagation speed and the duration of the ballistic phase, respectively. From fits to the MSD_T, the values of τ_bal were extracted and plotted in Figure 11**d** as a function of the cavity lifetime (cyan line). Clearly, a better quality of the cavity leads to a longer duration of the ballistic phase. Furthermore, because the cavity dispersion and, therefore, the group velocity of polaritons are independent of the decay rate of the cavity excitation, a longer lifetime of the upper polariton in the best-quality cavity results in a further propagation of the faster component, which is manifested in a higher MSD_T in Figure 11**f**. Both findings are in a good qualitative accordance with the experiment, as visible by comparing panels **e** and **f** of Figure 11.

Due to the disappearance of the fast-moving component, the total polariton wave packet contracts, and the MSD_T decreases (Figure 11**f**). Nevertheless, the transport does not cease, which happens due to the second, slower, component, which is long-lived and, therefore, should be comprised mostly of dark states with no group velocity, into which some population of the initially excited wave packet of upper polaritons has relaxed. Because the population is also reversibly transferred into the lower-lying LP states, the transport continues, and the MSD_T does not turn to zero after reaching its peak. Instead, the MSD_T decreases down to a certain value and then starts increasing again, but already linearly rather than quadratically, thus suggesting a diffusive transport. Applying a linear fit to the MSD of the slower component, the diffusion coefficient was extracted from $\mathrm{MSD}_\mathrm{diff} = 2Dt$ and found to increase with τ_cav (magenta line in Figure 11**d**). This result can be explained by the following reasoning. The overall diffusive propagation of the polariton wave packet is a sequence of ballistic propagation phases, which are occasionally interrupted when the population is "trapped" by the DS manifold. Because the duration of such ballistic phases is defined not only by the magnitude of non-adiabatic coupling which causes population transfer between lower polaritons and dark states, but also by the cavity lifetime, the diffusion coefficient depends on the Q-factor and increases with the cavity lifetime.

To conclude this section, we have performed MD simulations of excitation energy transport in microcavities with a different quality factor and with excitation conditions similar to those used in experiment [17]. The results of our simulations qualitatively agree with the experiment, showing a ballistic spreading of the polariton wave packet followed by contraction due to irreversible radiative decay of population from highly photonic fast-moving upper polaritonic states. Furthermore, both the duration of the ballistic phase and the diffusion coefficient in the subsequent diffusive phase increase with the cavity lifetime, thus emphasizing an importance of the cavity Q-factor as a means of tuning the excitation transport in organic microcavities.

4.3 Energy Transport in Different Types of Microcavity

From the point of view of the strong coupling phenomenon as such, it does not matter in what structure molecular excitations are strongly coupled to light, because the interaction leads to the appearance of hybrid states in any case. Hence, the mechanism of polariton transport should not depend on the structure either. Nevertheless, what the structure determines is the distribution of the electric field, dispersion of light, as well as the form of the electromagnetic wave sustained in one structure or another (Equation 27). All this should be accounted for when simulating realistic exciton-cavity systems.

In this section, we perform simulations based on the experiments in two specific structures, namely structures supporting surface lattice resonances, SLRs, and structures supporting Bloch surface waves, BSWs, and address how the propagation distance depends on the energy of the lower polaritons (Section 4.3.1) and what is the origin of a recently observed transport regime transition along the LP branch (Section 4.3.2) [20].

4.3.1 Surface Lattice Resonances (Publication III)

Publication III combines experimental results with molecular dynamics simulations. Let us start with a brief description of the experimental setup as well as the main observations.

The system under study is a Tetracene crystal deposited on top of a metallic nanoparticle array. Arrangement of the nanoparticles in the array allows for surface plasmon resonances localised on each nanoparticle to interact via coherent scattering by means of Rayleigh anomalies, *i.e.* diffraction orders parallel to the main plane of the array and arising when the following condition is fulfilled [44, 136]:

$$\pm\mathbf{k}_{\|,\mathrm{d}} = \mathbf{k}_{\|,\mathrm{inc}} + \mathbf{G}, \tag{61}$$

where $\mathbf{k}_{\|,\mathrm{d}}$ and $\mathbf{k}_{\|,\mathrm{inc}}$ are the parallel components of the diffracted and incident wave vectors, respectively, and $G = \frac{2\pi}{a_i} m$ is the reciprocal vector of the array with a_i lattice constant in $i = x, y$ in-plane directions and m the diffraction order.

The interaction between surface plasmon resonances results in the formation of a surface lattice resonance [137], or SLR, which is an electromagnetic wave distributed over the whole nanoparticle array. At the frequency of the SLR, the radiation damping is reduced, manifested as a much narrow peak in the extinction coefficient with respect to individual localised surface plasmon resonances [138], which suffer from strong ohmic and radiative losses. An enhanced lifetime of SLRs, in combination with a broad spatial distribution of the electric field makes it easier to achieve strong coupling with molecules located both directly above the nanoparticles and in between them. Additionally, by changing the shape of the nanoparticles and the distance between them, precise control over the dispersion in different directions is possible [44], making SLRs a good platform for studying polariton transport.

In the experiment, Frenkel excitons in the Tetracene crystal were strongly coupled to the SLR excited along the $(0, \pm 1)$ order of the Rayleigh anomaly in a silver nanoparticle array, with a dispersion along the y-direction given by

$$\omega_{\mathrm{RA}}^{(0,\pm 1)} = \mp \frac{c}{n} \left(k_y + \frac{2\pi}{a_y} \right) \tag{62}$$

with n the refractive index of the medium. The dispersion of the resulting SLR is shown as a red line in Figure 12**a** and was fitted to be used in MD simulations.

Following off-resonant excitation, a micrometer-scale propagation of the polariton wave packet was observed, which ias two orders of magnitude larger compared to the diffusion length, $L_D \lesssim 100$ nm, of singlet excitons and about ten times larger than the diffusion length, $L_D \approx 600$ nm, of triplet excitons in Tetracene crystals [32, 139].

To investigate the dependence of the propagation distance of polaritons along the LP branch, Fourier microscopy was utilised. By placing a pinhole at different positions in the imaging plane, emission originating from different spots away from the excitation was measured. As shown in Figure 12**c**, whilst both $(0, +1)$ and $(0, -1)$ modes of SLR are visible in the emission spectrum at the excitation spot, only one of the modes remains when moving the pinhole by 20 μm in the positive direction along the y-axis. At the same time, a gradual disappearance of the emission associated with high-energy polaritonic states is observed, indicating that these polaritons are not capable of propagating over such large distances. For low-energy polaritons, in turn, emission was registered even 20 μm away from the excitation spot, which was attributed to a high group velocity of these polaritons.

To bring theoretical insights into these observations, we carried out MD simulations of a similar Tetracene-SLR system. For that, a microscopic crystal was modelled as a one-dimensional chain of $N = 1024$ unit cells each containing 250 Tetracene monomers, one of which was described at the QM level (CIS/3-21G), and the rest of the monomers were described with a classical force field (Amber03, Figure 12**b**). Therefore, each unit cell contained one molecule participating

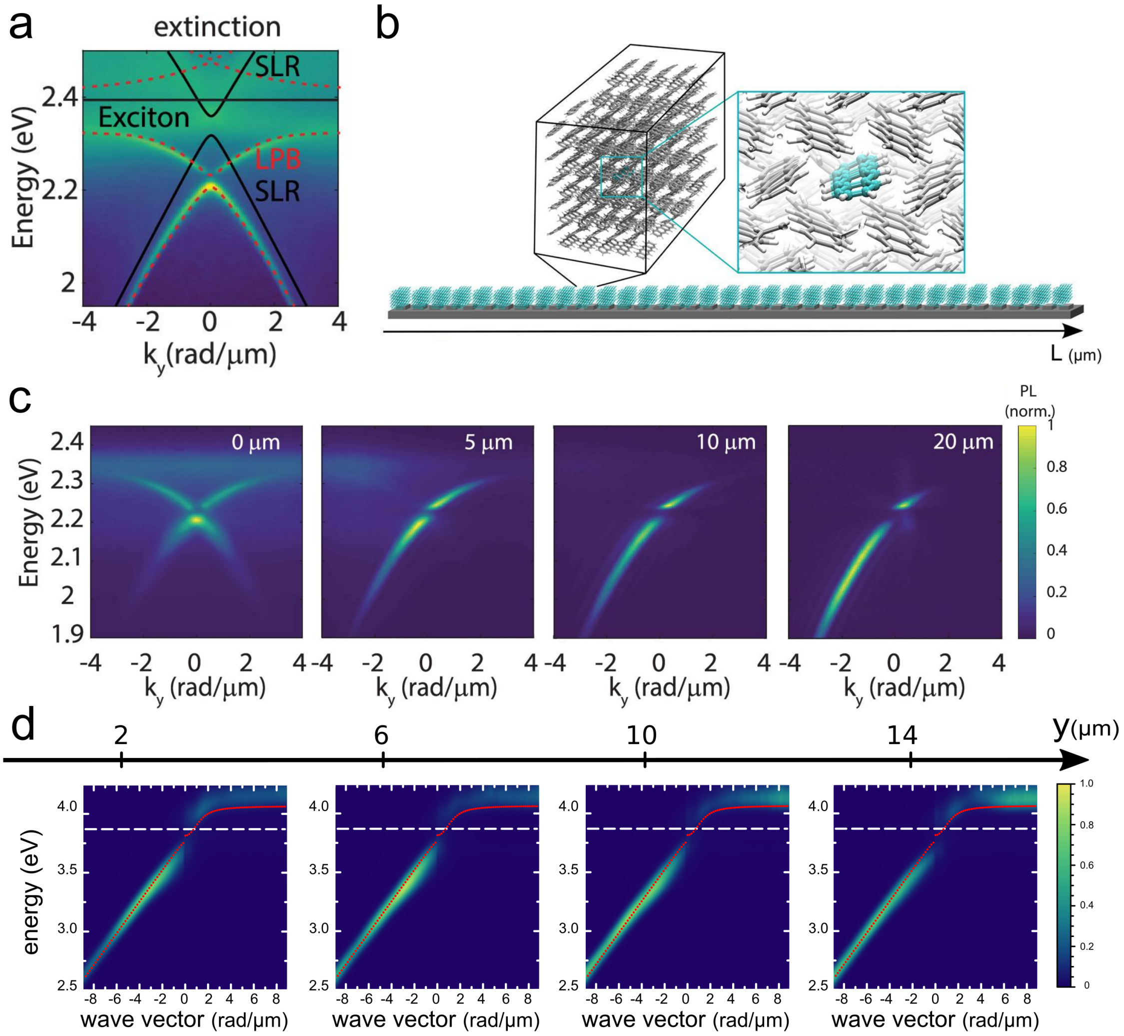

FIGURE 12 Panel **a**: Angle-resolved emission of the Tetracene-SLR system. The black lines show the dispersion of bare SLR modes and of Tetracene singlet exciton, and the red line shows the polariton dispersion. Panel **b**: Schematic representation of the simulated system. The inset shows one of the 1024 unit cells of the Tetracene crystal. In each unit cell, one of the Tetracene monomers is described at the QM level (colourful), and the remaining 1023 monomers are described at the MM level (black and white). Panel **c**: Angle-resolved emission observed through a pinhole placed at the excitation spot and $y = 5, 10$, and 20 μm away from it. Panel **d**: Angle-resolved photoluminescence spectra from the MD simulations extracted at various distances $(2, 6, 10$, and 14 μm) from the excitation spot along the y-axis. The dashed line shows the excitation energy of Tetracene at 3.82 eV at CIS/3-21G level of theory, and the dotted line shows the dispersion of the SLR.

in strong coupling, and the interaction between such "active" molecules was neglected.

Since the distribution of the electric field of the SLR along the nanoparticle array is non-uniform, molecules placed above the nanoparticles should experience a different field and hence interact with the SLR with a different strength than molecules located between the nanoparticles. Therefore, we placed the Tetracene unit cells at equal distances along a 36 μm long crystal and associated an electric field strength with each crystal according to the electric field distribution calculated using finite-difference time-domain simulations for 42 nm wide nanoparticles separated by 240 nm. The form of the electromagnetic wave was described as a plane-wave (Equation 27).

The dispersion of the SLR (black line in Figure 12**a**) as well as the decay rate along the k_y-vector was fitted to correspond to the experiment. Also, an energy offset of 1.44 eV was added to the SLR dispersion to compensate for the overestimation of the Tetracene excitation energy at CIS/3-21G level of theory.

To obtain distance-resolved photoluminescence spectra, we imitated the pinhole analysis by convolving the excitonic, Ψ_{exc}, and photonic (SLR), Ψ_{exc}, parts of the total wave function (Equation 35) with a rectangular mask-function:

$$|\Psi_{\text{exc}}^{\text{mask}}(y,t)\rangle = \sum_{y_j \geq y-\Delta y}^{y_j \leq y+\Delta y} \Psi_{\text{exc}}(y_j,t), \tag{63}$$

$$|\Psi_{\text{phot}}^{\text{mask}}(y,t)\rangle = \sum_{y_j \geq y-\Delta y}^{y_j \leq y+\Delta y} \Psi_{\text{phot}}(y_j,t), \tag{64}$$

where j is index of a unit cell and $\Delta y = 2$ μm is width of the mask. Then, the photonic part was Fourier transformed to the reciprocal space to obtain $|\Psi^{\text{mask}}\rangle = |\Psi_{\text{exc}}^{\text{mask}}(y,t)\rangle \otimes |\Psi_{\text{phot}}^{\text{mask}}(k_y,t)\rangle$. Because eigenstates $|\psi^m\rangle$ of the Tavis-Cummings Hamiltonian form a complete set, the wave function $|\Psi^{\text{mask}}\rangle$ can be expanded as a linear combination of these states with the expansion coefficients given by

$$d_m^{\text{mask}} = \langle \psi^m | \Psi^{\text{mask}} \rangle. \tag{65}$$

Emission through the pinhole was calculated as the "visibility" of the polaritonic states weighted by the expansion coefficients d_m^{mask}:

$$I_{\text{hole}}(y,E,k_{y,b}) \propto \sum_{i}^{s} \sum_{m}^{N+n_{\text{modes}}} |d_{m,i}^{\text{mask}}|^2 |\alpha_{b,i}^{m}|^2 \exp\left[-\frac{(E-\Delta E_i^m)^2}{2\sigma^2}\right] \tag{66}$$

with s the number of time steps and $\sigma = 0.05$ eV.

Figure 12**d** depicts the emission spectra extracted with a mask centred at $y = 2, 6, 10$, and 14 μm away from the excitation. As in the experiment, we observed the redistribution of the emission from the LP branch (below the dashed line associated with the excitation energy of Tetracene) towards low-energy states, which propagate faster.

To further quantify the energy-dependence of the polariton transport, in Figure 13**a** we plot the propagation length as a function of the excitonic contribution to lower polaritonic states. The plot exhibits a downward trend as the excitonic contribution and hence energy increases, which is caused by two factors. First, low-energy states possess a higher group velocity than high-energy states with almost a flat dispersion. Second, as energy increases, a gap between bright LP states and the molecular absorption spectrum reduces, facilitating a more intensive population exchange with the dense manifold of dark states. Such a population exchange renders transport diffusive and eventually results in a reduced propagation distance. In Section 4.3.2, we will address this phenomenon in more detail.

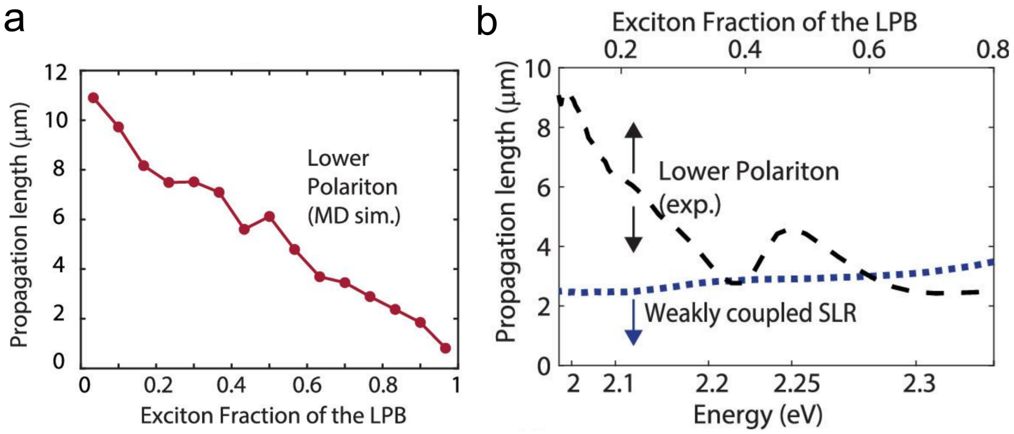

FIGURE 13 Panel **a**: Propagation length of lower polaritons as a function of the exciton fraction calculated with MD simulations. Panel **b**: Propagation length of lower polaritons and of a weakly coupled SLR as a function of energy (and exciton fraction for polaritons) obtained experimentally.

The trend presented in Figure 13**a** is in qualitative agreement with the experiment, which also shows a decrease in the propagation length with the energy of lower polaritons (Figure 13**b**). Also, in both calculated and experimental plots, we see a dip at the exciton fraction of around 0.4, which is due to a discontinuity in the polariton dispersion resulting from the gap between symmetric and antisymmetric field distributions of the modes in the SLR dispersion [140].

To conclude this section, MD simulations of a Tetracene crystal-SLR system were performed to complement experimental results and bring atomistic insights. While one could argue that the observed decrease in the propagation length with an increase in energy of the LP states can be simply explained by the group velocity argument, simulations of static two-level systems show a much further propagation than observed with the MD simulation, especially for high-energy states. This indicates the importance of the inclusion of molecular degrees of freedom since it allows for such effects as dynamical energy disorder and non-adiabatic coupling with the latter causing a constant population redistribution between propagating bright states and stationary dark states.

4.3.2 Bloch Surface Waves (Publication IV)

As has been discussed in Section 4.1, a polariton cloud spreads in a diffusive manner on a long timescale regardless of the excitation condition, due to reversible population exchange between stationary dark states and propagating bright states. While experiment [141] and theory [104, 142] suggest that the coherence of polaritons and, hence the propagation distance, increases with their photonic weight, it remains unclear whether propagation of individual wave packets constituting the whole polariton wave packet, is fully ballistic or might also be diffusive depending on the wave vector at which an individual wave packet is formed.

Recently, this question was addressed in an experimental study conducted by Balasubrahmaniyam *et al.* [20], in which spatio-temporal ultrafast pump-probe microscopy was used to explore polariton transport in a system of TDBC J-aggregates deposited on top of a DBR structure supporting BSWs. By probing the differential reflectivity, $\Delta R/R$, at different angles and energies after non-resonant excitation, a transition from ballistic propagation with a velocity close to the corresponding polariton group velocity, to diffusive propagation with a much lower velocity was observed for a decrease in the photonic contribution to the polaritonic states. This transition was attributed to the competition between molecular-scale disorder and long-range correlation due to strong coupling with the former prevailing at small photonic fractions.

Here, we mimic this experiment by means of MD simulations with the aim of discovering if the transition from ballistic to diffusive transport along the lower polariton branch in *organic* microcavities can be caused solely by the structural molecular disorder or whether such a transition involves reversible non-adiabatic population transfers between bright and dark states.

Before discussing the details of the simulation, let us say a few words about the origin of the formation of BSWs in a distributed Bragg reflector. DBR is a one-dimensional photonic crystal, a structure in which the dielectric constant varies periodically, *i.e.* $\varepsilon(x) = \varepsilon(x + A)$ with period A. Just like the periodicity of ions in an atomic crystal leads to the appearance of allowed bands and band gaps, periodicity of the dielectric constant of the medium leads to the appearance of the so-called pass-bands and stop-bands in photonic crystals. For a wave with the frequency lying in the range of a stop-band, multiple reflections of the wave from the boundaries between layers with a different dielectric constant result in the occurrence of destructive interference, which makes it impossible for the light to travel through the crystal within this frequency range. However, introduction of a defect, such as a layer with a thickness or dielectric constant different from that of the other layers, may allow for localised states to appear in the stop-band [143].

In addition to waves propagating in the volume, photonic crystals support surface waves propagating in both dielectric and air (states in pass-bands above the light line), propagating in the dielectric and decaying in air (states in pass-bands below the light line), as well as decaying in the dielectric and propagating in air (states in stop-bands above the light line) [144]. The introduction of a surface defect results in the appearance of a forth type of surface wave, which is a wave localised in both dielectric and air [145]. This is the Bloch surface wave.

Because BSWs exist in the stop-bands and below the light line [144], *i.e.* at angles larger than the critical angle for the total internal reflection, the radiation cannot be emitted into free space, which results in an extremely long lifetime far beyond lifetimes typical of Fabry-Pérot microcavities with metallic mirrors or plasmonic structures. As a consequence, the lifetime of polaritons formed due to strong coupling between excitons and BSWs can reach several hundreds to thousands of femtoseconds [9, 14, 146]. Because due to limited computational resources, we cannot perform simulations of large molecular ensembles ($N > 1000$) on a picosecond timescale and since, as we showed in Section 4.1, cavity losses do not violate the general mechanism of polariton transport, we consider it a reasonable approximation to not include the cavity decay in the following simulations.

While the BSW is a surface wave, evanescent in the direction (Figure 14), x, perpendicular to the surface, there is no restriction on the in-plane propagation over the surface of a photonic crystal, *i.e.* in the y and z directions. Therefore, the electric field distribution of the BSW in the air is defined as

$$E(x,y,z) = E_0 e^{-|K|x} e^{i(k_y y + k_z z)} \tag{67}$$

with E_0 the amplitude of the electric field at the surface of the photonic crystal, *i.e.* at $x = 0$, and K the complex Bloch wave number [147]. In the current work, we do not include multiple molecular layers, which allows us to neglect the x-dependence in equation 67. Additionally, we restrict the problem to one-dimensional transport along a chain of molecules in the z-direction. With these simplifications, the field distribution becomes $E(z) = E_0 e^{ik_z z}$ with the mode function, $\mathbf{f}_p(\mathbf{R}_c^j) = e^{ik_{z,p} z_j}$, as before, being a plane wave (Equation 27).

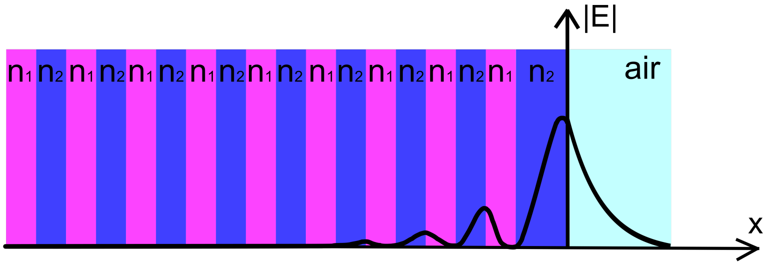

FIGURE 14 Schematic representation of a distributed Bragg reflector (DBR) supporting a Bloch surface wave (BSW). The DBR consists of alternating layers with different refractive indices, n_1 and n_2. Additionally, a surface defect layer with refractive index n_2 and a thickness different from the thicknesses of the other layers is introduced. The electric field strength distribution of the BSW is shown as a black line.

In addition to a longer lifetime, BSW-polaritons have an advantage in the value of the LP group velocity over polaritons in Fabry-Pérot cavities. In FP cavities, the group velocity turns to zero at $k_z \to 0$ and $k_z \to \infty$ (Figure 4). In the BSW structures, in turn, the dispersion is close to the light line in free space, and the group velocity of the LP branch can approach the speed of light. This results in a tremendous propagation of BSW-polaritons reaching tens to hundreds micrometers [9, 13, 14, 20].

To obtain a similar polariton dispersion as in the experiment, we fit the experimental dispersion of the BSW with a linear function (dashed-dotted line in

Figure 15**a**) and tune it to be resonant with the excitation energy of Methylene Blue (MeB) molecules, $\hbar\omega_{\mathrm{MeB}} = 2.50$ eV at TDDFT/B97//3-21G level of quantum chemistry (dashed line and inset in Figure 15**a**), at wave vector $k_z = 11.41\ \mu\mathrm{m}^{-1}$. With $N = 1024$ MeB molecules and an electric field strength of 0.071 MV/cm, the Rabi splitting is 131 meV, which is close to the Rabi splitting in the experimental study.

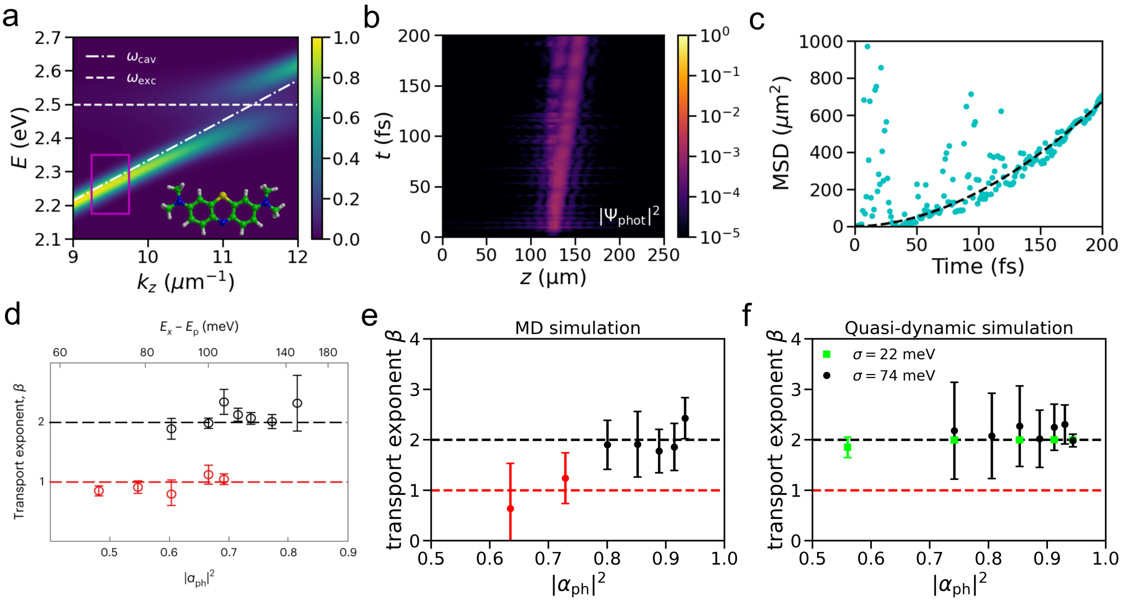

FIGURE 15 Panel **a**: Normalised angle-resolved absorption spectrum of the Methylene Blue-BSW system. The dashed line corresponds to the excitation energy of Methylene Blue at 2.50 meV, and the dashed-dotted line shows the BSW dispersion. Molecular structure of MeB is also shown. Panels **b**: Probability density, $|\Psi_{\mathrm{phot}}|^2$, of the photonic wave function extracted through the mask depicted as a pink rectangle in panel **a**. Panel **c**: MSD of the photonic wave function in panel **b**. The dashed line corresponds to the fit to $\mathrm{MSD} = 2D_\beta t^\beta$ with β the transport exponent. Panels **d** and **e**: The transport exponent as a function of the cavity modes contribution $|\alpha_{\mathrm{ph}}|^2$ to polaritonic states, extracted from the experiment (**d**) and MD simulations (**e**). Panel **d** is reproduced with permission from Balasubrahmaniyam et.al., *Nat. Mater.*, **22**, 338–344 (2023). Copyright 2023 Springer Nature Ltd. Panel **f**: Values extracted from quasi-dynamic simulations of two-level molecules with excitation energy disorder of $\sigma = 22$ meV (green squares) and $\sigma = 74$ meV (black circles). In panels **e** and **f**, the transport exponents were extracted from windows of width $\Delta k_z = 0.5\ \mu\mathrm{m}^{-1}$ centred between $k_z = 9.25\ \mu\mathrm{m}^{-1}$ and $k_z = 10.75\ \mu\mathrm{m}^{-1}$ with a step of $0.25\ \mu\mathrm{m}^{-1}$. The errors in panel **e** and **f** are standard deviations of, respectively, five and a hundred individual simulations.

The system was prepared in the first-excited state of a single molecule to model the off-resonant excitation scheme. Unlike previous sections, in which the propagation of the total polariton wave function (Equation 35) was plotted, here, we plot the propagation of a part of the wave function that includes states with energy lying in a certain energy (or wave number) window, and consider only the elements associated with the cavity mode excitation. In principle, we could include both photonic and excitonic elements in such a partial wave function, but in this case the propagation pattern would have been contaminated by the "noise" associated with molecular excitations. While such noise could be averaged out by running multiple simulations, with current computational resources, we could afford to perform five runs only. Therefore, in the following we plot the photonic partial wave function, for which it is easier to obtain "clean" data. We note though that this does not change the conclusions that we draw below.

As an example, Figure 15**b** illustrates the propagation of a partial photonic wave function, $|\Psi_{\text{phot}}|^2$, associated with the states in the window between $k_z = 9.25\ \mu\text{m}^{-1}$ and $k_z = 9.75\ \mu\text{m}^{-1}$ (purple rectangle in Figure 15**a**). The corresponding MSD is plotted in Figure 15**c**. By fitting the mean squared displacement as $\text{MSD}(t) = 2D_\beta t^\beta$, we can judge whether the propagation is ballistic or diffusive by the value of the transport exponent, β. Purely ballistic transport corresponds to $\beta = 2$, while diffusion corresponds to the transport exponent equal to unity with D_β being the diffusion coefficient.

Figure 15**e** demonstrates the value of the transport exponent for the partial photonic wave functions extracted from the windows of width $\Delta k_z = 0.5\ \mu\text{m}^{-1}$ and with the central wave number in the range between $k_z^c = 9.25\ \mu\text{m}^{-1}$ and $k_z^c = 10.75\ \mu\text{m}^{-1}$ with a step of $0.25\ \mu\text{m}^{-1}$. Because the centre of each window corresponds to a polariton state with a certain photonic Hopfield coefficient, $|\alpha_{\text{ph}}|^2$, the transport exponent is plotted as a function of this coefficient. Clearly, the upward shift of the window along the lower polariton branch towards the less photonic-like states is accompanied by a change in the transport exponent from a value of two to a value of one, indicating a transition between ballistic propagation and diffusion, in line with the experiment (Figure 15**d**).

Importantly, the observed transition cannot be reproduced with a simulation of two-level systems with a quasi-dynamic excitation energy disorder, in which excitation energies were randomly drawn from a Gaussian distribution and resampled every femtosecond of the simulation. In this situation, the transport exponent remains close to $\beta = 2$ in the full range of the LP states with a well-defined wave number (Figure 15**f**), *i.e.* for $|\alpha_{\text{ph}}|^2 > 0.64$ in simulation with the disorder strength, $\sigma = 74$ meV, of MeB used in the MD simulations, and for $|\alpha_{\text{ph}}|^2 > 0.45$ in simulation with the disorder strength, $\sigma = 22$ meV, of J-aggregates used in the experiment. We note that in our simulations, MeB molecules were used instead of J-aggregates due to the latter's complexity, which makes their simulation in a cavity currently intractable.

The result presented in Figure 15**f**, indicates the decisive role of molecular vibrations in modifying the mechanism of polariton transport along the lower polariton branch. Because the strength of non-adiabatic coupling is inversely proportional to the energy gap between polariton states (Equation 37), population transfer between dark states, which are distributed around the molecular absorption maximum, and the low-energy, highly-photonic LP states is unlikely, resulting in a scattering-free ballistic propagation of these states. Moving up in energy along the LP polariton branch reduces the energy gap and can lead to overlap with the dark states manifold and hence a significant increase in the probability that the excitation will be "trapped" in the dark states reservoir. Eventually, this renders propagation less ballistic-like and more diffusive-like as polaritonic states become closer in energy to the dark states.

We note that similar results were recently achieved by Xu *et al.* for the transport in a hybrid organic-inorganic halide perovskite-microcavity system [19]. In their experiment, a shift in the MSD from a quadratic to a linear dependence was observed for polaritonic states with a decreasing cavity modes contribution. Based on the semi-classical simulations, this change in the propagation character was attributed to the exciton-phonon scattering, which leads to an enhanced percentage of localized states.

In conclusion, the results of the current section show once again a crucial role of molecular vibrations in the mechanism of polariton transport and allow us to explain an experimentally observed turnover between ballistic propagation of low-energy lower polaritons and diffusive transport of high-energy LP states.

4.4 Photochemical Initiation of Polariton-Mediated Exciton Propagation (Publication V)

Usually, exciton-polariton transport is initiated with laser pulses, which either are resonant with polaritonic branches [16, 17] or excite an uncoupled higher-energy state of a single molecule [9, 10, 14, 15, 20]. While such a laser excitation is routinely feasible in laboratories, it is not suitable for optical devices meant for generating electricity out of solar irradiation, which is low-intensive, broad and incoherent. Therefore, the operation of a photovoltaic device, which makes use of strong light-matter coupling, may require an intermediate entity, which would absorb sunlight and transfer the excitation to polaritonic states to accelerate energy transport.

As such an entity, we propose to use a photoacid, which absorbs in the spectral range corresponding to the transparency window of the cavity mirror's material, and undergoes an ultrafast excited-state intramolecular proton transfer (ESIPT) reaction into a red-shifted excited-state photoproduct that can couple cooperatively with a large number of non-reactive molecules to the cavity modes leading eventually to polariton propagation. The idea is schematically illustrated in Figure 16**a**, where, as an example, we consider a system of a single 10-hydroxybenzo[h]quinoline (HBQ, inset in Figure 16**b**) molecule and many MeB molecules in a multimode Fabry-Pérot microcavity with a symmetric dispersion (white dashed line in Figure 16**b**). Upon excitation into the S_1 state of HBQ at 3.96 eV at TDDFT/CAM-B3LYP//3-21G level of theory (purple line in Figure 16**b**), the HBQ molecule undergoes ultrafast ESIPT reaction into a photoproduct state characterised by a broad emission spectrum with the peak at 2.58 eV (blue area in Figure 16**c**), which turns out to match the absorption spectrum of

MeB peaked at 2.50 eV (red area in Figure 16**c** and red line in Figure 16**b**) at the TDDFT/B97//3-21G level of theory. If the cavity is tuned to be resonant with both the Franck–Condon state of MeB and the photoproduct state of HBQ, both molecular species enter cooperative strong coupling with the cavity, which results in the formation of mixed light-matter states. These states can be populated from the dark states associated with both HBQ and MeB via non-adiabatic coupling (blue arrow in Figure 16**a**) and transfer the excitation with a high speed according to the polariton dispersion (Figure 16**b**).

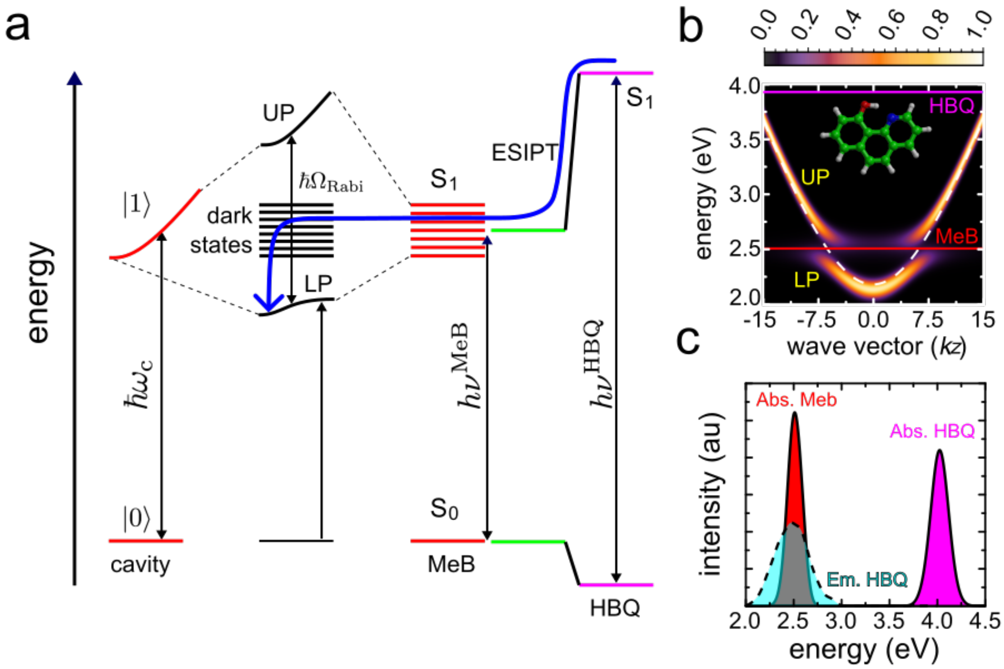

FIGURE 16 Panel **a**: Schematic illustration of photochemically-induced polariton transport. After photoexcitation of 10-hydroxybenzo[h]quinoline (HBQ) at $h\nu^{\text{HBQ}}$, the molecule undergoes an ESIPT reaction and enters strong coupling, which results in population transfer to the DS manifold. Due to reversible population exchanges between dark and bright states, part of the population initially localised in a single HBQ molecule ends up in bright states (blue arrow) and can be transported owing to the group velocity of the latter states. Panel **b**: Normalised angle-resolved absorption spectrum of the molecule-cavity system. The solid purple and red lines show the excitation energy of HBQ and MeB, respectively, and the dashed line shows the cavity dispersion. An illustration of an HBQ molecule is also shown. Panel **c**: Normalised absorption (magenta) and emission (cyan) spectra of HBQ and absorption spectrum of MeB (red).

To test the idea, we performed simulations of $N_{\text{HBQ}} = 1$ HBQ molecule and $N_{\text{MeB}} = 1023$ MeB molecules in a Fabry-Pérot microcavity with $n_{\text{modes}} = \pm 120$ modes, which yields a symmetric dispersion (dashed white line in Figure 16**b**), and a decay rate $\gamma_{\text{cav}} = 66.7$ ps^{-1} typical of microcavities with metallic mirrors. With an electric field strength $|\mathbf{E}| = 0.21$ MV cm^{-1}, the Rabi splitting was set to $\hbar\Omega_R = 282$ meV. After the initial excitation into the highest energy eigenstate of the system, $|\Psi^{1263}\rangle$, which is dominated by the S_1 state of the HBQ molecule ($|\beta^{1263}_{\mathrm{HBQ}}|^2 > 0.999$, Equation 34), a rapid ESIPT reaction occurs, which is manifested as a change of the distance between the hydroxyl oxygen and the proton, as depicted in Figure 17**a**. As a result of the excited-state energy shift due to the reaction, the molecule becomes resonant with both MeB molecules and the cavity and hence enters the strong coupling regime.

Due to the collective coupling, the HBQ molecule exchanges the population with the MeB molecules (Figure 17**d**) and the cavity light modes, leading to excitation transport (Figure 17**b**). Concomitantly, a part of the population decays to the ground state due to the cavity contribution to the polaritonic states (blue line in Figure 17**c**). Because the population exchange between propagating bright states and stationary dark states is reversible, the excitation transport is diffusive-like, which is manifested as a linear increase of the MSD in Figure 17**e**.

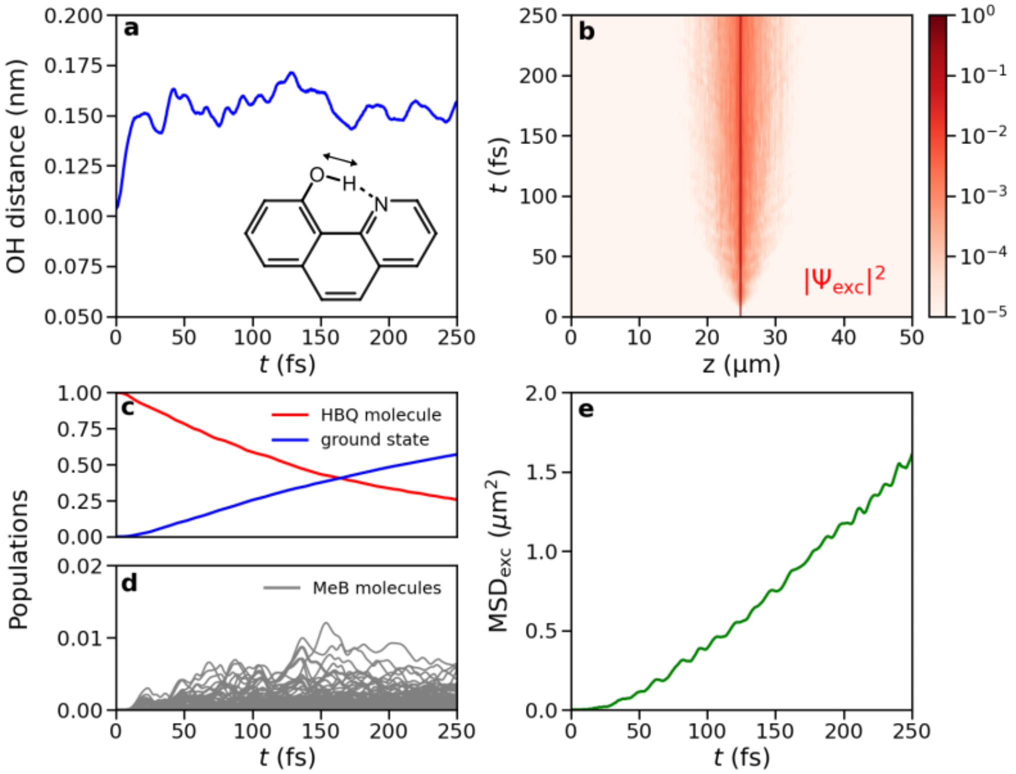

FIGURE 17 Excitation-energy transport in the HBQ-MeB-cavity system. Panel **a**: Distance between the oxygen and proton as a function of time after excitation to the highest energy polariton state, which is mostly contributed by the S_1 state of HBQ (*i.e.*, $|\beta_{\mathrm{HBQ}}|^2 \approx 0.99$). Panel **b**: Time-space map of the probability density of the excitonic part of the wave function, $|\Psi_{\mathrm{exc}}|^2$. Panels **c** and **d** demonstrate the contribution of the HBQ molecule (red) and the Methylene Blue molecules (grey) to the total wave function, as well as the ground state population (blue). Panel **e**: MSD of the excitonic wave packet.

We should note that whereas with the chosen levels of quantum chemistry the emission spectrum of HBQ matches the absorption spectrum of MeB, in reality it does not. Because the current study only serves for the demonstration of the possibility to initiate excitation energy transport via an ultrafast chemical reaction, this mismatch is not a problem. Nevertheless, the practical realisation of the idea requires molecules with matching absorpsion and emission spectra, although such a requirement is not strict as the lower polaritons can also be populated via the radiative pumping mechanism if the emission of the reactive molecule overlaps with the LP branch [148, 149].

Finally, we note that polariton transport can also be initiated via internal conversion from a higher-energy state if its energy corresponds to the transparency window of the cavity mirrors. However, such an excitation would require rather strong oscillator strength, thus limiting the selection of suitable molecules. Another potential advantage of the photochemical initiation of polariton transport is that the reacting molecules can, in principle, be introduced in the cavity in low concentrations and at specific locations inside the cavity.

In conclusion, we have demonstrated that enhanced excitation energy transport in a cavity can be induced with an ESIPT reaction. Due to a high absorption cross-section of HBQ, it could be possible to initiate the transport with incoherent light through the transparency window of the microcavity.

5 SUMMARY AND OUTLOOK

Over the past two decades, the phenomenon of strong light-matter coupling has been extensively studied from both experimental and theoretical perspectives, but a gap remains between these two perspectives in terms of what systems are being studied. On the one hand, the majority of experiments are performed with Fabry-Pérot microcavities or distributed Bragg reflectors, which couple millions of molecules. On the other hand, computer simulations can only handle small molecular ensembles, which have often been restricted to just a few molecules.

In this dissertation, we have used our multiscale molecular dynamics approach to narrow down this gap. The approach combines quantum description of active molecules involved in strong coupling with classical treatment of solvent molecules, and propagates the total wave function, which depends on electronic, nuclear and photonic degrees of freedom, in a semi-classical manner. That is, we apply Born-Oppenheimer approximation and separate electronic plus photonic DOF, which are described in a quantum manner, from nuclear DOF, which are treated classically. With this approach, we can go beyond a single molecules/single cavity mode treatment often employed in fully quantum mechanical simulations. For example, in the studies presented in the dissertation, up to 1024 molecules with their solvent environment were simulated.

It is worth mentioning that simulations can be performed with a variety of molecules and cavity structures, although the description of the latter is rather simplified, which allows for the generalisation of the observed effects of strong coupling.

With our method, we have also explored excited-state relaxation of polaritons [75], as well as chemical reactivity in a cavity [150]. In this dissertation, the attention was paid to the in-plane excitation energy transport.

Starting from simulations of Rhodamine, Methylene Blue and Tetracene molecules in a Fabry-Pérot microcavity in Publication I, we have explored the general mechanism of in-plane polariton transport. In all simulations, a μm-range propagation of the excitation on a subpicosecond timescale was observed, which is a few orders of magnitude greater than a typical diffusion length of excitons in organic semiconductors.

Based on the analysis of the performed simulations, a crucial role of molecular motions on the wave packet's dynamics was suggested. For example, upon resonant excitation of polariton states, a transition from purely ballistic propagation to diffusive-like propagation was observed, in contrast to the simulation of static two-level systems, in which the transport remained ballistic throughout the simulation time. This transition was attributed to molecular vibrations-induced non-adiabatic population transfers between propagating bright states and immobile dark states, which causes a sufficient part of the population to be "trapped" in the dark states manifold, which eventually renders the transport diffusive.

At off-resonant excitation into the first excited state of a single molecule, the initial state is a superposition of both bright and dark states. Although the bright states propagate ballistically with their group velocities, their motion is continuously interrupted due to the population transfer into dark states. As a result, the transport is diffusive from the very beginning of the simulation. Thus, regardless of the excitation condition, excitation energy transport in organic molecules is a diffusive-like process on a long timescale, which, and we point this important fact out again, is well beyond the diffusion length of excitons in bare organic molecules.

While dark states slow down transport of polaritons and render the propagation diffusive, they also extend the lifetime of the molecule-cavity system, so that polariton transport can be observed on timescales much longer than is prescribed by the cavity lifetime.

After exploring the general mechanism of polariton transport, we have investigated the effect of the cavity quality factor in Publication II. In line with a recent experiment [17], our simulations show a ballistic spreading of a polariton wave packet followed by contraction. This behaviour was explained in terms of irreversible radiative decay of population from highly photonic UP states, which move ballistically with their group velocities and barely relax into dark states due to a large energy gap.

Then, in Publications III and IV, we have investigated how the propagation length and transport mechanism of polaritons change along the LP branch. In Publication III, a simulation of exciton transport in a Tetracene crystal strongly coupled to a surface lattice resonance mode of a nanoparticle array was performed. The simulation results qualitatively agree with the experiment and show a decrease in the propagation distance as the energy of lower polaritons increases. This is because high-energy states have lower group velocities and are energetically closer to dark states, which influences their motion. In Publication IV, a molecule-BSW system similar to that in a recent experiment [20], was simulated. In accordance with that experiment, our simulations demonstrate a transition between ballistic and diffusive propagation as the photonic contribution to polaritonic states decreases. Importantly, such a transition was not observed in a simulation of molecules with frozen nuclear degrees of freedom, which indicates the decisive role of non-adiabatic coupling in changing the transport regime along the LP branch.

Finally, we have proposed and tested an idea of a photochemical initiation of polariton transport. By simulating a single reactive molecule (HBQ) and multiple non-reactive molecules (Methylene Blue) cooperatively coupled in a cavity, we have shown that after the excitation and the subsequent reaction of HBQ, the molecule enters strong coupling and exchanges its population with bright polaritonic states, which, indeed, leads to enhanced excitation transport of a micrometer range.

For an organic solar cell to operate, four important conditions can be identified: *i)* efficient absorption of sunlight, *ii)* long-range transport of excitation, allowing an increase in the width of the active layer, *iii)* efficient charge separation, and *iv)* charge transfer to the electrodes. While cavity-enhanced transport of excitation, *i.e.* condition *iii)*, was thoroughly investigated in this dissertation, it is also worth briefly commenting on the possibility of fulfilling the other three conditions in a cavity.

The strong light-matter interaction in a cavity results in a redistribution of the molecular absorption spectrum. In particular, the absorption peak associated with the molecular excitation coupled to a cavity mode is split into two peaks corresponding to the lower and upper polaritons. Although this may result in a decrease in photon energy loss [38], it remains unclear whether such a redistribution leads to a higher or lower absorption of solar irradiation, indicating the need for further studies, both theoretical and experimental. In addition, the absorption of sunlight is deteriorated by the high reflectivity of planar cavities such as FP or DBR microcavity, resulting in poor *external* quantum efficiency of solar cells, as was the case in three recent experiments [38–40], despite an increase in *internal* quantum efficiency [39, 40]. Photochemical initiation of polariton transport proposed in Publication IV, may be one possible solution to this challenge owing to the choice of a reactive molecule with an absorption matching the cavity transparency window. As an alternative, open cavity structures can be used, in which the active material involved in the strong coupling is deposited on top of the structure.

In a standard organic solar cell, after an exciton reaches the interface between the absorber layer and the electron (hole) transport layer, this exciton is split into an electron and a hole, which then move to the opposite electrodes due to the built-in electric field created due to differences in the HOMO-LUMO energy levels in the absorber and transport layers. To the best of our knowledge, the efficiency of such charge separation for the excitation transported by polaritons has has yet to be investigated. Studying this effect is one of the future directions [53, 151].

Transport of charges, *i.e.* of electrons and holes, could also be influenced by the strong light-matter coupling. For example, an enhancement of charge conductivity in the VSC regime has been reported [152–154]. However, the effect of the ESC on charge transport is still an open question and should be the subject of further research.

From a computational point of view, a future direction for studying excitation energy transfer in cavities could be to increase the number of molecules in the simulations to approach the sizes of experimental molecular ensembles with

$10^5 - 10^8$ molecules [64–67]. Although explicitly modeling such large molecular ensembles is currently an impossible task even for semi-classical methods, let alone fully quantum approaches, several methods have been proposed in which large molecular ensembles are modeled in an effective way. [155–161]. Recently, we proposed an approach in which one part of the full ensemble of molecules is modeled explicitly, while the other part is coarse-grained into a set of so-called supermolecules (Publication APIV). Each of these supermolecules represents the coordinated dynamics of multiple (M) identical molecules and interacts with the cavity field with an enhanced strength, *i.e.* $\hat{H}_{\text{int}} = \sqrt{M}\hat{H}_1^{\text{int}}$ with $\hat{H}_1^{\text{int}}$ strength of the interaction between a cavity light mode and a single molecule (Equation 17). Future work will aim to use the supermolecule approach to study how polariton transport changes as experimentally significant numbers of molecules are approached, and to model transport in a two-dimensional cavity to capture such effect as elastic scattering of polaritons.

In conclusion, we have performed a comprehensive study of the in-plane excitation energy transport in optical microcavities. We believe that this work brings important insights into the field of polaritonics and hope that it will help to rationally design organic optoelectronic devices based on the explored phenomenon.

REFERENCES

[1] E.A. Alsema and M.J. de Wild. “Environmental Impacts of Crystalline Silicon Photovoltaic Module Production”. In: *MRS OPL* 895 (2005).

[2] *BP Statistical Review of World Energy*. 71st ed. British Petroleum Co., London, 2022.

[3] *Global energy transformation: A roadmap to 2050*. 2019th ed. International Renewable Energy Agency, Abu Dhabi, 2019. ISBN: 978-92-9260-121-8.

[4] *World Energy Outlook*. IEA, Paris, 2019. URL: https://www.iea.org/reports/world-energy-outlook-2019.

[5] V. M. Agranovich and Y. N. Gartstein. “Nature and Dynamics of Low-Energy Exciton Polaritons in Semiconductor Microcavities”. In: *Phys. Rev. B* 75 (2007), p. 075302.

[6] J. Feist and F. J. Garcia-Vidal. “Extraordinary Exciton Conductance Induced by Strong Coupling”. In: *Phys. Rev. Lett.* 114 (2015), p. 196402.

[7] J. Schachenmayer et al. “Cavity enhanced transport of excitons”. In: *Phys. Rev. Lett.* 114 (2015), p. 196403.

[8] T. Freixanet et al. “In-plane Propagation of Excitonic Cavity Polaritons”. In: *Phys. Rev. B* 61 (2000), p. 7233.

[9] G. Lerario et al. “High-speed flow of interacting organic polaritons”. In: *LSA* 6 (2017), e16212.

[10] G. G. Rozenman et al. “Long-Range Transport of Organic Exciton-Polaritons Revealed by Ultrafast Microscopy”. In: *ACS Photonics* 5 (2018), pp. 105–110.

[11] D. M. Myers et al. “Polariton-enhanced exciton transport”. In: *Phys. Rev. B* 98 (2018), p. 235302.

[12] Y. Zakharko et al. “Radiative Pumping and Propagation of Plexcitons in Diffractive Plasmonic Crystals”. In: *Nano Lett.* 18 (2018), pp. 4927–4933.

[13] F. Barachati et al. “Interacting polariton fluids in a monolayer of tungsten disulfide”. In: *Nat. Nanotechnol.* 13 (2018), pp. 906–909.

[14] S. Hou et al. “Ultralong-Range Energy Transport in a Disordered Organic Semiconductor at Room Temperature Via Coherent Exciton-Polariton Propagation”. In: *Adv. Mater.* 32 (2020), p. 2002127.

[15] M. Wurdack et al. “Motional narrowing, ballistic transport, and trapping of room-temperature exciton polaritons in an atomically-thin semiconductor”. In: *Nat. Comm.* 12 (2021).

[16] R. Pandya et al. “Microcavity-like exciton-polaritons can be the primary photoexcitation in bare organic semiconductors”. In: *Nat. Commun.* 12 (2021).

[17] R. Pandya et al. “Tuning the Coherent Propagation of Organic Exciton-Polaritons through Dark State Delocalization”. In: *Adv. Sci.* 9 (2022), p. 2105569.

[18] M. A. Berghuis et al. “Controlling Exciton Propagation in Organic Crystals through Strong Coupling to Plasmonic Nanoparticle Arrays”. In: *ACS Photonics* 9 (2022), pp. 2263–2272.

[19] D. Xu et al. “Ultrafast imaging of polariton propagation and interactions”. In: *Nat. Comm.* 14 (2023), p. 3881.

[20] M. Balasubrahmaniyam et al. “From enhanced diffusion to ultrafast ballistic motion of hybrid light–matter excitations”. In: *Nat. Mater.* 22 (2023), pp. 338–344.

[21] L. Jin et al. “Enhanced Two-Dimensional Exciton Propagation via Strong Light–Matter Coupling with Surface Lattice Plasmons”. In: *ACS Photonics* 10 (2023), pp. 1983–1991.

[22] Y. Chen et al. “Unraveling the Ultrafast Coherent Dynamics of Exciton Polariton Propagation at Room Temperature”. In: *Nano Lett.* 23 (2023), pp. 8704–8711.

[23] *Photovoltaics Report*. Fraunhofer Institute for Solar Energy Systems, ISE, 2024.

[24] F. Haase et al. “Laser contact openings for local poly-Si-metal contacts enabling 26.1%-efficient POLO-IBC solar cells”. In: *Sol. Energy Mater. Sol. Cells.* 186 (2018), pp. 184–193.

[25] A. Richter, M. Hermle, and S. W. Glunz. “Reassessment of the Limiting Efficiency for Crystalline Silicon Solar Cells”. In: *IEEE J. Photovolt.* 3 (2013), pp. 1184–1191.

[26] R. M. France et al. “Triple-junction solar cells with 39.5% terrestrial and 34.2% space efficiency enabled by thick quantum well superlattices”. In: *Joule* 6 (2022), pp. 1121–1135.

[27] A. Baiju and M. Yarema. “Status and challenges of multi-junction solar cell technology”. In: *Front. Energy Res.* 10 (2022).

[28] *Best research cell efficiencies chart*. National Renewable Energy Laboratory, 2024. URL: https://www.nrel.gov/pv/cell-efficiency.html.

[29] S. Khatoon et al. “Perovskite solar cell’s efficiency, stability and scalability: A review”. In: *Mater. Sci. Energy Technol.* 6 (2023), pp. 437–459.

[30] O. V. Mikhnenko, P. W. M. Blom, and T.-Q. Nguyen. “Exciton diffusion in organic semiconductors”. In: *Energy Environ. Sci.* 8 (2015), pp. 1867–1888.

[31] J. B. Aladekomo, S. Arnold, and M. Pope. “Perovskite solar cell’s efficiency, stability and scalability: A review”. In: *Phys. Status Solidi* 80 (1977), pp. 333–340.

[32] G. M. Akselrod et al. “Visualization of Exciton Transport in Ordered and Disordered Molecular Solids”. In: *Nat. Comm.* 5 (2014).

[33] S. Rafique et al. “Fundamentals of bulk heterojunction organic solar cells: An overview of stability/degradation issues and strategies for improvement”. In: *Renew. Sust. Energ. Rev.* 84 (2018), pp. 43–53.

[34] A. J. Sneyd, D. Beljonne, and A. Rao. “A New Frontier in Exciton Transport: Transient Delocalization”. In: *J. Chem. Phys. Lett.* 13 (2022), pp. 6820–6830.

[35] F. -F. Kong et al. “Wavelike electronic energy transfer in donor–acceptor molecular systems through quantum coherence”. In: *Nat. Nanotechnol.* 17 (2022), pp. 729–736.

[36] A. Sneyd et al. “Efficient energy transport in an organic semiconductor mediated by transient exciton delocalization”. In: *Sci. Adv.* 7 (2021).

[37] S. Giannini and J. Blumberger. “Charge Transport in Organic Semiconductors: The Perspective from Nonadiabatic Molecular Dynamics”. In: *Acc. Chem. Res.* 55 (2022), pp. 819–830.

[38] V. C. Nikolis et al. “Strong light-matter coupling for reduced photon energy losses in organic photovoltaics”. In: *Nature Commun.* 10 (2019).

[39] . M. A. de Jong et al. “Enhancement of the internal quantum efficiency in strongly coupled P3HT-C60 organic photovoltaic cells using Fabry–Perot cavities with va´ried cavity confinement”. In: *Nanophotonics* 13 (2024), pp. 2531–2540.

[40] Yahui Tang et al. “Strong LightMatter Coupling Leads to a Longer Charge Carrier Lifetime in Cavity Organic Solar Cells”. In: *ACS Photonics* 11 (2024), pp. 1627–1637.

[41] M. S. Rider and W. L. Barnes. “Something from nothing: linking molecules with virtual light”. In: *Contemporary Physics* 62.4 (2022), pp. 217–232.

[42] K. Nagarajan, A. Thomas, and T. W. Ebbesen. “Chemistry under Vibrational Strong Coupling”. In: *J. Am. Chem. Soc.* 41 (2021), pp. 16877–16889.

[43] R. Chikkaraddy et al. “Single-molecule strong coupling at room temperature in plasmonic nanocavities”. In: *Nature* 535 (2016), pp. 127–130.

[44] M. Ramezani et al. “Dispersion Anisotropy of Plasmon–Exciton–Polaritons in Lattices of Metallic Nanoparticles”. In: *ACS Photonics* 5 (2017), pp. 233–239.

[45] G. Lerario et al. “Room temperature Bloch surface wave polaritons”. In: *Opt. Lett.* 39 (2014), pp. 2068–2071.

[46] P. A. Thomas, K. S. Menghrajani, and W. L. Barnes. “Cavity-Free Ultrastrong Light-Matter Coupling”. In: *J. Phys. Chem. Lett.* 12 (2021), pp. 6914–6918.

[47] A. Canales et al. “Abundance of cavity-free polaritonic states in resonant materials and nanostructures”. In: *J. Chem. Phys.* 154 (2021).

[48] A. Canales et al. “Self-Hybridized Vibrational-Mie Polaritons in Water Droplets”. In: *Phys. Rev. Lett.* 132 (2024).

[49] T. Schwartz et al. “Polariton Dynamics under Strong Light-Molecule Coupling”. In: *ChemPhysChem* 14 (2013), pp. 125–131.

[50] X. Zhong et al. “Energy Transfer between Spatially Separated Entangled Molecules”. In: *Angew. Chem. Int. Ed.* 56 (2017), pp. 9034–9038.

[51] K. Georgiou et al. “Control over Energy Transfer between Fluorescent BODIPY Dyes in a Strongly Coupled Microcavity”. In: *ACS Photonics* 5 (2018), pp. 258–266.

[52] Kyriacos Georgiou et al. “Ultralong-Range Polariton-Assisted Energy Transfer in Organic Microcavities”. In: *Angew. Chem. Int. Ed.* 60 (2021), pp. 16661–16667.

[53] M. Wang, M. Hertzog, and K. Börjesson. “Polariton-assisted excitation energy channeling in organic heterojunctions”. In: *Nature Communications* 12.1 (2021).

[54] P. Bhatt et al. “Long-Range Energy Transfer in Strongly Coupled Donor–Acceptor Phototransistors”. In: *Nano Lett.* 23 (2023), pp. 5004–5011.

[55] T. Pajunpää et al. “Polariton-assisted long-distance energy transfer between excitons in two-dimensional semiconductors”. In: *Phys. Rev. B* 109 (2024), p. 195409.

[56] A. Cargioli et al. “Active control of polariton-enabled long-range energy transfer”. In: *Phys. Rev. B* 13.14 (2024), pp. 2541–2551.

[57] Yi Yu et al. “Barrier-free reverse-intersystem crossing in organic molecules by strong light-matter coupling”. In: *Nature Commun.* 12 (2021).

[58] A. Mischok et al. “Highly efficient polaritonic light-emitting diodes with angle-independent narrowband emission”. In: *Nature Photonics* 17 (2023), pp. 393–400.

[59] S. Kéna-Cohen and S. R. Forrest. “Room-temperature polariton lasing in an organic single-crystalmicrocavity”. In: *Nat. Photonics* 4 (2010), pp. 371–375.

[60] A. Kavokin et al. “Polariton condensates for classical and quantum computing”. In: *Nat. Rev. Phys.* 4 (2022), pp. 435–451.

[61] F. J. Garcia-Vidal, C. Ciuti, and T. W. Ebbessen. “Manipulating Matter by Strong Coupling to Vacuum Fields”. In: *Science* 373 (2021).

[62] T. Khazanov et al. “Embrace the darkness: An experimental perspective on organic exciton–polaritons”. In: *Chem. Phys. Rev.* 4 (2023).

[63] A. Mandal et al. “Theoretical Advances in Polariton Chemistry and Molecular Cavity Quantum Electrodynamics”. In: *Chem. Rev.* 123 (2023), pp. 9786–9879.

[64] R. Houdré, R. P. Stanley, and M. Ilegems. “Vacuum-field Rabi splitting in the presence of inhomogeneous broadening: Resolution of a homogeneous linewidth in an inhomogeneously broadened system”. In: *Phys. Rev. A* 53 (1996), pp. 2711–2715.

[65] J. del Pino, J. Feist, and F. J. Garcia-Vidal. "Quantum Theory of Collective Strong Coupling of Molecular Vibrations with a Microcavity Mode". In: *New J. Phys.* 17 (2015).

[66] E. Eizner et al. "Inverting Singlet and Triplet Excited States using Strong Light-Matter Coupling". In: *Sci. Adv.* 5 (2019).

[67] L. A. Martínez-Martínez et al. "Triplet harvesting in the polaritonic regime: A variational polaron approach". In: *J. Chem. Phys.* 151 (2019).

[68] J. Flick et al. "Cavity Born-Oppenheimer Approximation for correlated Electron-Nuclear-Photon Systems". In: *J. Chem. Theory Comput.* 13 (2017), pp. 1616–1625.

[69] J. Flick et al. "Atoms and Molecules in Cavities: From Weak to Strong Coupling in QED Chemistry". In: *Proc. Natl. Acad. Sci. USA* 114 (2017), pp. 3026–3034.

[70] T. S. Haugland et al. "Coupled Cluster Theory for Molecular Polaritons: Changing Ground and Excited States". In: *Phys. Rev. X* 10 (2020).

[71] C. Fábri et al. "Born–Oppenheimer approximation in optical cavities: from success to breakdown". In: *Chem. Sci.* 12 (2021), pp. 1251–1258.

[72] H.-L. Luk et al. "Multiscale Molecular Dynamics Simulations of Polaritonic Chemistry". In: *J. Chem. Theory Comput.* 13 (2017), pp. 4324–4335.

[73] R. H. Tichauer, J. Feist, and G. Groenhof. "Multi-scale Dynamics Simulations of Molecular Polaritons: the Effect of Multiple Cavity Modes on Polariton Relaxation". In: *J. Chem. Phys.* 154 (2021).

[74] Ilia Sokolovskii et al. "Multi-scale molecular dynamics simulations of enhanced energy transfer in organic molecules under strong coupling". In: *Nature Commun.* 14 (2023), p. 6613.

[75] R. H. Tichauer et al. "Identifying Vibrations that Control Non-Adiabatic Relaxation of Polaritons in Strongly Coupled Molecule-Cavity Systems". In: *J. Phys. Chem. Lett.* 13 (2022), pp. 6259–6267.

[76] M. Tavis and F. W. Cummings. "Approximate solutions for an N-molecule radiation-field Hamiltonian". In: *Phys. Rev.* 188 (1969), pp. 692–695.

[77] F. H. M. Faisal. *Theory of Multiphoton Processes*. Physics of Atoms and Molecules. Springer New York, NY, 1987. ISBN: 9781489919779.

[78] A. F. Kockum et al. "Ultrastrong coupling between light and matter". In: *Nat. Rev. Phys.* 1 (2019), pp. 19–40.

[79] C. Cohen-Tannoudji, J. Dupont-Roc, and G. Grynberg. *Photons and Atoms: Introduction to Quantum Electrodynamics*. Wiley-VCH, 1997. ISBN: 9783527618422.

[80] S. M. Dutra. *Cavity Quantum Electrodynamics: The Strange Theory of Light in a Box*. John Wiley Sons, Inc. All, 2004. ISBN: 9780471713463.

[81] V. Rokaj et al. "Light–matter interaction in the long-wavelength limit: no ground-state without dipole self-energy". In: *J. Phys. B: At. Mol. Opt. Phys.* 51 (2018).

[82] E. A. Power and S. Zienau. “Coulomb Gauge in Non-Relativistic Quantum Electro-Dynamics and the Shape of Spectral Lines”. In: *Phil. Trans. R. Soc. Lond. A* 251 (1959), pp. 427–454.

[83] R. G. Woolley. “Gauge invariant wave mechanics and the Power-Zienau-Woolley transformation”. In: *J. Phys. A: Math. Gen.* 13 (1980), p. 2795.

[84] C. Schäfer et al. “Relevance of the Quadratic Diamagnetic and Self-Polarization Terms in Cavity Quantum Electrodynamics”. In: *ACS Photonics* 7 (2020), pp. 975–990.

[85] M. Fox. *Quantum Optics. An introduction*. Oxford Master Series in Physics. Oxford University Press Inc., New York, 2006. ISBN: 9780198566731.

[86] E. T. Jaynes and F. W. Cummings. “Comparison of quantum and semiclassical radiation theories with application to the beam maser”. In: *Proc. IEEE* 51 (1963), pp. 89–109.

[87] J. Galego, F. J. Garcia-Vidal, and Johannes Feist. “Cavity-Induced Modifications of Molecular Structure in the Strong-Coupling Regime”. In: *Phys. Rev. X* 5 (2015).

[88] A. Sisto, D. R. Glowacki, and T. J. Martinez. “Ab Initio Nonadiabatic Dynamics of Multichromophore Complexes: A Scalable Graphical-Processing-Unit-Accelerated Exciton Framework”. In: *Acc. Chem. Res.* 47 (2014), pp. 2857–2866.

[89] A. Michaelides et al. “Preface: Special Topic Section on Advanced Electronic Structure Methods for Solids and Surfaces”. In: *J. Chem. Phys.* 143 (2015).

[90] P. Hohenberg and W. Kohn. “Imhomogeneous Electron Gas”. In: *Phys. Rev.* 136 (1964), pp. 864–871.

[91] G. Groenhof. “Introduction to QM/MM simulations”. In: *Meth. Mol. Biol.* 924 (2013), pp. 12489–12491.

[92] G. Groenhof, Vaibhav Modi, and Dmitry Morozov. “Observe while it happens: catching photoactive proteins in the act with non-adiabatic molecular dynamics simulations”. In: *Curr. Opin. Struct. Biol.* 61 (2020), pp. 106–112.

[93] E. Brunk and U. Rothlisberger. “Mixed Quantum Mechanical/Molecular Mechanical Molecular Dynamics Simulations of Biological Systems in Ground and Electronically Excited States”. In: *Chem. Rev.* 115 (2015), pp. 6217–6263.

[94] *Hybrid Quantum-Classical simulations (QM/MM) with CP2K interface*. https://www.gromacs.org/topic/qmmm.html. Accessed: 2024-07-09.

[95] A. Warshel and M. Levitt. “Theoretical studies of enzymatic reactions: Dielectric, electrostatic and steric stabilization of carbonium ion in the reaction of lysozyme”. In: *J. Mol. Biol.* 103 (1976), pp. 227–249.

[96] Martin J. Field, Paul A. Bash, and Martin Karplus. “A combined quantum mechanical and molecular mechanical potential for molecular dynamics simulations”. In: *J. Comput. Chem.* 11 (1990), pp. 700–733.

[97] C. Sánchez Muñoz, F. Nori, and S. De Liberato. “Resolution of superluminal signalling in non-perturbative cavity quantum electrodynamics”. In: *Nature Commun.* 9 (2018).

[98] N. M. Hoffmann et al. “Effect of many modes on self-polarization and photochemical suppression in cavities”. In: *J. Chem. Phys.* 153 (2020).

[99] R. F. Ribeiro. “Multimode polariton effects on molecular energy transport and spectral fluctuations”. In: *Comm. Chem.* 5 (2022).

[100] F. Herrera and W. L. Barnes. “Multiple Interacting Photonic Modes in Strongly Coupled Organic Microcavities”. In: *Arxiv* 2407.04904v1 (2024).

[101] M. Litinskaya. “Propagation and Localization of Polaritons in Disordered Organic Microcavities”. In: *Phys. Lett. A* 372 (2008), pp. 3898–3903.

[102] Gustavo J. R. Aroeira, Kyle T. Kairys, and Raphael F. Ribeiro. “Theoretical Analysis of Exciton Wave Packet Dynamics in Polaritonic Wires”. In: *J. Phys. Chem. Lett.* 14 (2023), pp. 5681–5691.

[103] H.B.G. Casimir. “On the attraction between two perfectly conducting plates”. In: *Proc. Kon. Ned. Akad. Wetensch. Proc.* 51 (1948), pp. 793–795.

[104] P. Michetti and G. C. La Rocca. “Polariton states in disordered organic microcavities”. In: *Phys. Rev. B.* 71 (2005), p. 115320.

[105] M. Kowalewski, K. Bennett, and S. Mukamel. “Cavity Femtochemistry: Manipulating Nonadiabatic Dynamics at Avoided Crossings”. In: *J. Phys. Chem. Lett.* 7 (2016), pp. 2050–2054.

[106] O. Vendrell. “Coherent dynamics in cavity femtochemistry: Application of the multi-configuration time-dependent Hartree method”. In: *Chem. Phys.* 509 (2018), pp. 55–65.

[107] O. Vendrell. “Collective Jahn-Teller Interactions through Light-Matter Coupling in a Cavity”. In: *Phys. Rev. Lett.* 121 (2018).

[108] I. S. Ulusoy, J. A. Gomez, and O. Vendrell. “Modifying the Nonradiative Decay Dynamics through Conical Intersections via Collective Coupling to a Cavity Mode”. In: *J. Phys. Chem. A* 123 (2019), pp. 8832–8844.

[109] I. S. Ulusoy and O. Vendrell. “Dynamics and spectroscopy of molecular ensembles in a lossy microcavity”. In: *J. Chem. Phys.* 153 (2020), p. 044108.

[110] E. Davidsson and M. Kowalewski. “Simulating photodissociation reactions in bad cavities with the Lindblad equation”. In: *J. Chem. Phys.* 153 (2020).

[111] M. Boggio-Pasqua et al. “Photochemical reactions in biological systems: probing the effect of the environment by means of hybrid quantum chemistry/molecular mechanics simulations”. In: *Phys. Chem. Chem. Phys.* 14 (2012), pp. 7912–7928.

[112] R. Crespo-Otero and M. Barbatti. "Recent Advances and Perspectives on Nonadiabatic Mixed Quantum-Classical Dynamics". In: *Chem. Rev.* 118 (2018), pp. 7026–7068.

[113] Ilia Sokolovskii and Gerrit Goenhof. "Non-Hermitian molecular dynamics simulations of exciton–polaritons in lossy cavities". In: *J. Chem. Phys.* 160 (2024), p. 092501.

[114] J. C. Tully. "Mixed quantum–classical dynamics". In: *Faraday Discuss.* 110 (0 1998), pp. 407–419.

[115] Daniel F. Styer et al. "Nine formulations of quantum mechanics". In: *Am. J. Phys.* 70 (2002), pp. 288–297.

[116] A. Kirrander and M. Vacher. *Ehrenfest Methods for Electron and Nuclear Dynamics*. John Wiley and Sons, 2020. Chap. 15, pp. 469–497. ISBN: 9781489919779.

[117] G. Groenhof et al. "Tracking Polariton Relaxation with Multiscale Molecular Dynamics Simulations". In: *J. Chem. Phys. Lett.* 10 (2019), pp. 5476–5483.

[118] L. Verlet. "Computer "Experiments" on Classical Fluids. I. Thermodynamical Properties of Lennard-Jones Molecules". In: *Phys. Rev.* 159 (1967), pp. 98–103.

[119] G. Granucci, M. Persico, and A. Toniolo. "Direct semiclassical simulation of photochemical processes with semiempirical wave functions". In: *J. Chem. Phys.* 114 (2001), pp. 10608–10615.

[120] J. C. Tully. "Molecular dynamics with electronic transitions". In: *J. Chem. Phys.* 93 (1990), pp. 1061–1071.

[121] S. Hammes-Schiffer and J. C. Tully. "Proton transfer in solution: molecular dynamics with quantum transitions". In: *J. Chem. Phys.* 101 (1994), pp. 4657–4667.

[122] P. Pechukas. "Time-dependent semiclassical scattering theory. I. Potential scattering". In: *Phys. Rev.* 181 (1969), pp. 166–174.

[123] P. Pechukas. "Time-dependent semiclassical scattering theory. II. Atomic collisions". In: *Phys. Rev.* 181 (1969), pp. 174–185.

[124] D. F. Coker and L. Xiao. "Methods for molecular dynamics with nonadiabatic transitions". In: *J. Chem. Phys.* 102 (1995), pp. 496–510.

[125] C. Zhu et al. "Coherent switching with decay of mixing: An improved treatment of electronic coherence for non-Born–Oppenheimer trajectories". In: *J. Chem. Phys.* 121 (2004), pp. 7658–7670.

[126] G. Granucci and M. Persico. "Critical appraisal of the fewest switches algorithm for surface hopping". In: *J. Chem. Phys.* 126 (2007).

[127] P. Vindel-Zandbergen et al. "Study of the Decoherence Correction Derived from the Exact Factorization Approach for Nonadiabatic Dynamics". In: *J. Chem. Theory Comput.* 17 (2021), pp. 3852–3862.

[128] J. Fregoni et al. "Manipulating azobenzene photoisomerization through strong light–molecule coupling". In: *Nat. Comm.* 9 (2018).

[129] J. Fregoni et al. "Photochemistry in the strong coupling regime: A trajectory surface hopping scheme". In: *J. Comp. Chem.* 41 (2020), pp. 2033–2044.

[130] P. Antoniou et al. "Role of Cavity Losses on Nonadiabatic Couplings and Dynamics in Polaritonic Chemistry". In: *J. Phys. Chem. Lett.* 11 (2020), pp. 9063–9069.

[131] D. Manzano. "A short introduction to the Lindblad master equation". In: *AIP Advances* 10 (2020).

[132] W. P. Schleich. *Quantum Optics in Phase Space*. Wiley-VCH Verlag Berlin GmbH, Berlin, 2001. ISBN: 9783527602971.

[133] G. D. Scholes, C. A. DelPo, and B. Kudisch. "Entropy Reorders Polariton States". In: *J. Phys. Chem. Lett.* 11 (2020), pp. 6389–6395.

[134] V. M. Agranovich, M. Litinskaia, and D. G. Lidzey. "Cavity polaritons in microcavities containing disordered organic semiconductors". In: *Phys. Rev. B* 67 (2003).

[135] S. Chibani et al. "Improving the Accuracy of Excited-State Simulations of BODIPY and Aza-BODIPY Dyes with a Joint SOS-CIS(D) and TD-DFT Approach". In: *J. Chem. Theory Comput.* 10 (2014), pp. 4574–4582.

[136] S. Hamdad et al. "The role of Rayleigh anomalies in the coupling process of plasmonic gratings and the control of the emission properties of organic molecules". In: *Sci. Rep.* 12 (2022).

[137] A. D. Humphrey and W. L. Barnes. "Plasmonic surface lattice resonances on arrays of different lattice symmetry". In: *Phys. Rev. B* 90 (2014).

[138] K. T. Carron et al. "Resonances of two-dimensional particle gratings in surface-enhanced Raman scattering". In: *J. Opt. Soc. Am. B* 3 (1986), pp. 430–440.

[139] S. R. Yost et al. "Triplet vs Singlet Energy Transfer in Organic Semiconductors: The Tortoise and the Hare". In: *J. Phys. Chem. C* 116 (2012), pp. 17369–17377.

[140] W. L. Barnes et al. "Physical origin of photonic energy gaps in the propagation of surface plasmons on gratings". In: *Phys. Rev. B* 64 (1996).

[141] L. Shi et al. "Spatial Coherence Properties of Organic Molecules Coupled to Plasmonic Surface Lattice Resonances in the Weak and Strong Coupling Regimes". In: *PRL* 112 (2014), p. 153002.

[142] G. Engelhardt and J. Cao. "Polariton Localization and Dispersion Properties of Disordered Quantum Emitters in Multimode Microcavities". In: *Phys. Rev. Lett.* 130 (2023), p. 213602.

[143] K. Sakoda. *Optical Properties of Photonic Crystals*. Optical Sciences. Springer Berlin Heidelberg, 2005. ISBN: 354020629.

[144] R. D. Meade et al. "Electromagnetic Bloch waves at the surface of a photonic crystal". In: *Phys. Rev. B* 44 (1991), p. 10961.

[145] W. M. Robertson et al. "Observation of surface photons on periodic dielectric arrays". In: *Opt. Lett.* 18 (1993), pp. 528–530.

[146] K. Rashidi et al. "Efficient and Tunable Photochemical Charge Transfer via Long-Lived Bloch Surface Wave Polaritons". In: *Arxiv* 2409.02067v1 (2024).

[147] V. Koju. "Computational modeling of Bloch surface waves in one-dimensional periodic and aperiodic multilayer structures". PhD thesis. Middle Tennessee State University, 2017.

[148] G. M. Akselrod et al. "Lasing through a strongly-coupled mode by intracavity pumping". In: *Opt. Express* 21 (2013), pp. 12122–12128.

[149] Juan B. Pérez-Sánchez and Joel Yuen-Zhou. "Radiative pumping vs vibrational relaxation of molecular polaritons: a bosonic mapping approach". In: *Arxiv* 2407.20594 (2024).

[150] A. Dutta et al. "Thermal disorder prevents the suppression of ultra-fast photochemistry in the strong light-matter coupling regime". In: *Nat. Commun.* 15 (2024).

[151] E. Orgiu et al. "Conductivity in organic semiconductors hybridized with the vacuum field". In: *Nature Materials* 14 (2015), pp. 1123–1129.

[152] P. Bhatt, K. Kaur, and J. George. "Enhanced Charge Transport in Two-Dimensional Materials through Light–Matter Strong Coupling". In: *ACS Nano* 15 (2021), pp. 13616–13622.

[153] K. Nagarajan et al. "Conductivity and Photoconductivity of a p-Type Organic Semiconductor under Ultrastrong Coupling". In: *ACS Nano* 14 (2020), pp. 10219–10225.

[154] S. Kumar et al. "Extraordinary Electrical Conductance through Amorphous Nonconducting Polymers under Vibrational Strong Coupling". In: *JACS* 146 (2024), pp. 18999–19008.

[155] E. Davidsson and M. Kowalewski. "Atom Assisted Photochemistry in Optical Cavities". In: *J. Phys. Chem. A* 124 (2020), pp. 4672–4677.

[156] F. C. Spano. "Exciton–phonon polaritons in organic microcavities: Testing a simple ansatz for treating a large number of chromophores". In: *J. Chem. Phys.* 152 (2020), p. 204113.

[157] C. Schäfer. "Polaritonic Chemistry from First Principles via Embedding Radiation Reaction". In: *J. Phys. Chem. Lett.* 13 (2022), pp. 6905–6911.

[158] P. Fowler-Wright, B. W. Lovett, and J. Keeling. "Efficient Many-Body Non-Markovian Dynamics of Organic Polaritons". In: *Phys. Rev. Lett.* 129 (2022), p. 173001.

[159] J. B. Pérez-Sánchez et al. “Simulating molecular polaritons in the collective regime using few-molecule models”. In: *Proc. Natl. Acad. Sci. USA* 120 (2023).

[160] J. B. Pérez-Sánchez et al. “Collective polaritonic effects on chemical dynamics suppressed by disorder”. In: *Phys. Rev. Res.* 6 (2024).

[161] T. E. Li. “Mesoscale Molecular Simulations of Fabry-Pérot Vibrational Strong Coupling”. In: *J. Chem. Theory Comput.* 20 (2024), pp. 7016–7031.

ORIGINAL PAPERS

PI

MULTI-SCALE MOLECULAR DYNAMICS SIMULATIONS OF ENHANCED ENERGY TRANSFER IN ORGANIC MOLECULES UNDER STRONG COUPLING

by

I. Sokolovskii, R.H. Tichauer, D. Morozov, J. Feist, G. Groenhof

Nature Communications, 14, 6613, **2023**.

https://doi.org/10.1038/s41467-023-42067-y nature communications

Article

https://doi.org/10.1038/s41467-023-42067-y

Multi-scale molecular dynamics simulations of enhanced energy transfer in organic molecules under strong coupling

Received: 6 February 2023

Accepted: 21 September 2023

Ilia Sokolovskii[1,3], Ruth H. Tichauer[1,2,3], Dmitry Morozov[1], Johannes Feist[2] & Gerrit Groenhof[1] ✉

Exciton transport can be enhanced in the strong coupling regime where excitons hybridize with confined light modes to form polaritons. Because polaritons have group velocity, their propagation should be ballistic and long-ranged. However, experiments indicate that organic polaritons propagate in a diffusive manner and more slowly than their group velocity. Here, we resolve this controversy by means of molecular dynamics simulations of Rhodamine molecules in a Fabry-Pérot cavity. Our results suggest that polariton propagation is limited by the cavity lifetime and appears diffusive due to reversible population transfers between polaritonic states that propagate ballistically at their group velocity, and dark states that are stationary. Furthermore, because long-lived dark states transiently trap the excitation, propagation is observed on timescales beyond the intrinsic polariton lifetime. These insights not only help to better understand and interpret experimental observations, but also pave the way towards rational design of molecule-cavity systems for coherent exciton transport.

Solar cells based on organic molecules are promising alternatives to the silicon-based technologies that dominate today's market, mostly because organic photovoltaics (OPV) are cheaper to mass-produce, lighter, more flexible and easier to dispose of. A key step in light harvesting is transport of excitons from where photons are absorbed to where this energy is needed for initiating a photochemical process[1], usually deeper inside the material of the solar cell. Because excitons in organic materials are predominantly localized onto single molecules, exciton transport proceeds via incoherent hops[2]. Such random-walk diffusion is, however, too slow to compete with ultra-fast deactivation processes of singlet excitons, such as radiative and non-radiative decay. As exciton diffusion is furthermore hindered by thermal disorder, propagation distances in organic materials typically remain below 10 nm[2]. Such short diffusion lengths limit the efficiency of solar energy harvesting and require complex morphologies of active layers into nanometer sized domains, e.g., bulk heterojunctions in OPVs, which not only complicates device fabrication, but also reduces device stability[3,4].

Distances of hundreds of nanometers have been observed for the diffusion of longer-lived triplet states[5], but because not all organic materials can undergo efficient intersystem crossing or singlet fission, it may be difficult to exploit triplet diffusion in general. Exciton mobility can also be increased through transient exciton delocalization[6–8], but as the direct excitonic interactions are weak in most organic materials, molecules need to be ordered to reach this enhanced transport regime.

Alternatively, permanent delocalization over large numbers of molecules can be achieved by strongly coupling excitons in the material to the confined light modes of optical cavities, such as Fabry-Pérot resonators (Fig. 1a) or nano-structured devices[9–11]. In this strong light-matter coupling regime the rate of energy exchange between molecular excitons and confined light modes exceeds the intrinsic

[1]Nanoscience Center and Department of Chemistry, University of Jyväskylä, P.O. Box 35, Jyväskylä 40014, Finland. [2]Departamento de Física Teórica de la Materia Condensada and Condensed Matter Physics Center (IFIMAC), Universidad Autónoma de Madrid, Madrid, Spain. [3]These authors contributed equally: Ilia Sokolovskii, Ruth H. Tichauer. ✉e-mail: gerrit.x.groenhof@jyu.fi

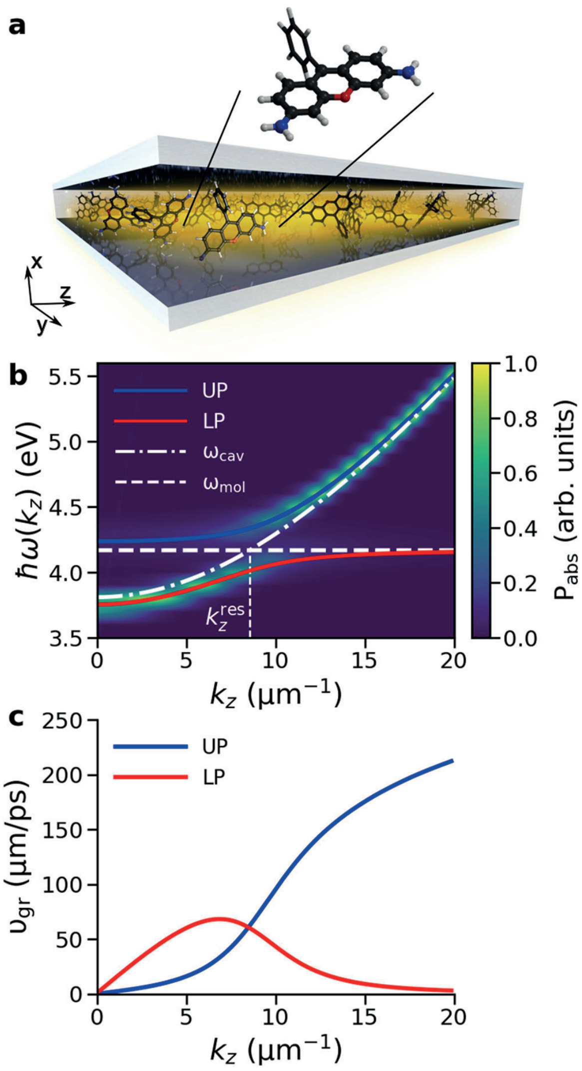

Fig. 1 | Rhodamine-cavity system. a Schematic illustration of an optical Fabry-Pérot microcavity filled with Rhodamine chromophores (not to scale). The quantum mechanical (QM) subsystem, shown in ball-and-stick representation in the inset, is described at the Hartree-Fock (HF/3-21G) level of theory in the electronic ground state (S_0), and at the Configuration Interaction level of theory, truncated at single electron excitations (CIS/3-21G), in the first singlet excited state (S_1). The molecular mechanical (MM) subsystem, consisting of the atoms shown in stick representation and the water molecules (not shown), is modeled with the Amber03 force field. **b** Normalized angle-resolved absorption spectrum (P_{abs}) of the cavity, showing Rabi splitting between lower polariton (LP, red line) and upper polariton (UP, blue line) branches. The cavity dispersion and excitation energy of the molecules (4.18 eV at the CIS/3-21G//Amber03 level of theory) are plotted with dot-dashed and dashed white lines, respectively. **c** Group velocity of the LP (red) and UP (blue), defined as the derivative of the frequency of polaritons $\omega(k_z)$ with respect to the in-plane wave-vector k_z, i.e., $\partial\omega(k_z)/\partial k_z$.

decay rates of both the excitons and the confined modes leading to the formation of new coherent light-matter states, called polaritons[12–20].

The majority of hybrid states in realistic molecule-cavity systems are dark[21–23], meaning that they have negligible contributions from the cavity photons. In contrast, the few states with such contributions are the bright polaritonic states that have dispersion and hence group velocity, defined as the derivative of the polariton energy with respect to in-plane momentum (i.e., k_z in Fig. 1b). In the out-of-plane cavity direction (i.e., perpendicular to the mirrors), these states are delocalized over the molecules inside the mode volume, while in the in-plane direction (i.e., parallel to the mirrors) they behave as quasi-particles with a low effective mass and large group velocity (i.e., fractions of the speed of light). These polariton properties can be exploited for both out-of-plane[9–11,24–33], and in-plane energy transport[34–54].

Indeed, at cryogenic temperatures, in-plane ballistic propagation at the group velocity of polaritons was observed for polariton wavepackets in a Fabry-Pérot microcavity containing an $In_{0.05}Ga_{0.95}As$ quantum well[34]. Ballistic propagation was also observed for polaritons formed between organic molecules and Bloch surface waves[38,42,51], while a combination of ballistic transport on an ultrashort timescale (sub-50 fs) and diffusive motion on longer timescales was observed for cavity-free polaritons[43], for which strong coupling was achieved through a mismatch of the refractive indices between thin layers of densely-packed organic molecules and a host material[55]. In contrast, experiments on strongly coupled organic J-aggregates in metallic micro-cavities suggest that molecular polaritons propagate in a diffusive manner and much more slowly than their group velocities[40]. Furthermore, despite a low cavity lifetime on the order of tens of femtoseconds in these experiments, propagation was observed over several picoseconds, which was attributed to a long lifetime of the lower polariton (LP)[17,40]. Here, we address these controversies by providing atomistic insights into polariton propagation with multiscale molecular dynamics (MD) simulations[56,57] of solvated Rhodamine molecules strongly coupled to the confined light modes of a one-dimensional (1D) Fabry-Pérot microcavity[58], shown schematically in Fig. 1a.

Results and discussion

Resonant excitation

First, we explore how polaritons propagate after resonant excitation of a Gaussian wavepacket of LP states with a broad-band laser pulse. In Fig. 2, we show the time evolution of the probability density of the polaritonic wave function, $|\Psi(t)|^2$ after such excitation in both a perfect lossless cavity with an infinite Q-factor ($\gamma_{cav} = 0\ ps^{-1}$, top panels) and a lossy cavity with a low Q-factor ($\gamma_{cav} = 66.7\ ps^{-1}$, bottom panels) containing 1024 Rhodamine molecules. Plots of wavepacket propagation in systems with 256 and 512 molecules are provided as Supplementary Information (SI, Figs. S5–S6), as well as animations of the wavepackets for all system sizes (Supplementary Movies 1–9 and 13–21).

Lossless cavity. In the perfect lossless cavity, the total wavepacket $|\Psi(t)|^2$ initially propagates ballistically close to the maximum group velocity of the LP branch ($\upsilon_{gr}^{LP,max} = 68\ \mu m ps^{-1}$, Fig. 1c), until around 100 fs (see animations in the SI), when it slows down as evidenced by a decrease in the slope of the expectation value of the position of the wavepacket $\langle z \rangle$ in Fig. 3a. The change from a quadratic to a linear time-dependence of the Mean Squared Displacement (Fig. 3c) at $t = 100$ fs furthermore suggests a transition from ballistic to diffusive motion.

During propagation, the wavepacket broadens and sharp features appear, visible as vertical lines in both the total and molecular wavepackets in Fig. 2a, b and as peaks in the wavepacket animations provided as SI. These peaks coincide with the z positions of molecules that contribute to the wavepacket with their excitations during propagation. Such peaks are not observed if there is no disorder and the molecular degrees of freedom are frozen (Fig. S16), but appear already at the start of the simulation when the initial configurations of the molecules are all different (Fig. S22). Similar observations were made by Agranovich and Gartstein[35] who attributed these peaks to energetic disorder among the molecular excitons. We therefore also assign these peaks to a partial localization of the wavepacket at the molecules due to structural disorder that alters their contribution to the wavepacket. In contrast, because the cavity modes are delocalized in space, the

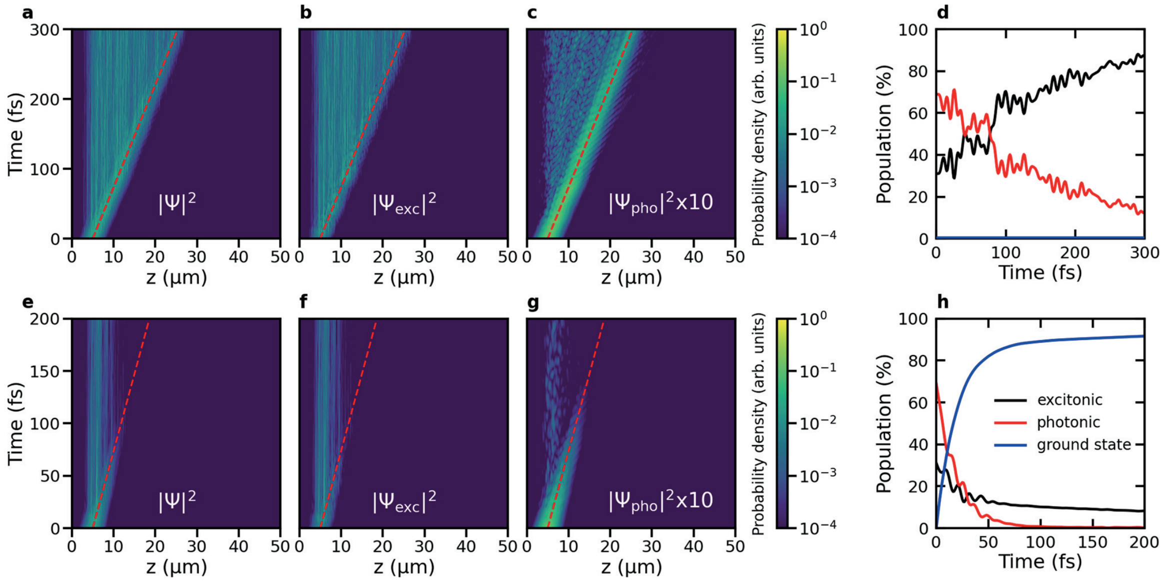

Fig. 2 | Polariton propagation after resonant excitation of a wavepacket in the lower polariton (LP) branch centered at $z = 5$ μm. a, **b**, and **c**: total probability density $|\Psi(z, t)|^2$, probability density of the molecular excitons $|\Psi_{exc}(z, t)|^2$ and of the cavity mode excitations $|\Psi_{pho}(z, t)|^2$, respectively, as a function of distance (z, horizontal axis) and time (vertical axis), in a cavity with perfect mirrors (i.e., $\gamma_{cav} = 0$ ps^{-1}). The red dashed line indicates propagation at the maximum group velocity of the LP (68 μmps^{-1}). **d** Contributions of molecular excitons (black) and cavity mode excitations (red) to $|\Psi(z, t)|^2$ as a function of time in the perfect cavity. Without cavity losses, no ground state population (blue) can build up. **e**–**g** $|\Psi(z, t)|^2$, $|\Psi_{exc}(z, t)|^2$ and $|\Psi_{pho}(z, t)|^2$, respectively, as a function of distance (z, horizontal axis) and time (vertical axis), in a lossy cavity ($\gamma_{cav} = 66.7$ ps^{-1}). **h** Contributions of the molecular excitons (black) and cavity mode excitations (red) to $|\Psi(z, t)|^2$ as a function of time. The population in the ground state, created by radiative decay through the imperfect mirrors, is plotted in blue. Source data are provided as a Source Data file.

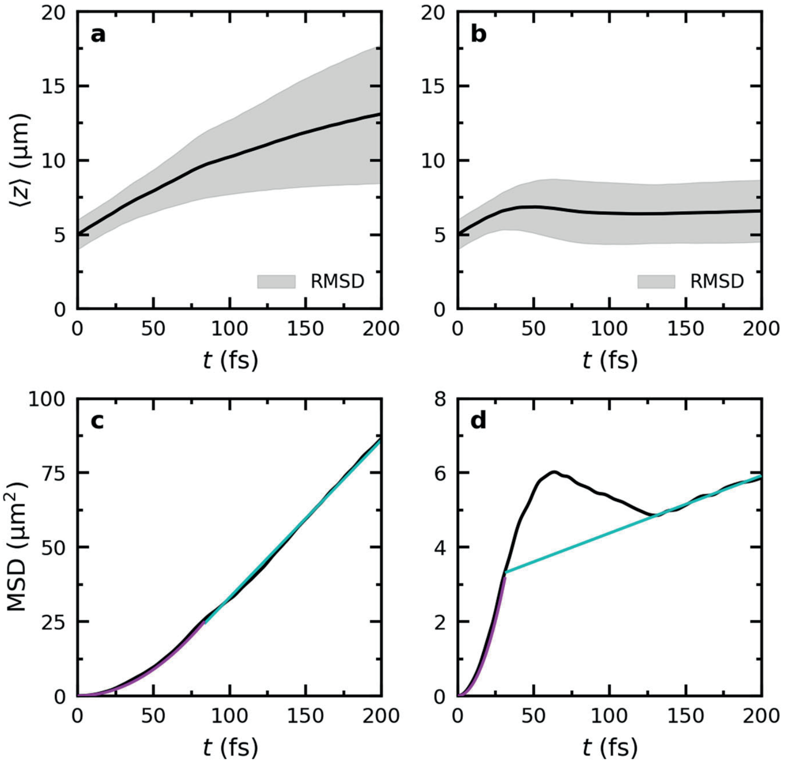

Fig. 3 | Propagation of the polaritonic wavepacket after on-resonant excitation. Top panels: Expectation value of the position of the total time-dependent wavefunction, $\langle z \rangle = \langle \Psi(z,t)|\hat{z}|\Psi(z,t)\rangle / \langle \Psi(z,t)|\Psi(z,t)\rangle$, in an ideal cavity (**a**, $\gamma_{cav} = 0$ ps^{-1}) and a lossy cavity (**b**, $\gamma_{cav} = 66.7$ ps^{-1}). The black lines represent $\langle z \rangle$ while the shaded area around the lines represents the root mean squared deviation (RMSD, i.e., $\sqrt{\langle (z(t) - \langle z(t) \rangle)^2 \rangle}$). Bottom panels: Mean squared displacement (MSD, i.e., $\langle (z(t) - \langle z(0) \rangle)^2 \rangle$) in the ideal (**c**) and the lossy (**d**) cavity. Magenta lines are quadratic fits to the MSD and cyan lines are linear fits. Source data are provided as a Source Data file.

photonic wavepacket remains smooth throughout the propagation (Fig. 2c).

The transition from ballistic propagation to diffusion around 100 fs coincides with the onset of the molecular excitons dominating the polaritonic wavepacket, as shown in Fig. 2d, in which we plot the contributions of the molecular excitons (black line) and cavity mode excitations (red line) to the total wave function (see Methods for details of this analysis). Because in the perfect cavity, photon leakage through the mirrors is absent (i.e., $\gamma_{\mathrm{cav}} = 0$ ps^{-1}), the decrease of cavity mode excitations is due to population transfer from bright LP states into the dark state manifold (Fig. S20b)[59–61]. Thus, while resonant excitation of LP states initially leads to ballistic motion with the central group velocity of the wavepacket, as evidenced by the quadratic dependence of the Mean Squared Displacement on time (Fig. 3c), population transfer into dark states turns the propagation into a diffusion process, as evidenced by a linear time-dependence of the Mean Squared Displacement after ~100 fs.

Since dark states lack group velocity, and are therefore stationary, while excitonic couplings between molecules are neglected in our model (see SI), propagation in the diffusive regime must still involve bright polariton states. Our simulations therefore suggest that while, initially, molecular vibrations drive population transfer from the propagating bright states into the stationary dark states[62], this process is reversible, causing new wavepackets to form continuously within the full range of LP group velocities. Likewise, the propagation of transiently occupied bright states is continuously interrupted by transfers into dark states, and re-started with different group velocities. This respawning process leads to the diffusive propagation of the excitation observed in Fig. 2, with an increasing wavepacket width (Fig. 3a), in line with experimental observations[40,42,43,51].

Lossy cavity. Including a competing radiative decay channel by adding photon losses through the cavity mirrors at a rate of $\gamma_{\mathrm{cav}} = 66.7$ ps^{-1}, leads to a rapid depletion of the polariton population (Fig. 2h), but does not affect the overall transport mechanism: the wavepacket still propagates in two phases, with a fast ballistic regime followed by slower diffusion. However, in contrast to the propagation in the ideal lossless cavity, we observe that the wavepacket temporarily contracts. This contraction is visible as a reduction of both the expectation value of $\langle z \rangle$ and the Mean Squared Displacement between 60 to 130 fs in the right panels of Fig. 3.

Initially, the propagation of the wavepacket is dominated by ballistic motion of the population in the bright polaritonic states moving at the maximum group velocity of the LP branch. However, due to non-adiabatic coupling[62], some of that population is transferred into dark states that are stationary. Because non-adiabatic population transfer is reversible, the wavepacket propagation undergoes a transition into a diffusion regime, which is significantly slower, as also observed in the ideal cavity (Fig. 3c).

In addition to these non-adiabatic transitions, radiative decay further depletes population from the propagating bright polaritonic states. Because before decay, this population has moved much further than the population that got trapped in the dark states, the expectation value of $\langle z \rangle$, as well as the Mean Squared Displacement, which were dominated initially by the fast-moving population, decrease until the slower diffusion process catches up and reaches the same distance around 130 fs (right panels in Fig. 3). Such contraction of the wavepacket in a lossy cavity is consistent with the measurements of Musser and co-workers, who also observe such contraction after on-resonant excitation of UP states[47].

Because of the contraction, it is difficult to see where the transition between the ballistic and diffusion regimes occurs in Fig. 3d. We therefore extrapolated the linear regime instead, and estimate the turn-over at 30 fs, where the quadratic fit to the ballistic regime intersects the extrapolated fit to the diffusion regime. As in the perfect lossless cavity, the transition between ballistic and diffusion regimes occurs when the population of molecular excitons exceeds the population of cavity mode excitations (Fig. 2h). However, due to the radiative decay of the latter, this turnover already happens around 30 fs in the lossy cavity simulations.

Owing to the short cavity mode lifetime (15 fs), most of the excitation has already decayed into the ground state at 100 fs, with a small remainder surviving in dark states (Fig. 2h) that lack mobility. Because cavity losses restrict the lifetime of bright LP states, the distance a wavepacket can reach is limited due to (i) a shortening of the ballistic phase, and (ii) a reduction of the diffusion coefficient (i.e., the slope of $\langle z \rangle$, Fig. 3b) in the second phase. Therefore, the overall velocity is significantly lower than in the perfect cavity, suggesting a connection between cavity Q-factor and propagation velocity[47], while also the broadening of the wavepacket is reduced (Fig. 3b). Furthermore, because the rate of population transfer is inversely proportional to the energy gap[62], and hence highest when the LP and dark states overlap[60], we speculate that the turn-over between the ballistic and diffusion regimes depends on the overlap between the absorption line width of the molecules and the polaritonic branches, and can hence be controlled by tuning the excitation energy to move the center of the initial polaritonic wavepacket along the LP branch. In addition, the direction of ballistic propagation can be controlled by varying the incidence angle of the on-resonant excitation pulse.

Comparison to experiments. Our observations are in line with transient microscopy experiments, in which broad-band excitation pulses were used to initiate polariton propagation. At low temperatures Freixanet et al. observed ballistic wavepacket propagation for a strongly coupled quantum dot[34]. If we suppress vibrations that drive population transfer by freezing the nuclear degrees of freedom, we also observe such purely ballistic motion (Figs. S16–S17). In contrast, in room temperature experiments on cavity-free molecular polaritons, Pandya et al.[43] identified two transport regimes: a short ballistic phase followed by diffusion. Based on the results of our simulations, we attribute the first phase to purely ballistic wavepacket propagation of photo-excited LP states. The slow-down of transport in the second phase is attributed to reversible trapping of population inside the stationary dark state manifold. Owing to the reversible transfer of population between these dark states and the LP states, propagation continues diffusively at time scales exceeding the polariton lifetime, in line with experiment[40,43].

Off-resonant excitation

Next, we investigate polariton propagation after an off-resonant excitation of the molecule-cavity system. Experimentally such off-resonant excitation conditions are achieved by optically pumping a higher-energy electronic state of the molecules[38,40,42,51], which then rapidly relaxes into the lowest energy excited state (S_1) according to Kasha's rule[63]. We therefore modeled off-resonant photo-excitation by starting the simulations directly in the S_1 state of a single molecule, located at $z = 5$ μm in the cavity (SI). In Fig. 4, we show the time evolution of the probability density of the total polaritonic wave function, $|\Psi(t)|^2$, after such excitation in both a perfect lossless cavity with an infinite Q-factor ($\gamma_{\mathrm{cav}} = 0$ ps^{-1}, top panels) and a lossy cavity with a low Q-factor ($\gamma_{\mathrm{cav}} = 66.7$ ps^{-1}, bottom panels) containing 1024 Rhodamine molecules. Plots of the wavepacket propagation in systems with 256 and 512 molecules are provided as SI (Figs. S9–S10), as well as animations of the wavepackets for all system sizes (Supplementary Movies 25–33 and 37–45).

Lossless cavity. In the lossless cavity with perfect mirrors, the excitation, initially localized at a single molecule, rapidly spreads to other molecules (see animation in the SI). In contrast to the ballistic movement observed for on-resonant excitation, the wavepacket spreads out

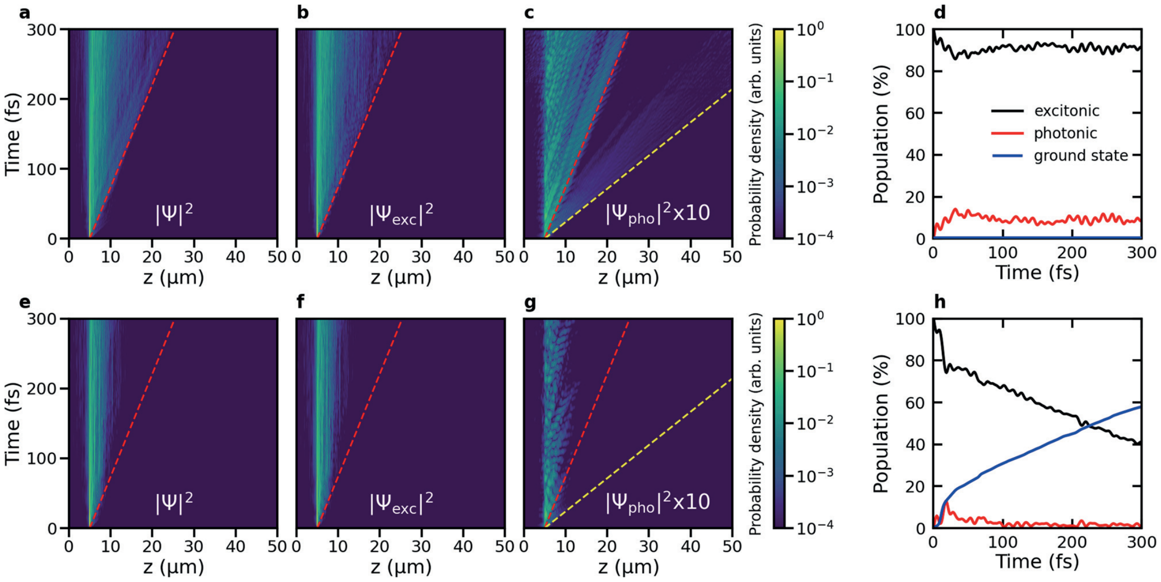

Fig. 4 | Polariton propagation after off-resonant excitation into the S$_1$ state of a single molecule located at z = 5 µm. a–c: Total probability density $|\Psi(z,t)|^2$, probability density of the molecular excitons $|\Psi_{\mathrm{exc}}(z,t)|^2$ and of the cavity mode excitations $|\Psi_{\mathrm{pho}}(z,t)|^2$, respectively, as a function of distance (z, horizontal axis) and time (vertical axis), in a cavity with perfect mirrors (i.e., $\gamma_{\mathrm{cav}} = 0$ ps^{-1}). The red and yellow dashed lines indicate propagation at the maximum group velocity of the lower polaritons (68 µmps^{-1}) and upper polaritons (212 µmps^{-1}), respectively. **d** Contributions of the molecular excitons (black) and cavity mode excitations (red) to $|\Psi(z,t)|^2$ as a function of time in the perfect cavity. Without cavity decay, there is no build-up of ground state population (blue). **e–g** $|\Psi(z,t)|^2$, $|\Psi_{\mathrm{exc}}(z,t)|^2$ and $|\Psi_{\mathrm{pho}}(z,t)|^2$, respectively, as a function of distance (z, horizontal axis) and time (vertical axis), in a lossy cavity (i.e., $\gamma_{\mathrm{cav}} = 66.7$ ps^{-1}). **h** Contributions of the molecular excitons (black), and cavity mode excitations (red) to $|\Psi(z,t)|^2$ as a function of time in the lossy cavity. The population in the ground state, created by radiative decay through the imperfect mirrors, is plotted in blue. Source data are provided as a Source Data file.

instead, with the front of the wavepacket propagating at a velocity that closely matches the maximum group velocity of the LP branch (68 µmps^{-1}, Fig. 1c), while the expectation value of the wavepacket position ($\langle z\rangle$, Fig. 5a) moves at a lower pace (~10 µmps^{-1}).

Because we do not include negative k_z-vectors in our cavity model, propagation can only occur in the positive z direction. With negative k_z-vectors, propagation in the opposite direction cancels such motion leading to $\langle z\rangle \approx 0$ (Fig. S15a). Nevertheless, since the Mean Squared Displacement is not affected by breaking the symmetry of the 1D cavity, and increases linearly with time in both uni- and bi-directional cavities (Figs. 5c and S15b), we consider it reasonable to assume that the mechanism underlying the propagation process is identical.

Because the population of dark states dominates throughout these simulations (Fig. 4d), and direct excitonic couplings are not accounted for in our model (SI), the observed propagation must again involve bright polariton states. Since the initial state, with one molecule excited, is not an eigenstate of the molecule-cavity system, population exchange from this state into the propagating bright states is not only due to displacements along vibrational modes that are overlapping with the non-adiabatic coupling vector[62], but also due to Rabi oscillations, in particular at the start of the simulation.

To quantify to what extent the overall propagation is driven by population transfers due to the molecular displacements, we performed additional simulations at 0 K with all nuclear degrees of freedom frozen. As shown in Fig. S18, the propagation is reduced at 0 K, and the wavepacket remains more localized on the molecule that was initially excited, than at 300 K. A quadratic time-dependence of the Mean Squared Displacement of the cavity mode contributions to the wavepacket (Fig. S19f) furthermore suggest that the mobility at 0 K is driven by the constructive and destructive interferences of the bright polaritonic states, which evolve with different phases (i.e., $e^{-iE_m t/\hbar}$).

The reduced mobility of the wavepacket at 0 K compared to 300 K (Fig. S19) confirms that thermally activated displacements of nuclear coordinates, which are absent at 0 K, are essential to drive population into the bright states and sustain the propagation of the polariton wavepacket. Thus, as during the diffusion phase observed for on-resonant excitation, ballistic motion of bright states is continuously interrupted and restarted with different group velocities, which makes the overall propagation appear diffusive with a Mean Squared Displacement that depends linearly on time (Fig. 5c), in line with experimental observations[40,42].

In the perfect cavity, propagation and broadening continue indefinitely due to the long-range ballistic motion of states with higher group velocities. Indeed, a small fraction at the front of the wavepacket, which moves even faster than the maximum group velocity of the LP (indicated by a yellow dashed line in Fig. 4c), is mostly composed of higher-energy UP states. These states not only have the highest in-plane momenta, but also relax most slowly into the dark state manifold of the perfect cavity due to the inverse dependence of the non-adiabatic coupling on the energy gap[57]. Momentum-resolved photo-luminenscence spectra at two distances from the initial excitation spot (Fig. S24) confirm that the front of the wavepacket is indeed composed of UP states: at short distances (z = 10 µm) from the excitation spot (z = 5 µm), the emission spectrum, accumulated over 100 fs simulation time, closely matches the full polariton dispersion of Fig. 1b, displaying both the LP and UP branches. In contrast, further away from the excitation spot (z = 20 µm), the emission exclusively originates from the higher energy UP states, suggesting that only these states can reach the longer distance within 100 fs.

Lossy cavity. Adding a radiative decay channel for the cavity mode excitations ($\gamma_{\mathrm{cav}} = 66.7$ ps^{-1}) restricts the distance over which polaritons propagate (Fig. 4e–g), but does not affect the overall transport mechanism, as we also observe a linear increase of the Mean Squared

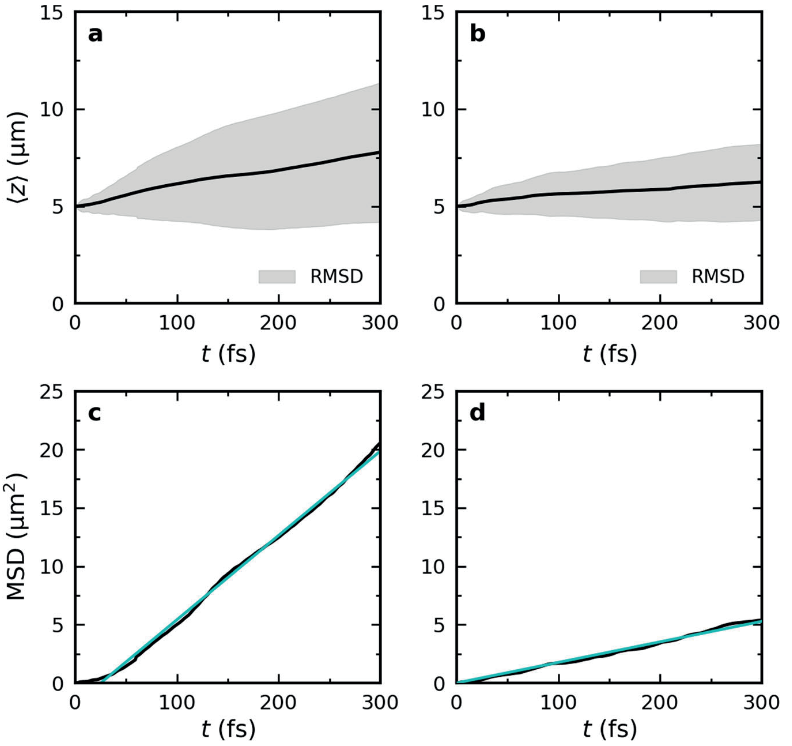

Fig. 5 | Propagation of the polaritonic wavepacket after off-resonant excitation. Top panels: Expectation value of the position of the total time-dependent wavefunction, $\langle z\rangle = \langle\Psi(z,t)|\hat{z}|\Psi(z,t)\rangle/\langle\Psi(z,t)|\Psi(z,t)\rangle$, in an ideal cavity (**a**, $\gamma_{\mathrm{cav}} = 0$ ps^{-1}) and a lossy cavity (**b**, $\gamma_{\mathrm{cav}} = 66.7$ ps^{-1}). The black lines represent $\langle z\rangle$ while the shaded area around the lines represents the root mean squared deviation (RMSD, i.e., $\sqrt{\langle(z(t)-\langle z(t)\rangle)^2\rangle}$). Bottom panels: Mean squared displacement (MSD, i.e., $\langle(\langle(z(t)-z(0))^2\rangle)\rangle$) in the ideal lossless cavity (**c**) and the lossy cavity (**d**). Cyan lines are linear fits to the MSD. Source data are provided as a Source Data file.

Displacement with time (Fig. 5d). While the propagation in the lossy cavity initially is very similar to that in the ideal lossless cavity, radiative decay selectively depletes population from the propagating bright states and the wavepacket slows down, as evidenced by the expectation value of the displacement, $\langle z\rangle$, levelling off in Fig. 5b. In addition, since the maximum distance a wavepacket can travel in a lossy cavity is determined by the cavity lifetime in combination with the group velocity[38], the broadening of the wavepacket is also more limited when cavity losses are included (Fig. 5b). Furthermore, even if dark states do not have a significant contribution from the cavity mode excitations, the reversible transfer of population between the dark state manifold and the decaying bright polaritonic states, also leads to a significant reduction of dark state population in the lossy cavity as compared to the ideal lossless cavity (Fig. 4d, h). Nevertheless, dark states still provide protection from cavity losses as the overall lifetime of the photo-excited molecule-cavity system (>150 fs) significantly exceeds that of the cavity modes (15 fs).

Comparison to experiments. In microscopy experiments relying on off-resonant optical pumping, polariton emission is typically observed between the excitation spot and a point several microns further away[38,40,42,46,51]. While such a broad emission pattern is reminiscent of a diffusion process, the match between the total distance over which that emission is detected on the one hand, and the product of the maximum LP group velocity and cavity lifetime on the other hand, suggests ballistic propagation. The results of our simulations are thus in qualitative agreement with such observations as also our results suggest that, while polariton propagation appears diffusive under off-resonant excitation conditions, the front of the wave packet propagates close to the maximum group velocity of the LP branch.

Based on the analysis of our MD trajectories we propose that on the experimentally accessible timescales, polariton propagation appears diffusive due to reversible population transfers between stationary dark states and propagating bright states. For lossy cavities, radiative decay of the cavity modes further slows down polariton transport such that the excitation reaches a maximum distance before decaying completely. Because a large fraction of the population resides in the non-decaying dark states, the lifetime of the molecule-cavity system is extended[60], and polariton propagation can be observed on timescales far beyond the cavity lifetime, in line with experiment[40].

Note that in our simulations we only couple excitons to the modes of the Fabry-Pérot cavity, whereas in experiments with micro-cavities constituted by metallic mirrors, excitons can in principle also couple to surface plasmon polaritons (SPPs) below the light line that are supported by these metal surfaces. While their role will depend on the details of the set-up (e.g., the materials used, energy of the relevant molecular excitations, etc.), we cannot rule out that reversible population transfer between dark states and SPP-exciton polaritons also contributes to the effective diffusion constant observed in those experiments[40,48]. However, because SPPs decay exponentially away from the metal surface, and SPP-exciton polaritons also have group velocity, the qualitative behavior is not expected to change.

Size dependence

The Rabi splitting depends on the vacuum field strength, $\mathbf{E}_y$, and the number of molecules, N, via $\hbar\Omega^{\mathrm{Rabi}} \approx 2\boldsymbol{\mu}^{\mathrm{TDM}}\cdot\mathbf{E}_y\sqrt{N}$, with $\boldsymbol{\mu}^{\mathrm{TDM}}$ the molecular transition dipole moment, which for organic molecules is on the order of a few Debye. Because the vacuum field strength of a cavity is inversely proportional to the square root of the mode volume (Eq. 3

in SI), the Rabi splitting scales with the molecular concentration in the mode volume, V_{cav}, of the cavity, i.e., $\hbar\Omega^{\text{Rabi}} \propto \sqrt{N/V_{\text{cav}}}$. Reaching the strong coupling regime to form polaritons with organic molecules in Fabry-Pérot cavities with mode volumes on the order of $V_{\text{cav}} \propto (\lambda_{\text{cav}}/n)^3$ (where λ_{cav} is the wavelength of the cavity mode and n the refractive index), thus requires collective coupling of many molecules (i.e., 10^5-10^8)[64–66]. Because the number of molecules we can include in our simulations is much smaller due to limitations on hard- and software, we investigated how that number affects the propagation by repeating simulations for different N. To keep the Rabi splitting constant, and hence the polariton dispersion the same, we scaled the mode volume with N, i.e., $V_{\text{cav}} = NV_{\text{cav},0}$, where $V_{\text{cav},0}$ is the mode volume required to achieve a Rabi splitting of 325 meV with a single Rhodamine molecule in the cavity.

With the exception of the smallest ensemble that lacks dark states, we observe for all other ensemble sizes that the propagation mechanism involves reversible population exchange between the stationary dark state manifold and propagating polaritons (Figs. S5–S13, SI). These additional simulations therefore underscore the role of dark states in the propagation process and suggest that the mechanism does not strongly depend on N. In contrast to the mechanism, however, the rates at which these population exchanges occur, depend on the number of molecules. Indeed, these rates are inversely proportional to N[23,62,67]. Because the number of dark states scales with N, whereas the number of polaritonic states is constant (Fig. S4), we observe that for the larger ensembles, the fraction of population residing within the dark state manifold is higher than for the smaller ensembles. Such differences affect (i) the propagation velocity (e.g., Fig. S14); (ii) the lifetime (e.g., right columns in Figs. 4 and S11) and therefore also (iii) the distance over which the exciton-polaritons are transferred (e.g., Figs. 5, and S11–S13).

Because the velocity is inversely proportional to N (Fig. S14), the propagation velocity in experiments, with 10^5-10^8 molecules inside the mode volume[64–66], is much lower than in our simulations. Nevertheless, because of the $1/N$ scaling, the effective polariton propagation velocity approaches the lower experimental limit of 10^5 coupled molecules[64] already around 1000 molecules. We therefore consider the results of the simulations with 1024 Rhodamines sufficiently representative for experiment and for providing qualitative insights into polariton propagation. Indeed, a propagation speed of 9.6 μmps^{-1} in the cavity containing 1024 molecules is about an order of magnitude below the maximum group velocity of the LP (68 μmps^{-1}) in line with experiments on organic microcavities[40], and cavity-free polaritons[43].

Summary and outlook

To conclude, we have investigated exciton transport in cavities filled with Rhodamine molecules by means of atomistic MD simulations that not only include the details of the cavity mode structure[57,58], but also the chemical details of the material[56]. The results of our simulations suggest that transport is driven by an interplay between propagating bright polaritonic states and stationary dark states. Reversible population exchanges between these states interrupt ballistic motion in bright states and make the overall propagation process appear diffusive. While for off-resonant excitation of the molecule-cavity system, these exchanges are essential to transfer population from the initially excited molecule into the bright polaritonic branches and start the propagation process, the exchanges limit the duration of the initial ballistic phase for on-resonant excitation. As radiative decay of the cavity modes selectively depletes the population in bright states, ballistic propagation is restricted even further if the cavity is lossy. Because dark states lack in-plane momentum, the reversible population exchange between dark and bright states causes diffusion in all directions. Therefore, under off-resonant excitation conditions, the propagation direction cannot be controlled. In contrast, because bright states carry momentum, the propagation direction in the ballistic phase can be controlled precisely by tuning the incidence angle and excitation wavelength under on-resonant excitation conditions.

The rate at which population transfers between bright and dark states depends on the non-adiabatic coupling vector, whose direction and magnitude are determined by the Huang-Rhys factor in combination with the frequency of the Franck-Condon active vibrations[62], both of which are related to the molecular Stokes shift[68]. In addition, because the non-adiabatic coupling is inversely proportional to the energy gap[62], the Stokes shift in combination with the Rabi splitting, also determines the region on the LP branch into which population transfers after off-resonant excitation of a single molecule[69–72]. We therefore speculate that the Stokes shift can be an important control knob for tuning the coherent propagation of polaritons.

Because our Rhodamine model features the key photophysical characteristics of an organic dye molecule, we speculate that the propagation mechanism observed in our simulations is generally valid for exciton transport in strongly-coupled organic micro-cavities, in which the absorption line width of the material exceeds the Rabi splitting and there is a significant overlap between bright and dark states. To confirm this, we have also performed simulations of exciton transport in cavities containing Tetracene and Methylene Blue and observed that the propagation mechanism remains the same (Figs. S25–S30, Supplementary Movies 10–12 and 46–48). Future work will be aimed at investigating how the propagation can be controlled by tuning molecular parameters, temperature, Rabi splitting (Fig. S23), or cavity Q-factor[73]. Because we include the structural details of both cavity and molecules, our simulations, which are in qualitative agreement with experiments, could be used to systematically optimize molecule-cavity systems for enhancing energy transfer.

Methods

Multiscale Tavis-Cummings simulation model

We used the multi-scale Tavis-Cummings model, introduced by Luk et al.[56], and extended to the multiple modes of a one-dimensional (1D) Fabry-Pérot micro-cavity[58] by Tichauer et al.[57], to perform molecular dynamics (MD) simulations of 1024 solvated Rhodamine molecules strongly coupled to the confined light modes of a 1D Fabry-Pérot micro-cavity, shown in Fig. S1[58]. In this model, we apply the Born-Oppenheimer approximation to separate the nuclear degrees of freedom, which we treat classically, from the electronic degrees of freedom and the cavity modes. Within the single-excitation subspace, probed experimentally under weak driving conditions, and employing the rotating wave approximation (RWA), valid for light-matter coupling strengths below 10% of the material excitation energy[74], we model the electronic plus cavity mode degrees of freedom with the Tavis-Cummings model of Quantum Optics[75,76]. In the long-wavelength approximation, the interaction between the molecular excitons and the cavity modes are modeled as the inner products between the transition dipole moments and the vacuum field associated with an excitation of the Fabry-Pérot cavity modes. The multi-scale Tavis-Cummings model is described in our previous works[56,57,60], and we provide a concise summary of the details relevant to this work in Section 1 of the SI.

Rhodamine model

The electronic ground state (S_0) of the Rhodamine molecules was modeled at the hybrid Quantum Mechanics / Molecular Mechanics (QM/MM) level[77,78], using the restricted Hartree-Fock (HF) method in combination with the 3-21G basis set[79] for the QM subsystem, which contains the fused rings of the molecule. The MM subsystem, consisting of the rest of the molecule and 3,684 TIP3P waters[80], was modeled with the Amber03 force field[81]. The first electronic excited state (S_1) of the QM region was modeled with Configuration Interaction, truncated at single electron excitations (CIS/3-21G//Amber03). At this level of theory, the excitation energy of Rhodamine is 4.18 eV, which is significantly overestimated with respect to experiments. This discrepancy is due to the limited size of the basis set and the neglect of electron-electron correlation in the ab initio methods we used. While including electron-electron correlation into the description of the QM region improves the vertical excitation energy, we show in the SI that this does not significantly change the topology of the relevant potential energy surfaces (Fig. S3), which determines the molecular dynamics. Further details of the Rhodamine simulation setup, as well as the full details of additional simulations of Tetracene in cyclohexane and of Methylene Blue in water, are provided in the SI.

Molecular dynamics of Rhodamine-cavity systems

Cavity model. After a 200 ns equilibration at the force field level, and a further 100 ps equilibration at the QM/MM level, the 1024 Rhodamine molecules were placed with equal inter-molecular distances on the z-axis of a periodic 1D cavity[35,58] of length $L_z = 50\ \mu\text{m}$, where z indicates the in-plane direction (i.e., parallel to the mirrors). With a distance of $L_x = 163$ nm between the mirrors (cavity width), where x indicates the out-of-plane direction (i.e., perpendicular to the mirrors), the fundamental mode of the cavity has an energy of $\hbar\omega_0 = 3.81$ eV at normal incidence (i.e., $k_z = 0$) and hence its dispersion is red-detuned with respect to the molecular excitation energy at 4.18 eV (horizontal dashed white line in Fig. 1b). The dispersion, $\omega_{\text{cav}}(k_z) = \sqrt{\omega_0^2 + c^2k_z^2/n^2}$ (dot-dashed white line in Fig. 1b), was modeled with 160 modes ($0 \le p \le 159$ for $k_z = 2\pi p/L_z$, with c the speed of light and n the refractive index)[35]. With a cavity vacuum field strength of 0.26 MVcm^{-1}, the Rabi splitting, defined as the energy difference between the bright lower (LP) and upper polariton (UP) branches at the wave-vector k_z^{res} where the cavity dispersion matches the molecular excitation energy (Fig. 1b), was ~ 325 meV. While the choice for a 1D cavity model with only positive k_z vectors was motivated by the necessity to keep our simulations computationally tractable, it precludes the observation of elastic scattering events that would change the direction (i.e., in-plane momentum, $\hbar\mathbf{k}$) of propagation. Furthermore, with only positive k_z vectors, polariton motion is restricted to the $+z$ direction, but we show in the SI (Fig. S15) that this assumption does not affect our conclusions about the transport mechanism. To maximize the collective light-matter coupling strength, the transition dipole moments of the Rhodamine molecules were aligned to the vacuum field at the start of the simulation. The same starting coordinates were used for all Rhodamines, but different initial velocities were selected randomly from a Maxwell-Boltzmann distribution at 300 K. We checked that adding disorder by randomly selecting configurations from the equilibrium QM/MM trajectory, or by randomly placing molecules on the z-axis, does not affect the conclusions of our work (Figs. S21 and 22).

Mean-field molecular dynamics. Ehrenfest MD trajectories were computed by numerically integrating Newton's equations of motion using a leap-frog algorithm with a 0.1 fs timestep[82]. The multi-mode Tavis-Cummings Hamiltonian (Eq. 4 in SI) was diagonalized at each time-step to obtain the (adiabatic) polaritonic eigenstates[75,76]:

$$|\psi^m\rangle = \left(\sum_j^N \beta_j^m \hat{\sigma}_j^+ + \sum_p^{n_{\text{mode}}} \alpha_p^m \hat{a}_p^\dagger\right)\left|\text{S}_0^1\text{S}_0^2..\text{S}_0^{N-1}\text{S}_0^N\right\rangle|0\rangle \qquad (1)$$

with eigenenergies E_m. Here, $|\text{S}_0^1\text{S}_0^2..\text{S}_0^{N-1}\text{S}_0^N\rangle|0\rangle$ represents the wave function of the molecule-cavity system in the ground state, in which neither the molecules, nor the cavity modes are excited. The creation operators $\hat{\sigma}_j^+ = |\text{S}_1^j\rangle\langle\text{S}_0^j|$ and $\hat{a}_p^\dagger = |1_p\rangle\langle 0_p|$ excite molecule j and cavity mode p with in-plane momentum $k_z = 2p\pi/L_z$, respectively. The β_j^m and α_p^m expansion coefficients thus reflect the contribution of the molecular excitons ($|\text{S}_1^j\rangle$) and of the cavity mode excitations ($|1_p\rangle$) to polariton $|\psi^m\rangle$.

The total wavefunction, $|\Psi(t)\rangle$, was coherently propagated along with the classical degrees of freedom of the molecules as a time-dependent superposition of the polaritonic eigenstates:

$$|\Psi(t)\rangle = \sum_m c_m(t)|\psi^m\rangle \qquad (2)$$

where $c_m(t)$ are the time-dependent expansion coefficients of the time-independent eigenstates $|\psi^m\rangle$. A unitary propagator in the local diabatic basis was used to integrate these coefficients[83], while the nuclear degrees of freedom of the molecules were evolved on the mean-field potential energy surface.

Results reported in this work were obtained as averages over at least two trajectories. For all simulations we used Gromacs 4.5.3[84], in which the multi-mode Tavis-Cummings QM/MM model was implemented[57], in combination with Gaussian16[85]. Further details of the simulations, including other ensemble sizes for the Rhodamine-cavity systems, and different molecules, i.e., Tetracene and Methylene Blue (Fig. S2), are provided in the SI.

Excitation conditions. Resonant excitation into the LP branch by a short broad-band laser pulse, as often used in time-resolved experiments[34,43,47], was modeled by preparing a Gaussian wavepacket of LP states centered at $\hbar\omega = 3.94$ eV where the group velocity of the LP branch is highest, and with a bandwidth of $\sigma = 0.707\ \mu\text{m}^{-1}$ [35]. Thus, the expansion coefficients of the wave function, $|\Psi(t=0)\rangle$ (Eq. 2), were initiated as

$$c_m(t=0) = \left(\frac{\zeta}{2\pi^3}\right)^{\frac{1}{4}} \exp[-\zeta(k_z^m - k_c)^2] \qquad (3)$$

with $\zeta = 10^{-12}\text{m}^2$ characterizing the width of the wavepacket and k_z^m the expectation value of the in-plane momentum of polariton $|\psi_m\rangle$ (i.e., $\langle k_z^m\rangle = \sum_p^{n_{\text{mode}}} |\alpha_p^m|^2 k_{z,p} / \sum_p^{n_{\text{mode}}} |\alpha_p^m|^2$).

Experimentally, an off-resonant excitation in a molecule-cavity system is achieved by optically pumping a higher-energy electronic state of the molecules[38,40,42,51], which then rapidly relaxes into the lowest energy excited state (S_1) according to Kasha's rule[63]. We therefore modeled off-resonant photo-excitation by starting the simulations directly in the S_1 state of a single molecule, located at $z = 5\ \mu\text{m}$ in the cavity. This was achieved by initiating the expansion coefficients of the wave function (Eq. 2) as $c_m(t=0) = \beta_j^m$. A more detailed derivation of these initial conditions is provided in the SI.

We assume that the intensity of the excitation pulse in both cases is sufficiently weak for the system to remain within the single-excitation subspace in our simulations. We thus exclude multi-photon absorption and model the interaction with the pump pulse as an instantaneous absorption of a single photon.

Cavity lifetime. Because the light-confining structures used in previous experiments (e.g., Fabry-Pérot cavities[34,40,47,48], Bloch surface waves[38,42,51], or plasmonic lattices[41,46,54]) span a wide range of quality factors (Q-factors), we also investigated the effect of the cavity mode lifetime on the transport by performing simulations in an ideal lossless cavity with no photon decay (i.e., $\gamma_{\text{cav}} = 0\ \text{ps}^{-1}$), and a lossy cavity with decay rate of 66.7 ps^{-1}. This decay rate corresponds to a lifetime of 15 fs, which is in the same order of magnitude as the 2–15 fs lifetimes reported for metallic Fabry-Pérot cavities in experiments[40,86–88]. Cavity losses were modeled as a first-order decay of population from eigenstates with contributions from cavity mode excitations. Assuming that the intrinsic decay rates γ_{cav} are the same for all modes, the total loss rate of an eigenstate, $|\psi^m\rangle$, is calculated as the product of γ_{cav} and the total photonic weight, $\sum_p|\alpha_p^m|^2$, of that eigenstate.

In addition to cavity loss, also internal conversion via the conical intersection seam between the S_1 and S_0 potential energy surfaces[89] can provide a decay channel for the excitation. However, because in our Rhodamine model the minimum energy conical intersection is 1.3 eV higher in energy than the vertical excitation (Supplementary Table 1 in SI) and is therefore unlikely to be reached on the timescale of our simulations, we neglect internal conversion processes altogether.

Wavefunction analysis

To monitor the propagation of the wavepacket, we plotted the probability density of the total time-dependent wave function $|\Psi(t)|^2$ at the positions of the molecules, z_j, as a function of time (Figs. 2 and 4). We thus represent the density as a discrete distribution at grid points that correspond to the molecular positions, rather than a continuous distribution. In addition to the total probability density, $|\Psi(t)|^2$, we also plotted the probability densities of the excitonic $|\Psi_{\text{exc}}(t)|^2$ and photonic $|\Psi_{\text{pho}}(t)|^2$ contributions separately (b, f and c, g, respectively, of Figs. 2 and 4).

The amplitude of $|\Psi_{\text{exc}}(t)\rangle$ at position z_j in the 1D cavity (with $z_j=(j-1)L_z/N$ for $1\leq j\leq N$) is obtained by projecting the excitonic basis state in which molecule j at position z_j is excited ($|\phi_j\rangle=\hat{\sigma}_j^+|\phi_0\rangle$), on the total wave function (Eq. 2):

$$\begin{aligned}\left|\Psi_{\text{exc}}(z_j,t)\right\rangle &= \hat{\sigma}_j^+|\phi_0\rangle\langle\phi_0|\hat{\sigma}_j|\Psi(t)\rangle\\ &= \sum_m^{N+n_{\text{mode}}} c_m(t)\beta_j^m\hat{\sigma}_j^+|\phi_0\rangle\end{aligned} \tag{4}$$

where the β_j^m are the expansion coefficients of the excitonic basis states in polaritonic state $|\psi^m\rangle$ (Eq. 1) and $c_m(t)$ the time-dependent expansion coefficients of the total wavefunction $|\Psi(t)\rangle$ (Eq. (2)).

The cavity mode excitations are described as plane waves that are delocalized in real space. We therefore obtain the amplitude of the cavity modes in polaritonic eigenstate $|\psi^m\rangle$ at position z_j by Fourier transforming the projection of the cavity mode excitation basis states, in which cavity mode p is excited ($\left|\phi_p\right\rangle=\hat{a}_p^\dagger|\phi_0\rangle$):

$$\begin{aligned}\left|\psi_{\text{pho}}^m(z_j)\right\rangle &= \mathcal{FT}^{-1}\left[\sum_p^{n_{\text{mode}}}\hat{a}_p^\dagger|\phi_0\rangle\langle\phi_0|\hat{a}_p|\psi^m\rangle\right]\\ &= \frac{1}{\sqrt{N}}\sum_p^{n_{\text{mode}}}\alpha_p^m e^{i2\pi z_j p}\hat{a}_p^\dagger|\phi_0\rangle\end{aligned} \tag{5}$$

where the α_p^m are the expansion coefficients of the cavity mode excitations in polaritonic state $|\psi^m\rangle$ (Eq. 1) and we normalize by $1/\sqrt{N}$ rather than $1/\sqrt{L_z}$, as we represent the density on the grid of molecular positions. The total contribution of the cavity mode excitations to the wavepacket at position z_j at time t is then obtained as the weighted sum over the Fourier transforms:

$$\begin{aligned}\left|\Psi_{\text{pho}}(z_j,t)\right\rangle &= \sum_m^{N+n_{\text{mode}}} c_m(t)\times\mathcal{FT}^{-1}\left[\sum_p^{n_{\text{mode}}}\hat{a}_p^\dagger|\phi_0\rangle\langle\phi_0|\hat{a}_p|\psi^m\rangle\right]\\ &= \sum_m^{N+n_{\text{mode}}} c_m(t)\frac{1}{\sqrt{N}}\sum_p^{n_{\text{mode}}}\alpha_p^m e^{i2\pi z_j p}\hat{a}_p^\dagger|\phi_0\rangle\end{aligned} \tag{6}$$

with $c_m(t)$ the time-dependent expansion coefficients of the adiabatic polaritonic states $|\psi^m\rangle$ in the total wavefunction $|\Psi(t)\rangle$ (Eq. 2).

Data availability

All data, including simulations models, input files, trajectories and structures, analysis scripts and programs, including raw data, are available for download from IDA - Research Data Storage[90]. Source data are provided with this paper.

Code availability

The GROMACS-4.5.3 fork, in which the multi-scale Tavis-Cummings model used in this work, was implemented, is available for download from GitHub[91].

References

1. Croce, R. & Amerongen, H. V. Natural strategies for photosynthetic light harvesting. *Nat. Chem. Biol.* **10**, 492–501 (2014).
2. Mikhnenko, O. V., Blom, P. W. M. & Nguyen, T.-Q. Exciton diffusion in organic semiconductors. *Energy Environ. Sci.* **8**, 1867–1888 (2015).
3. Cao, H. et al. Recent progress in degradation and stabilization of organic solar cells. *J. Power Sources* **264**, 168–183 (2014).
4. Rafique, S., Abdullah, S. M., Sulaiman, K. & Iwamoto, M. Fundamentals of bulk heterojunction organic solar cells: an overview of stability/degradation issues and strategies for improvement. *Renew. Sust. Energ. Rev.* **84**, 43–53 (2018).
5. Akselrod, G. M. et al. Visualization of exciton transport in ordered and disordered molecular solids. *Nat. Comm.* **5**, 3646 (2014).
6. Sneyd, A. et al. Efficient energy transport in an organic semiconductor mediated by transient exciton delocalization. *Sci. Adv.* **7**, eabh4232 (2021).
7. Kong, F. F. et al. Wavelike electronic energy transfer in donor-acceptor molecular systems through quantum coherence. *Nat. Nanotechnol.* **17**, 729–736 (2022).
8. Sneyd, A. J., Beljonne, D. & Rao, A. A new frontier in exciton transport: transient delocalization. *J. Chem. Phys. Lett.* **13**, 6820–6830 (2022).
9. Feist, J. & Garcia-Vidal, F. J. Extraordinary exciton conductance induced by strong coupling. *Phys. Rev. Lett.* **114**, 196402 (2015).
10. Schachenmayer, J., Genes, C., Tignone, E. & Pupillo, G. Cavity enhanced transport of excitons. *Phys. Rev. Lett.* **114**, 196403 (2015).
11. Wellnitz, D., Pupillo, G. & Schachenmayer, J. Disorder enhanced vibrational entanglement and dynamics in polaritonic chemistry. *Comm. Phys.* **5**, 120 (2022).
12. Skolnick, M. S., Fisher, T. A. & Whittaker, D. M. Strong coupling phenomena in quantum microcavity structures. *Semicond. Sci. Technol.* **13**, 645–669 (1998).
13. Litinskaya, M., Reineker, P. & Agranovich, V. M. Exciton-polaritons in organic microcavities. *J. Lumin.* **119**, 277–282 (2006).
14. Törmä, P. & Barnes, W. L. Strong coupling between surface plasmon polaritons and emitters: a review. *Rep. Prog. Phys.* **78**, 013901 (2015).
15. Ribeiro, R. F., Martinéz-Martinéz, L. A., Du, M., Campos-Gonzalez-Angule, J. & Yuen-Zhou, J. Polariton chemistry: controlling molecular dynamics with optical cavities. *Chem. Sci.* **9**, 6325–6339 (2018).
16. Hertzog, M., Wang, M., Mony, J. & Börjesson, K. Strong light–matter interactions: a new direction within chemistry. *Chem. Soc. Rev.* **48**, 937–961 (2019).
17. Garcia-Vidal, F. J., Ciuti, C. & Ebbessen, T. W. Manipulating matter by strong coupling to vacuum fields. *Science* **373**, 336 (2021).
18. Fregoni, J., Garcia-Vidal, F. J. & Feist, J. Theoretical challenges in polaritonic chemistry. *ACS Photon.* **9**, 1096–1107 (2022).
19. Ruggenthaler, M., Sidler, D. & Rubio, A. Understanding polaritonic chemistry from ab initio quantum electrodynamics. *arXiv* https://doi.org/10.48550/arXiv.2211.04241 (2022).
20. Rider, M. S. & Barnes, W. L. Something from nothing: linking molecules with virtual light. *Contemp. Phys.* **62**, 217–232 (2022).
21. Agranovich, V. M., Litinskaia, M. & Lidzey, D. G. Cavity polaritons in microcavities containing disordered organic semiconductors. *Phys. Rev. B* **67**, 085311 (2003).
22. Litinskaya, M., Reineker, P. & Agranovich, V. M. Fast polariton relaxation in strongly coupled organic microcavities. *J. Lumin.* **110**, 364–372 (2004).
23. del Pino, J., Feist, J. & Garcia-Vidal, F. J. Quantum theory of collective strong coupling of molecular vibrations with a microcavity mode. *N. J. Phys.* **17**, 053040 (2015).

24. Coles, D. M. et al. Polariton-mediated energy transfer between organic dyes in a strongly coupled optical microcavity. *Nat. Mater.* **13**, 712–719 (2014).
25. Zhong, X. et al. Non-radiative energy transfer mediated by hybrid light-matter states. *Angew. Chem. Int. Ed.* **55**, 6202–6206 (2016).
26. Zhong, X. et al. Energy transfer between spatially separated entangled molecules. *Angew. Chem. Int. Ed.* **56**, 9034–9038 (2017).
27. Georgiou, K. et al. Control over energy transfer between fluorescent bodipy dyes in a strongly coupled microcavity. *ACS Photon.* **5**, 258–266 (2018).
28. Groenhof, G. & Toppari, J. J. Coherent light harvesting through strong coupling to confined light. *J. Phys. Chem. Lett.* **9**, 4848–4851 (2018).
29. Xiang, B. et al. Intermolecular vibrational energy transfer enabled by microcavity strong light-matter coupling. *Science* **368**, 665–667 (2020).
30. Georgiou, K., Jayaprakash, R., Othonos, A. & Lidzey, D. G. Ultralong-range polariton-assisted energy transfer in organic microcavities. *Angew. Chem. Int. Ed.* **60**, 16661–16667 (2021).
31. Son, M. et al. Energy cascades in donor-acceptor exciton-polaritons observed by ultrafast two- dimensional white-light spectroscopy. *Nat. Comm.* **13**, 7305 (2022).
32. Engelhardt, G. & Cao, J. Unusual dynamical properties of disordered polaritons in microcavities. *Phys. Rev. B* **105**, 064205 (2022).
33. Bhatt, P., Dutta, J., Kaur, K. & George, J. Long-range energy transfer in strongly coupled donor-acceptor phototransistors. *Nano. Lett.* **23**, 5004—5011 (2023).
34. Freixanet, T., Sermage, B., Tiberj, A. & Planel, R. In-plane propagation of excitonic cavity polaritons. *Phys. Rev. B* **61**, 7233 (2000).
35. Agranovich, V. M. & Gartstein, Y. N. Nature and dynamics of low-energy exciton polaritons in semiconductor microcavities. *Phys. Rev. B* **75**, 075302 (2007).
36. Litinskaya, M. Propagation and localization of polaritons in disordered organic microcavities. *Phys. Lett. A* **372**, 3898–3903 (2008).
37. Michetti, P. & Rocca, G. C. L. Polariton dynamics in disordered microcavities. *Phys. E* **40**, 1926–1929 (2008).
38. Lerario, G. et al. High-speed flow of interacting organic polaritons. *Light Sci. Appl.* **6**, e16212 (2017).
39. Myers, D. M., Mukherjee, S., Beaumariage, J. & Snoke, D. W. Polariton-enhanced exciton transport. *Phys. Rev. B* **98**, 235302 (2018).
40. Rozenman, G. G., Akulov, K., Golombek, A. & Schwartz, T. Long-range transport of organic exciton-polaritons revealed by ultrafast microscopy. *ACS Photon.* **5**, 105–110 (2018).
41. Zakharko, Y. et al. Radiative pumping and propagation of plexcitons in diffractive plasmonic crystals. *Nano. Lett.* **18**, 4927–4933 (2018).
42. Hou, S. et al. Ultralong-range energy transport in a disordered organic semiconductor at room temperature via coherent exciton-polariton propagation. *Adv. Mater.* **32**, 2002127 (2020).
43. Pandya, R. et al. Microcavity-like exciton-polaritons can be the primary photoexcitation in bare organic semiconductors. *Nat. Commun.* **12**, 6519 (2021).
44. Wurdack, M. et al. Motional narrowing, ballistic transport, and trapping of room-temperature exciton polaritons in an atomically-thin semiconductor. *Nat. Comm.* **12**, 5366 (2021).
45. Ferreira, B., Rosati, R. & Malic, E. Microscopic modeling of exciton-polariton diffusion coefficients in atomically thin semiconductors. *Phys. Rev. Mat.* **6**, 034008 (2022).
46. Berghuis, M. A. et al. Controlling exciton propagation in organic crystals through strong coupling to plasmonic nanoparticle arrays. *ACS Photon.* **9**, 123 (2022).
47. Pandya, R. et al. Tuning the coherent propagation of organic exciton-polaritons through dark state delocalization. *Adv. Sci.* **9**, 2105569 (2022).
48. Xu, D. et al. Ultrafast imaging of coherent polariton propagation and interactions. *Nat. Comm.* **14**, 3881 (2023).
49. Ribeiro, R. F. Multimode polariton effects on molecular energy transport and spectral fluctuations. *Comm. Chem.* **5**, 48 (2022).
50. Allard, T. F. & Weick, G. Disorder-enhanced transport in a chain of lossy dipoles strongly coupled to cavity photons. *Phys. Rev. B* **106**, 245424 (2022).
51. Balasubrahmaniyam, M., Simkovich, A., Golombek, A., Ankonina, G. & Schwartz, T. Unveiling the mixed nature of polaritonic transport: From enhanced diffusion to ballistic motion approaching the speed of light. *Nat. Mater.* **22**, 338–344 (2023).
52. Aroeira, G. J. R., Kairys, K. & Ribeiro, R. F. Theoretical analysis of exciton wave packet dynamics in polaritonic wires. *J. Phys. Chem. Lett.* **14**, 5681–5691 (2023).
53. Engelhardt, G. & Cao, J. Polariton localization and dispersion properties of disordered quantum emitters in multimode microcavities. *Phys. Rev. Lett.* **130**, 213602 (2023).
54. Jin, L. et al. Enhanced two-dimensional exciton propagation via strong light-matter coupling with surface lattice plasmons. *ACS Photon.* **10**, 1983–1991 (2023).
55. Dähne, L., Biller, E. & Baumgärtel, H. Polariton-induced color tuning of thin dye layers. *Angew. Chem. Int. Ed.* **37**, 646–649 (1998).
56. Luk, H. L., Feist, J., Toppari, J. J. & Groenhof, G. Multiscale molecular dynamics simulations of polaritonic chemistry. *J. Chem. Theory Comput.* **13**, 4324–4335 (2017).
57. Tichauer, R. H., Feist, J. & Groenhof, G. Multi-scale dynamics simulations of molecular polaritons: the effect of multiple cavity modes on polariton relaxation. *J. Chem. Phys.* **154**, 104112 (2021).
58. Michetti, P. & Rocca, G. C. L. Polariton states in disordered organic microcavities. *Phys. Rev. B.* **71**, 115320 (2005).
59. Georgiou, K. et al. Generation of anti-stokes fluorescence in a strongly coupled organic semiconductor microcavity. *ACS Photon.* **5**, 4343–4351 (2018).
60. Groenhof, G., Climent, C., Feist, J., Morozov, D. & Toppari, J. J. Tracking polariton relaxation with multiscale molecular dynamics simulations. *J. Chem. Phys. Lett.* **10**, 5476–5483 (2019).
61. Takahashi, S. & Watanabe, K. Decoupling from a thermal bath via molecular polariton formation. *J. Phys. Chem. Lett.* **11**, 1349–1356 (2020).
62. Tichauer, R. H., Morozov, D., Sokolovskii, I., Toppari, J. J. & Groenhof, G. Identifying vibrations that control non-adiabatic relaxation of polaritons in strongly coupled molecule-cavity systems. *J. Phys. Chem. Lett.* **13**, 6259–6267 (2022).
63. Kasha, M. Characterization of electronic transitions in complex molecules. *Disc. Farad. Soc.* **9**, 14–19 (1950).
64. Houdré, R., Stanley, R. P. & Ilegems, M. Vacuum-field rabi splitting in the presence of inhomogeneous broadening: resolution of a homogeneous linewidth in an inhomogeneously broadened system. *Phys. Rev. A* **53**, 2711–2715 (1996).
65. Eizner, E., Martínez-Martínez, L. A., Yuen-Shou, J. & Kéna-Cohen, S. Inverting singlet and triplet excited states using strong light-matter coupling. *Sci. Adv.* **5**, aax4482 (2019).
66. Martínez-Martínez, L. A., Eizner, E., Kéna-Cohen, S. & Yuemn-Zhou, K. Triplet harvesting in the polaritonic regime: a variational polaron approach. *J. Chem. Phys.* **151**, 054106 (2019).
67. Pérez-Sánchez, J. B., Koner, A., Stern, N. P. & Yuen-Zhou, J. Simulating molecular polaritons in the collective regime using few-molecule models. *Proc. Natl Acad. Sci. USA.* **120**, e2219223120 (2023).
68. de Jong, M., Seijo, L., Meijerink, A. & Rabouw, F. T. Resolving the ambiguity in the relation between stokes shift and huang-rhys parameter. *Phys. Chem. Chem. Phys.* **17**, 16959–16969 (2015).

69. Grant, R. T. et al. Efficient radiative pumping of polaritons in a strongly coupled microcavity by a fluorescent molecular dye. *Adv. Opt. Mater.* **4**, 1615–1623 (2016).
70. Baieva, S., Hakamaa, O., Groenhof, G., Heikkilä, T. T. & Toppari, J. J. Dynamics of strongly coupled modes between surface plasmon polaritons and photoactive molecules: the effect of the stokes shift. *ACS Photon.* **4**, 28–37 (2017).
71. Lüttgens, J. M., Berger, F. J. & Zaumseil, J. Population of exciton-polaritons via luminescent sp3 defects in single-walled carbon nanotubes. *ACS Photon.* **8**, 182–193 (2021)..
72. Hulkko, E. et al. Effect of molecular stokes shift on polariton dynamics. *J. Chem. Phys.* **154**, 154303 (2021).
73. Tichauer, R. H., Sokolovskii, I. & Groenhof, G. Tuning coherent propagation of organic exciton-polaritons through the cavity q-factor. Adv. Sci. https://onlinelibrary.wiley.com/doi/10.1002/advs.202302650 (2023).
74. Forn-Díaz, P., Lamata, L., Rico, E., Kono, J. & Solano, E. Ultrastrong coupling regimes of light-matter interaction. *Rev. Mod. Phys.* **91**, 025005 (2019).
75. Jaynes, E. T. & Cummings, F. W. Comparison of quantum and semiclassical radiation theories with application to the beam maser. *Proc. IEEE* **51**, 89–109 (1963).
76. Tavis, M. & Cummings, F. W. Approximate solutions for an n-molecule radiation-field Hamiltonian. *Phys. Rev.* **188**, 692–695 (1969).
77. Warshel, A. & Levitt, M. Theoretical studies of enzymatic reactions: dielectric, electrostatic and steric stabilization of carbonium ion in the reaction of lysozyme. *J. Mol. Biol.* **103**, 227–249 (1976).
78. Groenhof, G. Introduction to qm/mm simulations. *Meth. Mol. Biol.* **924**, 12489–12491 (2013).
79. Ditchfield, R., Hehre, W. J. & Pople, J. A. Self-consistent molecular-orbital methods. ix. an extended Gaussian-type basis for molecular-orbital studies of organic molecules. *J. Chem. Phys.* **54**, 724–728 (1971).
80. Jorgensen, W. L., Chandrasekhar, J., Madura, J. D., Impey, R. W. & Klein, M. L. Comparison of simple potential functions for simulatin liquid water. *J. Chem. Phys.* **79**, 926–935 (1983).
81. Duan, Y. et al. A point-charge force field for molecular mechanics simulations of proteins based on condensed-phase quantum mechanical calculations. *J. Comput. Chem.* **24**, 1999–2012 (2003).
82. Verlet, L. Computer “experiments" on classical fluids. i. thermodynamical properties of Lennard-jones molecules. *Phys. Rev.* **159**, 98–103 (1967).
83. Granucci, G., Persico, M. & Toniolo, A. Direct semiclassical simulation of photochemical processes with semiempirical wave functions. *J. Chem. Phys.* **114**, 10608–10615 (2001).
84. Hess, B., Kutzner, C., van der Spoel, D. & Lindahl, E. Gromacs 4: Algorithms for highly efficient, load-balanced, and scalable molecular simulation. *J. Chem. Theory Comput.* **4**, 435–447 (2008).
85. Frisch, M. J. et al. *Gaussiañ6 Revision C.01* (Gaussian Inc., 2016).
86. Schwartz, T. et al. Polariton dynamics under strong light-molecule coupling. *Chem.Phys.Chem* **14**, 125–131 (2013).
87. George, J. et al. Ultra-strong coupling of molecular materials: spectroscopy and dynamics. *Farad. Discuss.* **178**, 281–294 (2015).
88. Wu, F. et al. Optical cavity-mediated exciton dynamics in photosynthetic light harvesting 2 complexes. *Nat. Comm.* **13**, 6864 (2022).
89. Boggio-Pasqua, M., Burmeister, C. F., Robb, M. A. & Groenhof, G. Photochemical reactions in biological systems: probing the effect of the environment by means of hybrid quantum chemistry/molecular mechanics simulations. *Phys. Chem. Chem. Phys.* **14**, 7912–7928 (2012).
90. Sokolovskii, I., Tichauer, R. H., Morozov, D., Feist, J. & Groenhof, G. Multi-scale molecular dynamics simulations of enhanced energy transfer in organic molecules under strong coupling. *IDA—Res. Data Stor.* **11**, 4938–4946 (2023).
91. Sokolovskii, I., Tichauer, R. H., Morozov, D., Feist, J. & Groenhof, G. Multi-scale molecular dynamics simulations of enhanced energy transfer in organic molecules under strong coupling. *GitHub* **156**, 134106 (2023).

Acknowledgements

This work was supported by the Academy of Finland (Grant No. 323996 and 332743 to G.G.), the European Research Council (Grant No. ERC-2016-StG-714870 to J.F.), and by the Spanish Ministry for Science, Innovation, Universities-Agencia Estatal de Investigación (AEI) to J.F. through Grants PID2021-125894NB-I00 and CEX2018-000805-M (through the María de Maeztu program for Units of Excellence in Research and Development). We thank J. Jussi Toppari, A. M. Berghuis, J. Gómez Rivas, T. Schwartz, M. Balusubrahmaniyam and D. Sanvitto for fruitful discussions. We also thank the Center for Scientific Computing (CSC-IT Center for Science) for generous computational resources, and N. Runenberg for his assistance in running the simulations on these resources.

Author contributions

G.G. and J.F. acquired funding; I.S., R.H.T., and G.G. performed the Molecular Dynamics simulations; D.M. performed the Quantum Chemistry calculations; I.S., R.H.T., D.M., J.F., and G.G. performed data analysis; I.S., R.H.T., and G.G. designed the research; I.S., R.H.T., and G.G. wrote the paper, which all authors revised and edited. I.S. and R.H.T. contributed equally to this work. All authors approved the final version of the paper.

Competing interests

The authors declare no competing interests.

Additional information

Supplementary information The online version contains supplementary material available at https://doi.org/10.1038/s41467-023-42067-y.

Correspondence and requests for materials should be addressed to Gerrit Groenhof.

Peer review information *Nature Communications* thanks the anonymous, reviewer(s) for their contribution to the peer review of this work. A peer review file is available.

PII

TUNING THE COHERENT PROPAGATION OF ORGANIC EXCITON-POLARITONS THROUGH THE CAVITY Q-FACTOR

by

R.H. Tichauer, I. Sokolovskii, G. Groenhof

Advanced Science, 10, 2302650, **2023**.

https://doi.org/10.1002/advs.202302650

ADVANCED SCIENCE
Open Access
www.advancedscience.com

Tuning the Coherent Propagation of Organic Exciton-Polaritons through the Cavity Q-factor

Ruth H. Tichauer, Ilia Sokolovskii, and Gerrit Groenhof**

Transport of excitons in organic materials can be enhanced through polariton formation when the interaction strength between these excitons and the confined light modes of an optical resonator exceeds their decay rates. While the polariton lifetime is determined by the Q(uality)-factor of the optical resonator, the polariton group velocity is not. Instead, the latter is solely determined by the polariton dispersion. Yet, experiments suggest that the Q-factor also controls the polariton propagation velocity. To understand this observation, the authors perform molecular dynamics simulations of Rhodamine chromophores strongly coupled to Fabry–Pérot cavities with various Q-factors. The results suggest that propagation in the aforementioned experiments is initially dominated by ballistic motion of upper polariton states at their group velocities, which leads to a rapid expansion of the wavepacket. Cavity decay in combination with non-adiabatic population transfer into dark states, rapidly depletes these bright states, causing the wavepacket to contract. However, because population transfer is reversible, propagation continues, but as a diffusion process, at lower velocity. By controlling the lifetime of bright states, the Q-factor determines the duration of the ballistic phase and the diffusion coefficient in the diffusive regime. Thus, polariton propagation in organic microcavities can be effectively tuned through the Q-factor.

1. Introduction

Achieving long-range energy transfer in organic media is a key requirement for enhancing the efficiency of opto-electronic devices, such as organic diodes or solar cells, in which energy transport is limited by the incoherent diffusion mechanism that governs the motion of Frenkel excitons through materials. Recent experiments suggest that strongly coupling such excitons to the confined, but “delocalized”, modes of an optical resonator (called a cavity in what follows) can enhance transport through hybridization of the molecular excitons with the confined light modes into polaritons.[1–15]

Polaritons are coherent superpositions of molecular and cavity mode excitations that form when the interaction (g) between molecular excitons and cavity modes exceeds their decay rates (κ_{mol} and γ_{cav}, respectively).[16–18] The vast majority of these light–matter hybrid states have a negligible contribution from the cavity mode excitations and are therefore “dark”, forming a manifold of states, distributed around the molecular absorption maximum as illustrated in **Figure 1**b. The fewer remaining states are bright and dispersive owing to their cavity mode contributions. They constitute the upper (UP) and lower polariton (LP) branches, also depicted in Figure 1b, that behave as quasi-particles with low effective mass and large group velocity,[19] defined as the derivative of the polariton energy with respect to k_z-vector ($v_g = \partial\omega/\partial k_z$, Figure 1c). The low effective mass and large group velocity of polaritons can be exploited for controlled and long-ranged *in-plane* energy transport. Indeed, “in-plane” polariton propagation has been observed in a variety of excitonic materials coupled to the confined light modes of Fabry-Pérot cavities,[7,15] Bloch Surface Waves,[5,11,20] Surface Lattice Resonances,[14] and resonances arising from a dielectric constant mismatch between the excitonic medium and the surrounding environment.[12]

While these observations are in line with theoretical predictions,[19,21–24] the propagation velocity observed in these experiments, is significantly lower than the group velocities inferred from the polariton dispersion ($v_g = \partial\omega/\partial k_z$). In previous work,[25] we used multi-scale molecular dynamics (MD) simulations to resolve this discrepancy, and showed that irrespective of the initial excitation conditions, polariton propagation is a diffusion process on long timescales (> 100 fs). This diffusion is due to reversible population transfers between the stationary dark state manifold and the highly mobile bright polariton states, which render the propagation speed much lower than the

R. H. Tichauer
Departamento de Física Teórica de la Materia Condensada and
Condensed Matter Physics Center (IFIMAC)
Universidad Autónoma de Madrid
Madrid E-28049, Spain
E-mail: ruth.tichauer@uam.es
I. Sokolovskii, G. Groenhof
Nanoscience Center and Department of Chemistry
University of Jyväskylä
P.O. Box 35, 40014 Jyväskylä, Finland
E-mail: gerrit.x.groenhof@jyu.fi

The ORCID identification number(s) for the author(s) of this article can be found under https://doi.org/10.1002/advs.202302650

DOI: 10.1002/advs.202302650

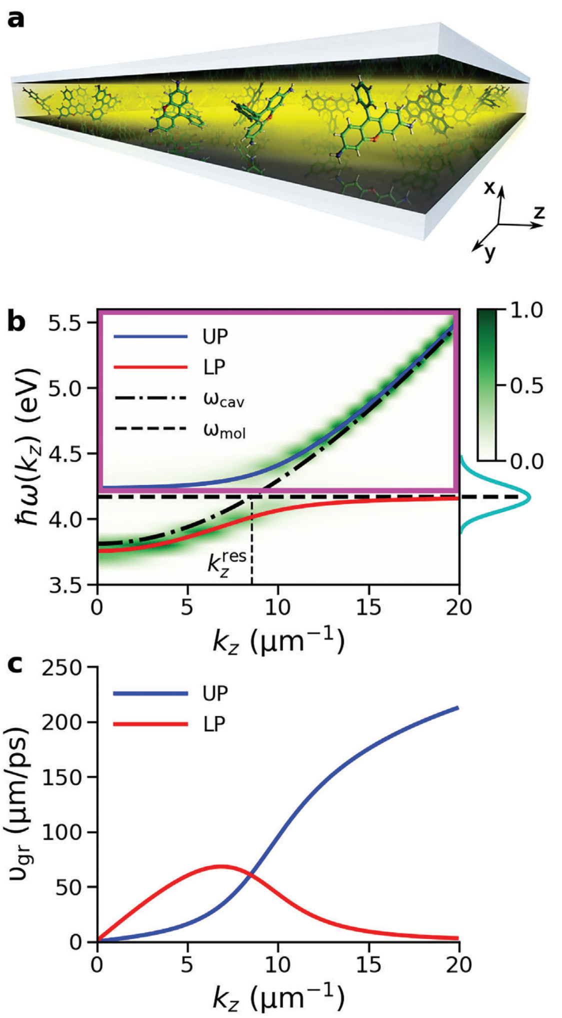

Figure 1. a) Schematic illustration of an optical Fabry-Pérot micro-cavity filled with Rhodamine chromophores (not to scale). b) Normalised angle-resolved absorption spectrum of the cavity, showing Rabi splitting between the lower polariton (LP, red line) and the upper polariton (UP, blue line) branches. The cavity dispersion and absorption maximum of the molecules (4.18 eV at the CIS/3-21G//Amber03 level of theory) are plotted by point-dashed and dashed lines, respectively. The cyan line on the vertical axis depicts the absorption spectrum of Rhodamine. The purple frame encloses the range of polaritonic states excited instantaneously by the broad-band pump pulse. c) Group velocity of the LP (red) and UP (blue), defined as $\partial\omega(k_z)/\partial k_z$.

polariton group velocities.[14,25,26] Nevertheless, even if on longer timescales, propagation is not ballistic, polariton diffusion can significantly outperform exciton diffusion, which is typically limited to a few nanometers in organic materials.[7]

While we observed that cavity loss, caused by photon leakage through imperfect mirrors, reduces the distance over which polaritons propagate, we had not systematically investigated the effect of the cavity mode lifetime, $\tau_{cav} = \gamma_{cav}^{-1}$, which is related to the quality factor (Q-factor) via $Q = \omega_{cav}\tau_{cav}$. The cavity mode lifetime, in combination with the molecular dephasing rate (κ_{mol}), determines how strong the light-matter interaction (g) needs to be for the molecule-cavity system to enter the strong coupling regime (for which various criteria are commonly employed:[18] i) $g \geqslant \gamma_{cav}, \kappa_{mol}$; ii) $g^2 \geqslant (\gamma_{cav} - \kappa_{mol})^2/4$; iii) $g^2 \geq (\gamma_{cav}^2 + \kappa_{mol}^2)/2$; or iv) $g \geqslant (\gamma_{cav} + \kappa_{mol})/2$). Indeed, the Rabi splitting between the LP and UP branches ($\Omega^{Rabi} = 2\sqrt{g^2N - (\gamma_{cav} - \kappa_{mol})^2/4}$, with N the number of molecules collectively coupled to the confined light modes, Figure 1) depends on both γ_{cav} and κ_{mol}. Therefore, as shown in Figure S6 (Supporting Information, SI), the Q-factor influences the Rabi splitting, but only marginally for systems that are well within the strong coupling regime. For such systems, the Q-factor only influences the lifetime of organic polaritons, but not the light-matter coupling strength.[27] Yet, in recent femtosecond transient absorption microscopy (fs-TAM) experiments on BODIPY-R dyes in Fabry-Pérot cavities with varying Q-factors, Pandya et al. observed that the polariton propagation velocity can be enhanced by increasing the cavity Q-factor.[15] As emphasized by the authors, such "unexpected link between the Q-factor and polariton velocity, is not captured by current models of exciton-polaritons".

To address this controversy and determine how the cavity Q-factor influences the propagation of organic polaritons, we performed atomistic MD simulations of Rhodamine chromophores strongly coupled to the confined light modes of one-dimensional (1D) uni-directional Fabry-Pérot cavities[28,29] with three different cavity mode lifetimes: τ_{cav} = 15, 30, and 60 fs. As before, the hydrated Rhodamines were modeled at the hybrid Quantum Mechanics / Molecular Mechanics (QM/MM) level.[30,31] We calculated mean-field semi-classical MD trajectories of 512 molecules, including their solvent environment, strongly coupled to the 160 confined light modes of a red-detuned cavity (370 meV below the excitation energy of Rhodamine, which is 4.18 eV at the CIS/3-21G//Amber03 level of theory employed here, see Computational Details and Supporting Information for details). Because in the fs-TAM measurements of Pandya et al.[15] the 10 fs broadband pump pulses populate mostly UP states, we modeled the initial excitation by preparing a Gaussian wavepacket of UP states centered at $\hbar\omega$= 4.41 eV with a bandwidth of σ = 7.07 μm^{-1}.[19] The energy range of the states excited initially in this superposition is indicated by the magenta box in Figure 1b.

2. Results and Discussion

In **Figure 2**, we show the time evolution of the probability density of the polaritonic wave function ($|\Psi(t)|^2$, Equation 3), after instantaneous excitation of a Gaussian wavepacket of UP states in three Fabry-Pérot microcavities supporting cavity modes with 15, 30, and 60 fs lifetimes, and containing 512 Rhodamine molecules. Animations of the propagation of the total, molecular and photonic wavepackets are provided as Supporting Information.

In all cavities the wavepacket initially broadens due to the wide range of UP group velocities. Around 30 fs, however, the wavepacket splits into (i) a faster component with a short lifetime that depends on the Q-factor, and (ii) a slower component that is long-lived, but almost stationary. While the lifetime of the slower component is hardly affected by the cavity lifetime, its broadening is Q-factor dependent (Figure 2a–f). The long lifetime

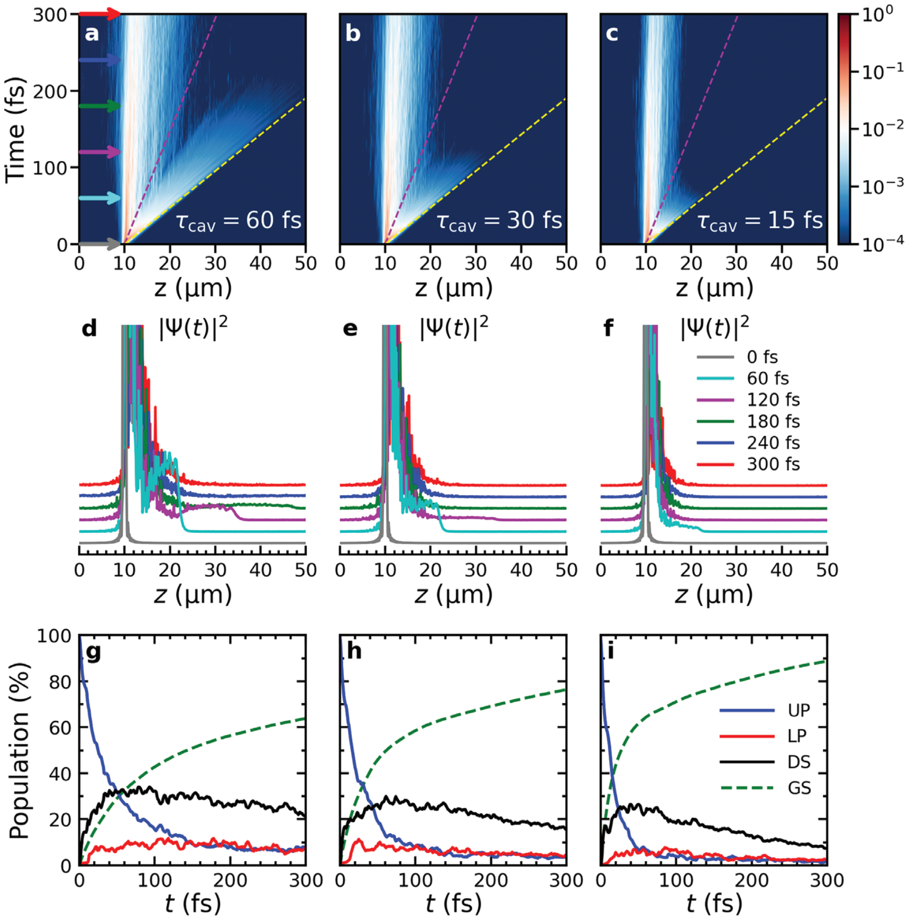

Figure 2. Polariton propagation after resonantly exciting a wavepacket of states in the UP branch centered at z=10 µm. a–c) Probability density of the total wave function, $|\Psi(t)|^2$, as a function of distance (horizontal axis) and time (vertical axis) in cavities with different Q-factors (i.e., $\tau_{\text{cav}} = 60$, 30 and 15 fs, respectively). Colored arrows in panel a correspond to the time points of the 1D projection in panels (d–f). The dashed purple and yellow lines indicate propagation at the maximum group velocity of the LP (68 µm ps^{-1}) and UP (212 µmps^{-1}) branches, respectively. d–f) Probability density of the total polariton wave function, $|\Psi(t)|^2$, at different time points as a function of distance. g–i) Populations of the UP (blue), LP (red), and dark (DS, black) states, as well as of the ground state (GS, green dashed line) as functions of time.

of the slower part suggests that it is composed mostly of dark states that lack group velocity, and into which some population of the initially excited UP states has relaxed. Nevertheless, due to thermally driven population transfer from these dark states back into propagating polaritons,[32] the slower part still propagates. Because this transfer process is reversible and leads to transient occupation of polaritonic states over a wide range of k_z-vectors in both LP and UP branches, propagation occurs in a diffusive manner.[14,25,26]

In contrast, the faster component of the wavepacket is mainly composed of the higher-energy UP states, which have high group velocity. Because the rate at which population transfers from these UP states into the dark state manifold is inversely proportional to the energy gap,[33] the main decay channel for these states is radiative emission through the imperfect cavity mirrors. Thus, the lifetime and hence propagation distance of the faster wavepacket component is Q-factor dependent, which is reflected by a faster rise of ground-state population when the cavity mode lifetime decreases (green dashed lines in Figure 2g–i).

After the rapid initial expansion of the total wavepacket due to the population in the UP states (blue lines in Figure 2g-i), transfer into the dark states (black lines), in combination with irreversible radiative decay from states with the highest group velocity, causes the wavepacket to contract. The extent of this contraction as well as the moment at which it takes place, depends on the cavity mode lifetime, as indicated by both the position, $<z>$, and Mean Squared Displacement (MSD) of the wavepackets in **Figure 3**.

Whereas during the expansion phase propagation is dominated by ballistic motion of fast UP states that reach longer distances for higher Q-factors (or equivalently, higher cavity mode lifetimes τ_{cav}), as indicated by the maximum of the MSD (∽68, 23, and 7 µm^2), after contraction, propagation continues as diffusion which is indicated by the linearity of the MSD at the end of

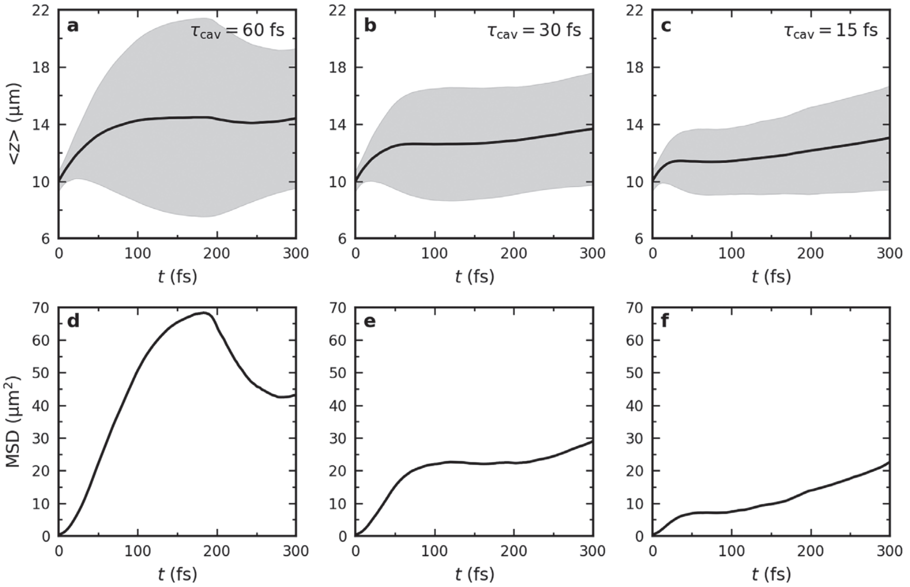

Figure 3. Top panels: Expectation value of the position of the total time-dependent wavefunction $\langle z\rangle = \langle\Psi(t)|\hat{z}(t)|\Psi(t)\rangle/\langle\Psi(t)|\Psi(t)\rangle$ after on-resonant excitation of UP states in cavities with different Q-factors (i.e., $\tau_{\text{cav}} = 60$ (left), 30 (middle) and 15 fs (right). The black lines represent $\langle z\rangle$ while the shaded areas indicate the root mean squared deviation (RMSD, i.e., $\sqrt{\langle(z(t) - \langle z(t)\rangle)^2\rangle}$). Bottom panels: Mean squared displacement (MSD, i.e., $\langle\Psi(t)|(\hat{z}(t) - \hat{z}(0))^2|\Psi(t)\rangle/\langle\Psi(t)|\Psi(t)\rangle$) in the same cavities.

the simulations (Figure 3). Diffusion emerges as a consequence of reversible population transfers between stationary dark states and mobile bright states at all k_z-vectors in both the UP and LP branches.[25] The turnover from ballistic propagation into diffusion is Q-factor dependent and occurs later when the cavity mode lifetime is higher (Figure 3).

While simulations provide detailed mechanistic insights into polariton propagation, direct observation of such details is challenging experimentally, in particular because the multiple contributions to a single transient spectral signal of a molecule-cavity system cannot always be unambiguously disentangled.[34] In their fs-TAM experiments, Pandya et al.[15] monitored the propagation of the wavepacket, $\Psi(z, t)$, by probing transient changes in cavity transmission at a wavelength that is sensitive to LP absorption. As explained in the SI, to mimic such pump-probe conditions in our simulations, we extracted position-dependent transient changes in the transmission from our trajectories as follows:

$$\frac{\Delta T(z,t)}{T_0} = \exp\left(\epsilon_{\text{a}} d|\Psi(z,t)|^2\right) - 1 \tag{1}$$

with $\Delta T(z, t) = T(z, t) - T_0$ the difference between $T(z, t)$, the transmission at position z and time t after excitation, and $T_0 = T(z, 0)$, the transmission before excitation. The variable ε_{a} is the absorption coefficient and d the path length. Because the value of ϵ_{a} cannot be derived directly from MD simulations, we treated it together with d as a single parameter. Here, we used $\epsilon_{\text{a}}d = 0.5$, but, as we show in SI, varying this parameter does not change the results qualitatively. As was done in experiments,[7,15,20] we characterize the propagation of the total wavepacket by the MSD of the transient signal, in our case of the transient transmission ($\Delta T/T_0$, Equation 1):

$$\begin{aligned}\text{MSD}_T &= \sum_i^N \left(z_i - z_0\right)^2 \frac{\Delta T(z,t)}{T_0} \\ &= \sum_i^N \left(z_i - z_0\right)^2 \left[\exp\left(\epsilon_{\text{a}} d|\Psi(z_i,t)|^2\right) - 1\right]\end{aligned} \tag{2}$$

with z_0 the expectation value of the position of the wavepacket at the start of the simulation ($t = 0$) and the sum is over the positions z_i of the $N = 512$ molecules. Full details of this analysis are provided in SI.

In **Figure 4**a, we plot the MSD_T of the transient differential transmission for our cavity systems. As in the experiments (Figure 2c in Pandya et al.[15]), we observe that after a rapid initial increase, the MSD_T of the signal decreases. Based on our simulations we attribute this observation to the fast expansion of the wavepacket followed by the contraction. Because two propagation regimes were observed in our simulations, we analyzed these regimes separately. In contrast, Pandya et al. assumed a single ballistic phase, and extracted the velocity and duration of that phase from a global fit to the full MSD_{T} of the measured $\Delta T/T_0$ signal.

Because in the initial stages of the ballistic regime ($t < \tau_{\text{cav}}$) propagation is dominated by the population in UP states with well-defined dispersion, the propagation speed is independent of the Q-factor and determined solely by the UP group velocity (Figure 1c) in all cavities (Figure S2b in SI). However, the duration of this ballistic regime, τ_{bal}, extracted from the $\Delta T/T_0$ signal

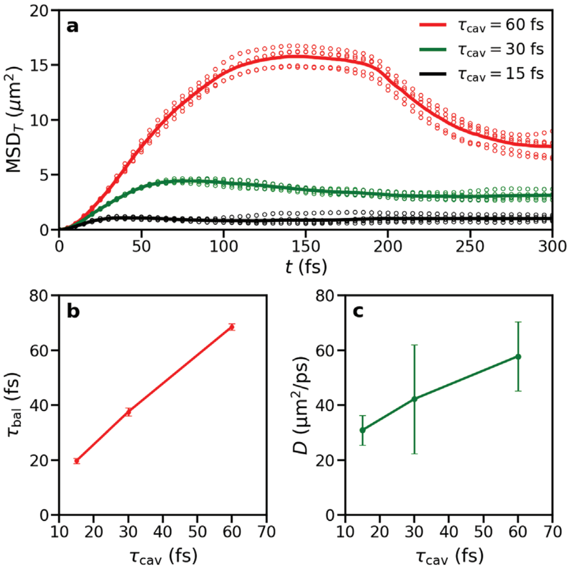

Figure 4. a) Mean squared displacement of the transmission signal (MSD$_T$) for different cavity mode lifetimes: $\tau_{cav} = 60$ (red), 30 (green) and 15~fs (black). Circles represent data points for individual runs, while the curves show the averages over all trajectories (five for each τ_{cav}). b) The duration of the ballistic phase as a function of cavity mode lifetime. c) The diffusion coefficient in the diffusion regime as a function of cavity mode lifetime.

by fitting the same function as Pandya et al. to the initial rise of the MSD$_T$ (SI), depends on the cavity lifetime, and lasts longer if the cavity Q-factor is higher, as shown in Figure 4b. Therefore, as in the MSD plots of the total wavepacket in Figure 3, the MSD$_T$ of the $\Delta T/T_0$ signal also reaches the highest value in the cavity with highest Q-factor (or equivalently, the longest cavity mode lifetime τ_{cav}), in line with the fs-TAM measurements. Because the initial ballistic propagation is dominated by population in the higher energy UP states that, isolated from the dark state manifold, decay through the imperfect cavity mirrors rather than transferring into the dark state manifold due to the inverse scaling of the transfer rate with the energy gap,[33] the start of the wavepacket contraction is related to the duration of the ballistic phase τ_{bal}. Indeed, by varying the center of the wavepacket (SI), and hence the energy gap to the dark states, the time at which contraction occurs can be controlled. According to the function used for fitting the MSD$_T$ data (Equation S28, SI), the maximum of MSD$_T$ occurs at $t = 2\tau_{bal} \approx 2\tau_{cav}$. Therefore, the moment at which contraction of the total wavepacket begins is proportional to the cavity lifetime (Figure 4a).

Whereas in their model Pandya et al. consider only ballistic propagation on a sub-ps timescale, our simulations suggest that also diffusion contributes to propagation on those timescales, when solely the slower part of the wavepacket remains. Therefore, to characterize also this regime, we calculated the diffusion coefficient by fitting the linear regime of the MSD (SI). However, because in the MSD$_T$ of the transient transmission (Figure 4a), the linear regime is difficult to discern, we performed the linear fit to the MSD associated with the slower component of the wavepacket at the end of the trajectories (Figure S5, SI). In Figure 4c, we plot the diffusion coefficients as a function of cavity mode lifetime. Because the overall diffusion process is a sequence of ballistic propagation phases, interrupted by stationary phases, and the duration of the ballistic phases is determined by non-adiabatic coupling, which sets the rate for reversible population transfer into the dark state manifold, in combination with cavity decay, which sets the rate for irreversible loss via the imperfect cavity mirrors, the diffusion coefficient depends on the Q-factor and increases with cavity lifetime (Figure 4c).

Because in our simulations we cannot couple as many molecules to the cavity as in experiment (i.e., 10^5–10^8 molecules[35–37]), we overestimate the diffusion coefficient. As we could show previously,[33] the rate of population transfer from dark to bright states is inversely proportional to N, whereas the rate in the opposite direction is independent of N. Therefore, the population in the bright propagating states is overestimated when only 512 molecules are coupled to the cavity, leading to a faster diffusion. The overestimation of the diffusion coefficient thus leads to a much more pronounced increase of the wavepacket MSD than in experiment, where the total population residing in the propagating states is significantly lower,[20] and diffusion would be hardly observable on sub-ps timescales. Nevertheless, despite these quantitative differences, our simulations provide a qualitative picture that is in line with experimental observations.[15]

The results of our simulations suggest that the cavity lifetime controls both the duration and length of the initial ballistic phase (Figure 4b) as well as the diffusion constant in the diffusive regime (Figure 4c). Thus, without affecting polariton group velocity, the cavity Q-factor provides an effective means to tune energy transport in the strong coupling regime. Our results therefore provide a rationale for the link between the Q-factor and the propagation velocity, reported by Pandya et al., that is based on a current model of exciton-polaritons.[29,38]

Because our model combines established approaches from Quantum Optics, Quantum Chemistry and Molecular Dynamics,[29,38] our explanation does not rely on additional assumptions beyond the approximations underlying those approaches. Our explanation for the observations of Pandya et al. is, however, quite different from theirs,[15] who, by making the additional assumption that the overlap between the molecular absorption spectrum and the cavity line width, determines which molecules can couple to the cavity, proposed that increasing the cavity Q-factor reduces the energetic disorder and thereby increases the delocalization of dark states.[15] Because the rate of population transfer between the dark state manifold and the polaritonic states depends on wave function overlap,[33] increasing the delocalization in the dark states is speculated to enhance the thermal population exchange with bright states,[32] thereby regenerating the highly propagating polariton states. However, the assumption that the cavity line-width determines which molecules couple seems to contrast previous findings that "Rabi splitting occurs from a collective contribution of the whole inhomogeneous band of electronic state and not from a sharp selection of the state exactly resonant with the photon mode".[35] Nevertheless, although our explanation requires fewer assumptions, additional fs-TAM experiments, in which temperature and dye concentration are varied to control the heterogeneous absorption line width and non-adiabatic coupling, are urgently needed to test the validity of both explanations. As the duration of the ballistic phase depend on cavity lifetime, increasing Q-factor would reduce the time and spacial resolution required for observing the contraction and the transition into the diffusion regime upon resonantly pumping a wavepacket of well-isolated UP states, and thus facilitate these new experiments. Moreover, as additional sets of simulations, in which we i) varied the exciton-photon detuning of the fundamental cavity mode at $k_z = 0$ by 100 meV, and ii) used narrow-band pulses to instantaneously excite wavepackets of UP states centered at different k_z vectors (SI), suggest, the duration of the ballistic phase and hence the moment at which the transition and contraction occur, are not very sensitive to such energy detuning of the cavity, but can be controlled by varying the energy and spectral range of the excitation pulse.

3. Computational Details

We performed mean-field semi-classical[39] MD simulations of 512 Rhodamine chromophores with their solvent environment, strongly coupled to 1D Fabry-Pérot cavities with different radiative lifetimes: $\tau_{\text{cav}} = 15$ fs, 30 fs, and 60 fs. To model the interactions between the molecules and the confined light modes of the cavity, we used a Tavis-Cummings Hamiltonian, in which the molecular degrees of freedom are included.[29,38] A brief description of our multi-scale cavity MD approach is provided as Supporting Information.

In our simulations the Rhodamine molecules were modelled at the QM/MM level, with the QM region containing the fused ring system of the molecule (Figure S2, Supporting Information). The ground-state electronic structure of the QM subsystem was described at the restricted Hartree-Fock (HF) method in combination with the 3-21G basis set,[40] while the excited-state electronic structure was modeled with Configuration Interaction, truncated at single electron excitations (CIS/3-21G). The MM region, which contains the rest of the chromophore as well as the solvent (3684 water molecules), was modeled with the Amber03 force field[41] in combination with the TIP3P water model.[42] At this level of QM/MM theory, the excitation energy of the Rhodamine molecules is 4.18 eV.[38] In previous work, we showed that despite the overestimation of the vertical excitation energy, the topology of the potential energy surfaces is not very sensitive to the level of theory for Rhodamine.[32]

The uni-directional 1D cavity with a length of $L_z = 50$ µm, with z indicating the in-plane direction ($L_x = 163$ nm is the distance between the mirrors and x thus indicates the out-of-plane direction, see Figure S1 in the SI), was red-detuned by 370 meV with respect to the molecular excitation energy (4.18 eV at the CIS/3-21G//Amber03 level of theory, dashed line in Figure 1b), such that at wave vector $k_z = 0$, the cavity resonance is $\hbar\omega_0 = 3.81$ eV. The cavity dispersion, $\omega_{\text{cav}}(k_z) = \sqrt{\omega_0^2 + c^2k_z^2/n^2}$, was modelled with 160 modes ($0 \leqslant p \leqslant 159$ for $k_z = 2\pi p/L_z$), with c the speed of light and n the refractive index. Here, we used $n = 1$. See Supporting Information for further details on the cavity model.

The Rhodamine molecules were placed with equal intermolecular distances on the z-axis of the cavity. To maximize the collective light-matter coupling strength, the transition dipole moments of the Rhodamine molecules were aligned to the vacuum field at the start of the simulation. The same starting coordinates were used for all Rhodamines, but different initial velocities were selected randomly from a Maxwell–Boltzmann distribution at 300 K.

With a cavity vacuum field strength of 0.36 MV cm^{-1} (0.0000707 au), the Rabi splitting, defined as the energy difference between the bright lower (LP) and upper polariton (UP) branches at the wave-vector k_z^{res} where the cavity dispersion matches the molecular excitation energy (Figure 1b), is ∽325 meV for all cavities ($\tau_{\text{cav}} = 15$ fs, 30 fs, and 60 fs). While the choice for a 1D cavity model with only positive k_z vectors was motivated by the necessity to keep our simulations computationally tractable, it precludes the observation of elastic scattering events that would change the direction (i.e., in-plane momentum, $\hbar\mathbf{k}$) of propagation. Furthermore, with only positive k_z vectors, polariton motion is restricted to the $+z$ direction, but we could show previously[25] that this assumption does not affect the mechanism of the propagation process.

Ehrenfest MD trajectories were computed by numerically integrating Newton's equations of motion using a leap-frog algorithm with a 0.1 fs timestep. The multi-mode Tavis-Cummings Hamiltonian (See Supporting Information) was diagonalized at each timestep to obtain the $N + n_{\text{mode}}$ (adiabatic) polaritonic eigenstates $|\psi^m>$ and energies E^m. The total polaritonic wavefunction $|\Psi(t)>$ was coherently propagated along with the classical degrees of freedom of the N molecules as a time-dependent superposition of the $N + n_{\text{mode}}$ time-independent adiabatic polaritonic states:

$$|\Psi(t)\rangle = \sum_{m}^{N+n_{\text{mode}}} c_m(t)|\psi^m\rangle \tag{3}$$

where $c_m(t)$ are the time-dependent expansion coefficients of the time-independent polaritonic eigenstates $|\psi^m>$ (SI). A unitary propagator in the *local* diabatic basis was used to integrate these coefficients,[43] while the nuclear degrees of freedom of the N molecules evolve on the mean-field potential energy surface. Results reported in this work were obtained as averages over five trajectories for each cavity lifetime. For all simulations we used Gromacs 4.5.3,[44] in which the multi-mode Tavis-Cummings QM/MM model was implemented,[29] in combination with Gaussian16.[45] Further details of the simulations are provided in the Supporting Information.

4. Conclusion

To summarize, we have investigated the effect of the cavity Q-factor on polariton propagation by means of atomistic MD simulations. The results of our simulations suggest that after the initial ballistic expansion, the wavepacket contracts due to irreversible radiative decay of population from states with the highest group velocities. In line with experiments, we find that the Q-factor determines the propagation velocity and distance of organic polaritons via their lifetimes without affecting group velocities. Our findings therefore resolve the unexpected correlation between Q-factor and propagation velocity reported by Pandya et al.[15] Our results furthermore underscore that to understand the mechanism of polariton propagation and interpret experiments, it is necessary to include: i) atomic details for the material; ii) multiple modes for cavity dispersion; iii) cavity decay; and iv) sufficiently many molecules to have dark states providing an exciton reservoir. In particular, treating the molecular degrees of freedom of many molecules is essential for observing wavepacket contraction that is caused by cavity loss in combination with reversible non-adiabatic population transfer between propagating bright states and the stationary long-lived dark state manifold. Our work suggests that an ab initio description of molecules in multi-mode cavities could pave the way to systematically design or optimize polariton-based devices for enhanced energy transport.

Supporting Information

Supporting Information is available from the Wiley Online Library or from the author.

Acknowledgements

R.H.T. and I.S. contributed equally to this work. The authors thank Dmitry Morozov for his help during the project and Johannes Feist for insightful discussions. R.H.T. thanks Jacopo Fregoni and I.S. and G.G. thank Pavel Buslaev and Jussi Toppari for valuable discussions. We also thank CSC-IT center for scientific computing in Espoo, Finland, for very generous computational resources, and for assistance in running the simulations. This work was supported by the Academy of Finland (Grant 323996), the European Research Council (Grant No. ERC-2016-StG-714870 to Johannes Feist), and by the Spanish Ministry for Science, Innovation, Universities-Agencia Estatal de Investigación (AEI) through Grants (PID2021-125894NB-I00 and CEX2018-000805-M (through the María de Maeztu program for Units of Excellence in Research and Development).

Conflict of Interest

The authors declare no conflict of interest.

Data Availability Statement

The data that support the findings of this study are available from the corresponding author upon reasonable request.

Keywords

excitation energy transfer, Fabry–Pérot cavity, molecular dynamics, polariton, strong light–matter coupling

Received: April 25, 2023
Revised: August 22, 2023
Published online:

---

[1] T. Freixanet, B. Sermage, A. Tiberj, R. Planel, *Phys. Rev. B* **2000**, *61*, 7233.
[2] D. M. Coles, N. Somaschi, P. Michetti, C. Clark, P. G. Lagoudakis, P. G. Savvidis, D. G. Lidzey, *Nat. Mater.* **2014**, *13*, 712.
[3] X. Zhong, T. Chervy, S. Wang, J. George, A. Thomas, J. A. Hutchison, E. Devaux, C. Genet, T. W. Ebbesen, *Angew. Chem. Int. Ed.* **2016**, *55*, 6202.
[4] X. Zhong, T. Chervy, L. Zhang, A. Thomas, J. George, C. Genet, J. A. Hutchison, T. W. Ebbesen, *Angew. Chem. Int. Ed.* **2017**, *56*, 9034.
[5] G. Lerario, D. Ballarini, A. Fieramosca, A. Cannavale, A. Genco, F. Mangione, S. Gambino, L. Dominici, M. D. Giorgi, G. Gigli, D. Sanvitto, *Light Sci. Appl.* **2017**, *6*, e16212.
[6] D. M. Myers, S. Mukherjee, J. Beaumariage, D. W. Snoke, *Phys. Rev. B* **2018**, *98*, 235302.
[7] G. G. Rozenman, K. Akulov, A. Golombek, T. Schwartz, *ACS Photonics* **2018**, *5*, 105.
[8] Y. Zakharko, M. Rother, A. Graf, B. Hähnlein, M. Brohmann, J. Pezoldt, J. Zaumseil, *Nano Lett.* **2018**, *18*, 4927.
[9] K. Georgiou, P. Michetti, L. Gai, M. Cavazzini, Z. Shen, D. G. Lidzey, *ACS Photonics* **2018**, *5*, 258.
[10] B. Xiang, R. F. Ribeiro, M. Du, L. Chen, Z. Yang, J. Wang, J. Yuen-Zhou, W. Xiong, *Science* **2020**, *368*, 665.
[11] S. Hou, M. Khatoniar, K. Ding, Y. Qu, A. Napolov, V. M. Menon, S. R. Forrest, *Adv. Mater.* **2020**, *32*, 2002127.
[12] R. Pandya, R. Y. S. Chen, Q. Gu, J. Sung, C. Schnedermann, O. S. Ojambati, R. Chikkaraddy, J. Gorman, G. Jacucci, O. D. Onelli, T. Willhammar, D. N. Johnstone, S. M. Collins, P. A. Midgley, F. Auras, T. Baikie, R. Jayaprakash, F. Mathevet, R. Soucek, M. Du, A. M. Alvertis, A. Ashoka, S. Vignolini, D. G. Lidzey, J. J. Baumberg, R. H. Friend, T. Barisien, L. Legrand, A. W. Chin, J. Yuen-Zhou, et al., *Nat. Commun.* **2021**, *12*, 6519.
[13] K. Georgiou, R. Jayaprakash, A. Othonos, D. G. Lidzey, *Angew. Chem. Int. Ed.* **2021**, *60*, 16661.
[14] M. A. Berghuis, R. H. Tichauer, L. de Jong, I. Sokolovskii, P. Bai, M. Ramezani, S. Murai, G. Groenhof, J. G. Rivas, *ACS Photonics* **2022**, *9*, 123.
[15] R. Pandya, A. Ashoka, K. Georgiou, J. Sung, R. Jayaprakash, S. Renken, L. Gai, Z. Shen, A. Rao, A. J. Musser, *Adv. Sci.* **2022**, 2105569.
[16] P. Törmä, W. L. Barnes, *Rep. Prog. Phys.* **2015**, *78*, 013901.
[17] P. Forn-Díaz, L. Lamata, E. Rico, J. Kono, E. Solano, *Rev. Mod. Phys.* **2019**, *91*, 025005.
[18] M. S. Rider, W. L. Barnes, *Contemp. Phys.* **2022**, *62*, 217.
[19] V. Agranovich, Y. Gartstein, *Phys. Rev. B* **2007**, *75*, 075302.
[20] M. Balasubrahmaniyam, A. Simkovich, A. Golombek, G. Ankonina, T. Schwartz, *Nat. Mater.* **2023**, *22*, 338.
[21] P. Michetti, G. C. La Rocca, *Phys. Rev. B* **2008**, *77*, 195301.
[22] M. Litinskaya, *Phys. Lett. A* **2008**, *372*, 3898.
[23] T. F. Allard, G. Weick, *Phys. Rev. B* **2022**, *106*, 245424.
[24] G. Engelhardt, J. Cao, *Phys. Rev. B* **2022**, *105*, 064205.
[25] I. Sokolovskii, R. H. Tichauer, D. Morozov, J. Feist, G. Groenhof, *arXiv* **2022**, 2209.07309.
[26] D. Xu, A. Mandal, J. M. Baxter, S.-W. Cheng, I. Lee, H. Su, S. Liu, D. R. Reichman, M. Delor, *Nat. Commun.* **2023**, *14*, 3881.
[27] L. Tropf, C. P. Dietrich, S. Herbst, A. L. Kanibolotsky, P. J. Skabara, F. Würthner, I. D. W. Samuel, M. C. Gather, S. Hoefling, *Appl. Phys. Lett.* **2017**, *110*, 153302.
[28] P. Michetti, G. C. L. Rocca, *Phys. Rev. B.* **2005**, *71*, 115320.
[29] R. Tichauer, J. Feist, G. Groenhof, *J. Chem. Phys* **2021**, *154*, 104112.
[30] A. Warshel, M. Levitt, *J. Mol. Biol.* **1976**, *103*, 227.
[31] M. Boggio-Pasqua, C. F. Burmeister, M. A. Robb, G. Groenhof, *Phys. Chem. Chem. Phys.* **2012**, *14*, 7912.
[32] G. Groenhof, C. Climent, J. Feist, D. Morozov, J. J. Toppari, *J. Chem. Phys. Lett.* **2019**, *10*, 5476.
[33] R. H. Tichauer, D. Morozov, I. Sokolovskii, J. J. Toppari, G. Groenhof, *J. Phys. Chem. Lett.* **2022**, *13*, 6259.
[34] S. Renken, R. Pandya, K. Georgiou, R. Jayaprakash, L. Gai, Z. Shen, D. G. Lidzey, A. Rao, A. J. Musser, *J. Chem. Phys.* **2021**, *155*, 154701.
[35] R. Houdré, R. P. Stanley, M. Ilegems, *Phys. Rev. A* **1996**, *53*, 2711.

[36] E. Eizner, L. A. Martínez-Martínez, J. Yuen-Shou, S. Kéna-Cohen, *Sci. Adv.* **2019**, *5*, eaax4484.

[37] L. A. Martínez-Martínez, E. Eizner, S. Kéna-Cohen, J. Yuen-Zhou, *J. Chem. Phys.* **2019**, *151*, 054106.

[38] H.-L. Luk, J. Feist, J. J. Toppari, G. Groenhof, *J. Chem. Theory Comput.* **2017**, *13*, 4324.

[39] P. Ehrenfest, *Z. Phys.* **1927**, *45*, 445.

[40] R. Ditchfield, W. J. Hehre, J. A. Pople, *J. Chem. Phys.* **1971**, *54*, 724.

[41] Y. Duan, C. Wu, S. Chowdhury, M. C. Lee, G. M. Xiong, W. Zhang, R. Yang, P. Cieplak, R. Luo, T. Lee, J. Caldwell, J. M. Wang, P. Kollman, *J. Comput. Chem.* **2003**, *24*, 1999.

[42] W. L. Jorgensen, J. Chandrasekhar, J. D. Madura, R. W. Impey, M. L. Klein, *J. Chem. Phys.* **1983**, *79*, 926.

[43] G. Granucci, M. Persico, A. Toniolo, *J. Chem. Phys.* **2001**, *114*, 10608.

[44] B. Hess, C. Kutzner, D. van der Spoel, E. Lindahl, *J. Chem. Theory Comput.* **2008**, *4*, 435.

[45] M. J. Frisch, G. W. Trucks, H. B. Schlegel, G. E. Scuseria, M. A. Robb, J. R. Cheeseman, G. Scalmani, V. Barone, G. A. Petersson, H. Nakatsuji, X. Li, M. Caricato, A. V. Marenich, J. Bloino, B. G. Janesko, R. Gomperts, B. Mennucci, H. P. Hratchian, J. V. Ortiz, A. F. Izmaylov, J. L. Sonnenberg, D. Williams-Young, F. Ding, F. Lipparini, F. Egidi, J. Goings, B. Peng, A. Petrone, T. Henderson, D. Ranasinghe, et al., *Gaussian 16 Revision C.01*, Gaussian Inc., Wallingford CT **2016**.

PIII

CONTROLLING EXCITON PROPAGATION IN ORGANIC CRYSTALS THROUGH STRONG COUPLING TO PLASMONIC NANOPARTICLE ARRAYS

by

A.M. Berghuis, R.H. Tichauer, L.M.A. de Jong, I. Sokolovskii, P. Bai, M. Ramezani, S. Murai, G. Groenhof, J. Gomez Rivas

ACS Photonics, 9, 2263 – 2272, **2022**.

https://doi.org/10.1021/acsphotonics.2c00007

ACS Photonics

pubs.acs.org/journal/apchd5 Article

Controlling Exciton Propagation in Organic Crystals through Strong Coupling to Plasmonic Nanoparticle Arrays

Anton Matthijs Berghuis,* Ruth H. Tichauer, Lianne M. A. de Jong, Ilia Sokolovskii, Ping Bai, Mohammad Ramezani, Shunsuke Murai, Gerrit Groenhof,* and Jaime Gómez Rivas*

Cite This: https://doi.org/10.1021/acsphotonics.2c00007 Read Online

ACCESS | Metrics & More | Article Recommendations | Supporting Information

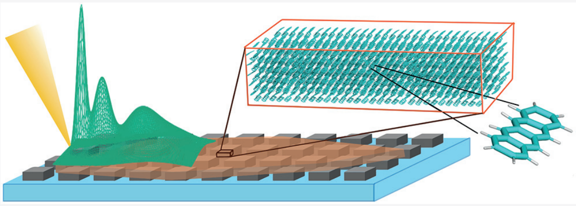

ABSTRACT: Exciton transport in most organic materials is based on an incoherent hopping process between neighboring molecules. This process is very slow, setting a limit to the performance of organic optoelectronic devices. In this Article, we overcome the incoherent exciton transport by strongly coupling localized singlet excitations in a tetracene crystal to confined light modes in an array of plasmonic nanoparticles. We image the transport of the resulting exciton−polaritons in Fourier space at various distances from the excitation to directly probe their propagation length as a function of the exciton to photon fraction. Exciton−polaritons with an exciton fraction of 50% show a propagation length of 4.4 μm, which is an increase by 2 orders of magnitude compared to the singlet exciton diffusion length. This remarkable increase has been qualitatively confirmed with both finite-difference time-domain simulations and atomistic multiscale molecular dynamics simulations. Furthermore, we observe that the propagation length is modified when the dipole moment of the exciton transition is either parallel or perpendicular to the cavity field, which opens a new avenue for controlling the anisotropy of the exciton flow in organic crystals. The enhanced exciton−polariton transport reported here may contribute to the development of organic devices with lower recombination losses and improved performance.

KEYWORDS: *strong light−matter coupling, polariton transport, molecular dynamics simulations, tetracene, plasmonics, nanoparticle array*

INTRODUCTION

Energy transport is a crucial process in organic optoelectronic devices, such as organic photovoltaics (OPV) or organic light-emitting diodes (OLEDs). Because excitons in organic semiconductors (Frenkel excitons) have large binding energies and are predominantly localized onto single molecules, exciton transport proceeds via incoherent hopping. This hopping process is hampered by thermal and structural disorder, which limits exciton diffusion lengths to values below 10 nm for most materials.[1]

Even in organic crystals with suppressed structural disorder, such as tetracene (Tc), the singlet exciton diffusion length is on the order of 50 nm only,[2] though it can be increased by an order of magnitude through dark triplet states.[3] The short diffusion lengths represent a bottleneck for the development of optoelectronic devices as they require complex morphologies of active layers in nanometer sized domains, for example, bulk heterojunctions in OPV, which not only complicate the fabrication, but also reduce device stability.[4,5]

To overcome limitations related to short exciton diffusion lengths in organic materials and increase the distance over which energy can be transported, it has been proposed to strongly couple Frenkel excitons to the confined light modes of an optical cavity.[6,7] In this light−matter interaction regime, excitons and optical modes hybridize into new light−matter states, called polaritons.[8−10] Being coherent superpositions of material excitations and confined photons, polaritons not only have a very small effective mass but also possess group velocity, which can be exploited to transfer polaritonic wavepackets over long distances. Indeed, in an early study from 2000, inorganic exciton polaritons displayed ballistic propagation within an InGaAs quantum well placed inside an optical microcavity.[11] Later, long-range exciton polariton propagation was also experimentally demonstrated for organic media where excitons were coupled to Bloch surface waves[12,13] and for plasmonic nanoparticle arrays coupled to excitons in carbon nanotubes.[14] A much smaller enhancement of the transport length was achieved for Frenkel excitons strongly coupled to confined light modes of an optical microcavity[15] and for polaritons in cavity-free systems,[16] where the polaritons transport mechanism appeared to be (partially) diffusive. The reason for the

Received: January 3, 2022

different behavior of polaritons is not clear as a description of the underlying processes on the molecular/excitonic level is missing, leaving the polariton-enhanced transport mechanism open for interpretation.

In this Article, we demonstrate improved exciton−polariton transport via strong coupling of excitons in tetracene (Tc) to surface lattice resonances (SLRs) in open cavities formed by nanoparticle arrays. We also employ multiscale Molecular Dynamics (MD) simulations to unravel the properties of the propagating polaritons.

SLRs are optical modes in nanoparticle arrays that arise from the interaction of the localized surface plasmon resonances and the in-plane diffractive orders. SLRs have controllable dispersion, enabling the engineering of long-range transport of excitations.[17−24] Moreover, owing to the open architecture of plasmonic lattices, SLRs are easy to integrate with organic semiconductors.[25,26] We selected Tc crystals as the excitonic material because of its intrinsic long exciton diffusion length and promising properties in upconversion photovoltaics.[27−29]

We achieve strong coupling by aligning the transition dipole moment of Tc excitons, oriented along one of the axes of the crystal, to the SLR field and investigate the propagation of the coupled exciton−polaritons. We observe that polariton transport depends strongly on the relative orientation between the transition dipole moment of Tc and the SLR field, demonstrating selective transport defined by the nanoparticle array. Experimental observations are reproduced by atomistic multiscale MD simulations, providing further support that also the excitonic component of polaritons propagates over long distances. We find that the propagation length of Tc singlet excitons coupled to SLR modes is 2 orders of magnitude larger than the diffusion length of singlet excitons for exciton−polaritons with an exciton fraction of 50%. This remarkable enhancement and the possibility to control it by the relative orientation between the crystal and the nanoparticle array opens new opportunities for controlling exciton flows in organic devices.

RESULTS AND DISCUSSION

Cavity Design. We have designed a cavity of silver nanoparticles with a lattice constant of 240 × 360 nm^2 and a particle size of 42 × 100 nm^2 (see Supporting Information (SI) Figure S1). The individual nanoparticles support localized surface plasmon resonances (LSPRs) with a fundamental energy of ≃2.7 eV for a polarization along the short axis (see SI, Figure S1). These localized resonances couple to the in-plane diffraction orders, resulting in transverse electric (TE) and transverse magnetic (TM) surface lattice resonances. In this manuscript we investigate SLRs corresponding to the first diffraction order along the y-direction (i.e., the (0,−1) and (0, +1) orders), corresponding to a period of 360 nm (see Figure 1; see SI, S1 for a description of the terminology). We focus on the TE mode, as this mode has a larger group velocity than the TM mode, especially at low k-vectors.

Propagation and Dispersion Characterization. A saturated solution of tetracene (99.99% Sigma-Aldrich) in toluene was dropcasted on the nanoparticle array, resulting in the growth of thin crystals (50−200 nm) with relatively large lateral dimensions (up to 500 μm), as described in refs 30 and 31. Then, a small region of the Tc crystal, placed on top of the cavity, was excited by a focused laser beam (λ = 450 nm). We measured the emitted light from the coupled system with a confocal microscope (Nikon Ti-Eclipse with 100x 0.9 NA objective lens). The fwhm of the detected laser spot is approximately 900 nm, which after deconvolution with the point spread function of our system ∼400 nm, comes down to a spot size of ∼800 nm. When the transition dipole moment in Tc is oriented orthogonal to the cavity field, we observe negligible propagation, as shown in Figure 1a. However, propagation over several micrometers is observed when the crystal is rotated such that the dipole moment is aligned to the field associated with the SLR defining the cavity (Figure 1b). The slight asymmetry of the observed propagation is due to a few degrees misalignment between the cavity field and the dipoles of Tc excitons.

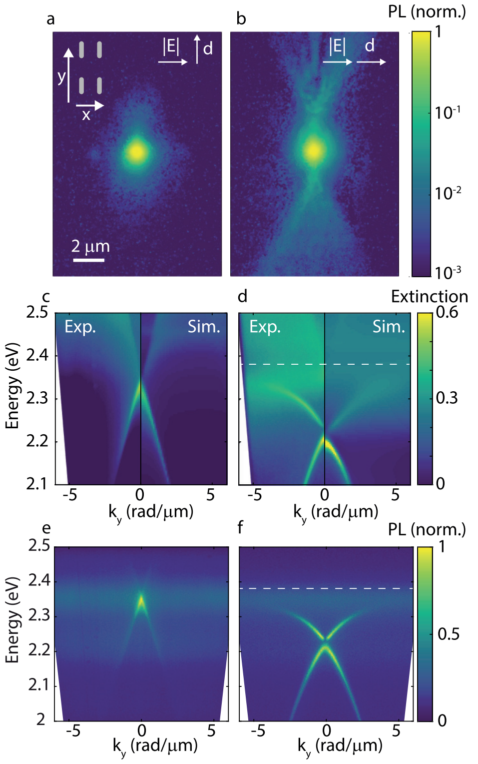

Figure 1. Fluorescence images following a focused laser excitation of a Tc crystal placed on top of the plasmonic cavity (a and b), with the $S_0 \rightarrow S_1$ transition dipole moment in Tc oriented perpendicular (weak coupling regime) (a), and parallel (strong coupling regime) (b) to the SLR field. Dispersion of the extinction along the propagation direction (k_y) of the weakly (c) and strongly (d) coupled system. The left panel of each figure displays the experimental data, while the right panels are results from the FDTD simulations. Emission for the weakly (e) and strongly (f) coupled system. Strong coupling is evidenced in (d) and (f) by the bending of the exciton−polariton band away from the exciton energy at 2.38 eV.

To investigate the propagation of exciton-polaritons in more detail, we have measured their dispersion by retrieving the angle-resolved extinction and emission spectra using Fourier microscopy. When the SLR field and the dipole moment are orthogonal, the dispersion of the TE mode is very similar to that of the nanoparticle array defining the bare cavity (see SI, Figure S1), that is, for energies much lower than the LSPR (∼2.7 eV), the dispersion appears as straight lines, as described by the grating equation (left panel of Figure 1c). This indicates that there is no strong coupling between the SLR cavity mode

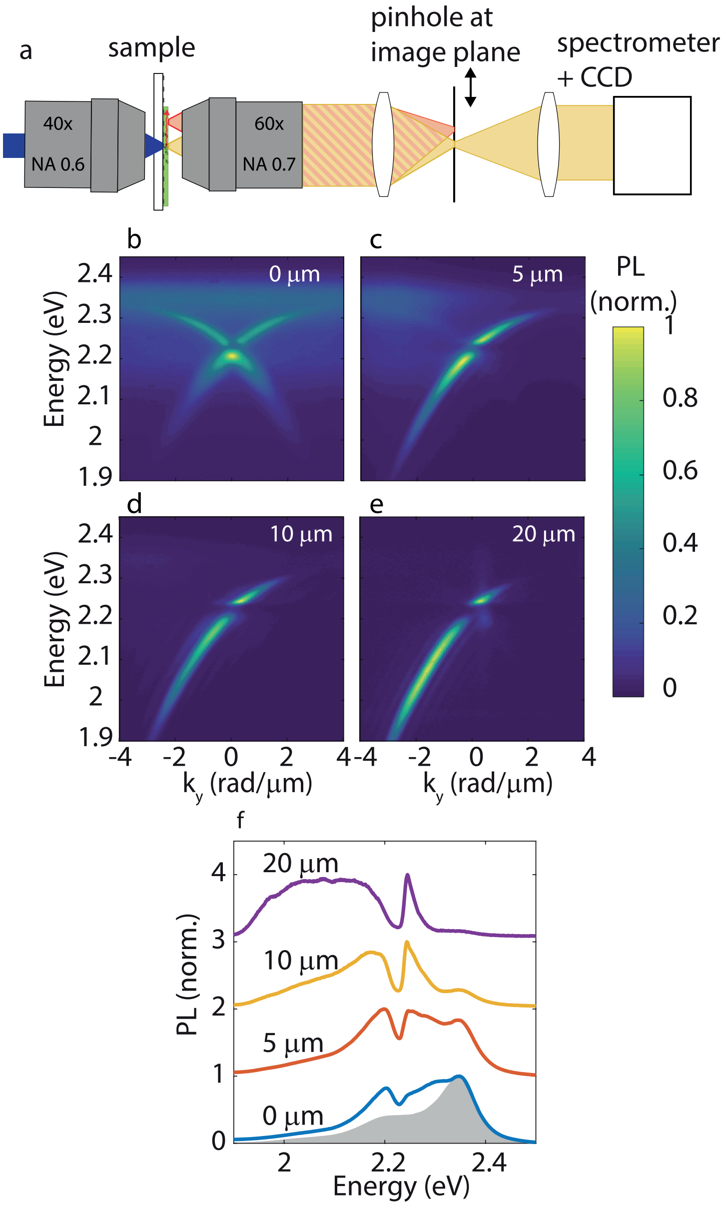

Figure 2. Schematic representation of the experiment (a). The strongly coupled Tc crystal is excited at position $y = 0$. The fluorescence is detected by selecting the emission from a small area ($d = 6.7$ μm) at a certain distance from the excitation spot by changing the position of a pinhole in an intermediate imaging plane. The back focal plane is mapped on the slit of a spectrometer that measures light with $k_x = 0$ via a grating on a CCD. Emission measured at different distances (0, 5, 10, and 20 μm) away from the excitation spot (b−e). Emission integrated over k_y for the four previous distances from the excitation spot (f). The gray shaded area corresponds to emission from uncoupled molecules.

and the Tc exciton resonance. We compare the experimental results with a finite-difference time-domain (FDTD) simulation of the nanoparticle array covered with a 140 nm thick Tc crystal for which we use the dielectric tensor, as measured by Tavazzi et al.[32] (SI, Figure S3). The simulated dispersion, plotted on the right panel of Figure 1c for positive in-plane momentum k_y, shows an excellent agreement with the experimental data (note that due to the 180° rotational symmetry, the system is invariant under reflection over $k_y = 0$).

When the dipole moment of Tc excitons and the cavity field are oriented parallel, there is a clear bending of the mode away from the exciton transition energy at 2.38 eV, indicating the formation of exciton−polariton states and strong light−matter coupling (left panel of Figure 1d). The experimental results are verified by FDTD simulations, as plotted in the right panel of Figure 1d. An interesting feature in these plots is the gap in the dispersion at $k_y = 0$, where the (0,+1) and (0,−1) TE modes cross. This splitting corresponds to symmetric (bright) and antisymmetric (dark) field distributions of the modes.[26,33] At this crossing point, the group velocity of the modes is much lower, which leads to a reduced propagation length, as we will show later. The dispersion measurements and simulations

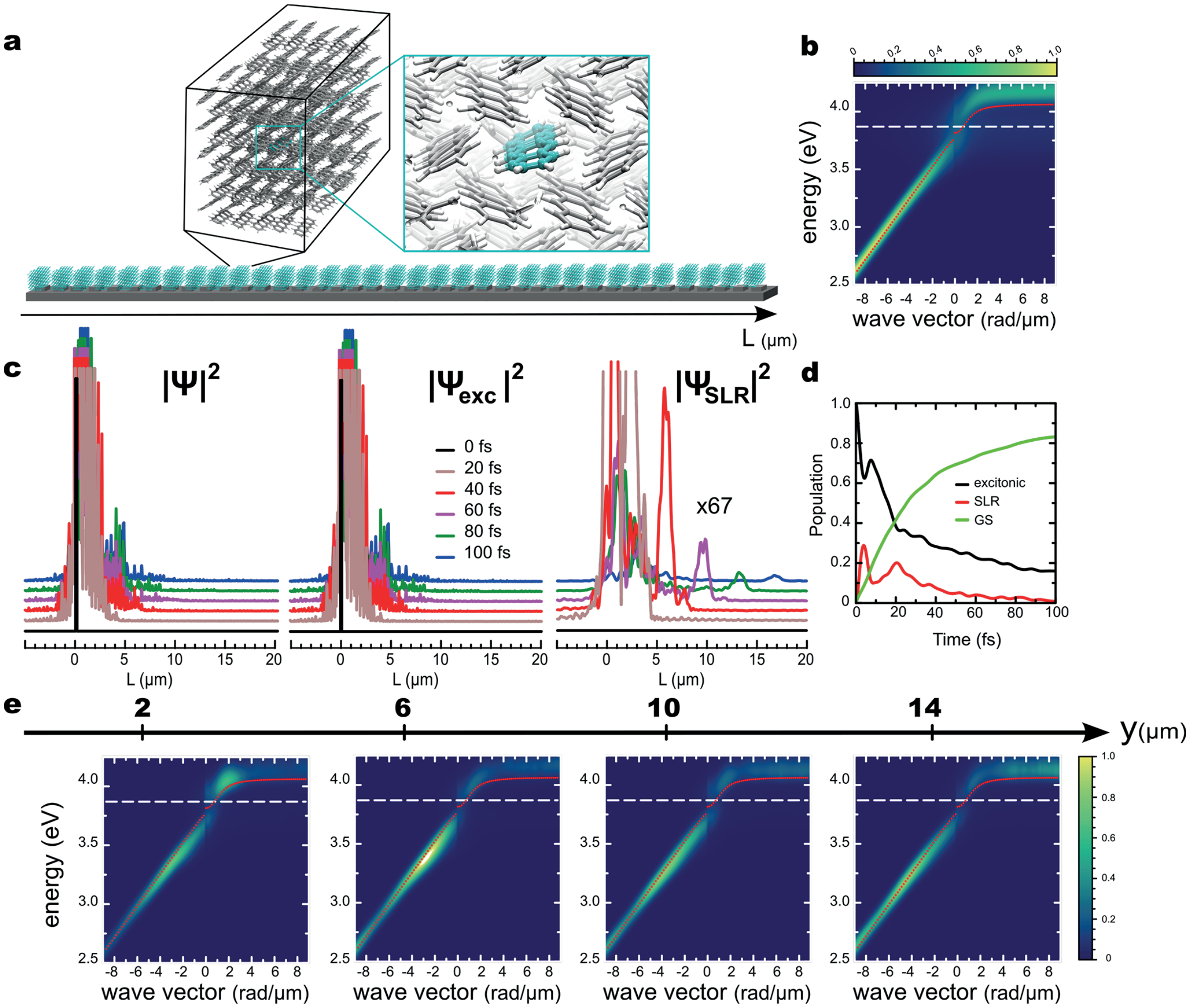

Figure 3. Schematic illustration of the simulation setup with the insets showing one of the 512 unit cells modeled in MD simulations (a). The Tc monomer described at the QM level is shown in ball-and-stick representation, while monomers in the MM subsystem are represented by sticks. Angle-resolved absorption spectrum when the crystal is strongly coupled to the modes of the (0,+1) SLR (b). Wave-packet motion along the +*y*-direction (c). For clarity, a vertical offset is added to wave packets at different time points. Time evolution of the excitonic (black) and photonic (red) fractions of polaritons in the Tc-SLRs strongly coupled system, as well as population of the ground state occupation (green), in which no photon is present (d). Angle-resolved photoluminescence spectra observed through pinholes located at various distances along the *y*-axis (e). Intensities in these plots are scaled by the same factor for each pinhole.

show a very clear lower polariton band (LPB), while the upper polariton band (UPB) is hardly visible, which could be explained by the additional coupling to higher vibronic modes. The UPB is visible with TM polarization only at higher k-vectors (SI, Figure S2) and shows a splitting of 220 meV, which confirms that this system is in the strong coupling regime.[31]

The effect of strong coupling is also clear in the modified dispersion of the emission spectra measured upon excitation by a 450 nm laser. The dispersion of the emission overlaps with the extinction for both the weakly (Figure 1e) and the strongly coupled cases (Figure 1f). While the emission is barely enhanced for the weakly coupled system, there is a very strong enhancement of the emission from the LPB for the strongly coupled system. This observation is in agreement with earlier studies[34] and can be understood by the efficient internal conversion from excited states to the LPB.[35]

In order to study the properties of the propagating LPB, we have imaged the Fourier plane of the emission at different distances from the excitation using a Fourier microscope with an intermediate imaging plane (40× excitation objective NA 0.6, 60× collection objective NA 0.7). For these measurements, we place a pinhole in the intermediate imaging plane corresponding to a 6.7 μm diameter spot on the sample (see setup illustration in Figure 2a). By choosing the position of the pinhole in the imaging plane, we can select the emission originating from a well-defined distance from the excitation. In Figure 2b−e, we image emission at distances of 0 to 20 μm away from the excitation spot where we normalize each image to its maximum intensity. The LPB modes are slightly less "sharp" than in Figure 1f, as the pinhole in the intermediate imaging plane leads to a lower resolution in the Fourier plane. At $y = 0$, the Fourier plane shows emission from both the (0,+1) and the (0,−1) LPB and emission from uncoupled excitons (Figure 2b). Moving the pinhole in the imaging plane away from the excitation spot in the +y-direction, the (0,−1) exciton-polariton mode, which propagates in the −y-direction, is not visible anymore and also the emission from uncoupled excitons is reduced (Figure 2c). Moving further away from the excitation spot, emission from uncoupled excitons disappears completely (Figure 2d,e). In addition to the vanishing emission of uncoupled excitons, the intensity distribution of the LPB emission changes as a function of the distance from the excitation spot, indicating an energy-dependent propagation length. At $y = 5$ μm from the excitation, the LPB is most intense at high energies (from 2.1−2.3 eV). Further away, at 10 and 20 μm, the highest intensity shifts to lower energies. In particular, the exciton−polariton at energies close to the Tc exciton energy disappears completely since it has a high exciton fraction and the lowest group velocity. Emission at $k = 0$ and 2.19 eV disappears as well in Figure 2d,e since the group velocity of the LPB is zero due to the interaction between the forward and backward propagating TE modes, forming a standing exciton−polariton mode. To stress further these effects, the spectra of the emission integrated over the wave vector are plotted in Figure 2f and compared to the fluorescence of the uncoupled Tc (shown by the gray shaded area in the same figure). The red shift of polariton emission as the distance from the excitation increases is very clear in this figure. Despite this red shift, it should be noted that for all wavelengths the emission intensity decreases as a function of distance from the excitation spot. We will quantitatively discuss the propagation length in Figure 4, but first we discuss the underlying molecular processes of polariton transport by means of MD simulations.

Molecular Dynamics Simulations. To obtain atomistic insights into polariton propagation, we performed multiscale Quantum Mechanics/Molecular Mechanics (QM/MM) MD simulations of a Tc crystal strongly coupled to the (0,+1) SLR mode in a periodic one-dimensional lattice of length 36 μm (Figure 3a). Because we are interested in the propagation along the +y-direction, the (0,+1) SLR was modeled only.

In line with observations from the imaging experiments, also the MD simulations suggest a rapid propagation of exciton−polaritons over several micrometers after nonresonant excitation into a single Tc monomer of the crystal. Figure 3b shows the absorption of the Tc crystal interacting with the (0,+1) SLR as a function of the wave vector. The avoided crossing between the upper and lower absorption branches suggests that the system is in the strong coupling regime, with a Rabi splitting of ∼250 meV. Because the nuclear degrees of freedom are described classically in our simulations, we can only couple the vertical $S_0 \rightarrow S_1$ transition without vibronic progression. Therefore, the UPB is clearly visible in our simulations, in contrast to the experiment.

As shown in Figure 3c and in animations provided in the SI, the wave packet $\Psi(t)$ spreads out during the simulations, covering an increasing area of the Tc crystal with time. This panel also resolves how much excitons in each Tc unit cell contribute to the amplitude of $|\Psi(t)|^2$. These contributions are manifested by the spikes that indicate where excitons are transiently located during the wave packet propagation. The finite lifetime of SLR modes which establishes a competing channel to polariton propagation through radiative decay into the overall ground state (green curve in Figure 3d), restricts the maximum propagation length in our simulations to below 20 μm in 100 fs (Figure 3c and Figures S8(c) and S9(c) in the SI). While this distance is independent of the number of Tc unit cells in our simulations, we observe that the wave packet survives longer with increasing number of Tc crystal unit cells (see animations provided as SI). The latter dependency can be explained by the density of dark states, which increases with the number of strongly coupled Tc unit cells. Because these dark states lack a SLR contribution, the dark state manifold acts as a reservoir that extends the lifetime of the strongly coupled system.[36,37] While transient population of dark states increases the lifetime in our system, we note that if the decay of the confined light modes were much slower than that of the exciton, the lifetime of dark states would become the limiting factor in the propagation process, as observed for Bloch Surface Wave Polaritons.[12,13]

Closer inspection of the MD trajectories reveals that relaxation of the photoexcited Tc molecule induces a transfer of population into polaritonic states, as manifested by the increase of the SLR mode contribution in Figure 3d. These polaritonic states then propagate along the + y direction with their group velocities. Even if propagation is ballistic, it appears diffusive because (i) the group velocities of polaritonic states span a wide range (Figure S10 in the SI), with bright states propagating at their respective group velocity and stationary dark states not propagating at all, and (ii) reversible population transfers between these states. Because the group velocities are higher for polaritonic states at lower energies, but level off at higher energies where the polaritonic states are dominated by excitonic contributions, the SLR-dominated lower energy wave-packets propagate faster, and reach a longer propagation distance, despite their shorter lifetime. In Figure 3, this is manifested by *(i)* a narrow peak in the plot of $|\Psi_{\mathrm{SLR}}(t)|^2$ that travels ahead of the rest of the wave packet (Figure 3c) and by *(ii)* a red-shift in the maximum intensity of the photoemission at further distances (Figure 3e). The latter observation is in agreement with the dispersion measurements and suggest that the MD simulations capture the polariton dynamics, at least qualitatively.

Propagation Length. To quantify experimentally the propagation length of exciton−polaritons as a function of energy, we map the emission intensity as a function of the distance from the laser excitation (Figure 4a). To reduce the contribution of scattered uncoupled emission of Tc, we follow the method proposed by Zakharko and co-workers:[14] We excite the crystal 2 μm away from the edge of the array, and normalize the measurements to the emission intensity at the edge. We also verify the observed exciton-polariton propagation using FDTD simulations. For these simulations, we consider a system of 25 × 61 silver particles covered with Tc and place a radiating point dipole that simulates the focused laser excitation, at the edge of this finite array. The dipole is oriented with a moment along the dominant SLR electric field component in the center of four particles (see SI, Figure S5). This choice is motivated to increase the coupling of the emission to the SLR and to reduce the quenching of this emission by avoiding the near-field coupling to higher order multipoles in the nanoparticles. The square of the electric field amplitude $|E|^2$ in the Tc crystal obtained by FDTD simulations, is plotted in Figure 4b after normalization at a position 1.5 μm away from the dipole to exclude the near-field contribution of the point dipole emission. The simulated exciton−polariton

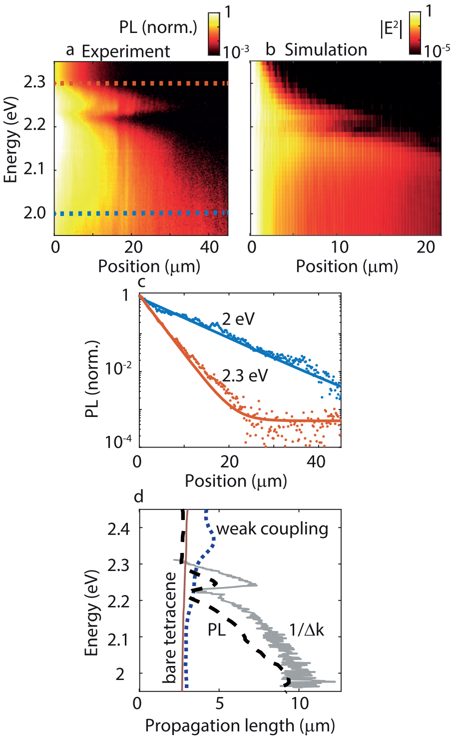

Figure 4. Real space map of the propagation of exciton-polaritons as a function of energy, normalized by the intensity at a distance of 2 μm away from the laser excitation (a). FDTD simulation of the propagated squared electric field intensity $|E|^2$ in an array of 61 × 25 particles with a dipole at $y = 0$ (b). Cross section of the emission intensity as a function of distance from the excitation spot (c) for an energy of 2 eV (blue circles) and 2.3 eV (orange circles), corresponding to the horizontal lines in (a). The solid lines are exponential fits to the data. The propagation length obtained from fitting the decay at energies between 1.95 and 2.45 eV is plotted in (d) with the black dashed curve. This curve matches excellently with the propagation length obtained from the dispersion of Figure 1f as $1/\Delta k_y$, given by the gray curve. The red curve corresponds to the measured propagation length in the Tc crystal in absence of the particle array.

propagation agrees qualitatively with the experimental propagation data. This simulation shows an increasing value of the propagation length for low energies and a similar dip in this propagation length at approximately 2.2 eV, where the (0, +1) and (0,−1) polaritons cross. It should be noted, however, that the decay of $|E^2|$ in the FDTD simulation is roughly a factor of 2 faster compared to the experiment as can be appreciated from the different color scales used in Figure 4a,b and from the cross sections plotted in SI, Figure S5. This quantitative discrepancy between simulations and experiments could be due to a reduction of the quality factor of the resonances in the simulations due to the limited dimension of the array,[38] and the fact that a single point dipole can not fully capture the effects of the laser excitation.

We fit the experimental data of the decaying fluorescence with an exponential function ($e^{-\frac{y}{L_p}}$ + background), where L_p is the propagation length, and y is the distance from the excitation source. The emission intensity decay and the fit to the data are given in Figure 4c for an energy of 2.3 eV, that is, close to the exciton resonance (orange circles and curve), and for 2 eV, that is, far away from the exciton resonance (blue circles and curve), clearly showing the difference in propagation length. In Figure 4d, we show with a black dashed curve the results of the fits to the decay of the fluorescence intensity as a function of the energy. We also obtain the propagation length from the far-field emission as the inverse of the imaginary component of the wave vector ($1/\mathrm{Im}(k_y)$) of the LPB, corresponding to $1/\Delta k_y$[39,40] for each energy (gray curve in Figure 4d). This line width is determined by fitting a Lorentzian function to the emission spectrum of Figure 1f. The propagation length for the strongly coupled case is clearly much larger than for the case when the cavity field and Tc dipoles are orthogonal, as appreciated when comparing the propagation lengths obtained from the real space images of the fluorescence and plotted with the blue dotted curve in Figure 4d. The origin of the propagation for the weakly coupled system is the coupling of emission into the SLR, followed by out-coupling at a different position.

The red curve in Figure 4d indicates the propagation length of the exciton in the Tc crystal outside of the array (including internal reflections in the substrate), where the propagation is either due to the diffusion of triplets that annihilate into singlets[3,41] or to the emission and reabsorption of the fluorescence.

The exciton−polariton propagation length, as determined from the dispersion measurements and the real space emission spectra, are in excellent agreement and show a propagation length of 9 μm at 1.95 eV. Low-energy polaritons have a high photonic content, which explains such a long propagation distance. This length is only a few microns shorter than the propagation length of the bare SLR, which propagates up to 15 μm at low energies (see SI, Figure S1(e)). The excitonic/photonic fraction of exciton−polaritons are given by the mixing coefficients that can be estimated by fitting the dispersion measurements to the Hamiltonian of the coupled system,[42]

$$H = \begin{bmatrix} E_{\mathrm{SLR}} - i\frac{\gamma_{\mathrm{SLR}}}{2} & g_1 & g_2 \\ g_1 & E_{\mathrm{exc1}} - i\frac{\gamma_{\mathrm{exc1}}}{2} & 0 \\ g_2 & 0 & E_{\mathrm{exc2}} - i\frac{\gamma_{\mathrm{exc2}}}{2} \end{bmatrix} \qquad (1)$$

where E_{SLR} is the angle-dependent energy dispersion of the SLR, which is obtained through the coupling of the LSPR and the Rayleigh Anomalies (RAs), as obtained with a similar coupled model and plotted in Figure 5a with the black curve. γ_{SLR} are the losses of the SLR, which depend on the in-plane momentum as they increase when the cavity dispersion approaches the LSPR energy (SI, S7). E_{exc1} and E_{exc2} are the two excitonic transitions of Tc, that is, the $S_0 \rightarrow S_1$ transition and the vibronic progression, centered at 2.38 and 2.57 eV, respectively, with their losses estimated from the fwhm of the spectrum, yielding $\gamma_{\mathrm{exc1}} = \gamma_{\mathrm{exc2}} = 140$ meV. The exciton energy of 2.38 eV is indicated in Figure 5a with the horizontal black line. The coupling strengths between the SLR and the exciton transitions are denoted by g_1 and g_2, respectively, with $g_1 = 160$ meV and $g_2 = 60$ meV. The fact that g_1 is larger than the losses indicates that the system is in the strong coupling regime.[43] The diagonalization of this matrix gives the eigenvalues and

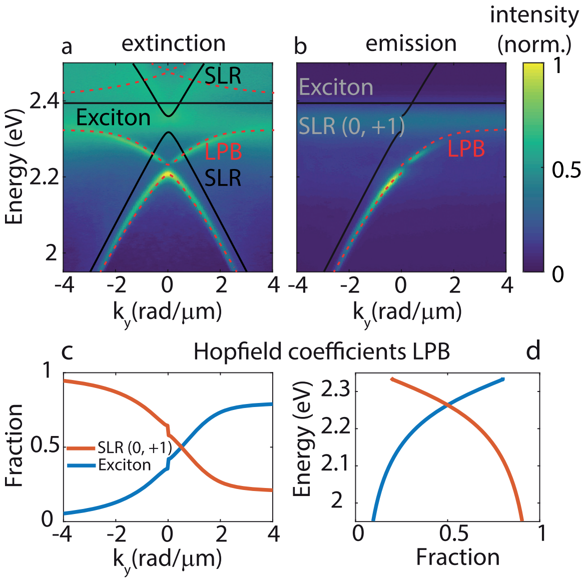

Figure 5. Dispersion measurements and fitted dispersion (red dashed curves) of the strongly coupled system with a coupled oscillator model (a). The black curves are the dispersion of the uncoupled SLR and exciton. Fluorescence map obtained by exciting the system at the edge of the array in order to only excite the (0,+1) TE SLR (b). The fluorescence follows the same dispersion as the extinction map. The SLR fraction (orange curve) and exciton fraction (blue curve) of the LPB as obtained by the coupled oscillator model is shown in (c) as a function of the in-plane momentum and in (d) as a function of LPB energy.

eigenvectors of the coupled system. The eigenvalues are plotted with the red dashed curves in Figure 5a as a function of the in-plane wave vector.

For propagation in the +*y*-direction, we are only interested in the LPB since emission from the middle and upper polaritons cannot be detected due to fast internal conversion to dark states and LPB. We only look at the propagation along the +*y*-direction and therefore focus on the TE LPB mode. We can visualize this mode when the Tc crystal is excited at the edge of the particle array and look at the fluorescence in the Fourier plane. In Figure 5b, we can see that this mode overlaps with the fitted TE polariton mode (red-dashed curve). As a reference, the exciton transition at 2.38 eV and the uncoupled SLR are plotted with the black line and curve in the same figure.

The exciton fraction and SLR fraction of the different polariton modes are given by the mixing coefficients that are obtained by squaring the amplitude of the eigenvectors.[44] The mixing coefficients for the (0,+1) TE LPB are plotted in Figure 5c as a function of the in-plane wave vector. The exciton fraction of the (0,+1) mode (blue curve in Figure 5c) increases as LPB approaches the exciton transition at larger wave vectors, while the SLR fraction decreases (orange curve). The small jump in both curves at $k_y = 0$ corresponds to the gap in the LPB due to the coupling of the (0,+1) and (0,−1) SLRs that is visible in Figures 1d and 5a. The SLR and exciton fractions as a function of LPB energy are plotted in Figure 5d, showing the reduction of the SLR fraction and increase of the exciton fraction as the LPB approaches the exciton energy.

We are mostly interested in the exciton fraction that gets transported through the LPB mode. Combining the data of Figures 5d and 4d, we obtain the propagation length as a function of exciton fraction, which is plotted with the black dashed curve in Figure 6a. In general, this curve shows a decreasing trend for higher exciton fractions, which is to be expected due to the localized character of excitons. The reduced polariton propagation at the crossing point of the forward and backward propagation SLRs at $k_y = 0$, is visible as a dip in the propagation length at 2.21 eV. From the figure we can see that at an exciton fraction of 50%, the propagation length is 4.4 μm. In the same figure, we also plot the propagation length as measured for the weakly coupled system (blue dotted curve). The much shorter propagation length when the dipoles are orthogonal illustrates again the effect of the relative dipole orientation on the transport properties of the system. We speculate that the measured propagation length in the weakly coupled crystal is due to singlet fission resulting in long-lived triplet states followed by triplet−triplet annihilation at a distance from the excitation spot or scattering of the pump laser.

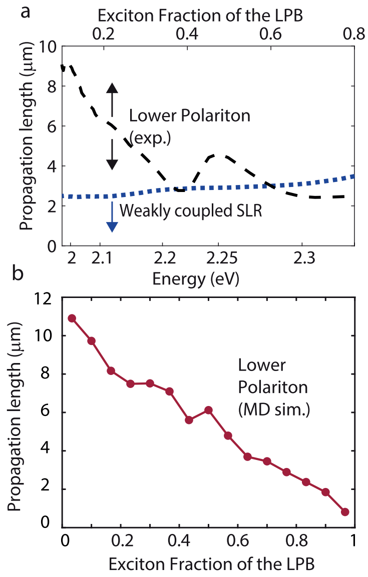

Figure 6. (a) Propagation length as a function of exciton fraction of the LPB (black dashed curve), obtained by combining the propagation length for each energy (Figure 4c) and the exciton fraction of the LPB as a function of energy (Figure 5d). A propagation length up to 9 μm is reached for low exciton fractions, but even at an exciton fraction of 0.5, the propagation length is 4.4 μm. The dip in propagation length at an exciton fraction of 0.4 corresponds to the gap in the dispersion of the LPB. The blue dashed curve shows the measured propagation length of excitons in a weakly coupled Tc crystal, that is, a crystal with the dipoles perpendicular to the cavity field. (b) Propagation length as a function of exciton fraction of the LPB obtained from the MD simulations.

A similar trend is observed when plotting the propagation length as a function of exciton fraction from MD simulations (Figure 6b). However, in contrast to experiment, the minimum propagation length goes to zero with increasing exciton fraction. This difference arises because the initial excitation in the simulation is localized on a single QM subsystem and the purely excitonic states do not display a diffusive behavior because neither singlet−triplet intersystem crossing, nor excitonic couplings governing incoherent hopping of excitons between adjacent Tc monomers are included in the MD model. While including the excitonic couplings in our simulation model is straightforward,[45] a direct comparison to the experimental incoherent propagation length would not be meaningful as the time scales that we can reach in our simulations are on the order of hundreds of femtoseconds and hence much shorter than the time scales associated with incoherent hopping.

We note that the polariton propagation length in our simulations does not depend on the size of the crystal (compare wavefronts in panel (c) of Figures 3 and S8 and S9 of the SI). Therefore, the agreement between experiment and simulations support the interpretation that exciton transport is significantly enhanced under strong coupling between the singlet excitons and the SLR modes.

CONCLUSIONS

The anisotropic properties of Tc make this organic semiconductor an ideal platform for studying polariton propagation. By choosing the orientation of the strongest excitonic transition dipole moment with respect to the field in an open plasmonic cavity formed by an array of Ag nanoparticles, we were able to switch from the weak to the strong coupling regime. In the strong coupling regime, we measured an exciton polariton transport length with a decay constant of 4.4 μm at 50% exciton fraction, that showed a strong dependence on the photonic fraction of the exciton−polaritons. Because the propagation enhancement is highest for the lower energy polaritons, exploiting such enhanced propagation requires an acceptor with an excitation energy matching the energies of these LPB states.

A one-to-one comparison of the ballistic transport length in strongly coupled Tc and the exciton diffusion length of uncoupled Tc crystals is not straightforward, as the ballistic transport is directional, while diffusion is a random walk process. We can however conclude that the exciton polariton propagation length is 2 orders of magnitude larger than the diffusion length of singlet excitons in Tc ($L_D \approx 50$ nm),[2] and a factor 10 larger than triplet mediated exciton diffusion $L_D \approx 560$ nm.[3] MD simulations qualitatively confirm the enhanced exciton-polariton transport and reveal that through relaxation of the photoexcited Tc molecule, exciton polaritons are populated and propagate with their respective group velocities until they decay at the rate determined by the finite lifetime of the open cavity. The wave-packets cover distances of several μm in 100 fs, which is orders of magnitude faster than bare exciton diffusion that proceeds on a ns to μs time scale.

METHODS

Molecular Dynamics Simulations. Three sets of simulations were performed, in which the macroscopic crystal is modeled as 256, 512, and 1024 unit cells (see Figure 3a). Each unit cell of these crystals contains 250 Tc monomers, one of which is described at the QM level, while the other 249 Tc monomers are modeled with the Gromos96-54a7 molecular mechanics force field.[46] The electronic ground state (S_0) of the QM subsystem was modeled at the restricted Hartree-Fock level (RHF), while the configuration interaction method truncated to single excitations (CIS) was used to describe the first singlet excited state (S_1). In both RHF and CIS calculations, the single-configuration electronic wave functions were expanded in the 3-21G basis set.[47] The large system sizes in our simulations (up to 30720 QM and 7649280 MM atoms) necessitated this rather low level of theory, which resulted in an overestimation of the first singlet excited state by ∼1.4 eV.

Because we are interested in the dynamics of polariton transfer in the positive y-direction, we only considered the (0, +1) SLR and modeled this SLR with 101 modes equidistant in the k_y-space (-8.73 rad μm^{-1} $\leq k \leq 8.73$ rad μm^{-1}) in a periodic one-dimensional lattice with a length of 36 μm. A nonlinear fit to the experimentally determined dispersion of the SLRs was done to obtain an analytical expression for the SLRs dispersion $E_{SLR}(k_y)$ used during the simulations (see exact procedure in the SI). To account for the systematic blueshift of the Tc excitation energy due to the low level of QM theory employed in our simulations, a 1.44 eV energy offset was added to the SLR dispersion. The Tc crystal unit cells were placed directly on top of the plasmonic silver nanoparticles that were modeled implicitly as an inhomogeneous electric field with a spatial distribution that reflects the local field strength (see Figure S6 and details in section S8.1 of the SI). The finite SLR lifetime was included in the simulations as a k_y-vector dependent first-order decay of the confined light modes (see Figure S7 and details in section S8.1 of the SI). We used the Ehrenfest, or mean-field, method to compute trajectories of the strongly coupled SLR−Tc system with a time step of 0.1 fs. The temperature was kept constant by coupling the simulation boxes to a thermal bath at 300 K, modeled by a stochastic thermostat.[48] To model the nonresonant excitation with the pump laser, we started the simulations with the QM subsystem of the first unit cell ($j = 1$) in the first electronic excited singlet state ($S_1^{j=1}$). A complete description of the simulations is included in the SI.

ASSOCIATED CONTENT

Supporting Information

The Supporting Information is available free of charge at https://pubs.acs.org/doi/10.1021/acsphotonics.2c00007.

Animations of the propagating polaritonic wavepacket in the MD simulations (MP4)

Details on the bare nanoparticle array, strong coupling measurements of the TM mode, dielectric function of tetracene as used in FDTD simulations, propagation measurements on a weakly coupled sample, propagation from FDTD simulations, fits of the SLR dispersion, and detailed description of the MD simulations (PDF)

AUTHOR INFORMATION

Corresponding Authors

Anton Matthijs Berghuis − *Department of Applied Physics and Eindhoven Hendrik Casimir Institute, Eindhoven University of Technology, 5600 MB Eindhoven, The Netherlands;* orcid.org/0000-0002-1896-7119;
Email: a.m.berghuis@tue.nl
Gerrit Groenhof − *Nanoscience Center and Department of Chemistry, University of Jyväskylä, 40014 Jyväskylä, Finland;* orcid.org/0000-0001-8148-5334;
Email: gerrit.x.groenhof@jyu.fi
Jaime Gómez Rivas − *Department of Applied Physics and Eindhoven Hendrik Casimir Institute, Eindhoven University of Technology, 5600 MB Eindhoven, The Netherlands; Institute for Complex Molecular Systems ICMS, Eindhoven*

University of Technology, 5612 AJ Eindhoven, The Netherlands; orcid.org/0000-0002-8038-0968; Email: j.gomez.rivas@tue.nl

Authors

Ruth H. Tichauer − *Nanoscience Center and Department of Chemistry, University of Jyväskylä, 40014 Jyväskylä, Finland*

Lianne M. A. de Jong − *Department of Applied Physics and Eindhoven Hendrik Casimir Institute, Eindhoven University of Technology, 5600 MB Eindhoven, The Netherlands*

Ilia Sokolovskii − *Nanoscience Center and Department of Chemistry, University of Jyväskylä, 40014 Jyväskylä, Finland;* orcid.org/0000-0003-3367-0660

Ping Bai − *Department of Applied Physics and Eindhoven Hendrik Casimir Institute, Eindhoven University of Technology, 5600 MB Eindhoven, The Netherlands*

Mohammad Ramezani − *Department of Applied Physics and Eindhoven Hendrik Casimir Institute, Eindhoven University of Technology, 5600 MB Eindhoven, The Netherlands;* orcid.org/0000-0002-1863-9123

Shunsuke Murai − *Department of Material Chemistry, Graduate School of Engineering, Kyoto University, 6158510 Kyoto, Japan;* orcid.org/0000-0002-4597-973X

Complete contact information is available at: https://pubs.acs.org/10.1021/acsphotonics.2c00007

Funding

This research is funded by the Innovational Research Incentives Scheme of the Nederlandse Organisatie voor Wetenschappelijk Onderzoek (NWO; Vici Grant 680-47-628) and the Academy of Finland (Grant 323996).

Notes

The authors declare no competing financial interest.

■ ACKNOWLEDGMENTS

We thank Johannes Feist for fruitful discussions.

■ REFERENCES

(1) Mikhnenko, O. V.; Blom, P. W. M.; Nguyen, T.-Q. Exciton Diffusion in Organic Semiconductors. *Energy Environ. Sci.* **2015**, *8*, 1867−1888.

(2) Yost, S. R.; Hontz, E.; Yeganeh, S.; Van Voorhis, T. Triplet vs Singlet Energy Transfer in Organic Semiconductors: The Tortoise and the Hare. *J. Phys. Chem. C* **2012**, *116*, 17369−17377.

(3) Akselrod, G. M.; Deotare, P. B.; Thompson, N. J.; Lee, J.; Tisdale, W. A.; Baldo, M. A.; Menon, V. M.; Bulovic, V. Visualization of Exciton Transport in Ordered and Disordered Molecular Solids. *Nat. Commun.* **2014**, *5*, 3646.

(4) Motaung, D. E.; Malgas, G. F.; Arendse, C. J. Insights into the stability and thermal degradation of P3HT:C60 blended films for solar cell applications. *J. Mater. Sci.* **2011**, *46*, 4942−4952.

(5) Cao, H.; He, W.; Mao, Y.; Lin, X.; Ishikawa, K.; Dickerson, J. H.; Hess, W. P. Recent progress in degradation and stabilization of organic solar cells. *J. Power Sources* **2014**, *264*, 168−183.

(6) Feist, J.; Garcia-Vidal, F. J. Extraordinary exciton conductance induced by strong coupling. *Phys. Rev. Lett.* **2015**, *114*, 196402.

(7) Schachenmayer, J.; Genes, C.; Tignone, E.; Pupillo, G. Cavity enhanced transport of excitons. *Phys. Rev. Lett.* **2015**, *114*, 196403.

(8) Kéna-Cohen, S.; Forrest, S. R. Giant Davydov splitting of the lower polariton branch in a polycrystalline tetracene microcavity. *Phys. Rev. B* **2008**, *77*, 73205.

(9) Berghuis, A. M.; Halpin, A.; Le-Van, Q.; Ramezani, M.; Wang, S.; Murai, S.; Gómez Rivas, J. Enhanced Delayed Fluorescence in Tetracene Crystals by Strong Light-Matter Coupling. *Adv. Funct. Mater.* **2019**, *29*, 1901317.

(10) Polak, D.; et al. Manipulating molecules with strong coupling: harvesting triplet excitons in organic exciton microcavities. *Chem. Sci.* **2020**, *11*, 343−354.

(11) Freixanet, T.; Sermage, B.; Tiberj, A.; Planel, R. In-plane propagation of excitonic cavity polaritons. *Physical Review B - Condensed Matter and Materials Physics* **2000**, *61*, 7233−7236.

(12) Lerario, G.; Ballarini, D.; Fieramosca, A.; Cannavale, A.; Genco, A.; Mangione, F.; Gambino, S.; Dominici, L.; De Giorgi, M.; Gigli, G.; Sanvitto, D. High-speed flow of interacting organic polaritons. *Light: Science and Applications* **2017**, *6*, 16212.

(13) Hou, S.; Khatoniar, M.; Ding, K.; Qu, Y.; Napolov, A.; Menon, V. M.; Forrest, S. R. Ultralong-Range Energy Transport in a Disordered Organic Semiconductor at Room Temperature Via Coherent Exciton-Polariton Propagation. *Adv. Mater.* **2020**, *32*, 2002127.

(14) Zakharko, Y.; Rother, M.; Graf, A.; Hähnlein, B.; Brohmann, M.; Pezoldt, J.; Zaumseil, J. Radiative Pumping and Propagation of Plexcitons in Diffractive Plasmonic Crystals. *Nano Lett.* **2018**, *18*, 4927−4933.

(15) Rozenman, G. G.; Akulov, K.; Golombek, A.; Schwartz, T. Long-Range Transport of Organic Exciton-Polaritons Revealed by Ultrafast Microscopy. *ACS Photonics* **2018**, *5*, 105−110.

(16) Pandya, R.; et al. Microcavity-like exciton-polaritons can be the primary photoexcitation in bare organic semiconductors. *Nat. Commun.* **2021**, *12*, 6519.

(17) Quinten, M.; Leitner, A.; Krenn, J. R.; Aussenegg, F. R. Electromagnetic energy transport via linear chains of silver nanoparticles. *Opt. Lett.* **1998**, *23*, 1331.

(18) Félidj, N.; Aubard, J.; Lévi, G.; Krenn, J. R.; Schider, G.; Leitner, A.; Aussenegg, F. R. Enhanced substrate-induced coupling in two-dimensional gold nanoparticle arrays. *Physical Review B - Condensed Matter and Materials Physics* **2002**, *66*, 245407.

(19) Christ, A.; Tikhodeev, S. G.; Gippius, N. A.; Kuhl, J.; Giessen, H. Waveguide-plasmon polaritons: Strong coupling of photonic and electronic resonances in a metallic photonic crystal slab. *Phys. Rev. Lett.* **2003**, *91*, 183901.

(20) Maier, S. A.; Kik, P. G.; Atwater, H. A.; Meltzer, S.; Harel, E.; Koel, B. E.; Requicha, A. A. Local detection of electromagnetic energy transport below the diffraction limit in metal nanoparticle plasmon waveguides. *Nat. Mater.* **2003**, *2*, 229−232.

(21) Weber, W. H.; Ford, G. W. Propagation of optical excitations by dipolar interactions in metal nanoparticle chains. *Physical Review B - Condensed Matter and Materials Physics* **2004**, *70*, 125429.

(22) Maier, S. A.; Atwater, H. A. Plasmonics: Localization and guiding of electromagnetic energy in metal/dielectric structures. *J. Appl. Phys.* **2005**, *98*, 011101.

(23) Auguié, B.; Barnes, W. L. Collective Resonances in Gold Nanoparticle Arrays. *Phys. Rev. Lett.* **2008**, *101*, 143902.

(24) Kravets, V. G.; Kabashin, A. V.; Barnes, W. L.; Grigorenko, A. N. Plasmonic Surface Lattice Resonances: A Review of Properties and Applications. *Chem. Rev.* **2018**, *118*, 5912−5951.

(25) Zou, S.; Janel, N.; Schatz, G. C. Silver nanoparticle array structures that produce remarkably narrow plasmon lineshapes. *J. Chem. Phys.* **2004**, *120*, 10871−10875.

(26) Rodriguez, S. R.; Abass, A.; Maes, B.; Janssen, O. T.; Vecchi, G.; Gómez Rivas, J. Coupling Bright and Dark Plasmonic Lattice Resonances. *Physical Review X* **2011**, *1*, 021019.

(27) Wu, T. C.; Thompson, N. J.; Congreve, D. N.; Hontz, E.; Yost, S. R.; Van Voorhis, T.; Baldo, M. A. Singlet Fission Efficiency in Tetracene-Based Organic Solar Cells. *Appl. Phys. Lett.* **2014**, *104*, 193901.

(28) Rao, A.; Friend, R. H. Harnessing Singlet Exciton Fission to Break the Shockley−Queisser Limit. *Nature Reviews Materials* **2017**, *2*, 17063.

(29) Einzinger, M.; Wu, T.; Kompalla, J. F.; Smith, H. L.; Perkinson, C. F.; Nienhaus, L.; Wieghold, S.; Congreve, D. N.; Kahn, A.; Bawendi, M. G.; Baldo, M. A. Sensitization of Silicon by Singlet Exciton Fission in Tetracene. *Nature* **2019**, *571*, 90−94.

(30) Burdett, J. J.; Bardeen, C. J. Quantum beats in crystalline tetracene delayed fluorescence due to triplet pair coherences produced by direct singlet fission. *J. Am. Chem. Soc.* **2012**, *134*, 8597−8607.

(31) Berghuis, A. M.; Serpenti, V.; Ramezani, M.; Wang, S.; Gómez Rivas, J. Light-Matter Coupling Strength Controlled by the Orientation of Organic Crystals in Plasmonic Cavities. *J. Phys. Chem. C* **2020**, *124*, 12030−12038.

(32) Tavazzi, S.; Raimondo, L.; Silvestri, L.; Spearman, P.; Camposeo, A.; Polo, M.; Pisignano, D. Dielectric Tensor of Tetracene Single Crystals: The Effect of Anisotropy on Polarized Absorption and Emission Spectra. *J. Chem. Phys.* **2008**, *128*, 154709.

(33) Barnes, W.; Preist, T.; Kitson, S.; Sambles, J. Physical origin of photonic energy gaps in the propagation of surface plasmons on gratings. *Physical Review B - Condensed Matter and Materials Physics* **1996**, *54*, 6227−6244.

(34) Grant, R. T.; Michetti, P.; Musser, A. J.; Gregoire, P.; Virgili, T.; Vella, E.; Cavazzini, M.; Georgiou, K.; Galeotti, F.; Clark, C.; Clark, J.; Silva, C.; Lidzey, D. G. Efficient Radiative Pumping of Polaritons in a Strongly Coupled Microcavity by a Fluorescent Molecular Dye. *Advanced Optical Materials* **2016**, *4*, 1615−1623.

(35) Lidzey, D. G.; Bradley, D. D.; Virgili, T.; Armitage, A.; Skolnick, M. S.; Walker, S. Room Temperature Polariton Emission from Strongly Coupled Organic Semiconductor Microcavities. *Phys. Rev. Lett.* **1999**, *82*, 3316−3319.

(36) Groenhof, G.; Climent, C.; Feist, J.; Morozov, D.; Toppari, J. J. Tracking Polariton Relaxation with Multiscale Molecular Dynamics Simulations. *J. Chem. Phys. Lett.* **2019**, *10*, 5476−5483.

(37) Tichauer, R.; Feist, J.; Groenhof, G. Multi-Scale Dynamics Simulations of Molecular Polaritons: the Effect of Multiple Cavity Modes on Polariton Relaxation. *J. Chem. Phys.* **2021**, *154*, 104112.

(38) Rodriguez, S.; Schaafsma, M.; Berrier, A.; Gómez Rivas, J. Collective resonances in plasmonic crystals: Size matters. *Physica B: Condensed Matter* **2012**, *407*, 4081−4085.

(39) Manjavacas, A.; Garcia de Abajo, F. J. Robust plasmon waveguides in strongly interacting nanowire arrays. *Nano Lett.* **2009**, *9*, 1285−1289.

(40) Vecchi, G.; Giannini, V.; Gómez Rivas, J. Surface modes in plasmonic crystals induced by diffractive coupling of nanoantennas. *Physical Review B - Condensed Matter and Materials Physics* **2009**, *80*, 201401.

(41) Berghuis, A. M.; Raziman, T. V.; Halpin, A.; Wang, S.; Curto, A. G.; Rivas, J. G. Effective Negative Diffusion of Singlet Excitons in Organic Semiconductors. *J. Phys. Chem. Lett.* **2021**, *12*, 1360−1366.

(42) Garrido Alzar, C. L.; Martinez, M. A. G.; Nussenzveig, P. Classical analog of electromagnetically induced transparency. *American Journal of Physics* **2002**, *70*, 37−41.

(43) Skolnick, M. S.; Fisher, T. A.; Whittaker, D. M. Strong Coupling Phenomena in Quantum Microcavity Structures. *Semicond. Sci. Technol.* **1998**, *13*, 645−669.

(44) Hopfield, J. J. Theory of the contribution of excitons to the complex dielectric constant of crystals. *Phys. Rev.* **1958**, *112*, 1555−1567.

(45) Luk, H.-L.; Feist, J.; Toppari, J. J.; Groenhof, G. Multiscale Molecular Dynamics Simulations of Polaritonic Chemistry. *J. Chem. Theory Comput.* **2017**, *13*, 4324−4335.

(46) Huang, W.; Lin, Z.; van Gunsteren, W. F. Validation of the GROMOS 54A7 Force Field with Respect to -Peptide Folding. *J. Chem. Theory Comput.* **2011**, *7*, 1237−1243.

(47) Hehre, W. J.; Stewart, R. F.; Pople, J. A. Self-Consistent Molecular-Orbital Methods. I. Use of Gaussian Expansions of Slater-Type Atomic Orbitals. *J. Chem. Phys.* **1969**, *51*, 2657−2664.

(48) Bussi, G.; Donadio, D.; Parrinello, M. Canonical sampling through velocity rescaling. *J. Chem. Phys.* **2007**, *126*, 014101.

PIV

DISENTANGLING ENHANCED DIFFUSION AND BALLISTIC MOTION OF EXCITONS COUPLED TO BLOCH SURFACE WAVES WITH MOLECULAR DYNAMICS SIMULATIONS

by

I. Sokolovskii, Y. Luo, G. Groenhof

Submitted to ACS Photonics, **2024**.

Disentangling enhanced diffusion and ballistic motion of excitons coupled to Bloch surface waves with molecular dynamics simulations

Ilia Sokolovskii,* Yunyi Luo, and Gerrit Groenhof

Nanoscience Center and Department of Chemistry, University of Jyväskylä, P.O. Box 35, 40014 Jyväskylä, Finland.

E-mail: ilia.sokolovskii@jyu.fi

Abstract

Placing a organic material on top of a Bragg mirror can significantly enhance exciton transport. Such enhancement has been attributed to strong coupling between the evanescent Bloch surface waves (BSW) on the mirror, and the excitons in the material. In this regime, the BSW and excitons hybridize into Bloch surface wave polaritons (BSWP), new quasi-particles with both photonic and excitonic character. While recent experiments unveiled a mixed nature of the enhanced transport, the role of the material degrees of freedom in this process remains unclear. To clarify their role, we performed atomistic molecular dynamics simulations of an ensemble of Methylene blue molecules, a prototype organic emitter, strongly coupled to BSW. In contrast to the established static models of polaritons, even with disorder included, our dynamic simulations reveal a correlation between the photonic content of the BSWP and the nature of the transport. In line with experiment, we find ballistic motion for polaritons with high photonic character, and enhanced diffusion if the photonic content is low. Our simulations furthermore suggest that the diffusion is due to thermally activated vibrations that drive population transfer between the stationary dark states and mobile bright polaritonic states.

1 Introduction

The propagation of Frenkel excitons in organic materials is a diffusion process in which the excitons hop between adjacent molecules via dipole-dipole coupling (Förster mechanism)[1] or a wave function overlap (Dexter mechanism)[2]. Because the efficiency of these mechanisms depends on intermolecular separation and orientiation, structural molecular disorder has a negative impact on exciton transfer, resulting in a limited diffusion length of Frenkel excitons, typically below 10 nm[3].

The propagation distance can be increased by placing organic molecules into an optical microcavity[4]. There, excitons can strongly interact with confined light modes of the cavity. If the strength of such interaction exceeds the rates associated with losses in the system, excitons and cavity modes hybridize into polaritons[5,6], which inherit the properties of both constituents of the interaction, including dispersion and hence group velocity. This allows for a long-range propagation of polaritons beyond the diffusion length of Frenkel excitons, as has been demonstrated in various types of cavities[7–14].

Theory has provided important insights into the mechanisms by which strong coupling can enhance exciton transport[15–25], but the description of the material in these works has been limited to two-level systems. To go beyond such simplified model systems and consider the vibrational degrees of freedom, we developed a simulation model based on multi-scale molecular dynamics,[26,27] in which the structural details of the material are explicitly included. With such simulations, we could show that polariton wave packets propagate in a diffusive manner due to reversible population exchanges between stationary dark states and propagating bright states, which are populated along the whole lower polariton branch[28,29]. While experiment[30] and theory[23,31] suggest that the coherence of polaritons, and hence the propagation distance, increases with their photonic weight, it remains unclear whether propagation of individual wave packets constituting the whole polariton wave packet, is fully ballistic or might also be diffusive depending on the wave vector at which an individual wave packet is formed.

Recently, this question was addressed in two separate experimental studies. In the first study, conducted by Balasubrahmaniyam *et al.*[14], spatiotemporal ultrafast pump-probe microscopy was used to track polariton transport in a system of 5,5’,6,6’-tetrachloro-1,1’-diethyl-3,3’-di(4-sulfobutyl)-benzimidazolocarbocyanine (TDBC) J-aggregates deposited on top of a distributed Bragg reflector (DBR) supporting Bloch surface waves (BSWs). By probing the differential reflectivity, $\Delta R/R$, at different angles and energies after off-resonant excitation into the J-aggregates, a transition from ballistic propagation with a velocity close to the corresponding polariton group velocity, to diffusive propagation with a much lower velocity, was observed when the photonic contribution to the polaritonic states decreased. This transition was attributed to a competition between molecular-scale disorder and long-range correlation due to strong coupling, with the former prevailing at small photonic fractions.

In the second study, carried out by Xu *et al.*[13], polariton transport was observed in a variety of inorganic exciton-cavity structures by means of a momentum-resolved ultrafast polariton imaging technique. As in Balasubrahmaniyam *et al.*[14], both a deviation of the propagation speed from the polariton group velocity and a transition from ballistic to diffusive transport was observed as the photonic contribution to the polaritonic states decreased and was attributed to a more intensive scattering by lattice phonons.

Thus, the results of the two experiments agree that polariton transport undergoes a crossover between ballistic and diffusion regimes when the polariton states become more exciton-like. However, in the case of organic molecules, it remains unclear whether this crossover is due to reversible non-adiabatic population transfers between bright and dark states, or whether such a transition can be caused solely by the structural molecular disorder. With the aim of addressing this question, we mimic the experiment of Balasubrahmaniyam *et al.* by means of multiscale quantum mechanics/molecular mechanics (QM/MM) molecular dynamics (MD) simulations[26,32]. The results of our simulations suggest that the change in the transport regime is, indeed, caused by reversible population exchanges between polaritonic states, which underlines the importance of molecular vibrations in the transport of organic exciton-polaritons.

2 Theoretical background

Before discussing the details of the simulations, we briefly discuss the origin of the formation of BSWs in a distributed Bragg reflector (DBR). As illustrated in Figure 1, a DBR is a one-dimensional photonic crystal, a structure in which the dielectric constant varies periodically, *i.e.*, $\varepsilon(x) = \varepsilon(x+A)$ with period A. Just like the periodicity of ions in an atomic crystal leads to the appearance of allowed bands and band gaps, periodicity of the dielectric constant in the DBR leads to the appearance of the so-called pass-bands and stop-bands. For a wave with a frequency inside a stop-band, multiple reflections of the wave from the boundaries between layers with a different dielectric constant result in the occurrence of destructive interference, which makes it impossible for the light to travel through the DBR. However, the introduction of a defect, such as a layer with a thickness or dielectric constant different from that of the other layers, may allow for localised states to appear in the stop-band[33].

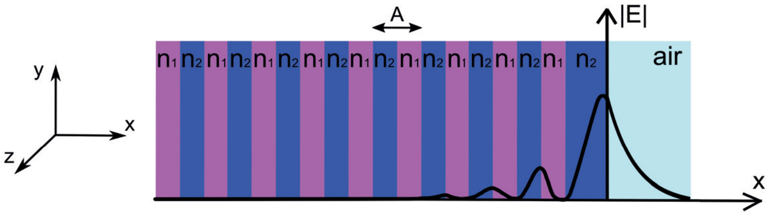

Figure 1: Schematic representation of a distributed Bragg reflector (DBR) supporting a Bloch surface wave (BSW). The DBR consists of alternating layers with different refractive indices, n_1 and n_2, with period A along the x-axis. Additionally, a surface defect layer with refractive index n_2 and a thickness different from the thicknesses of the other layers is introduced. The electric field strength distribution of the BSW is shown as a black line.

In addition to waves propagating within the volume, photonic crystals support surface waves propagating in both dielectric and air (states in pass-bands above the light line), propagating in the dielectric and decaying in air (states in pass-bands below the light line), as well as decaying in the dielectric and propagating in air (states in stop-bands above the light line)[34]. The introduction of a surface defect results in the appearance of a fourth type of surface wave, which is a wave localised in both dielectric and air[35]. This is the Bloch surface wave.

Because BSWs exist in the stop-bands and below the light line[34], *i.e.*, at angles larger than the critical angle for total internal reflection, the radiation cannot be emitted into free space, which results in an extremely long lifetime that is significantly higher than for typical Fabry-Pérot microcavities with metallic mirrors, or for plasmonic structures. As a consequence, the lifetime of polaritons formed due to strong coupling between excitons and BSWs can reach several hundreds to thousands of femtoseconds[7,9,36].

Because the BSW is a surface wave, evanescent in the direction, x, perpendicular to the surface (Figure 1), there is no restriction on the in-plane propagation over the surface of the Bragg mirror, *i.e.*, in the y- and z-directions. Therefore, the electric field distribution of the BSW in the air is defined as

$$E(x, y, z) = E_0 e^{-|K|x} e^{i(k_y y + k_z z)} \tag{1}$$

with E_0 the amplitude of the electric field at the surface of the photonic crystal, *i.e.*, at $x = 0$, and K the complex Bloch wave number[37]. Because in our simulations, we only consider a single layer of molecules, we neglect the x-dependence in Equation 1. Furthermore, we also restrict ourselves to model one-dimensional transport along a chain of molecules in the z-direction. With these simplifications, the field distribution becomes $E(z) = E_0 e^{ik_z z}$.

A major advantage of BSW-polaritons over Fabry-Pérot cavities is the much higher group velocity of the LP branch. In the BSW structures, the dispersion is close to the light line in free space, and the group velocity of the LP branch can approach the speed of light. This results in a tremendous propagation of BSW-polaritons reaching tens to hundreds micrometers[7,9,14,38].

3 Simulation details

In this work, we perform QM/MM molecular dynamics simulations of $N = 1024$ Methylene blue molecules (MeB, Figure 2**a**) in water coupled to a BSW structure. The S_0 and S_1 electronic states of MeB are modelled with density functional theory (DFT)[39]and time-dependent (TD)DFT[40] based on the Casida equations[41], respectively, using the B97 functional[42] and the 3-21G basis set. The water molecules are described with the TIP3P model[43]. The BSW is discretized into $n_{\text{modes}} = 120$ modes. To obtain a similar polariton dispersion as in the experiment, we fit the experimental dispersion of the BSW with a linear function (dashed-dotted line in Figure 2**b**) and tune it to be resonant with the excitation energy of MeB molecules (*i.e.*, $\hbar\omega_{\text{MeB}} = 2.50$ eV at the TDDFT/B97//3-21G level of theory; dashed line in Figure 2**b**) at wave vector $k_z = 11.41\ \mu\text{m}^{-1}$. With an electric field strength of 0.071 MV cm^{-1}, the Rabi splitting is 131 meV, which is close to the Rabi splitting in the experimental study[14]. We note that in our simulations, MeB molecules were used instead of J-aggregates due to the latter's complexity, which makes their simulation in a cavity currently intractable. We also note that at the level of TDDFT theory employed in this work, the excitation energies of MeB are overestimated. Similar discrepancies have been reported in previous works[44,45], and were attributed to the large difference in the charge density between the ground and excited state, which is notoriously difficult to describe accurately with TDDFT[46].

In our MD simulations, we apply the Born-Oppenheimer approximation[26,47] to separate the nuclear degrees of freedom, which are treated classically, from the electronic plus photonic degrees of freedom, which are treated quantum mechanically with the QM/MM extension of the Tavis-Cummings Hamiltonian[48,49]:

$$\begin{aligned}\hat{H}^{\text{TC}} \quad = \quad & \textstyle\sum_j^N \hbar\omega_{\text{exc}}(\mathbf{R}_j)\hat{\sigma}_j^+\hat{\sigma}_j^- + \sum_j^N V_{\text{S}_0}(\mathbf{R}_j) + \sum_p^{n_{\text{modes}}} \hbar\omega_{\text{cav}}(\mathbf{k}_{z,p})\hat{a}_p^\dagger\hat{a}_p \\ & - \textstyle\sum_j^N \sum_p^{n_{\text{modes}}} \sqrt{\frac{\hbar\omega_{\text{cav}}(\mathbf{k}_{z,p})}{2\epsilon_0 V}}\boldsymbol{\mu}(\mathbf{R}_j)\cdot\left[e^{ik_{z,p}z_j}\hat{\sigma}_j^+\hat{a}_p + e^{-ik_{z,p}z_j}\hat{\sigma}_j^-\hat{a}_p^\dagger\right],\end{aligned} \tag{2}$$

where $\hat{\sigma}_j^+ = |\text{S}_1^j\rangle\langle\text{S}_0^j|$ is an operator that excites molecule j with nuclear coordinates $\mathbf{R}_j$ from the electronic ground state $|\text{S}_0^j\rangle$ with energy $V_{\text{S}_0}(\mathbf{R}_j)$ into the first electronic excited state $|\text{S}_1^j\rangle$ with energy $V_{\text{S}_1}(\mathbf{R}_j)$. Accordingly, the excitation energy is defined as $\hbar\omega_{\text{exc}}(\mathbf{R}_j) = V_{\text{S}_1}(\mathbf{R}_j) - V_{\text{S}_0}(\mathbf{R}_j)$. Likewise, $\hat{\sigma}_j^- = |\text{S}_0^j\rangle\langle\text{S}_1^j|$ de-excites molecule j from electronic excited state $|\text{S}_1^j\rangle$ into the electronic ground state $|\text{S}_0^j\rangle$. Operators $\hat{a}_p^\dagger$ and $\hat{a}_p$ create and annihilate a photon of energy $\hbar\omega_{\text{cav}}(\mathbf{k}_{z,p})$ in BSW mode p with in-plane momentum $\mathbf{k}_{z,p}$ along the surface of the BSW structure. Finally, $\boldsymbol{\mu}(\mathbf{R}_j)$ is the transition dipole moment of molecule j, and z_j is the position of molecule j on the surface of the

BSW structure.

The Ehrenfest molecular dynamics approach is used to model the classical degrees of freedom[50], which evolve on a potential energy surface that is the expectation value of the energy of the total wave function of the quantum degrees of freedom: $V(\mathbf{R}) = \langle\Psi|\hat{H}|\Psi\rangle$. The total wave function, $|\Psi(t)\rangle$, is propagated along the classical trajectory as a linear combination of diabatic product states between the N molecular excitations and n_{modes} BSW modes:

$$|\Psi(t)\rangle = \sum_{j}^{N+n_{\text{modes}}} d_j(t)|\phi_j\rangle, \tag{3}$$

where

$$|\phi_j\rangle = \hat{\sigma}_j^{+}|\mathrm{S}_0^1\mathrm{S}_0^2..\mathrm{S}_0^{N-1}\mathrm{S}_0^N\rangle \otimes |00..0\rangle \tag{4}$$

for $1 \leq j \leq N$, and

$$|\phi_{j>N}\rangle = \hat{a}_{j-N}^{\dagger}|\mathrm{S}_0^1\mathrm{S}_0^2..\mathrm{S}_0^{N-1}\mathrm{S}_0^N\rangle \otimes |00..0\rangle \tag{5}$$

for $N < j \leq N+n_{\text{modes}}$. State $|\phi_j\rangle$ corresponds to molecule j in its first electronic excited state (S_1^j), while the other molecules are in the ground state ($\mathrm{S}_0^{i\neq j}$) and the photonic states are empty, whereas state $|\phi_{j>N}\rangle$ corresponds to one of the BSW modes excited, with all molecules in the ground state. In Equation 3, $d_j(t)$ are the time-dependent expansion coefficients of the total wave function, which reflect the population of each molecule and each photonic mode during the evolution of the system. These coefficients are propagated with a unitary propagator[29]. A more detailed description of the method can be found in previous publications[26,27,29].

To mimic the initial conditions of the experiment, in which a single J-aggregate was pumped[14], we prepare the MeB-BSW system in the first excited electronic state (S_1) of a single MeB molecule, *i.e.*, $d_j(0) = 1$ and $d_{i\neq j}(0) = 0$ in Equation 3, located at $z_j = 125$ μm, which is the centre of the DBR surface of width $L_z = 250$ μm. A total of five Ehrenfest QM/MM trajectories are computed for 200 fs with an integration timestep of 0.5 fs. Because these MD trajectories are run for much shorter than the lifetime of the BSW, we neglect decay in our simulations. The temperature was kept constant at 300 K with the v-rescale thermostat[51]. Further details of the simulations performed in this article are presented in the Supporting Information (SI).

For the analysis of the trajectories, we also expand the total time-dependent wave function in the basis of the eigenstates of the Tavis-Cummings Hamiltonian, as follows:

$$|\Psi(t)\rangle = \sum_j c_m(t)|\psi_m\rangle, \tag{6}$$

where

$$|\psi_m\rangle = \left(\sum_j^N \beta_j^m \hat{\sigma}_j^+ + \sum_p^{n_{\text{modes}}} \alpha_p^m \hat{a}_p^\dagger\right) |\text{S}_0^1\text{S}_0^2..\text{S}_0^{N-1}\text{S}_0^N\rangle \otimes |0\rangle. \tag{7}$$

The β_j^m and α_p^m expansion coefficients denote contributions of the molecular excitons ($|\text{S}_1^j\rangle$) and of the photonic modes ($|1_p\rangle$) to adiabatic state $|\psi_m\rangle$. These coefficients are obtained by diagonalizing the matrix representation of $\hat{H}^{\text{TC}}$ (Equation 2) in the basis of the diabatic product states (Equation 4-5). The time-dependent expansion coefficients, $c_j(t)$, in this adiabatic representation are thus related to the time-dependent expansion coefficients, $d_j(t)$, in the diabatic representation (Equation 3) via the unitary matrix, **U**, that diagonalizes the Tavis-Cummings matrix (*i.e.*, $c_m(t) = \sum_j^{N+n_{\text{modes}}} U_{mj}^\dagger d_j(t)$, with $U_{jm} = \beta_j^m$ if $j \leq N$ and $U_{jm} = \alpha_{j-N}^m$ if $j > N$).

To explore how the photonic character of the eigenstates affects their contribution to the overall transport, we decompose the total wave function into *partial* wave functions, $|\Psi_{\text{phot}}^{\text{part}}(t)\rangle$, within a narrow range of wave vectors. These partial wave functions are linear combinations of eigenstates (Equation 7) in fixed intervals of wave vectors (or energies). Each interval, called a window, w_i, is centered at $k_{z,i}$ and ranges from $k_{z,i}^{\text{min}}$ to $k_{z,i}^{\text{max}}$. The expansion coefficients, $c_{j\in w_i}(t)$, of these partial wave functions are thus obtained by projecting the adiabatic states within a window onto the total time-dependent wave function in the adiabatic representation (Equation 6).

In this analysis, we consider only the elements associated with the BSW modes, *i.e.*, the second term in Equation 7. This choice is justified by the fact that the excitonic part of the total wave function is more responsive to the excitation energy disorder[15], and unambiguous resolution of the transport regime based on the full partial wave function, which includes both excitonic and cavity components (*i.e.*, both terms in Equation 7) would have required averaging over more simulations than we can currently afford to run (five). Nevertheless, as we show in detail in the SI (Section 3.1), this choice does not change the conclusions that we draw below as the analysis of the propagation of a partial wave function with inclusion of both excitonic and photonic elements, yields very similar results, albeit with higher noise levels.

4 Results and Discussion

In Figure 2**c**, we show the time evolution of the probability density of the total polaritonic wave function, $|\Psi(t)|^2$, after excitation of a single MeB molecule, located at 125 μm. The wave packet rapidly expands, with the front of the wavepacket moving at the group velocity of the lower polartion (Figure 2S), and the tail remaining at the position where the molecule was excited. Such spreading of the wave packet suggests that the overall transport mechanism is a combination of ballistic motion and diffusion. To disentangle these two processes, we analyse how polaritonic states contribute to the transport as a function of their photonic content. To perform this analysis, we monitor the propagation of adiabatic states within fixed windows of k_z-vectors, two of which are illustrated as rectangles in Figure 2**b**.

In Figure 3**a** and **b**, we show the propagation of the partial photonic wave functions, $|\Psi_{\text{phot}}|^2$, associated with states in the window from $k_z = 9.25$ μm^{-1} to 9.75 μm^{-1}, and with states in the window from $k_z = 10.25$ μm^{-1} to $k_z = 10.75$ μm^{-1} (purple and orange rectangles in Figure 2**b**, respectively). The mean squared displacements (MSD) of these partial photonic wave packets are plotted in Figure 3**c**. The MSD plots for the other windows, as well as the probability densities, are shown in the SI (Section 3.1). By fitting the mean squared displacement to the general expression for MSD,

$$\text{MSD}(t) = 2D_\beta t^\beta, \tag{8}$$

we determine whether the propagation is ballistic or diffusive from the value of the transport exponent, β. Purely ballistic transport corresponds to $\beta = 2$, whereas pure diffusion corresponds to

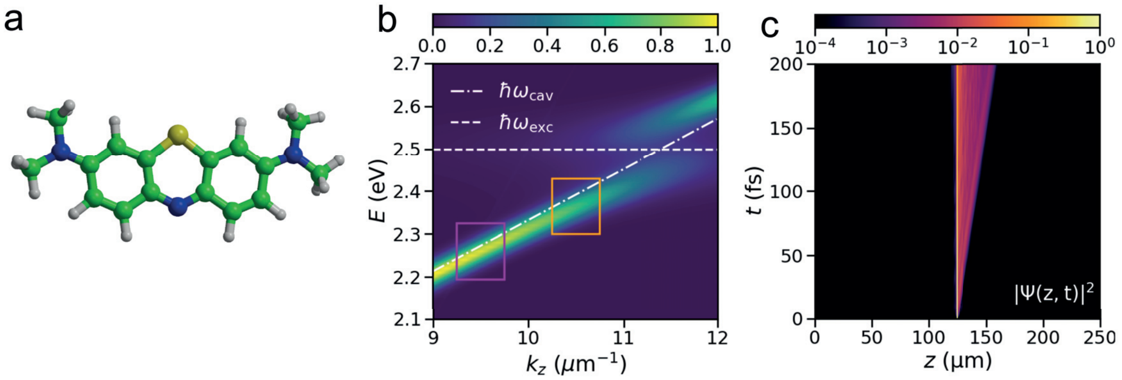

Figure 2: Panel **a**: Molecular structure of Methylene Blue (MeB) molecule. The electronic ground (S_0) and excited (S_1) states are calculated at the QM level with density functional theory (DFT) and time-dependent (TD)DFT, respectively, using the B97 functional and the 3-21G basis set. The solvent molecules (water, not shown) are described at the MM level with the TIP3P model. Carbon atoms are shown in green, nitrogen atoms – in blue, sulfur atom – in yellow, and hydrogen atoms – in grey. Panel **b**: Normalised angle-resolved absorption spectrum of the MeB-Bloch surface wave (BSW) system. The dashed line corresponds to the excitation energy of MeB at 2.50 meV at the TDDFT/B97//3-21G level of theory, and the dashed-dotted line shows the BSW dispersion. The purple and orange rectangles indicate two specific windows of the wave vector, through which the partial photonic wave function, $|\Psi_{\text{phot}}^{\text{part}}\rangle$, was extracted and plotted in Figure 3. Panel **c**: Space-time map of the probability amplitude of the total wave function, $|\Psi(z,t)|^2$.

the transport exponent equal to unity with D_β becoming the diffusion coefficient.

In Figure 3**e** we plot the value of the transport exponent for the partial photonic wave functions extracted from the windows of width $\Delta k_z = 0.5\ \mu\text{m}^{-1}$ and with the central wave vector in the range between $k_z^c = 9.25\ \mu\text{m}^{-1}$ and $k_z^c = 10.75\ \mu\text{m}^{-1}$ with a step of $0.25\ \mu\text{m}^{-1}$, as a function of the Hopfield coefficient ($|\alpha_{\text{ph}}|^2$, Equation 7) at the center of the windows (Table S2). The plot suggests that shifting the window upwards along the lower polariton branch towards states with a lower photonic content is accompanied by a change in the transport exponent, β from two to one, indicating a transition between ballistic propagation and diffusion, in line with the experiment (Figure 3**d**)[14].

Such transition from ballistic to diffusive transport cannot be reproduced in simulations of two-level systems with a quasi-dynamic excitation energy disorder. In these simulations (Section 3.2 in the SI), the disorder was modelled by randomly drawing the excitation energies of the two-level

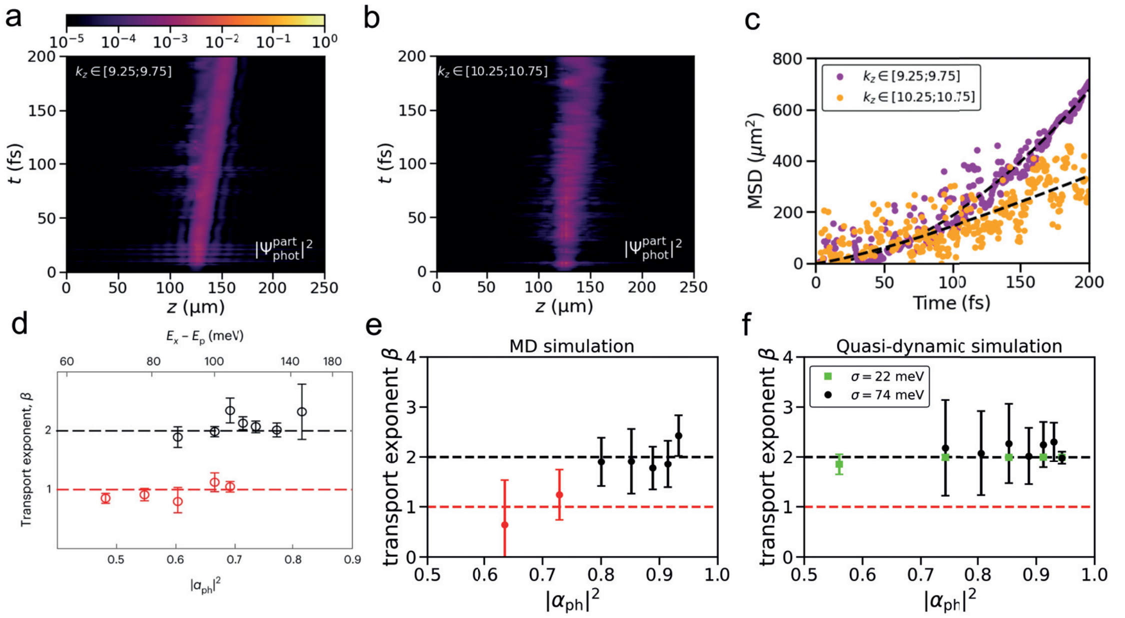

Figure 3: Panels **a**-**b**: Probability density, $|\Psi^{\text{part}}_{\text{phot}}|^2$, of the partial photonic wave function extracted through the windows depicted as purple (**a**) and orange (**b**) rectangles in Figure 2**b**. Panel **c**: MSD of the photonic wave function in panels **a**-**b**. The dashed lines correspond to the fit to $\text{MSD} = 2D_\beta t^\beta$ with β the transport exponent. Panels **d** and **e**: The transport exponent as a function of the cavity modes contribution $|\alpha_{\text{ph}}|^2$ to polaritonic states, extracted from the experiment (**d**) and MD simulations (**e**). Panel **d** is reproduced with permission from Balasubrahmaniyam et.al., *Nat. Mater.*, **22**, 338–344 (2023). Copyright 2023 Springer Nature Ltd. Panel **f**: Values extracted from simulations of two-level molecules with quasi-dynamic excitation energy disorder of $\sigma = 22$ meV (green squares) and $\sigma = 74$ meV (black circles). In panels **e** and **f**, the transport exponents were extracted from windows of width $\Delta k_z = 0.5\ \mu\text{m}^{-1}$ centred between $k_z = 9.25\ \mu\text{m}^{-1}$ and $k_z = 10.75\ \mu\text{m}^{-1}$ with a step of $0.25\ \mu\text{m}^{-1}$ (Table S2). The errors in panel **e** and **f** are standard deviations of, respectively, five and a hundred individual simulations.

systems from a Gaussian distribution

$$p(E) = \frac{1}{\sqrt{2\pi}\sigma} \exp\left[-\frac{(E - E_0)^2}{2\sigma^2}\right], \tag{9}$$

and resampling these energies every femtosecond of simulation.[52] In Expression 9, E_0 is the mean value, and σ is the "disorder strength" that determines the absorption line-width of the disordered two-level system. As shown in Figure 3**f**, the transport exponent remains close to $\beta = 2$ in the full range of LP states with well-defined wave vectors[53,54]. For $\sigma = 74$ meV, which matches the line-width of MeB QM/MM model used in our atomistic MD simulations, LP states are well defined for states with $|\alpha_{\text{ph}}|^2 > 0.64$, whereas for $\sigma = 22$ meV, which is typical of J-aggregates[55,56], the LP is well-defined for states with $|\alpha_{\text{ph}}|^2 > 0.45$.

Comparing the data for MD and quasi-dynamic simulations in Figure 3**e** and **f**, thus suggests a decisive role of molecular vibrations in modifying the mechanism of polariton transport along the lower polariton branch. Because the strength of non-adiabatic coupling is inversely proportional to the energy gap between polariton states[57], population transfer between dark states, which are distributed around the molecular absorption maximum on the one hand, and the low-energy, highly-photonic LP states on the other hand, is unlikely, resulting in a scattering-free ballistic propagation of population in these states. Moving up in energy along the LP branch towards higher k_z-vectors, reduces the energy gap and can lead to overlap with the dark states manifold. Therefore, the transfer rate, and hence the likelihood of population getting transiently trapped in the dark states reservoir increases significantly. Eventually, a continuous population exchange between stationary dark states and propagating bright states, replenished from the reservoir, renders propagation less ballistic-like and more diffusive-like as polaritonic states become closer in energy to the dark states.

To further demonstrate the importance of molecular vibrations for the observed crossover between regimes of polariton transport, we performed MD simulations of $N = 1024$ MeB molecules in vacuum with restraints imposed on the length of all bonds and constraints on the out-of-plane motion of carbon and nitrogen atoms (Section 3.3 in the SI). Because the nonadiabatic coupling is dependent on the overlap between the nonadiabatic coupling vector between polariton states, $|\psi_m\rangle$ and $|\psi_l\rangle$,

$$\mathbf{d}_{m,l} = \frac{\langle\psi_l|\nabla_{\mathbf{R}}\hat{H}^{\text{TC}}|\psi_m\rangle}{E_m - E_l}, \tag{10}$$

with $\mathbf{R}$ the vector containing coordinates of all atoms in a molecule, and the vector of atomic velocities, $\dot{\mathbf{R}}$[57], the imposed restrictions lead to the reduction of the nonadiabatic coupling via suppression of molecular motions, *i.e.*, $\dot{\mathbf{R}}$. As a result, all polariton states with a well-defined wave vector display ballistic transport with a propagation velocity close to the central group velocity of each window (Figure S9), and no crossover occurs.

Finally, because the rate of the population exchange between dark and bright polariton states depends on the density of the latter states[58–64], we performed simulations in a system of $N = 120$ MeB molecules and $n_{\text{modes}} = 120$ BSW modes, which contains purely polaritonic states in the absence of excitation energy disorder, and no dark states (Section 3.4 in the SI). The simulation shows a nearly equal population of the molecular excitons and of the BSW modes (Figure S11), which indicates a less intensive population transfer into the manifold of dark states. As a consequence, the transition from ballistic motion to diffusion along the LP branch is not complete within the range of states with well-defined wave vectors, and the effect can only be fully captured when the ratio between the number of dark and bright states $N_{\text{dark}}/N_{\text{bright}} \gg 1$, as is the case in most experiments.

5 Conclusion

To summarize, we have performed molecular dynamics simulations of polariton transport in a system of Methylene blue molecules strongly coupled to the Bloch surface wave. In accordance with experiment,[14] our simulations demonstrate a transition between ballistic and diffusive propagation as the photonic contribution to polaritonic states decreases. Importantly, such a transition was not observed in a simulation of molecules with frozen nuclear degrees of freedom, which indicates the decisive role of non-adiabatic coupling in changing the transport regime along the LP branch.

Author Information

Corresponding Author

Email: ilia.sokolovskii@jyu.fi

ORCID

I. Sokolovskii: 0000-0003-3367-0660

G. Groenhof: 0000-0001-8148-5334

Funding

This work was supported by the Academy of Finland (Grant 332743).

Notes

The authors declare no competing financial interests.

Acknowledgements

We thank Tal Schwartz and M. Balasubrahmaniyam for fruitful discussions and for sharing the BSW dispersion data. We thank the Center for Scientific Computing (CSC-IT Center for Science) for very generous computer resources.

References

(1) Förster, T. Experimentelle und theoretische Untersuchung des zwischenmolekularen Übergangs von Elektronenanregungsenergie. *Z. Naturforsch. A* **1949**, *4*, 321–327.

(2) Dexter, D. L. A Theory of Sensitized Luminescence in Solids. *J. Chem. Phys.* **1953**, *21*, 836–850.

(3) Mikhnenko, O. V.; Blom, P. W. M.; Nguyen, T.-Q. Exciton diffusion in organic semiconductors. *Energy Environ. Sci.* **2015**, *8*, 1867–1888.

(4) Sandik, G.; Feist, J.; García-Vidal, F. J.; Schwartz, T. Cavity-enhanced energy transport in molecular systems. *Nature Materials* **2024**,

(5) Törmä, P.; Barnes, W. L. Strong coupling between surface plasmon polaritons and emitters: a review. *Rep. Prog. Phys.* **2015**, *78*, 013901.

(6) Rider, M. S.; Barnes, W. L. Something from nothing: linking molecules with virtual light. *Contemporary Physics* **2022**, *62*, 217–232.

(7) Lerario, G.; Ballarini, D.; Fieramosca, A.; Cannavale, A.; Genco, A.; Mangione, F.; Gambino, S.; Dominici, L.; Giorgi, M. D.; Gigli, G.; Sanvitto, D. High-speed flow of interacting organic polaritons. *Light Sci. Appl.* **2017**, *6*, e16212.

(8) Rozenman, G. G.; Akulov, K.; Golombek, A.; Schwartz, T. Long-Range Transport of Organic Exciton-Polaritons Revealed by Ultrafast Microscopy. *ACS Photonics* **2018**, *5*, 105–110.

(9) Hou, S.; Khatoniar, M.; Ding, K.; Qu, Y.; Napolov, A.; Menon, V. M.; Forrest, S. R. Ultralong-Range Energy Transport in a Disordered Organic Semiconductor at Room Temperature Via Coherent Exciton-Polariton Propagation. *Adv. Mater.* **2020**, *32(28)*, 2002127.

(10) Pandya, R.; Chen, R. Y. S.; Gu, Q.; Sung, J.; Schnedermann, C.; Ojambati, O. S.; Chikkaraddy, R.; Gorman, J.; Jacucci, G.; Onelli, O. D.; Willhammar, T.; Johnstone, D. N.; Collins, S. M.; Midgley, P. A.; Auras, F.; Baikie, T.; Jayaprakash, R.; Mathevet, F.; Soucek, R.; Du, M.; Alvertis, A. M.; Ashoka, A.; Vignolini, S.; Lidzey, D. G.; Baumberg, J. J.; Friend, R. H.; Barisien, T.; Legrand, L.; Chin, A. W.; Yuen-Zhou, J.; Saikin, S. K.; Kukura, P.; Musser, A. J.; Rao, A. Microcavity-like exciton-polaritons can be the primary photoexcitation in bare organic semiconductors. *Nat. Commun.* **2021**, *12*, 6519.

(11) Pandya, R.; Ashoka, A.; Georgiou, K.; Sung, J.; Jayaprakash, R.; Renken, S.; Gai, L.; Shen, Z.; Rao, A.; Musser, A. J. Tuning the Coherent Propagation of Organic Exciton-Polaritons through Dark State Delocalization. *Adv. Sci.* **2022**, *9*, 2105569.

(12) Berghuis, M. A.; Tichauer, R. H.; de Jong, L.; Sokolovskii, I.; Bai, P.; Ramezani, M.; Murai, S.; Groenhof, G.; Rivas, J. G. Controlling Exciton Propagation in Organic Crystals through Strong Coupling to Plasmonic Nanoparticle Arrays. *ACS Photonics* **2022**, *9*, 123.

(13) Xu, D.; Mandal, A.; Baxter, J. M.; Cheng, S.-W.; Lee, I.; Su, H.; Liu, S.; Reichman, D. R.;

Delor, M. Ultrafast imaging of coherent polariton propagation and interactions. *Nat. Comm.* **2023**, *14*, 3881.

(14) Balasubrahmaniyam, M.; Simkovich, A.; Golombek, A.; Ankonina, G.; Schwartz, T. Unveiling the mixed nature of polaritonic transport: From enhanced diffusion to ballistic motion approaching the speed of light. *Nat. Mater.* **2023**, *22*, 338–344.

(15) Agranovich, V. M.; Gartstein, Y. N. Nature and Dynamics of Low-Energy Exciton Polaritons in Semiconductor Microcavities. *Phys. Rev. B* **2007**, *75*, 075302.

(16) Litinskaya, M. Propagation and Localization of Polaritons in Disordered Organic Microcavities. *Phys. Lett. A* **2008**, *372*, 3898–3903.

(17) Schachenmayer, J.; Genes, C.; Tignone, E.; Pupillo, G. Cavity enhanced transport of excitons. *Phys. Rev. Lett.* **2015**, *114*, 196403.

(18) Feist, J.; Garcia-Vidal, F. J. Extraordinary Exciton Conductance Induced by Strong Coupling. *Phys. Rev. Lett.* **2015**, *114*, 196402.

(19) Allard, T. F.; Weick, G. Disorder-enhanced transport in a chain of lossy dipoles strongly coupled to cavity photons. *Phys. Rev. B* **2022**, *106*, 245424.

(20) Ribeiro, R. F. Multimode polariton effects on molecular energy transport and spectral fluctuations. *Comm. Chem.* **2022**, *5*, 48.

(21) Aroeira, G. J. R.; Kairys, K. T.; Ribeiro, R. F. Theoretical Analysis of Exciton Wave Packet Dynamics in Polaritonic Wires. *J. Phys. Chem. Lett.* **2023**, *14*, 5681–5691.

(22) Osipov, A. N.; Iorsh, I. V.; Yulin, A. V.; Shelykh, I. A. Transport regimes for exciton polaritons in disordered microcavities. *Phys. Rev. B* **2023**, *108*, 104202.

(23) Engelhardt, G.; Cao, J. Polariton Localization and Dispersion Properties of Disordered Quantum Emitters in Multimode Microcavities. *Phys. Rev. Lett.* **2023**, *130*, 213602.

(24) Tutunnikov, I.; Qutubuddin, M.; Sadeghpour, H. R.; Cao, J. Characterization of Polariton Dynamics in a Multimode Cavity: Noise-enhanced Ballistic Expansion. *ArXiv* **2024**, *2410.11051v1*.

(25) Zhou, Z.; Chen, H.-T.; Sukharev, M.; Subotnik, J. E.; Nitzan, A. Nature of polariton transport in a Fabry-Perot cavity. *Phys. Rev. A* **2024**, *109*, 033717.

(26) Luk, H. L.; Feist, J.; Toppari, J. J.; Groenhof, G. Multiscale Molecular Dynamics Simulations of Polaritonic Chemistry. *J. Chem. Theory Comput.* **2017**, *13*, 4324–4335.

(27) Tichauer, R. H.; Feist, J.; Groenhof, G. Multi-scale Dynamics Simulations of Molecular Polaritons: the Effect of Multiple Cavity Modes on Polariton Relaxation. *J. Chem. Phys.* **2021**, *154*, 104112.

(28) Sokolovskii, I.; Tichauer, R. H.; Morozov, D.; Feist, J.; Groenhof, G. Multi-scale molecular dynamics simulations of enhanced energy transfer in organic molecules under strong coupling. *Nature Commun.* **2023**, *14*, 6613.

(29) Sokolovskii, I.; Goenhof, G. Non-Hermitian molecular dynamics simulations of exciton–polaritons in lossy cavities. *J. Chem. Phys.* **2024**, *160*, 092501.

(30) Shi, L.; Hakala, T. K.; Rekola, H. T.; Martikainen, J.-P.; Moerland, R. J.; Törmä, P. Spatial Coherence Properties of Organic Molecules Coupled to Plasmonic Surface Lattice Resonances in the Weak and Strong Coupling Regimes. *PRL* **2014**, *112*, 153002.

(31) Michetti, P.; Rocca, G. C. L. Polariton states in disordered organic microcavities. *Phys. Rev. B.* **2005**, *71*, 115320.

(32) Warshel, A.; Levitt, M. Theoretical studies of enzymatic reactions: Dielectric, electrostatic and steric stabilization of carbonium ion in the reaction of lysozyme. *J. Mol. Biol.* **1976**, *103*, 227–249.

(33) Sakoda, K. *Optical Properties of Photonic Crystals*; Optical Sciences; Springer Berlin Heidelberg, 2005.

(34) Meade, R. D.; Brommer, K. D.; Rappe, A. M.; Joannopoulos, J. D. Electromagnetic Bloch waves at the surface of a photonic crystal. *Phys. Rev. B* **1991**, *44*, 10961.

(35) Robertson, W. M.; Arjavalingam, G.; Meade, R. D.; Brommer, K. D.; Rappe, A. M.; Joannopoulos, J. D. Observation of surface photons on periodic dielectric arrays. *Opt. Lett.* **1993**, *18*, 528–530.

(36) Rashidi, K.; Michail, E.; Salcido-Santacruz, B.; Paudel, Y.; Menon, V. M.; Sfeir, M. Y. Efficient and Tunable Photochemical Charge Transfer via Long-Lived Bloch Surface Wave Polaritons. *Arxiv* **2024**, *2409.02067v1*.

(37) Koju, V. Computational modeling of Bloch surface waves in one-dimensional periodic and aperiodic multilayer structures. Ph.D. thesis, Middle Tennessee State University, 2017.

(38) Barachati, F.; Fieramosca, A.; Hafezian, S.; Gu, J.; Chakraborty, B.; Ballarini, D.; Martinu, L.; Menon, V.; Sanvitto, D.; Kéna-Cohen, S. Interacting polariton fluids in a monolayer of tungsten disulfide. *Nat. Nanotechnol.* **2018**, *13*, 906–909.

(39) Hohenberg, P.; Kohn, W. Imhomogeneous Electron Gas. *Phys. Rev.* **1964**, *136*, 864–871.

(40) Runge, E.; Gross, E. K. U. Density-Functional Theory for Time-Dependent Systems. *Phys. Rev. Lett.* **1984**, *52*, 997–1000.

(41) Casida, M. E.; Jamorski, C.; Casida, K. C.; Salahub, D. R. Molecular excitation energies to high-lying bound states from time-dependent density-functional response theory: Characterization and correction of the time-dependent local density approximation ionization threshold. *J. Chem. Phys.* **1998**, *108*, 4439–4449.

(42) Becke, A. D. Density-functional thermochemistry. V. Systematic optimization of exchange-correlation functionals. *J. Chem. Phys.* **1997**, *107*, 8554–8560.

(43) Jorgensen, W. L.; Chandrasekhar, J.; Madura, J. D.; Impey, R. W.; Klein, M. L. Comparison of simple potential functions for simulatin liquid water. *J. Chem. Phys.* **1983**, *79*, 926–935.

(44) de Queiroz, T. B.; de Figueroa, E. R.; Coutinho-Neto, M. D.; Maciel, C. D.; Tapavicza, E.; Hashemi, Z.; Leppert, L. First principles theoretical spectroscopy of methylene blue: Between limitations of time-dependent density functional theory approximations and its realistic description in the solvent. *The Journal of Chemical Physics* **2021**, *154*, 044106.

(45) Dunnett, A. J.; Gowland, D.; Isborn, C. M.; Chin, A. W.; Zuehlsdorff, T. J. Influence of non-adiabatic effects on linear absorption spectra in the condensed phase: Methylene blue. *The Journal of Chemical Physics* **2021**, *155*, 144112.

(46) Le Guennic, B.; Jacquemin, D. Taking Up the Cyanine Challenge with Quantum Tools. *Accounts of Chemical Research* **2015**, *48*, 530–537.

(47) Galego, J.; Garcia-Vidal, F. J.; Feist, J. Cavity-Induced Modifications of Molecular Structure in the Strong-Coupling Regime. *Phys. Rev. X* **2015**, *5*, 041022.

(48) Jaynes, E. T.; Cummings, F. W. Comparison of quantum and semiclassical radiation theories with application to the beam maser. *Proc. IEEE* **1963**, *51*, 89–109.

(49) Tavis, M.; Cummings, F. W. Approximate solutions for an N-molecule radiation-field Hamiltonian. *Phys. Rev.* **1969**, *188*, 692–695.

(50) Ehrenfest, P. Bemerkung über die angenäherte Gültigkeit der klassischen Mechanik innerhalb der Quantenmechanik. *Z. Phys.* **1927**, *45*, 445–457.

(51) Bussi, G.; Donadio, D.; Parrinello, M. Canonical sampling through velocity rescaling. *J. Chem. Phys.* **2007**, *126*, 014101.

(52) Cui, B.; Sukharev, M.; Nitzan, A. Short-time particle motion in one and two-dimensional lattices with site disorder. *J. Chem. Phys.* **2023**, *158*, 164112.

(53) Agranovich, V. M.; Litinskaia, M.; Lidzey, D. G. Cavity polaritons in microcavities containing disordered organic semiconductors. *Phys. Rev. B* **2003**, *67*, 085311.

(54) Litinskaya, M.; Reineker, P.; Agranovich, V. M. Fast polariton relaxation in strongly coupled organic microcavities. *J. Lumin.* **2004**, *110*, 364–372.

(55) Hobson, P. A.; Barnes, W. L.; Lidzey, D. G.; Gehring, G. A.; Whittaker, D. M.; Skolnick, M. S.; Walker, S. Strong exciton–photon coupling in a low-Q all-metal mirror microcavity. *Appl. Phys. Lett.* **2002**, *81*, 3519–3521.

(56) Wenus, J.; Ceccarelli, S.; Lidzey, D. G.; Tolmachev, A. I.; Slominskii, J. L.; Bricks, J. L. Optical strong coupling in microcavities containing J-aggregates absorbing in near-infrared spectral range. *Org. Electron.* **2007**, *8*, 120–126.

(57) Tichauer, R. H.; Morozov, D.; Sokolovskii, I.; Toppari, J. J.; Groenhof, G. Identifying Vibrations that Control Non-Adiabatic Relaxation of Polaritons in Strongly Coupled Molecule-Cavity Systems. *J. Phys. Chem. Lett.* **2022**, *13*, 6259–6267.

(58) del Pino, J.; Feist, J.; Garcia-Vidal, F. J. Quantum Theory of Collective Strong Coupling of Molecular Vibrations with a Microcavity Mode. *New J. Phys.* **2015**, *17*, 053040.

(59) Ulusoy, I. S.; Gomez, J. A.; Vendrell, O. Modifying the Nonradiative Decay Dynamics through Conical Intersections via Collective Coupling to a Cavity Mode. *J. Phys. Chem. A* **2019**, *123*, 8832–8844.

(60) Eizner, E.; Martínez-Martínez, L. A.; Yuen-Shou, J.; Kéna-Cohen, S. Inverting Singlet and Triplet Excited States using Strong Light-Matter Coupling. *Sci. Adv.* **2019**, *5*, aax4482.

(61) Davidsson, E.; Kowalewski, M. The role of dephasing for dark state coupling in a molecular Tavis–Cummings model. *J. Chem. Phys.* **2023**, *159*, 044306.

(62) Bhuyan, R.; Lednev, M.; Feist, J.; Börjesson, K. The Effect of the Relative Size of the Exciton Reservoir on Polariton Photophysics. *Adv. Opt. Mater.* **2023**, *12*, 2301383.

(63) Pérez-Sánchez, J. B.; Yuen-Zhou, J. Radiative pumping vs vibrational relaxation of molecular polaritons: a bosonic mapping approach. 2024; `https://arxiv.org/abs/2407.20594`.

(64) Sokolovskii, I.; Morozov, D.; Groenhof, G. One molecule to couple them all: Toward realistic numbers of molecules in multiscale molecular dynamics simulations of exciton-polaritons. *J. Chem. Phys.* **2024**, *161*, 134106.

PV

PHOTOCHEMICAL INITIATION OF POLARITON-MEDIATED EXCITON PROPAGATION

by

I. Sokolovskii, G. Groenhof

Nanophotonics, 13, 2687 – 2694, **2024**.

https://doi.org/10.1515/nanoph-2023-0684

DE GRUYTER Nanophotonics 2024; aop

Letter

Ilia Sokolovskii and Gerrit Groenhof*

Photochemical initiation of polariton-mediated exciton propagation

https://doi.org/10.1515/nanoph-2023-0684
Received October 11, 2023; accepted December 20, 2023;

Abstract: Placing a material inside an optical cavity can enhance transport of excitation energy by hybridizing excitons with confined light modes into polaritons, which have a dispersion that provides these light–matter quasi-particles with low effective masses and very high group velocities. While in experiments, polariton propagation is typically initiated with laser pulses, tuned to be resonant either with the polaritonic branches that are delocalized over many molecules, or with an uncoupled higher-energy electronic excited state that is localized on a single molecule, practical implementations of polariton-mediated exciton transport into devices would require operation under low-intensity incoherent light conditions. Here, we propose to initiate polaritonic exciton transport with a photo-acid, which upon absorption of a photon in a spectral range not strongly reflected by the cavity mirrors, undergoes ultra-fast excited-state proton transfer into a red-shifted excited-state photoproduct that can couple collectively with a large number of suitable dye molecules to the modes of the cavity. By means of atomistic molecular dynamics simulations we demonstrate that cascading energy from a photo-excited donor into the strongly coupled acceptor-cavity states via a photochemical reaction can indeed induce long-range polariton-mediated exciton transport.

Keywords: strong light-matter coupling; exciton-polariton; quantum chemistry; quantum optics; molecular dynamics; exciton transport

1 Introduction

Organic opto-electronic materials offer many advantages over their silicon counterparts, such as lower production cost, smaller weight, higher flexibility and easier disposability, but are hampered by low exciton mobility [1]. Enhancing that mobility therefore has become a major optimization target and several solutions have been proposed, which include increasing the lifetime via triplet formation [2], [3], ordering molecules to increase exciton delocalization [4]–[7], or coupling the excitons to the confined light modes of an optical resonator [8]–[16]. Because the latter solution does not require chemical modifications of the molecules, which may compromise other properties, utilizing strong light–matter coupling could be a promising route towards improving the performance of organic opto-electronic devices.

Because the confinement of light into smaller volumes by an optical resonator increases the interaction with molecular transitions [17], the enhanced exciton mobility in the strong coupling regime has been attributed to hybridization of excitons and confined light modes into polaritons [18]–[23], which can form when the interaction strength exceeds the decay rates of both excitons and cavity modes [24], [25]. The hybrid states with contributions from cavity modes are bright and can hence be accessed optically [26]–[28]. Because the cavity mode energy depends on the in-plane momentum, or wave-vector, k_z, these states have dispersion and form the upper and lower polaritonic branches, as shown in Figure 1f. These branches are separated by the Rabi splitting, which is defined as the energy gap at the wave-vector for which the energy of the exciton and cavity dispersion is resonant. Most of the hybrid states, however, have negligible contribution from the cavity modes, and are hence dark [29]. These dark states therefore also lack dispersion and form a quasi-degenerate manifold instead that is situated in between the two bright polaritonic branches.

Owing to their dispersion, the bright polaritonic states support ballistic propagation of population at their group velocity (*i.e.*, $v_g = \partial\omega(k_z)/\partial k_z$, with $\hbar\omega(k_z)$ the energy of a polariton with in-plane momentum k_z,

---

***Corresponding author: Gerrit Groenhof**, Nanoscience Center and Department of Chemistry, University of Jyväskylä, P.O. Box 35, 40014 Jyväskylä, Finland, E-mail: gerrit.x.groenhof@jyu.fi. https://orcid.org/0000-0001-8148-5334
Ilia Sokolovskii, Nanoscience Center and Department of Chemistry, University of Jyväskylä, P.O. Box 35, 40014 Jyväskylä, Finland, E-mail: ilia.i.sokolovskii@jyu.fi. https://orcid.org/0000-0003-3367-0660

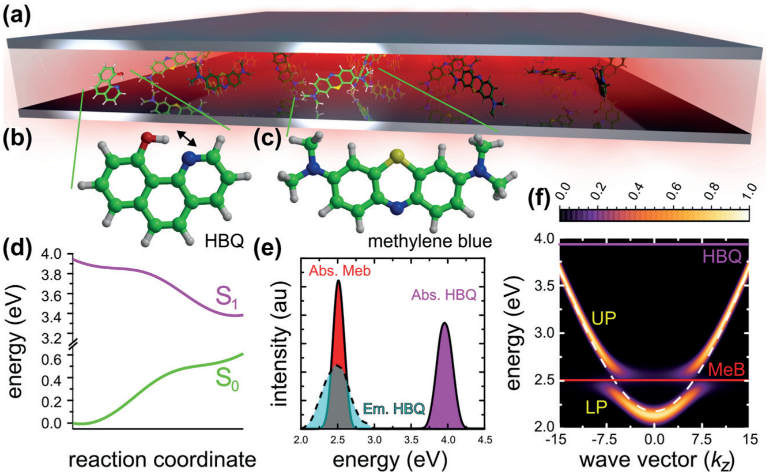

Figure 1: Illustration of a Fabry–Pérot microcavity (panel (a), not to scale) containing a 10-hydroxybenzo[h]quinoline donor molecule (HBQ, panel (b)) and 1023 methylene blue acceptor molecules (MeB, panel (c)). The first singlet excited states (S_1) of the MeB molecules are coupled to the 239 modes of the cavity. Upon absorbing a photon at a frequency where the mirrors have become more transparent (∼3.96 eV at the TDA-CAMB3LYP/3-21G level of theory, Figure S4 in SM), the uncoupled HBQ undergoes ultra-fast intra-molecular proton transfer on the S_1 excited-state potential energy surface (panel (d)) into an excited-state photo-product that is resonant with both the absorption maximum of MeB and the cavity. Panel (e) shows the normalised QM/MM absorption (magenta) and emission (cyan) spectra of HBQ and the absorption spectrum of MeB (red). The normalised angle-resolved absorption spectrum of the molecule-cavity system (panel (f)) shows the Rabi splitting of 282 meV between the lower polariton (LP) and upper polariton (UP) branches. The cavity dispersion is plotted as a white dashed line, while the excitation maxima of the MeB molecules (∼2.5 eV at the TD-B97/3-21G level of theory) and HBQ are plotted as straight red and magenta lines, respectively.

Figure S3 in Supplementary Material, SM) [15], [18], [19], [22], [23], [30], [31]. However, while in inorganic micro-cavities, such ballistic propagation was indeed observed [32], [33], transport in organic micro-cavities is a diffusion process because of rapid dephasing in disordered organic materials [19]. Results from molecular dynamics (MD) simulations suggest that such dephasing is due to reversible exchange of population between the stationary dark states and propagating polaritonic states [13], [34], [35]. Although polariton-mediated exciton transport is not ballistic in organic systems, polaritonic diffusion can still dramatically outperform the intrinsic exciton diffusivity of the material [9], [16]. However, despite several experimental realizations [8], [9], [13]–[15], and an emerging theoretical understanding of polariton propagation in organic microcavities [18]–[23], [30], [31], [36], [37], strong light–matter coupling has so far not been leveraged systematically for practical applications.

One of the obstacles on the path to polaritonic devices for enhanced exciton transfer is that polariton propagation requires laser excitation of either wavepackets of polaritonic states [11], [14], or higher-energy electronic states of the molecules [8]–[10], [16]. Yet, for practical applications, such as light-harvesting, it will be essential that transport can also be initiated with low-intensity incoherent light sources. To address this specific challenge for a Fabry–Pérot optical resonator, we propose to initiate polariton propagation in a strongly coupled molecule-cavity system with a suitable donor that, upon excitation at wavelengths for which the cavity mirrors are transparent [38], undergoes a rapid photo-chemical reaction into an excited-state photo-product with an emission maximum that is resonant with both the cavity and acceptor dye molecules. As illustrated in Figures 1 and 2, such system could potentially be realized if we combine 10-hydroxybenzo[h]quinoline (HBQ) that upon excitation at 375 nm or 360 nm undergoes ultra-fast excited-state intra-molecular proton transfer (ESIPT) on a femtosecond timescale into a photo-product with a broad emission centered at 620 nm [39], [40], with methylene blue (MeB) in an optical micro-cavity made of silver mirrors and resonant with the broad absorption peaks of MeB at 668 nm or 609 nm (Figure S4, in the Supplementary Material). Here, we demonstrate the feasibility of this concept by means of hybrid quantum mechanics/molecular mechanics (QM/MM) molecular dynamics simulations [41], [42].

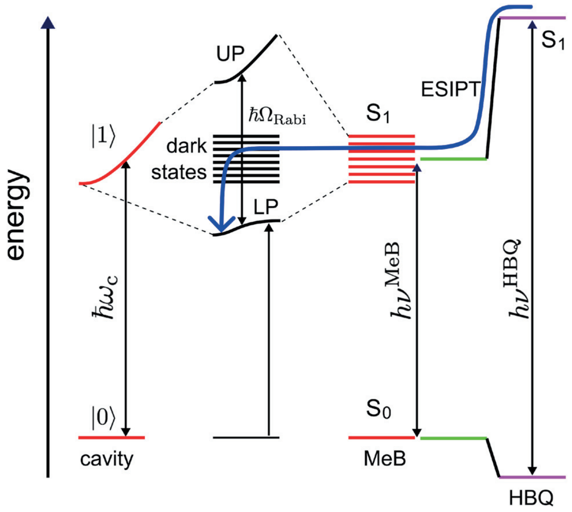

Figure 2: Simplified Jablonski diagram of states involved in photo-chemically induced polariton propagation. The cavity modes and polaritons are schematically shown as continuous dispersions. After photo-excitation of HBQ at $h\nu^{\rm HBQ}$, excited-state intra-molecular proton transfer (ESIPT) brings the excited state population that was initially localized on HBQ, into the dark state manifold. Reversible population exchanges between the stationary dark states and the propagating lower polaritonic (LP) bright states cause the population to move away from the HBQ molecule and diffuse into the cavity [34]. The path along which the population arrives in the LP states is illustrated by a blue arrow.

2 Materials and methods

2.1 Multiscale Tavis–Cummings model

We performed QM/MM MD simulations [43], [44] of one HBQ molecule solvated in cyclohexane and 1023 hydrated MeB molecules strongly coupled to the confined light modes of a one dimensional Fabry–Pérot micro-cavity (Figure S1) [45]. Within the Born–Oppenheimer approximation, we separate the nuclear degrees of freedom, which we treat classically, from the electronic plus cavity degrees of freedom, which we treat quantum mechanically with the QM/MM extension of the traditional Tavis–Cummings model of quantum optics [46], [47]. In the Supplementary Material (SM), we provide a concise description of our multi-scale simulation approach, which was presented in detail in previous publications [41], [42], [48].

2.2 HBQ model

In the QM/MM Tavis–Cummings Hamiltonian, the electronic ground (S_0) and excited (S_1) states of HBQ were modeled with density functional theory (DFT) [49] and time-dependent density functional theory (TDDFT) [50] within the Tamm–Dancoff approximation (TDA) [51], respectively, using the CAM-B3LYP functional [52], [53] in combination with the 3-21G basis set [54]. The cyclohexane solvent molecules were modelled with the GROMOS 2016H66 force field [55]. At this level of theory, the vertical excitation energy of HBQ is $h\nu^{\rm HBQ} = 3.96$ eV (312 nm) with a full width at half maximum (FWHM) of 270 meV, while the energy gap to the ground state is 2.58 eV (480 nm, 500 meV FWHM) in the S_1 minimum (Figure 1e). Despite the overestimation of the S_1–S_0 energy gap with respect to experiment (3.3 eV for absorption and 2.0 eV for emission), our model provides potential energy surfaces (Figure 1d) that are in qualitative agreement with the more accurate description at the TPSSh/cc-pVDZ level of theory for this system (Figure S5 in SM) [56], [57].

2.3 MeB model

The S_0 and S_1 electronic states of MeB were modelled with DFT and TDDFT based on the Casida equations [58], respectively, using the B97 functional [59] and the 3-21G basis set. The water molecules were described with the TIP3P model [60]. Although at this level of theory, the vertical excitation energy of MeB is $h\nu^{\rm MeB} = 2.5$ eV (210 meV FWHM), and thus significantly overestimated with respect to experiment, there is a fortuitous overlap with the emission of HBQ that we exploit in this work (Figure 1e). Thus, while MeB may not be the optimal choice for a practical realization, this dye should be suitable for demonstrating the feasibility of inducing polariton-mediated exciton transport with a photo-chemical reaction in our simulations. Further details of the HBQ and MEB simulation setups are provided in the SM.

2.4 HBQ/MeB cavity model

From a QM/MM trajectory of HBQ in the S_0 state, single HBQ snapshots were selected and combined with 1023 frames from a QM/MM trajectory of MeB in S_0. These 1024 molecules, including their solvent environments, were placed at equal inter-molecular separations on the z-axis of a 1D [45], 50 μm long, symmetric optical Fabry–Pérot micro-cavity (Figure S1), with HBQ at the center of the cavity (*i.e.*, $z_{\rm HBQ} = 25$ μm). In our setup, z indicates the in-plane direction (*i.e.*, parallel to the mirrors). With a distance of $L_x = 284$ nm between the mirrors (cavity width), where x indicates the out-of-plane direction (*i.e.*, perpendicular to the mirrors), the fundamental mode of the cavity has an energy of $\hbar\omega_0 = 2.18$ eV at normal incidence (*i.e.*, $k_z = 0$) and hence its dispersion is red-detuned by 320 meV with respect to the Methylene Blue absorption maximum at 2.5 eV (vertical red line in Figure 1f). The dispersion of the cavity was modelled with 239 discrete modes (*i.e.*, $k_{z,p} = 2\pi p/L_z$ with $-119 \leq p \leq 119$ and $L_z = 50$ μm). To maximize the collective light–matter coupling strength, the transition dipole moments of all molecules were aligned to the vacuum field, which is parallel to the y-axis of the cavity, at the start of the simulation. With a vacuum field strength of $\mathbf{E}_y = 0.00004$ (0.21 MVcm^{-1}) the Rabi splitting, defined as the energy gap between the UP and LP at the wave vector where the molecular excitation energy matches the cavity mode energy, is 282 meV. Simulations were performed for a lossy cavity with a decay rate of $\hbar\gamma_{\rm cav} = 0.04$ eV or $\gamma_{\rm cav} = 66.7$ ps^{-1}. At such rate, the lifetime, $\tau_{\rm cav}$, of the lossy cavity is comparable to the 2–14 fs lifetimes of metallic Fabry–Pérot cavities used in experiments on strong coupling with organic molecules [9], [61], [62]. With a lifetime of 15 fs and a resonance at 2.18 eV, the quality-factor, defined as $Q = \omega_{\rm cav}\tau_{\rm cav}$, would be 50 for our cavity. In addition, we also performed simulations in a better cavity with a decay rate of $\gamma_{\rm cav} = 10$ ps^{-1}, as well as an ideal cavity with an infinite lifetime (*i.e.*, $\gamma_{\rm cav} = 0$ ps^{-1}).

Because the molecules do not interact directly, but rather via the cavity modes, there are no issues in using different QM/MM descriptions for HBQ and MeB. Although the solvents, as well as the force fields and QM methods, were chosen because of convenience, we emphasize that for the purpose of this work it is not essential to have the most accurate description of the bare excitation energies of the molecules, but rather to have a realistic model of the molecular degrees of freedom, including the solvent environment. We speculate that for practical realizations HBQ could be embedded via small micro-droplets of a suitable solvent within the polymer matrix containing MeB, or *vice versa*.

2.5 Molecular dynamics simulations

Ehrenfest MD trajectories were computed by numerically integrating Newton's equations of motion using a leap-frog algorithm with a 0.5 fs time step [63]. At each time step, the multi-mode Tavis–Cummings Hamiltonian (Equation (1) in SM) is constructed in the basis of product states between the N molecular excitations, obtained from QM/MM calculations [64], and the n_{mode} cavity mode excitations:

$$|\phi_j\rangle = \hat{\sigma}_j^+|S_0^1S_0^2..S_0^{N-1}S_0^N\rangle \otimes |00..0\rangle \tag{1}$$

for $1 \leq j \leq N$, and

$$|\phi_{j>N}\rangle = \hat{a}_{j-N}^\dagger|S_0^1S_0^2..S_0^{N-1}S_0^N\rangle \otimes |00..0\rangle \tag{2}$$

for $N < j \leq N + n_{\text{mode}}$. In these expressions, $|S_0^i\rangle$ indicates that molecule i is in the electronic ground state, while $|00..0\rangle$ indicates that the Fock states for all n_{mode} cavity modes are empty. The operators $\hat{\sigma}_j^+$ and $\hat{a}_p^\dagger$ excite molecule j and cavity mode p, respectively. Owing to the orthogonality of the electronic states and of the cavity modes, this basis is strictly diabatic within the single excitation subspace [48].

The total wave function, $|\Psi(t)\rangle$, was coherently propagated along with the classical degrees of freedom of the molecules as a time-dependent superposition of these diabatic product states (Equations (1) and (2)):

$$|\Psi(t)\rangle = \sum_j c_j(t)|\phi_j\rangle \tag{3}$$

with $c_j(t)$ the time-dependent expansion coefficients of the time-independent basis states $|\phi_j\rangle$. To account for the finite lifetime of the cavity modes, the wave function was propagated along the classical trajectory under the influence of an effective non-Hermitian Hamiltonian (SM), in which losses were added to the cavity mode energies (*i.e.*, $\hbar\omega(k_z) - i/2\hbar\gamma_{\text{cav}}$, with $\hbar\omega(k_z)$ the dispersion of the empty cavity, shown as a dashed white line in Figure 1f) [65]–[68].

To obtain also the adiabatic polaritonic eigenstates [46], [47], defined as

$$|\psi^m\rangle = \left(\sum_j^N \beta_j^m\hat{\sigma}_j^+ + \sum_p^{n_{\text{mode}}} \alpha_p^m\hat{a}_p^\dagger\right)|S_0^1S_0^2..S_0^{N-1}S_0^N\rangle|0\rangle \tag{4}$$

and required for analysis and the determination of the initial conditions for the simulations, we diagonalized the QM/MM Tavis–Cummings Hamiltonian (Equation (1) in SM). The β_j^m and α_p^m expansion coefficients reflect the contribution of the molecular excitons $\left(|S_1^j\rangle\right)$ and of the cavity mode excitations ($|1_p\rangle$) to the adiabatic state $|\psi^m\rangle$. All simulations were initiated in the highest-energy adiabatic state, $m = 1263$, for which $|\beta_{\text{HBQ}}^{1263}|^2 \approx 1$.

The simulations were performed with GROMACS version 4.5.3 [69], in which the multi-mode Tavis–Cummings QM/MM model was implemented [42], in combination with Gaussian16 [70]. The GROMACS source code is available for download from https://github.com/upper-polariton/GMXTC. The results presented in the main manuscript are averages over four trajectories, started with different initial conditions.

3 Results and discussion

In Figure 3, we plot the progress of the excited-state intramolecular proton transfer (ESIPT) reaction in HBQ, defined as the distance between the hydroxyl oxygen and the proton (a), the excitonic part of the total wavepacket $|\Psi_{\text{exc}}(z,t)|^2$ (b), the contributions of the molecular excitations to the total wave function, $|\Psi(z,t)|^2$ (c, d), and the mean squared displacement of the excitonic wavepacket (MSD$_{\text{exc}}$, e). After photo-excitation into the highest-energy eigenstate of the molecule-cavity system (*i.e.*, $|\psi^{1263}\rangle$, which is dominated by the S_1 electronic state of HBQ (*i.e.*, $|\beta_{\text{HBQ}}^{1263}|^2 > 0.999$, Figure 3c), the proton transfers from the hydroxyl oxygen to the nitrogen atom (Figure 3a). Because this enol to keto transformation is accompanied by a 1.4 eV red-shift of the S_1–S_0 energy gap (Figure 1d), HBQ becomes resonant with the MeB molecules as well as with the cavity modes (Figure 2), and enters the dark state manifold around 10 fs after excitation.

Because after the reaction, HBQ couples collectively with the MeB molecules to the cavity modes, population transfers from HBQ into the cavity modes (Figure S7), and starts propagating at the central group velocity of these modes. Although the propagation is ballistic, this motion is interrupted by population transfer from the propagating cavity modes into the strongly coupled MeB excitons (Figure 3d), which are stationary. Because this exchange is reversible (Figure S6), wavepacket propagation is diffusive rather than ballistic, as indicated by a linear dependence of the mean squared displacement on time (Figure 3e; for ballistic propagation, the MSD$_{\text{exc}}$ would be quadratic).

Because the excitation propagates along the molecules via the lossy cavity modes (Figure 3b), radiative decay competes with population transfer into the molecular states, which reduces the transport efficiency. To understand the influence of such losses, we repeated the simulations in a higher-Q cavity with a lifetime of 100 fs, as well as in an ideal cavity with an infinite lifetime. The results of these additional simulations, summarized in Figures S10 and S11, suggest that increasing the cavity Q-factor can significantly enhance the transport, in line with previous experiments [14] and simulations [35]. While the mechanism remains the same, the increase in the duration of the ballistic phases between the transfers from and into the molecular states, enhances the diffusion constant.

The initial structures for our simulations were sampled from equilibrium QM/MM trajectories at 300 K (SM) and therefore can capture the heterogeneity as indicated by the absorption line-widths of the molecules in Figure 1e. Because of such structural disorder, the ESIPT reaction rates

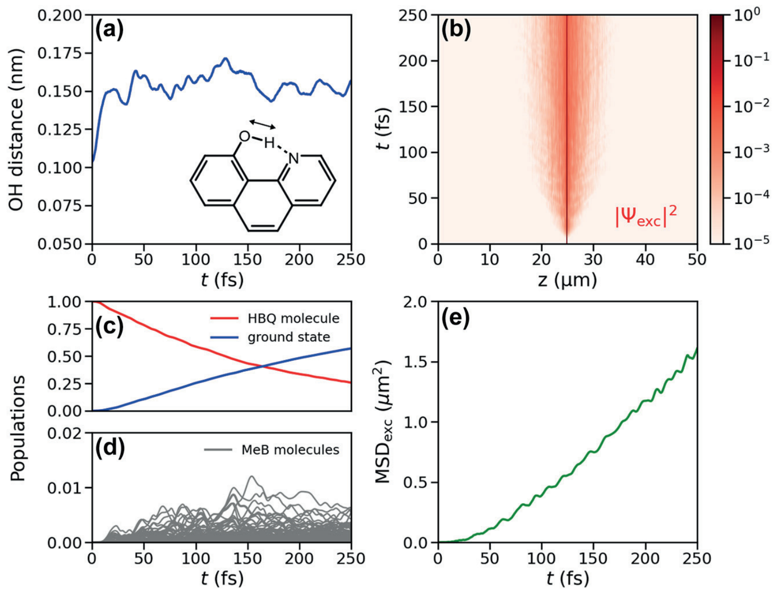

Figure 3: Panel (a) shows the distance between the oxygen and proton, which we use as the reaction coordinate for the excited-state proton transfer reaction (inset and see also Figure 1b) as a function of time after instantaneous excitation into the highest energy eigenstate of the molecule-cavity system, which is dominated by the S_1 state of HBQ (*i.e.*, $|\beta_{HBQ}|^2 \approx 0.99$, panel (c)). Panel (b) depicts the probability density of the excitonic part of the wave function $|\Psi_{exc}|^2$ as a function of the *z*-coordinate (horizontal axis) and time (vertical axis). Panels (c) and (d) show the contribution of the HBQ molecule (red) and the Methylene Blue molecules (grey) to the total wave function, as well as the population of the ground state (blue). Panel (e) shows the mean squared displacement (*i.e.*, $MSD_{exc} = \langle z(t) - z(0) \rangle^2$) of the excitonic wavepacket.

span a distribution. To confirm that the proton transfer in HBQ is required to initiate the polariton-mediated exciton transport process, we show in Figure S8 (SM) that for a system in which the ESIPT is delayed, also the transport starts at a later point in time, and that this time point coincides with the formation of the HBQ photo-product.

To provide further evidence that the photo-chemical reaction is essential for initiating transport, we also performed a simulation in which the bond distance between the oxygen and proton in HBQ is constrained [71]. Because with such constraint the proton cannot transfer, no photo-product that is resonant with the cavity can form. Therefore, population transfer is suppressed and exciton transport is not observed (Figure S9).

Because in our simulations, there are no restrictions on where the molecules are positioned, we could build a system in which HBQ was dissolved in cyclohexane but MeB in water. A practical realization, however, would likely require that both molecules are miscible within the same solvent or polymer material. While a wide variety of water-soluble photoacids [72], or other candidates for the photo-chemical initiation step are available, such compounds would not only require a sufficiently high absorptivity in the transparency windows of the cavity, but also a highly fluorescent photo-product, which itself must be formed with high quantum-yield.

Alternatively, if in addition to a bright S_1 electronic state, the strongly-coupled dye also has higher-energy electronic states that absorb within the transparency window of the cavity mirrors, polariton transport could be initiated via internal conversion from such higher-energy excited state into the S_1 state [73]. Indeed, laser excitation into a higher-energy electronic state has been used in previous experiments on polariton transport [8], [9], [13], [16]. However, for this mechanism to operate also under incoherent excitation conditions, the higher-energy transition has to be sufficiently strong, which could limit the selection of suitable molecules. Furthermore, if the transparency window is provided by a higher-order cavity mode, as in Figure S4 in SM, the higher-energy electronic transition of a single species can also strongly couple to the cavity and form delocalized polaritons with a rapid radiative decay channel that competes with the internal conversion process into a localized S_1 state. As initiating transport with a photo-chemical reaction does not require that the photo-reactive molecules are strongly coupled to the cavity, these molecules can be introduced at low concentration, potentially even at specific locations inside the cavity system, which might offer further advantages for practical applications of polariton-enhanced exciton transport.

Although at the level of theory employed in our simulations, the emission maximum of the HBQ photo-product matches the absorption maximum of the strongly coupled MeB acceptors, such matching is not a strict requirement. Instead, overlap with the lower polaritonic branch is sufficient, which can be controlled further by tuning the cavity resonance via the distance between the mirrors, or by tuning the coupling strength via the concentration of the acceptor dye. Indeed, as we show in the SM, adding a (artificial) blue-shift of 250 meV to the acceptor and the fundamental cavity mode, such that the emission maximum of HBQ overlaps with the LP branch rather than with the MeB absorption (Figure S12), does not affect the transport (Figure S13). The latter observation is consistent with experiments of Akselrod and co-workers who used emission from an uncoupled dye that is resonant with the lower polariton of a strongly coupled dye, to pump that lower polariton branch and trigger condensation [74].

The current limitations on computer hard- and software restrict the number of molecules we can model in our atomistic MD simulations to a few thousand, which is a few orders of magnitude smaller than the number of molecules in a real Fabry–Pérot cavity (*i.e.*, 10^6–10^8) [29], [75]. To reach the strong coupling regime under these conditions, and achieve a Rabi splitting of 282 meV, we therefore used a vacuum field strength that is significantly larger than in experiments. Because the light–matter coupling that drives the population transfer between dark and bright states, is inversely proportional to the number of molecules, N [29], [76], [77], the rate of population transfer also scales as $1/N$, and is thus much faster in our simulation than in experiment. In previous work [34], we had therefore investigated how the transport depends on N, and found that the propagation velocity scales as $1/N$ as well. Thus, even in the limit of realistic N, we would still expect polariton-mediated exciton transport to exceed the intrinsic exciton diffusion process in organic materials, in line with experimental observations [9].

4 Conclusions

To summarize, the results of our MD simulations suggest that long-range polariton-mediated exciton transport can be induced with an excited-state proton transfer reaction. While the excitation scheme proposed here resembles the off-resonant laser excitation conditions employed in previous experiments on polariton transport [8], [9], [13], [16], the absorption cross-section of HBQ should be high enough to initiate the propagation with incoherent light, in particular for a cavity with a thin silver top mirror, which is more than 50 % transparent at the required wave length (Figure S4, SM).

Acknowledgments: We thank Jussi Toppari, Johannes Feist and Ruth Tichauer for fruitful discussions. We thank Arpan Dutta for sharing the absorption spectrum of HBQ in PMMA and Dmitry Morozov for computing the potential energy profiles of proton transfer in HBQ. We thank the Center for Scientific Computing (CSC-IT Center for Science) for very generous computer resources.

Research funding: This work was supported by the Academy of Finland (DOI: 10.13039/501100002341, Grants 323996 and 332743).

Author contributions: G.G. acquired funding; I.S and G.G. performed the Molecular Dynamics simulations. I.S. analysed the data and prepared the figures; G.G. drafted the manuscript, which both authors revised and edited. Both authors have accepted responsibility for the entire content of this manuscript and approved its submission.

Conflict of interest: Authors state no conflicts of interest.

Data availability: The datasets generated and/or analyzed during the current study are available from the corresponding author upon reasonable request.

References

[1] O. V. Mikhnenko, P. W. M. Blom, and T.-Q. Nguyen, “Exciton diffusion in organic semiconductors,” *Energy Environ. Sci.*, vol. 8, no. 7, pp. 1867—1888, 2015.

[2] J. B. Aladekomo, S. Arnold, and M. Pope, “Triplet exciton diffusion and double photon absorption in tetracene,” *Phys. Status Solidi*, vol. 80, no. 1, pp. 333—340, 1977.

[3] G. M. Akselrod, *et al*, “Visualization of exciton transport in ordered and disordered molecular solids,” *Nat. Commun.*, vol. 5, no. 1, p. 3646, 2014.

[4] A. Sneyd, *et al*, “Efficient energy transport in an organic semiconductor mediated by transient exciton delocalization,” *Sci. Adv.*, vol. 7, no. 32, p. eabh4232, 2021.

[5] F. F. Kong, *et al*, “Wavelike electronic energy transfer in donor—acceptor molecular systems through quantum coherence,” *Nat. Nanotechnol.*, vol. 17, no. 1, pp. 729—736, 2022.

[6] A. J. Sneyd, D. Beljonne, and A. Rao, “A new Frontier in exciton transport: transient delocalization,” *J. Chem. Phys. Lett.*, vol. 13, no. 29, pp. 6820—6830, 2022.

[7] S. Stäter, *et al*, “Directed gradients in the excited-state energy landscape of poly(3-hexylthiophene) nanofibers,” *J. Am. Chem. Soc.*, vol. 145, no. 25, p. 13 780-13 787, 2023.

[8] G. Lerario, *et al*, “High-speed flow of interacting organic polaritons,” *Light Sci. Appl.*, vol. 6, no. 1, p. e16212, 2017.

[9] G. G. Rozenman, K. Akulov, A. Golombek, and T. Schwartz, “Long-range transport of organic exciton-polaritons revealed by

ultrafast microscopy," *ACS Photonics*, vol. 5, no. 1, pp. 105—110, 2018.

[10] S. Hou, *et al*., "Ultralong-range energy transport in a disordered organic semiconductor at room temperature via coherent exciton-polariton propagation," *Adv. Mater.*, vol. 32, no. 28, p. 2002127, 2020.

[11] R. Pandya, *et al*, "Microcavity-like exciton-polaritons can be the primary photoexcitation in bare organic semiconductors," *Nat. Commun.*, vol. 12, no. 1, p. 6519, 2021.

[12] M. Wurdack, *et al*, "Motional narrowing, ballistic transport, and trapping of room-temperature exciton polaritons in an atomically-thin semiconductor," *Nat. Commun.*, vol. 12, no. 1, p. 5366, 2021.

[13] M. A. Berghuis, *et al*, "Controlling exciton propagation in organic crystals through strong coupling to plasmonic nanoparticle arrays," *ACS Photonics*, vol. 9, no. 7, p. 123, 2022.

[14] R. Pandya, *et al*, "Tuning the coherent propagation of organic exciton-polaritons through dark state delocalization," *Adv. Sci.*, vol. 9, no. 18, p. 2105569, 2022.

[15] D. Xu, *et al*, "Ultrafast imaging of coherent polariton propagation and interactions," *Nat. Commun.*, vol. 14, no. 1, p. 3881, 2023.

[16] M. Balasubrahmaniyam, A. Simkovich, A. Golombek, G. Ankonina, and T. Schwartz, "Unveiling the mixed nature of polaritonic transport: from enhanced diffusion to ballistic motion approaching the speed of light," *Nat. Mater.*, vol. 22, no. 1, pp. 338—344, 2023.

[17] K. J. Vahala, "Optical microcavities," *Nature*, vol. 424, no. 1, pp. 839—846, 2003.

[18] V. M. Agranovich and Y. N. Gartstein, "Nature and dynamics of low-energy exciton polaritons in semiconductor microcavities," *Phys. Rev. B*, vol. 75, no. 7, p. 075302, 2007.

[19] M. Litinskaya, "Propagation and localization of polaritons in disordered organic microcavities," *Phys. Lett. A*, vol. 372, no. 21, pp. 3898—3903, 2008.

[20] J. Feist and F. J. Garcia-Vidal, "Extraordinary exciton conductance induced by strong coupling," *Phys. Rev. Lett.*, vol. 114, no. 19, p. 196402, 2015.

[21] J. Schachenmayer, C. Genes, E. Tignone, and G. Pupillo, "Cavity enhanced transport of excitons," *Phys. Rev. Lett.*, vol. 114, no. 19, p. 196403, 2015.

[22] G. Engelhardt and J. Cao, "Polariton localization and dispersion properties of disordered quantum emitters in multimode microcavities," *Phys. Rev. Lett.*, vol. 130, no. 21, p. 213602, 2023.

[23] G. J. R. Aroeira, K. Kairys, and R. F. Ribeiro, "Theoretical analysis of exciton wave packet dynamics in polaritonic wires," *J. Phys. Chem. Lett.*, vol. 14, no. 24, pp. 5681—5691, 2023.

[24] P. Törmä and W. L. Barnes, "Strong coupling between surface plasmon polaritons and emitters: a review," *Rep. Prog. Phys.*, vol. 78, no. 1, p. 013901, 2015.

[25] M. S. Rider and W. L. Barnes, "Something from nothing: linking molecules with virtual light," *Contemp. Phys.*, vol. 62, no. 4, pp. 217—232, 2022.

[26] D. G. Lidzey, D. D. C. Bradley, M. S. Skolnick, T. Virgili, S. Walker, and D. M. Whittaker, "Strong exciton-photon coupling in an organic semiconductor microcavity," *Nature*, vol. 395, no. 6697, pp. 53—55, 1998.

[27] V. M. Agranovich, M. Litinskaia, and D. G. Lidzey, "Cavity polaritons in microcavities containing disordered organic semiconductors," *Phys. Rev. B*, vol. 67, no. 8, p. 085311, 2003.

[28] M. Litinskaya, P. Reineker, and V. M. Agranovich, "Fast polariton relaxation in strongly coupled organic microcavities," *J. Lumin.*, vol. 110, no. 4, pp. 364—372, 2004.

[29] L. A. Martínez-Martínez, E. Eizner, S. Kéna-Cohen, and K. Yuemn-Zhou, "Triplet harvesting in the polaritonic regime: a variational polaron approach," *J. Chem. Phys.*, vol. 151, no. 5, p. 054106, 2019.

[30] P. Michetti and G. C. L. Rocca, "Polariton dynamics in disordered microcavities," *Phys. E*, vol. 40, no. 6, pp. 1926—1929, 2008.

[31] R. F. Ribeiro, "Multimode polariton effects on molecular energy transport and spectral fluctuations," *Commun. Chem.*, vol. 5, no. 1, p. 48, 2022.

[32] T. Freixanet, B. Sermage, A. Tiberj, and R. Planel, "In-plane propagation of excitonic cavity polaritons," *Phys. Rev. B*, vol. 61, no. 11, p. 7233, 2000.

[33] D. M. Myers, *et al*, "Polariton-enhanced exciton transport," *Phys. Rev. B*, vol. 98, no. 23, p. 235302, 2018.

[34] I. Sokolovskii, R. H. Tichauer, D. Morozov, J. Feist, and G. Groenhof, "Multi-scale molecular dynamics simulations of enhanced energy transfer in organic molecules under strong coupling," *Nat. Commun.*, vol. 14, no. 1, p. 6613, 2023.

[35] R. H. Tichauer, I. Sokolovskii, and G. Groenhof, "Tuning coherent propagation of organic exciton-polaritons through the cavity q-factor," *Adv. Sci.*, vol. 10, no. 33, p. 2302650, 2023.

[36] D. Wellnitz, G. Pupillo, and J. Schachenmayer, "Disorder enhanced vibrational entanglement and dynamics in polaritonic chemistry," *Commun. Phys.*, vol. 5, no. 1, p. 120, 2022.

[37] G. J. R. Aroeira, K. Kairys, and R. F. Ribeiro, "Coherent transient exciton transport in disordered polaritonic wires," *ArXiv:2311.07940*, 2023.

[38] J. A. Hutchison, T. Schwartz, C. Genet, E. Devaux, and T. W. Ebbesen, "Modifying chemical landscapes by coupling to vacuum fields," *Angew. Chem., Int. Ed.*, vol. 51, no. 7, pp. 1592—1596, 2012.

[39] C. H. Kim and T. Joo, "Coherent excited state intramolecular proton transfer probed by time-resolved fluorescence," *Phys. Chem. Chem. Phys.*, vol. 11, no. 44, p. 10 266-10 269, 2009.

[40] J. Lee, C. H. Kim, and T. Joo, "Active role of proton in excited state intramolecular proton transfer reaction," *J. Phys. Chem. A*, vol. 117, no. 7, pp. 1400—1405, 2013.

[41] H. L. Luk, J. Feist, J. J. Toppari, and G. Groenhof, "Multiscale molecular dynamics simulations of polaritonic chemistry," *J. Chem. Theory Comput.*, vol. 13, no. 9, pp. 4324—4335, 2017.

[42] R. H. Tichauer, J. Feist, and G. Groenhof, "Multi-scale dynamics simulations of molecular polaritons: the effect of multiple cavity modes on polariton relaxation," *J. Chem. Phys.*, vol. 154, no. 10, p. 104112, 2021.

[43] A. Warshel and M. Levitt, "Theoretical studies of enzymatic reactions: dielectric, electrostatic and steric stabilization of carbonium ion in the reaction of lysozyme," *J. Mol. Biol.*, vol. 103, no. 2, pp. 227—249, 1976.

[44] G. Groenhof, "Solving chemical problems with a mixture of quantum-mechanical and molecular mechanics calculations: nobel prize in chemistry 2013," *Angew. Chem., Int. Ed.*, vol. 52, no. 48, p. 12 489-12 491, 2013.

[45] P. Michetti and G. C. L. Rocca, "Polariton states in disordered organic microcavities," *Phys. Rev. B*, vol. 71, no. 11, p. 115320, 2005.

[46] E. T. Jaynes and F. W. Cummings, "Comparison of quantum and semiclassical radiation theories with application to the beam maser," *Proc. IEEE*, vol. 51, no. 1, pp. 89—109, 1963.

[47] M. Tavis and F. W. Cummings, “Approximate solutions for an n-molecule radiation-field Hamiltonian,” *Phys. Rev.*, vol. 188, no. 2, pp. 692—695, 1969.

[48] I. Sokolovskii and G. Groenhof, “Non-hermitian molecular dynamics of exciton-polaritons in lossy cavities,” *arXiv:2311.13453*, 2023.

[49] P. Hohenberg and W. Kohn, “Imhomogeneous electron gas,” *Phys. Rev.*, vol. 136, no. 3B, pp. 864—871, 1964.

[50] E. Runge and E. K. U. Gross, “Density-functional theory for time-dependent systems,” *Phys. Rev. Lett.*, vol. 52, no. 12, pp. 997—1000, 1984.

[51] S. Hirata and M. Head-Gordon, “Time-dependent density functional theory within the tamm—dancoff approximation,” *Chem. Phys. Lett.*, vol. 314, no. 3—4, pp. 291—299, 1999.

[52] A. D. Becke, “A new mixing of Hartree—Fock and local density-functional theories,” *J. Chem. Phys.*, vol. 98, no. 2, p. 1372, 1993.

[53] T. Yanai, D. P. Tew, and N. C. Handy, “A new hybrid exchange-correlation functional using the coulomb-attenuating method (cam-b3lyp),” *Chem. Phys. Lett.*, vol. 393, no. 1—3, pp. 51—57, 2004.

[54] R. Ditchfield, W. J. Hehre, and J. A. Pople, “Self-consistent molecular-orbital methods. ix. An extended Gaussian-type basis for molecular-orbital studies of organic molecules,” *J. Chem. Phys.*, vol. 54, no. 2, pp. 724—728, 1971.

[55] B. A. C. Horta, P. T. Merz, P. F. J. Fuchs, J. Dolenc, S. Riniker, and P. H. Hünenberger, “A gromos-compatible force field for small organic molecules in the condensed phase: the 2016h66 parameter set,” *J. Chem. Theory Comput.*, vol. 12, no. 8, pp. 3825—3850, 2016.

[56] V. N. Staroverov, G. E. Scuseria, J. Tao, and J. P. Perdew, “Comparative assessment of a new nonempirical density functional: molecules and hydrogen-bonded complexes,” *J. Chem. Phys.*, vol. 119, no. 23, pp. 12 129—12 137, 2003.

[57] D. Picconi, “Nonadiabatic quantum dynamics of the coherent excited state intramolecular proton transfer of 10-hydroxybenzo [h] quinoline,” *Photochem. Photobiol. Sci.*, vol. 20, no. 11, pp. 1455—1473, 2021.

[58] M. E. Casida, C. Jamorski, K. C. Casida, and D. R. Salahub, “Molecular excitation energies to high-lying bound states from time-dependent density-functional response theory: characterization and correction of the time-dependent local density approximation ionization threshold,” *J. Chem. Phys.*, vol. 108, no. 11, pp. 4439—4449, 1998.

[59] A. D. Becke, “Density-functional thermochemistry. v. systematic optimization of exchange-correlation functionals,” *J. Chem. Phys.*, vol. 107, no. 20, pp. 8554—8560, 1997.

[60] W. L. Jorgensen, J. Chandrasekhar, J. D. Madura, R. W. Impey, and M. L. Klein, “Comparison of simple potential functions for simulatin liquid water,” *J. Chem. Phys.*, vol. 79, no. 2, pp. 926—935, 1983.

[61] T. Schwartz, J. A. Hutchison, J. Leonard, C. Genet, S. Haacke, and T. W. Ebbesen, “Polariton dynamics under strong light-molecule coupling,” *ChemPhysChem*, vol. 14, no. 1, pp. 125—131, 2013.

[62] J. George, S. Wang, T. Chervy, A. Canaguier-Durand, G. Schaeffer, J.-M. Lehn, J. A. Hutchison, C. Genet, and T. W. Ebbesen, “Ultra-strong coupling of molecular materials: spectroscopy and dynamics,” *Faraday Discuss.*, vol. 178, pp. 281—294, 2015.

[63] L. Verlet, “Computer “experiments” on classical fluids. i. thermodynamical properties of Lennard—Jones molecules,” *Phys. Rev.*, vol. 159, no. 1, pp. 98—103, 1967.

[64] M. Boggio-Pasqua, C. F. Burmeister, M. A. Robb, and G. Groenhof, “Photochemical reactions in biological systems: probing the effect of the environment by means of hybrid quantum chemistry/molecular mechanics simulations,” *Phys. Chem. Chem. Phys.*, vol. 14, no. 22, pp. 7912—7928, 2012.

[65] I. S. Ulusoy and O. Vendrell, “Dynamics and spectroscopy of molecular ensembles in a lossy microcavity,” *J. Chem. Phys.*, vol. 153, no. 4, p. 044108, 2020.

[66] P. Antoniou, F. Suchanek, J. F. Varner, and J. J. Foley IV, “Role of cavity losses on nonadiabatic couplings and dynamics in polaritonic chemistry,” *J. Phys. Chem. Lett.*, vol. 11, no. 21, pp. 9063—9069, 2020.

[67] S. Felicetti, J. Fregoni, T. Schnappinger, S. Reiter, R. de Vivie-Riedle, and J. Feist, “Photoprotecting uracil by coupling with lossy nanocavities,” *J. Chem. Phys. Lett.*, vol. 11, no. 20, pp. 8810—8818, 2020.

[68] D. Hu, A. Mandal, B. M. Weight, and P. Huo, “Quasi-diabatic propagation scheme for simulating polariton chemistry,” *J. Chem. Phys.*, vol. 157, no. 19, p. 194109, 2022.

[69] B. Hess, C. Kutzner, D. van der Spoel, and E. Lindahl, “Gromacs 4: algorithms for highly efficient, load-balanced, and scalable molecular simulation,” *J. Chem. Theory Comput.*, vol. 4, no. 3, pp. 435—447, 2008.

[70] M. J. Frisch, *et al*., *Gaussiañ 16 Revision C.01*, Wallingford CT, Gaussian Inc, 2016.

[71] B. Hess, H. Bekker, H. J. C. Berendsen, and J. G. E. M. Fraaije, “LINCS: a linear constraint solver for molecular simulations,” *J. Comput. Chem.*, vol. 18, no. 12, pp. 1463—1472, 1997. Available at: .

[72] H. Kagel, M. Frohme, and J. Glökler, “Photoacids in biochemical applications,” *J. Cell. Biotechnol.*, vol. 4, no. 1—2, pp. 23—30, 2018.

[73] M. Kasha, “Characterization of electronic transitions in complex molecules,” *Discuss. Faraday Soc.*, vol. 9, pp. 14—19, 1950.

[74] G. M. Akselrod, E. R. Young, M. S. Bradley, and V. Bulović, “Lasing through a strongly-coupled mode by intra-cavity pumping,” *Opt. Express*, vol. 21, no. 10, p. 12 122-12 128, 2013.

[75] E. Eizner, L. A. Martínez-Martínez, J. Yuen-Zhou, and S. Kéna-Cohen, “Inverting singlet and triplet excited states using strong light-matter coupling,” *Sci. Adv.*, vol. 5, no. 12, p. aax4482, 2019.

[76] J. del Pino, J. Feist, and F. J. Garcia-Vidal, “Quantum theory of collective strong coupling of molecular vibrations with a microcavity mode,” *New J. Phys.*, vol. 17, no. 5, p. 053040, 2015.

[77] R. H. Tichauer, D. Morozov, I. Sokolovskii, J. J. Toppari, and G. Groenhof, “Identifying vibrations that control non-adiabatic relaxation of polaritons in strongly coupled molecule-cavity systems,” *J. Phys. Chem. Lett.*, vol. 13, no. 27, pp. 6259—6267, 2022.

Supplementary Material: This article contains supplementary material (https://doi.org/10.1515/nanoph-2023-0684).

DEPARTMENT OF CHEMISTRY, UNIVERSITY OF JYVÄSKYLÄ
RESEARCH REPORT SERIES

1. Vuolle, Mikko: Electron paramagnetic resonance and molecular orbital study of radical ions generated from (2.2)metacyclophane, pyrene and its hydrogenated compounds by alkali metal reduction and by thallium(III)trifluoroacetate oxidation. (99 pp.) 1976
2. Pasanen, Kaija: Electron paramagnetic resonance study of cation radical generated from various chlorinated biphenyls. (66 pp.) 1977
3. Carbon-13 Workshop, September 6-8, 1977. (91 pp.) 1977
4. Laihia, Katri: On the structure determination of norbornane polyols by NMR spectroscopy. (111 pp.) 1979
5. Nyrönen, Timo: On the EPR, ENDOR and visible absorption spectra of some nitrogen containing heterocyclic compounds in liquid ammonia. (76 pp.) 1978
6. Talvitie, Antti: Structure determination of some sesquiterpenoids by shift reagent NMR. (54 pp.) 1979
7. Häkli, Harri: Structure analysis and molecular dynamics of cyclic compounds by shift reagent NMR. (48 pp.) 1979
8. Pitkänen, Ilkka: Thermodynamics of complexation of 1,2,4-triazole with divalent manganese, cobalt, nickel, copper, zinc, cadmium and lead ions in aqueous sodium perchlorate solutions. (89 pp.) 1980
9. Asunta, Tuula: Preparation and characterization of new organometallic compounds synthesized by using metal vapours. (91 pp.) 1980
10. Sattar, Mohammad Abdus: Analyses of MCPA and its metabolites in soil. (57 pp.) 1980
11. Bibliography 1980. (31 pp.) 1981
12. Knuuttila, Pekka: X-Ray structural studies on some divalent 3d metal compounds of picolinic and isonicotinic acid N-oxides. (77 pp.) 1981
13. Bibliography 1981. (33 pp.) 1982
14. 6th National NMR Symposium, September 9-10, 1982, Abstracts. (49 pp.) 1982
15. Bibliography 1982. (38 pp.) 1983
16. Knuuttila, Hilkka: X-Ray structural studies on some Cu(II), Co(II) and Ni(II) complexes with nicotinic and isonicotinic acid N-oxides. (54 pp.) 1983
17. Symposium on inorganic and analytical chemistry May 18, 1984, Program and Abstracts. (100 pp.) 1984
18. Knuutinen, Juha: On the synthesis, structure verification and gas chromatographic determination of chlorinated catechols and guaiacols occuring in spent bleach liquors of kraft pulp mill. (30 pp.) 1984
19. Bibliography 1983. (47 pp.) 1984
20. Pitkänen, Maija: Addition of BrCl, B_2 and Cl_2 to methyl esters of propenoic and 2-butenoic acid derivatives and ^{13}C NMR studies on methyl esters of saturated aliphatic mono- and dichlorocarboxylic acids. (56 pp.) 1985
21. Bibliography 1984. (39 pp.) 1985
22. Salo, Esa: EPR, ENDOR and TRIPLE spectroscopy of some nitrogen heteroaromatics in liquid ammonia. (111 pp.) 1985

DEPARTMENT OF CHEMISTRY, UNIVERSITY OF JYVÄSKYLÄ
RESEARCH REPORT SERIES

23. Humppi, Tarmo: Synthesis, identification and analysis of dimeric impurities of chlorophenols. (39 pp.) 1985
24. Aho, Martti: The ion exchange and adsorption properties of sphagnum peat under acid conditions. (90 pp.) 1985
25. Bibliography 1985 (61 pp.) 1986
26. Bibliography 1986. (23 pp.) 1987
27. Bibliography 1987. (26 pp.) 1988
28. Paasivirta, Jaakko (Ed.): Structures of organic environmental chemicals. (67 pp.) 1988
29. Paasivirta, Jaakko (Ed.): Chemistry and ecology of organo-element compounds. (93 pp.) 1989
30. Sinkkonen, Seija: Determination of crude oil alkylated dibenzothiophenes in environment. (35 pp.) 1989
31. Kolehmainen, Erkki (Ed.): XII National NMR Symposium Program and Abstracts. (75 pp.) 1989
32. Kuokkanen, Tauno: Chlorocymenes and Chlorocymenenes: Persistent chlorocompounds in spent bleach liquors of kraft pulp mills. (40 pp.) 1989
33. Mäkelä, Reijo: ESR, ENDOR and TRIPLE resonance study on substituted 9,10-anthraquinone radicals in solution. (35 pp.) 1990
34. Veijanen, Anja: An integrated sensory and analytical method for identification of off-flavour compounds. (70 pp.) 1990
35. Kasa, Seppo: EPR, ENDOR and TRIPLE resonance and molecular orbital studies on a substitution reaction of anthracene induced by thallium(III) in two fluorinated carboxylic acids. (114 pp.) 1990
36. Herve, Sirpa: Mussel incubation method for monitoring organochlorine compounds in freshwater recipients of pulp and paper industry. (145 pp.) 1991
37. Pohjola, Pekka: The electron paramagnetic resonance method for characterization of Finnish peat types and iron (III) complexes in the process of peat decomposition. (77 pp.) 1991
38. Paasivirta, Jaakko (Ed.): Organochlorines from pulp mills and other sources. Research methodology studies 1988-91. (120 pp.) 1992
39. Veijanen, Anja (Ed.): VI National Symposium on Mass Spectrometry, May 13-15, 1992, Abstracts. (55 pp.) 1992
40. Rissanen, Kari (Ed.): The 7. National Symposium on Inorganic and Analytical Chemistry, May 22, 1992, Abstracts and Program. (153 pp.) 1992
41. Paasivirta, Jaakko (Ed.): CEOEC'92, Second Finnish-Russian Seminar: Chemistry and Ecology of Organo-Element Compounds. (93 pp.) 1992
42. Koistinen, Jaana: Persistent polychloroaromatic compounds in the environment: structure-specific analyses. (50 pp.) 1993
43. Virkki, Liisa: Structural characterization of chlorolignins by spectroscopic and liquid chromatographic methods and a comparison with humic substances. (62 pp.) 1993
44. Helenius, Vesa: Electronic and vibrational excitations in some

biologically relevant molecules. (30 pp.) 1993

45. Leppä-aho, Jaakko: Thermal behaviour, infrared spectra and x-ray structures of some new rare earth chromates(VI). (64 pp.) 1994
46. Kotila, Sirpa: Synthesis, structure and thermal behavior of solid copper(II) complexes of 2-amino-2- hydroxymethyl-1,3-propanediol. (111 pp.) 1994
47. Mikkonen, Anneli: Retention of molybdenum(VI), vanadium(V) and tungsten(VI) by kaolin and three Finnish mineral soils. (90 pp.) 1995
48. Suontamo, Reijo: Molecular orbital studies of small molecules containing sulfur and selenium. (42 pp.) 1995
49. Hämäläinen, Jouni: Effect of fuel composition on the conversion of fuel-N to nitrogen oxides in the combustion of small single particles. (50 pp.) 1995
50. Nevalainen, Tapio: Polychlorinated diphenyl ethers: synthesis, NMR spectroscopy, structural properties, and estimated toxicity. (76 pp.) 1995
51. Aittola, Jussi-Pekka: Organochloro compounds in the stack emission. (35 pp.) 1995
52. Harju, Timo: Ultrafast polar molecular photophysics of (dibenzylmethine)borondifluoride and 4-aminophthalimide in solution. (61 pp.) 1995
53. Maatela, Paula: Determination of organically bound chlorine in industrial and environmental samples. (83 pp.) 1995
54. Paasivirta, Jaakko (Ed.): CEOEC'95, Third Finnish-Russian Seminar: Chemistry and Ecology of Organo-Element Compounds. (109 pp.) 1995
55. Huuskonen, Juhani: Synthesis and structural studies of some supramolecular compounds. (54 pp.) 1995
56. Palm, Helena: Fate of chlorophenols and their derivatives in sawmill soil and pulp mill recipient environments. (52 pp.) 1995
57. Rantio, Tiina: Chlorohydrocarbons in pulp mill effluents and their fate in the environment. (89 pp.) 1997
58. Ratilainen, Jari: Covalent and non-covalent interactions in molecular recognition. (37 pp.) 1997
59. Kolehmainen, Erkki (Ed.): XIX National NMR Symposium, June 4-6, 1997, Abstracts. (89 pp.) 1997
60. Matilainen, Rose: Development of methods for fertilizer analysis by inductively coupled plasma atomic emission spectrometry. (41 pp.) 1997
61. Koistinen, Jari (Ed.): Spring Meeting on the Division of Synthetic Chemistry, May 15-16, 1997, Program and Abstracts. (36 pp.) 1997
62. Lappalainen, Kari: Monomeric and cyclic bile acid derivatives: syntheses, NMR spectroscopy and molecular recognition properties. (50 pp.) 1997
63. Laitinen, Eira: Molecular dynamics of cyanine dyes and phthalimides in solution: picosecond laser studies. (62 pp.) 1997
64. Eloranta, Jussi: Experimental and theoretical studies on some

quinone and quinol radicals. (40 pp.) 1997

65. Oksanen, Jari: Spectroscopic characterization of some monomeric and aggregated chlorophylls. (43 pp.) 1998
66. Häkkänen, Heikki: Development of a method based on laser-induced plasma spectrometry for rapid spatial analysis of material distributions in paper coatings. (60 pp.) 1998
67. Virtapohja, Janne: Fate of chelating agents used in the pulp and paper industries. (58 pp.) 1998
68. Airola, Karri: X-ray structural studies of supramolecular and organic compounds. (39 pp.) 1998
69. Hyötyläinen, Juha: Transport of lignin–type compounds in the receiving waters of pulp mills. (40 pp.) 1999
70. Ristolainen, Matti: Analysis of the organic material dissolved during totally chlorine-free bleaching. (40 pp.) 1999
71. Eklin, Tero: Development of analytical procedures with industrial samples for atomic emission and atomic absorption spectrometry. (43 pp.) 1999
72. Välisaari, Jouni: Hygiene properties of resol-type phenolic resin laminates. (129 pp.) 1999
73. Hu, Jiwei: Persistent polyhalogenated diphenyl ethers: model compounds syntheses, characterization and molecular orbital studies. (59 pp.) 1999
74. Malkavaara, Petteri: Chemometric adaptations in wood processing chemistry. (56 pp.) 2000
75. Kujala Elena, Laihia Katri, Nieminen Kari (Eds.): NBC 2000, Symposium on Nuclear, Biological and Chemical Threats in the 21st Century. (299 pp.) 2000
76. Rantalainen, Anna-Lea: Semipermeable membrane devices in monitoring persistent organic pollutants in the environment. (58 pp.) 2000
77. Lahtinen, Manu: *In situ* X-ray powder diffraction studies of Pt/C, CuCl/C and Cu_2O/C catalysts at elevated temperatures in various reaction conditions. (92 pp.) 2000
78. Tamminen, Jari: Syntheses, empirical and theoretical characterization, and metal cation complexation of bile acid-based monomers and open/closed dimers. (54 pp.) 2000
79. Vatanen, Virpi: Experimental studies by EPR and theoretical studies by DFT calculations of α-amino-9,10-anthraquinone radical anions and cations in solution. (37 pp.) 2000
80. Kotilainen, Risto: Chemical changes in wood during heating at 150-260 °C. (57 pp.) 2000
81. Nissinen, Maija: X-ray structural studies on weak, non-covalent interactions in supramolecular compounds. (69 pp.) 2001
82. Wegelius, Elina: X-ray structural studies on self-assembled hydrogen-bonded networks and metallosupramolecular complexes. (84 pp.) 2001
83. Paasivirta, Jaakko (Ed.): CEOEC’2001, Fifth Finnish-Russian Seminar: Chemistry and Ecology of Organo-Element Compounds. (163 pp.) 2001
84. Kiljunen, Toni: Theoretical studies on spectroscopy and

atomic dynamics in rare gas solids. (56 pp.) 2001

85. Du, Jin: Derivatives of dextran: synthesis and applications in oncology. (48 pp.) 2001
86. Koivisto, Jari: Structural analysis of selected polychlorinated persistent organic pollutants (POPs) and related compounds. (88 pp.) 2001
87. Feng, Zhinan: Alkaline pulping of non-wood feedstocks and characterization of black liquors. (54 pp.) 2001
88. Halonen, Markku: Lahon havupuun käyttö sulfaattiprosessin raaka-aineena sekä havupuun lahontorjunta. (90 pp.) 2002
89. Falábu, Dezsö: Synthesis, conformational analysis and complexation studies of resorcarene derivatives. (212 pp.) 2001
90. Lehtovuori, Pekka: EMR spectroscopic studies on radicals of ubiquinones Q-*n*, vitamin K_3 and vitamine E in liquid solution. (40 pp.) 2002
91. Perkkalainen, Paula: Polymorphism of sugar alcohols and effect of grinding on thermal behavior on binary sugar alcohol mixtures. (53 pp.) 2002
92. Ihalainen, Janne: Spectroscopic studies on light-harvesting complexes of green plants and purple bacteria. (42 pp.) 2002
93. Kunttu, Henrik, Kiljunen, Toni (Eds.): 4th International Conference on Low Temperature Chemistry. (159 pp.) 2002
94. Väisänen, Ari: Development of methods for toxic element analysis in samples with environmental concern by ICP-AES and ETAAS. (54 pp.) 2002
95. Luostarinen, Minna: Synthesis and characterisation of novel resorcarene derivatives. (200 pp.) 2002
96. Louhelainen, Jarmo: Changes in the chemical composition and physical properties of wood and nonwood black liquors during heating. (68 pp.) 2003
97. Lahtinen, Tanja: Concave hydrocarbon cyclophane π-prismands. (65 pp.) 2003
98. Laihia, Katri (Ed.): NBC 2003, Symposium on Nuclear, Biological and Chemical Threats – A Crisis Management Challenge. (245 pp.) 2003
99. Oasmaa, Anja: Fuel oil quality properties of wood-based pyrolysis liquids. (32 pp.) 2003
100. Virtanen, Elina: Syntheses, structural characterisation, and cation/anion recognition properties of nano-sized bile acid-based host molecules and their precursors. (123 pp.) 2003
101. Nättinen, Kalle: Synthesis and X-ray structural studies of organic and metallo-organic supramolecular systems. (79 pp.) 2003
102. Lampiselkä, Jarkko: Demonstraatio lukion kemian opetuksessa. (285 pp.) 2003
103. Kallioinen, Jani: Photoinduced dynamics of Ru(dcbpy)$_2$(NCS)$_2$ – in solution and on nanocrystalline titanium dioxide thin films. (47 pp.) 2004
104. Valkonen, Arto (Ed.): VII Synthetic Chemistry Meeting and XXVI Finnish NMR Symposium. (103 pp.) 2004

DEPARTMENT OF CHEMISTRY, UNIVERSITY OF JYVÄSKYLÄ
RESEARCH REPORT SERIES

105. Vaskonen, Kari: Spectroscopic studies on atoms and small molecules isolated in low temperature rare gas matrices. (65 pp.) 2004
106. Lehtovuori, Viivi: Ultrafast light induced dissociation of Ru(dcbpy)$(CO)_2I_2$ in solution. (49 pp.) 2004
107. Saarenketo, Pauli: Structural studies of metal complexing Schiff bases, Schiff base derived *N*-glycosides and cyclophane π-prismands. (95 pp.) 2004
108. Paasivirta, Jaakko (Ed.): CEOEC’2004, Sixth Finnish-Russian Seminar: Chemistry and Ecology of Organo-Element Compounds. (147 pp.) 2004
109. Suontamo, Tuula: Development of a test method for evaluating the cleaning efficiency of hard-surface cleaning agents. (96 pp.) 2004
110. Güneş, Minna: Studies of thiocyanates of silver for nonlinear optics. (48 pp.) 2004
111. Ropponen, Jarmo: Aliphatic polyester dendrimers and dendrons. (81 pp.) 2004
112. Vu, Mân Thi Hong: Alkaline pulping and the subsequent elemental chlorine-free bleaching of bamboo (*Bambusa procera*). (69 pp.) 2004
113. Mansikkamäki, Heidi: Self-assembly of resorcinarenes. (77 pp.) 2006
114. Tuononen, Heikki M.: EPR spectroscopic and quantum chemical studies of some inorganic main group radicals. (79 pp.) 2005
115. Kaski, Saara: Development of methods and applications of laser-induced plasma spectroscopy in vacuum ultraviolet. (44 pp.) 2005
116. Mäkinen, Riika-Mari: Synthesis, crystal structure and thermal decomposition of certain metal thiocyanates and organic thiocyanates. (119 pp.) 2006
117. Ahokas, Jussi: Spectroscopic studies of atoms and small molecules isolated in rare gas solids: photodissociation and thermal reactions. (53 pp.) 2006
118. Busi, Sara: Synthesis, characterization and thermal properties of new quaternary ammonium compounds: new materials for electrolytes, ionic liquids and complexation studies. (102 pp.) 2006
119. Mäntykoski, Keijo: PCBs in processes, products and environment of paper mills using wastepaper as their raw material. (73 pp.) 2006
120. Laamanen, Pirkko-Leena: Simultaneous determination of industrially and environmentally relevant aminopolycarboxylic and hydroxycarboxylic acids by capillary zone electrophoresis. (54 pp.) 2007
121. Salmela, Maria: Description of oxygen-alkali delignification of kraft pulp using analysis of dissolved material. (71 pp.) 2007
122. Lehtovaara, Lauri: Theoretical studies of atomic scale impurities in superfluid ^{4}He. (87 pp.) 2007
123. Rautiainen, J. Mikko: Quantum chemical calculations of structures, bonding, and spectroscopic properties of some sulphur and selenium iodine cations. (71 pp.) 2007
124. Nummelin, Sami: Synthesis, characterization, structural and

retrostructural analysis of self-assembling pore forming dendrimers. (286 pp.) 2008

125. Sopo, Harri: Uranyl(VI) ion complexes of some organic aminobisphenolate ligands: syntheses, structures and extraction studies. (57 pp.) 2008
126. Valkonen, Arto: Structural characteristics and properties of substituted cholanoates and *N*-substituted cholanamides. (80 pp.) 2008
127. Lähde, Anna: Production and surface modification of pharmaceutical nano- and microparticles with the aerosol flow reactor. (43 pp.) 2008
128. Beyeh, Ngong Kodiah: Resorcinarenes and their derivatives: synthesis, characterization and complexation in gas phase and in solution. (75 pp.) 2008
129. Välisaari, Jouni, Lundell, Jan (Eds.): Kemian opetuksen päivät 2008: uusia oppimisympäristöjä ja ongelmalähtöistä opetusta. (118 pp.) 2008
130. Myllyperkiö, Pasi: Ultrafast electron transfer from potential organic and metal containing solar cell sensitizers. (69 pp.) 2009
131. Käkölä, Jaana: Fast chromatographic methods for determining aliphatic carboxylic acids in black liquors. (82 pp.) 2009
132. Koivukorpi, Juha: Bile acid-arene conjugates: from photoswitchability to cancer cell detection. (67 pp.) 2009
133. Tuuttila, Tero: Functional dendritic polyester compounds: synthesis and characterization of small bifunctional dendrimers and dyes. (74 pp.) 2009
134. Salorinne, Kirsi: Tetramethoxy resorcinarene based cation and anion receptors: synthesis, characterization and binding properties. (79 pp.) 2009
135. Rautiainen, Riikka: The use of first-thinning Scots pine (*Pinus sylvestris*) as fiber raw material for the kraft pulp and paper industry. (73 pp.) 2010
136. Ilander, Laura: Uranyl salophens: synthesis and use as ditopic receptors. (199 pp.) 2010
137. Kiviniemi, Tiina: Vibrational dynamics of iodine molecule and its complexes in solid krypton - Towards coherent control of bimolecular reactions? (73 pp.) 2010
138. Ikonen, Satu: Synthesis, characterization and structural properties of various covalent and non-covalent bile acid derivatives of N/O-heterocycles and their precursors. (105 pp.) 2010
139. Siitonen, Anni: Spectroscopic studies of semiconducting single-walled carbon nanotubes. (56 pp.) 2010
140. Raatikainen, Kari: Synthesis and structural studies of piperazine cyclophanes – Supramolecular systems through Halogen and Hydrogen bonding and metal ion coordination. (69 pp.) 2010
141. Leivo, Kimmo: Gelation and gel properties of two- and three-component Pyrene based low molecular weight organogelators. (116 pp.) 2011
142. Martiskainen, Jari: Electronic energy transfer in light-harvesting complexes isolated from *Spinacia oleracea* and from three

photosynthetic green bacteria *Chloroflexus aurantiacus*, *Chlorobium tepidum*, and *Prosthecochloris aestuarii*. (55 pp.) 2011

143. Wichmann, Oula: Syntheses, characterization and structural properties of [O,N,O,X´] aminobisphenolate metal complexes. (101 pp.) 2011
144. Ilander, Aki: Development of ultrasound-assisted digestion methods for the determination of toxic element concentrations in ash samples by ICP-OES. (58 pp.) 2011
145. The Combined XII Spring Meeting of the Division of Synthetic Chemistry and XXXIII Finnish NMR Symposium. Book of Abstracts. (90 pp.) 2011
146. Valto, Piia: Development of fast analysis methods for extractives in papermaking process waters. (73 pp.) 2011
147. Andersin, Jenni: Catalytic activity of palladium-based nanostructures in the conversion of simple olefinic hydro- and chlorohydrocarbons from first principles. (78 pp.) 2011
148. Aumanen, Jukka: Photophysical properties of dansylated poly(propylene amine) dendrimers. (55 pp.) 2011
149. Kärnä, Minna: Ether-functionalized quaternary ammonium ionic liquids – synthesis, characterization and physicochemical properties. (76 pp.) 2011
150. Jurček, Ondřej: Steroid conjugates for applications in pharmacology and biology. (57 pp.) 2011
151. Nauha, Elisa: Crystalline forms of selected Agrochemical actives: design and synthesis of cocrystals. (77 pp.) 2012
152. Ahkola, Heidi: Passive sampling in monitoring of nonylphenol ethoxylates and nonylphenol in aquatic environments. (92 pp.) 2012
153. Helttunen, Kaisa: Exploring the self-assembly of resorcinarenes: from molecular level interactions to mesoscopic structures. (78 pp.) 2012
154. Linnanto, Juha: Light excitation transfer in photosynthesis revealed by quantum chemical calculations and exiton theory. (179 pp.) 2012
155. Roiko-Jokela, Veikko: Digital imaging and infrared measurements of soil adhesion and cleanability of semihard and hard surfaces. (122 pp.) 2012
156. Noponen, Virpi: Amides of bile acids and biologically important small molecules: properties and applications. (85 pp.) 2012
157. Hulkko, Eero: Spectroscopic signatures as a probe of structure and dynamics in condensed-phase systems – studies of iodine and gold ranging from isolated molecules to nanoclusters. (69 pp.) 2012
158. Lappi, Hanna: Production of Hydrocarbon-rich biofuels from extractives-derived materials. (95 pp.) 2012
159. Nykänen, Lauri: Computational studies of Carbon chemistry on transition metal surfaces. (76 pp.) 2012
160. Ahonen, Kari: Solid state studies of pharmaceutically important molecules and their derivatives. (65 pp.) 2012

DEPARTMENT OF CHEMISTRY, UNIVERSITY OF JYVÄSKYLÄ
RESEARCH REPORT SERIES

161. Pakkanen, Hannu: Characterization of organic material dissolved during alkaline pulping of wood and non-wood feedstocks. (76 pp.) 2012
162. Moilanen, Jani: Theoretical and experimental studies of some main group compounds: from closed shell interactions to singlet diradicals and stable radicals. (80 pp.) 2012
163. Himanen, Jatta: Stereoselective synthesis of Oligosaccharides by *De Novo* Saccharide welding. (133 pp.) 2012
164. Bunzen, Hana: Steroidal derivatives of nitrogen containing compounds as potential gelators. (76 pp.) 2013
165. Seppälä, Petri: Structural diversity of copper(II) amino alcohol complexes. Syntheses, structural and magnetic properties of bidentate amino alcohol copper(II) complexes. (67 pp.) 2013
166. Lindgren, Johan: Computational investigations on rotational and vibrational spectroscopies of some diatomics in solid environment. (77 pp.) 2013
167. Giri, Chandan: Sub-component self-assembly of linear and non-linear diamines and diacylhydrazines, formulpyridine and transition metal cations. (145 pp.) 2013
168. Riisiö, Antti: Synthesis, Characterization and Properties of Cu(II)-, Mo(VI)- and U(VI) Complexes With Diaminotetraphenolate Ligands. (51 pp.) 2013
169. Kiljunen, Toni (Ed.): Chemistry and Physics at Low Temperatures. Book of Abstracts. (103 pp.) 2013
170. Hänninen, Mikko: Experimental and Computational Studies of Transition Metal Complexes with Polydentate Amino- and Aminophenolate Ligands: Synthesis, Structure, Reactivity and Magnetic Properties. (66 pp.) 2013
171. Antila, Liisa: Spectroscopic studies of electron transfer reactions at the photoactive electrode of dye-sensitized solar cells. (53 pp.) 2013
172. Kemppainen, Eeva: Mukaiyama-Michael reactions with α-substituted acroleins – a useful tool for the synthesis of the pectenotoxins and other natural product targets. (190 pp.) 2013
173. Virtanen, Suvi: Structural Studies of Dielectric Polymer Nanocomposites. (49 pp.) 2013
174. Yliniemelä-Sipari, Sanna: Understanding The Structural Requirements for Optimal Hydrogen Bond Catalyzed Enolization – A Biomimetic Approach.(160 pp.) 2013
175. Leskinen, Mikko V: Remote β-functionalization of β’-keto esters. (105 pp.) 2014
176. 12th European Conference on Research in Chemistry Education (ECRICE2014). Book of Abstracts. (166 pp.) 2014
177. Peuronen, Anssi: N-Monoalkylated DABCO-Based N-Donors as Versatile Building Blocks in Crystal Engineering and Supramolecular Chemistry. (54 pp.) 2014
178. Perämäki, Siiri: Method development for determination and recovery of rare earth elements from industrial fly ash. (88 pp.) 2014

DEPARTMENT OF CHEMISTRY, UNIVERSITY OF JYVÄSKYLÄ
RESEARCH REPORT SERIES

179. Chernyshev, Alexander, N.: Nitrogen-containing ligands and their platinum(IV) and gold(III) complexes: investigation and basicity and nucleophilicity, luminescence, and aurophilic interactions. (64 pp.) 2014
180. Lehto, Joni: Advanced Biorefinery Concepts Integrated to Chemical Pulping. (142 pp.) 2015
181. Tero, Tiia-Riikka: Tetramethoxy resorcinarenes as platforms for fluorescent and halogen bonding systems. (61 pp.) 2015
182. Löfman, Miika: Bile acid amides as components of microcrystalline organogels. (62 pp.) 2015
183. Selin, Jukka: Adsorption of softwood-derived organic material onto various fillers during papermaking. (169 pp.) 2015
184. Piisola, Antti: Challenges in the stereoselective synthesis of allylic alcohols. (210 pp.) 2015
185. Bonakdarzadeh, Pia: Supramolecular coordination polyhedra based on achiral and chiral pyridyl ligands: design, preparation, and characterization. (65 pp.) 2015
186. Vasko, Petra: Synthesis, characterization, and reactivity of heavier group 13 and 14 metallylenes and metalloid clusters: small molecule activation and more. (66 pp.) 2015
187. Topić, Filip: Structural Studies of Nano-sized Supramolecular Assemblies. (79 pp.) 2015
188. Mustalahti, Satu: Photodynamics Studies of Ligand-Protected Gold Nanoclusters by using Ultrafast Transient Infrared Spectroscopy. (58 pp.) 2015
189. Koivisto, Jaakko: Electronic and vibrational spectroscopic studies of gold-nanoclusters. (63 pp.) 2015
190. Suhonen, Aku: Solid state conformational behavior and interactions of series of aromatis oligoamide foldamers. (68 pp.) 2016
191. Soikkeli, Ville: Hydrometallurgical recovery and leaching studies for selected valuable metals from fly ash samples by ultrasound-assisted extraction followed by ICP-OES determination. (107 pp.) 2016
192. XXXVIII Finnish NMR Symposium. Book of Abstracts. (51 pp.) 2016
193. Mäkelä, Toni: Ion Pair Recognition by Ditopic Crown Ether Based bis-Urea and Uranyl Salophen Receptors. (75 pp.) 2016
194. Lindholm-Lehto, Petra: Occurrence of pharmaceuticals in municipal wastewater treatment plants and receiving surface waters in Central and Southern Finland. (98 pp.) 2016
195. Härkönen, Ville: Computational and Theoretical studies on Lattice Thermal conductivity and Thermal properties of Silicon Clathrates. (89 pp.) 2016
196. Tuokko, Sakari: Understanding selective reduction reactions with heterogeneous Pd and Pt: climbing out of the black box. (85 pp.) 2016
197. Nuora, Piia: Monitapaustutkimus LUMA-Toimintaan liittyvissä oppimisympäristöissä tapahtuvista kemian oppimiskokemuksista. (171 pp.) 2016

DEPARTMENT OF CHEMISTRY, UNIVERSITY OF JYVÄSKYLÄ
RESEARCH REPORT SERIES

198. Kumar, Hemanathan: Novel Concepts on The Recovery of By-Products from Alkaline Pulping. (61 pp.) 2016
199. Arnedo-Sánchez, Leticia: Lanthanide and Transition Metal Complexes as Building Blocks for Supramolecular Functional Materials. (227 pp.) 2016
200. Gell, Lars: Theoretical Investigations of Ligand Protected Silver Nanoclusters. (134 pp.) 2016
201. Vaskuri, Juhani: Oppiennätyksistä opetussuunnitelman perusteisiin - lukion kemian kansallisen opetussuunnitelman kehittyminen Suomessa vuosina 1918-2016. (314 pp.) 2017
202. Lundell Jan, Kiljunen Toni (Eds.): 22nd Horizons in Hydrogen Bond Research. Book of Abstracts. 2017
203. Turunen, Lotta: Design and construction of halogen-bonded capsules and cages. (61 pp.) 2017
204. Hurmalainen, Juha: Experimental and computational studies of unconventional main group compounds: stable radicals and reactive intermediates. (88 pp.) 2017
205. Koivistoinen Juha: Non-linear interactions of femtosecond laser pulses with graphene: photo-oxidation, imaging and photodynamics. (68 pp.) 2017
206. Chen, Chengcong: Combustion behavior of black liquors: droplet swelling and influence of liquor composition. (39 pp.) 2017
207. Mansikkamäki, Akseli: Theoretical and Computational Studies of Magnetic Anisotropy and Exchange Coupling in Molecular Systems. (190 p. + included articles) 2018.
208. Tatikonda, Rajendhraprasad: Multivalent N-donor ligands for the construction of coordination polymers and coordination polymer gels. (62 pp.) 2018
209. Budhathoki, Roshan: Beneficiation, desilication and selective precipitation techniques for phosphorus refining from biomass derived fly ash. (64 pp.) 2018
210. Siitonen, Juha: Synthetic Studies on 1-azabicyclo[5.3.0]decane Alkaloids. (140 pp.) 2018
211. Ullah, Saleem: Advanced Biorefinery Concepts Related to Non-wood Feedstocks. (57 pp.) 2018
212. Ghalibaf, Maryam: Analytical Pyrolysis of Wood and Non-Wood Materials from Integrated Biorefinery Concepts. (106 pp.) 2018

DEPARTMENT OF CHEMISTRY, UNIVERSITY OF JYVÄSKYLÄ
DISSERTATIONS PUBLISHED IN THE JYU DISSERTATIONS RESEARCH SERIES

1. Bulatov, Evgeny: Synthetic and structural studies of covalent and non-covalent interactions of ligands and metal center in platinum(II) complexes containing 2,2′-dipyridylamine or oxime ligands. (58 pp.) 2019. JYU Dissertations 70.
2. Annala, Riia: Conformational Properties and Anion Complexes of Aromatic Oligoamide Foldamers. (80 pp.) 2019. JYU Dissertations 84.
3. Isoaho, Jukka Pekka: Dithionite Bleaching of Thermomechanical Pulp - Chemistry and Optimal Conditions. (73 pp.) 2019. JYU Dissertations 85.
4. Nygrén, Enni: Recovery of rubidium from power plant fly ash. (98 pp.) 2019. JYU Dissertations 136.
5. Kiesilä, Anniina: Supramolecular chemistry of anion-binding receptors based on concave macromolecules. (68 pp.) 2019. JYU Dissertations 137.
6. Sokolowska, Karolina: Study of water-soluble p-MBA-protected gold nanoclusters and their superstructures. (60 pp.) 2019. JYU Dissertations 167.
7. Lahtinen, Elmeri: Chemically Functional 3D Printing: Selective Laser Sintering of Customizable Metal Scavengers. (71 pp.) 2019. JYU Dissertations 175.
8. Larijani, Amir: Oxidative reactions of cellulose under alkaline conditions. (102 pp.) 2020. JYU Dissertations 217.
9. Kolari, Kalle: Metal-metal contacts in late transition metal polymers. (60 pp.) 2020. JYU Dissertations 220.
10. Kauppinen, Minttu: Multiscale computational investigation of catalytic properties of zirconia supported noble metals. (87 pp.) 2020. JYU Dissertations 231.
11. Ding, Xin: Halogen Bond in Crystal Engineering: Structural Studies on Crystals with Ruthenium Centered Complexes and 1-(4-Pyridyl)-4-thiopyridine Zwitterion as Halogen Bond Acceptors. (59 pp.) 2020. JYU Dissertations 323.
12. Neuvonen, Antti: Toward an Understanding of Hydrogen-Bonding Bifunctional Organocatalyst Conformations and Their Activity in Asymmetric Mannich Reactions. (77 pp.) 2020. JYU Dissertations 336.
13. Kortet, Sami: 2,5-Diarylpyrrolidines and Pyroglutamic-Acid-Derived 2-Diarylmethyl-5-Aryl-Pyrrolidines: Their Synthesis and Use in Asymmetric Synthesis. (221 pp.) 2020. JYU Dissertations 337.
14. Saarnio, Ville: Fluorescent probes, noble metal nanoparticles and their nanocomposites: detection of nucleic acids and other biological targets. (80 pp.) 2021. JYU Dissertations 361.
15. Chernysheva, Maria: σ-hole interactions: the effect of the donors and acceptors nature in selenoureas, thioureas, halogenated species, substituted benzenes, and their adducts. (72 pp.) 2021. JYU Dissertations 370.
16. Bulatova, Margarita: Noncovalent interactions as a tool for supramolecular self-assembly of metallopolymers. (62 pp.) 2021. JYU Dissertations 377.

DEPARTMENT OF CHEMISTRY, UNIVERSITY OF JYVÄSKYLÄ
DISSERTATIONS PUBLISHED IN THE JYU DISSERTATIONS RESEARCH SERIES

17. Romppanen, Sari: Laser-spectroscopic studies of rare earth element- and lithium-bearing minerals and rocks. (66 pp.) 2021. JYU Dissertations 393.
18. Kukkonen, Esa: Nonlinear optical materials through weak interactions and their application in 3D printing. (58 pp.) 2021. JYU Dissertations 441.
19. Kuosmanen, Riikka: The Effect of Structure on the Gel Formation Ability and the Properties of Bile Acid Based Supramolecular Organogels. (68 pp.) 2021. JYU Dissertations 465.
20. Reuna, Sini: Development of a Method for Phosphorus Recovery from Wastewaters. (67 pp.) 2022. JYU Dissertations 486.
21. Taipale, Essi: Synthetic and Structural Studies on the Effect of Non-Covalent Interactions on N(*sp2*)-Heterocyclic Molecules. (67 pp.) 2022. JYU Dissertations 496.
22. Järvinen, Teemu: Molecular Dynamics View on Matrix Isolation. (143 pp.) 2022. JYU Dissertations 544.
23. Kumar, Parveen: Synthesis and Structural Studies on Halogen(I) Complexes. (160 pp.) 2022. JYU Dissertations 549.
24. Forsblom, Samu: Design and Construction of Metal-Organic Polyhedra. (212 pp.) 2022. JYU Dissertations 569.
25. Korpelin, Ville: Computational Studies of Catalytic Active Site Properties and Reactions at the Metal–Oxide Interface. (78 pp.) 2022. JYU Dissertations 578.
26. Vuori, Hannu: Extending Benson Group Increment Theory to Compounds of Phosphorus, Silicon, and Boron with Computational Chemistry. (59 pp.) 2022. JYU Dissertations 581.
27. Pallerla, Rajanish: Studies Towards Synthesis of Favipiravir & Humilisin E. (139 pp.) 2023. JYU Dissertations 611.
28. Taponen, Anni: Radical-Ion Salts based on Thiazyls and Tetracyanoquinodimethane: Hysteretic Magnetic Bistability in a Multicomponent System. (66 pp.) 2023. JYU Dissertations 613.
29. Aho, Noora: Molecular Dynamics Simulations of Acids and Bases in Biomolecular Environments. (78 pp.) 2023. JYU Dissertations 614.
30. Sabooni Asre Hazer, Maryam: Electronic and Optical Properties of Gold Clusters with Carbene Ligands using Density Functional Theory Calculations. (68 pp.) 2023. JYU Dissertations 650.
31. Kinnunen, Virva-Tuuli: Improving the Accuracy of Single Particle ICP-MS Analyses of Au and Ag Nanoparticles. (67 pp.) 2023. JYU Dissertations 689.
32. Kulomäki, Suvi: Preconcentration, Speciation, and Determination of Mercury in Natural Waters by Inductively Coupled Plasma Mass Spectrometry. (61 pp.) 2023. JYU Dissertations 725.
33. Schirmer, Johanna: Effects of Two-Photon Oxidation for the Development of Graphene-Bio Interfaces. (69 pp.) 2023. JYU Dissertations 726.
34. Halmemies, Eelis: Chemical Changes in the Industrial Extractive-Containing Sidestreams of Norway Spruce (*Picea abies*) during Storage. (84 pp.) 2024. JYU Dissertations 737.

DEPARTMENT OF CHEMISTRY, UNIVERSITY OF JYVÄSKYLÄ
DISSERTATIONS PUBLISHED IN THE JYU DISSERTATIONS RESEARCH SERIES

35. Alaranta, Johanna: Synthesis of Monomethine Cyanine Dyes and Gold Nanoclusters and their Applications as Fluorescent Probes. (67 pp.) 2024. JYU Dissertations 766.
36. Chevigny, Romain: Out-of-equilibrium and in-equilibrium amino acid-based supramolecular gels: Transient self-assembly and hybrid materials. (79 pp.) 2024. JYU Dissertations 768.
37. Mahajan, Shreya: Exploring the Applicability of Amine-Containing Metal–Organic Frameworks on Direct Air Capture of Carbon Dioxide. (69 pp.) 2024. JYU Dissertations 819.
38. Lehmann, Annika: Experimental and Computational Studies of Reactive Main Group Species: Low-Coordinate Complexes, Multiple Bonding, and Hydrometallation. (65 pp.) 2024. JYU Dissertations 829.
39. Lempelto, Aku: Computational modelling of carbon dioxide reduction to methanol on heterogeneous zirconia-supported copper catalysts. (78 pp.) 2024. JYU Dissertations 839.